ATOMIC STRUCTURE AND NONELECTRONIC PROPERTIES
OF SEMICONDUCTORS

Nature of a Temperature Hysteresis of Effective Shear Modulus in Single-Crystal Silicon

A. V. Oleĭnich-Lysyuk^, B. I. Gutsulyak, and I. M. Fodchuk

National University, Chernovtsi, 58012 Ukraine
^e-mail: ss-dpt@chnu.cv.ua
Submitted June 29, 2004; accepted for publication September 30, 2004

Abstract—The behavior of the effective shear modulus G_{ef} and internal friction in Si is comprehensively studied in the temperature range in which an anomalous hysteresis $G_{ef}(T)$ exists. It is shown that this hysteresis is caused by mobile dislocations and that the pinning of these dislocations by radiation defects results in total blocking of the hysteresis. Metastable dynamics of the transformations responsible for the anomalous behavior of $G_{ef}(T)$ are detected. © 2005 Pleiades Publishing, Inc.

In our earlier studies, we showed that mechanical and mechanochemical treatment of single-crystal silicon surfaces during sample preparation causes an extraordinary "reverse" temperature hysteresis of the effective shear modulus G_{ef} [1]. Such an anomalous dependence $G_{ef}(T)$, which is accompanied by corresponding changes in the spectrum of elastic energy absorption, is typical of phase transformations. To our knowledge, this type of dependence has only been observed in systems exhibiting transformations resulting in the formation of incommensurate structures [2, 3]. The latter are formed in crystals in the form of intermediate (metastable) phases [2, 3]. Hence, in addition to stable modifications (to date, about ten polymorphic Si modifications have been detected), among which cubic and hexagonal (lonsdalite) modifications have been the most thoroughly studied [4–6], metastable polytype phases are formed in polymorphic silicon during directional plastic deformation [7]. Currently, it is known that metastable polytype structures can be formed in pure materials due to a coordinated motion of partial dislocations [8]. All of the above suggests that the observed "reverse" hysteresis of the modulus results from the formation of intermediate polytype phases in surface-deformed Si. If this assumption is valid, the "reverse" hysteresis should be metastable and depend heavily on the dislocation mobility. The objective of this study is to verify this assumption.

The samples to be studied were prepared according to the method described in [1]. The temperature and amplitude dependences of the internal friction and G_{ef} were measured at frequencies of 1–3 Hz in vacuum (~10^{-3} Pa) in the temperature range 20–450°C and at the strains $\gamma = 2$–7×10^{-5}. In order to change the state of the dislocation–impurity silicon structure, the samples were irradiated with ~18-MeV electrons and gamma-ray photons.

Figure 1 shows the temperature dependences of the squared frequency of the natural torsional vibrations $f^2 \propto G_{ef}$ occurring silicon after mechanical surface treatment followed by sample exposure at 200°C for an hour. It can be seen that the mechanical treatment of the surface initiates the anomalous hysteresis of the shear modulus in the range 20–200°C. The degree of hysteresis loop nonclosure at 100°C is 4.6%. Thermal annealing (TA) at 200°C does not qualitatively affect the hysteresis, though its loop narrows.

In contrast, TA at 400°C for an hour increases the "reverse" hysteresis loop almost to its initial value ($\Delta G_{ef}^T / G_{ef}^{20} = 4.1\%$ at 100°C). However, after such treatment at 200°C, $\Delta G_{ef}^T / G_{ef}^{20}$ increases almost three-
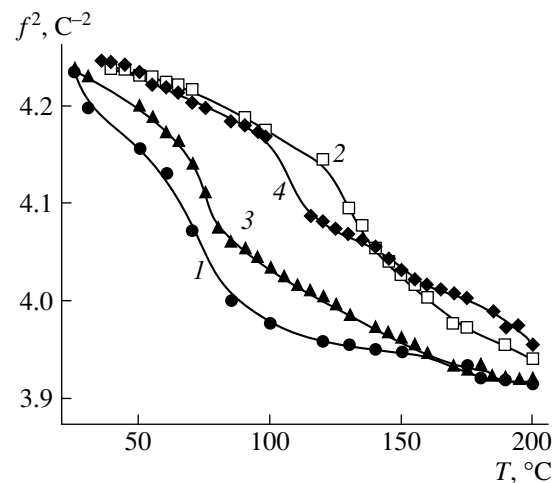

Fig. 1. Temperature dependences of f^2 in silicon ($f^2 \propto G_{ef}$) after mechanical treatment of its surface (*1, 2*) and 1-h annealing at 200°C (*3, 4*).
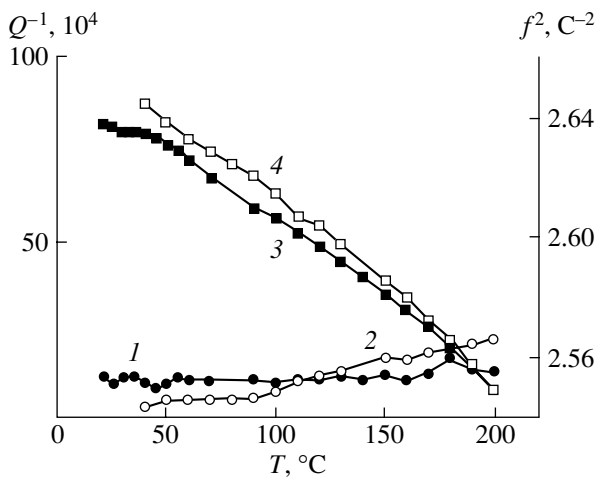
Fig. 2. Temperature dependences of the internal friction coefficient Q^{-1} (curves *1, 2*) and f^2 (*3, 4*) in silicon after chemical treatment and natural aging over one year; (*1, 3*) heating and (*2, 4*) cooling.
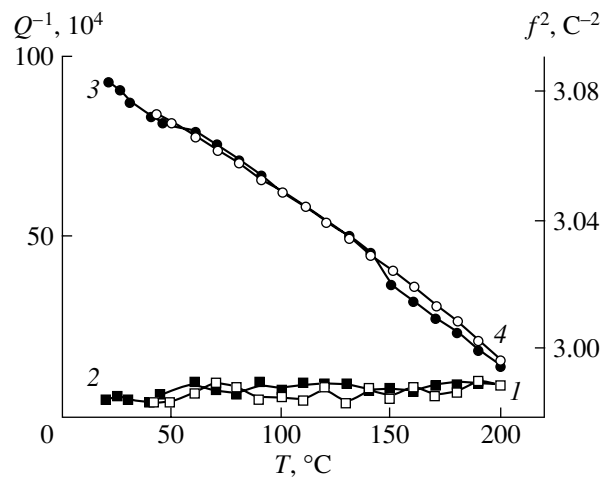

Fig. 3. Temperature dependences of the internal friction coefficient Q^{-1} (curves *1, 2*) and f^2 (*3, 4*) for silicon after exposure to an electron dose of 0.36 Mrad and the first heating; (*1, 3*) heating and (*2, 4*) cooling.

fold, which indicates an intensification of phase transformations at higher temperatures.

An analysis of the amplitude dependences of the internal friction and G_{ef} before and after the heat treatments showed that the state of the dislocation–impurity structure slightly changed as a result of TA. Immediately after the mechanical treatment, an increase in the strain amplitude γ produced an increase in internal friction and a decrease in G_{ef}, which is indicative of high dislocation mobility in mechanically treated silicon. After TA at 400°C, the internal friction, as well as γ, began to decrease gradually at unchanged $G_{ef}(\gamma)$, which apparently indicates a certain dislocation retardation at the oxygen precipitate particles [9]. The latter did not pin the dislocations but did limit their mobility.

Chemical treatment of the initial samples, used in practice to remove a deformed layer to a depth of 40–70 μm, somewhat changed both the amplitude and temperature dependences of the internal friction and G_{ef}: the internal friction decreased by a factor of 4–5 and the ratio $\Delta G_{ef}^T / G_{ef}^{20}$ decreased from 4.6 to 1.16% at 100°C. Furthermore, the rates of G_{ef} variation corresponding to the treatment amplitude and temperature became smaller. However, the influence of TA at 200 and 400°C on the elastic and inelastic characteristics of this group of samples generally remained unchanged but became less efficient. For example, annealing at 400°C, as in the former case, slightly decreased the dislocation mobility; however, this circumstance manifested itself only in a decrease in the curve slope $Q^{-1}(\gamma)$.

Natural aging of the chemically treated silicon samples at room-temperature over a one-year period caused an additional decrease in $\Delta G_{ef}^T / G_{ef}^{20}$ from 1.16 to 0.3% at 100°C, which may indicate that the formed structures have metastability (Fig. 2).

The heavy dependence of the magnitude and shape of the reverse hysteresis on the dislocation mobility led us to the hypothesis that this transformation may be decreased or totally blocked by immobilizing transformation dislocations, e.g., due to the formation of Cottrell atmospheres from second phase particles, radiation defects, and so on. In order to verify this assumption, Si samples exhibiting a pronounced reverse hysteresis G_{ef} in the range 20–200°C were irradiated.

The irradiation of these samples with high-energy (~18 MeV) electrons at a dose $D_e = 0.18$ Mrad led to an unexpected result: the reverse hysteresis of the shear modulus after the first heating of the irradiated material to 400°C extended to the entire range of 20 to 400°C. The behavior of the amplitude dependences indicated limited mobility of the dislocations pinned at primary and secondary radiation defects. In contrast, the behavior of the modulus $G_{ef}(\gamma)$ indicated rather high dislocation compliance. Apparently, dislocation loops, which are not involved in the formation of the amplitude dependences, were formed in Si during its irradiation with electrons. After the second heating to 400°C, the reverse hysteresis became "direct," which is typical of first-order phase transitions, and was also observed in almost the entire temperature range under study.

A twofold increase in the electron dose ($D_e = 0.36$ Mrad) resulted in appreciable suppression of the reverse hysteresis in the entire temperature range except for an insignificant difference between the curves above 140°C (Fig. 3). It should be noted that TA of these samples at 400°C did not restore the reverse hysteresis in the range 20–200°C; however, it formed another higher temperature reverse hysteresis in the range 250–350°C, which totally disappeared after irradiation with electrons and gamma-ray photons ($D_e = 0.36$ Mrad plus $D_\gamma = 0.04$ Mrad).

A comparative analysis of the amplitude dependences of the internal friction and G_{ef} after electron and combined irradiation shows that the electrons generate both point and dislocation-type defects in Si crystals, since Q^{-1} remains almost unchanged as γ increases, while G_{ef} decreases; moreover, the rates of these changes are different as the strain increases and decreases. This behavior of the shear modulus cannot be accounted for only by the generation of point defects in the structure: these effects are related to the dislocations. However, the newly generated dislocation defects are apparently not involved in the formation of superstructures, since this process initially blocks the formation of incommensurate structures (the reverse hysteresis transforms into a direct one) and then blocks the formation of commensurate structures as the electron dose increases (the hysteresis disappears in the entire temperature range). In this case, the hysteresis is partially restored in the range 250–350°C after irradiation with an electron dose $D_e = 0.36$ Mrad and TA at 400°C, but it is not restored after combined irradiation and TA in this range.

All of the above confirms the assumption on the dominant role of the dislocations and their neighborhood in the formation of a reverse temperature hysteresis G_{ef} in Si after mechanical treatment of the surface. Both types (low- and high-temperature) of temperature hysteresis G_{ef} bear a strong resemblance to the formation of multilayer metastable structures in their behavior and dependence on external factors [8]. These structures, as has already been noted, are observed in pure materials in the form of intermediate structures during polymorphic transformations unrelated to diffusion. However, confirmation of this assumption requires specially planned direct structural studies.

Thus, this study allows us to conclude the following:

(i) Mechanical treatment of a single-crystal Si surface gives rise to two regions in which the reverse hysteresis of the shear modulus manifests: low- (20–200°C) and high-temperature (250–350°C) regions.

(ii) The low-temperature reverse hysteresis of G_{ef} is metastable and depends heavily on the existence of mobile dislocations (it decreases as their mobility is lowered and is totally suppressed when the dislocations are pinned by radiation defects). The high-temperature hysteresis is formed during heat treatments at 400°C.

REFERENCES

1. A. V. Oleĭnich-Lysyuk, N. P. Beshleĭ, and I. M. Fodchuk, Fiz. Tekh. Poluprovodn. (St. Petersburg) **37**, 1337 (2003) [Semiconductors **37**, 1299 (2003)].

2. O. G. Vlokh, A. V. Kityk, O. M. Mokryĭ, and V. G. Gribik, Fiz. Tverd. Tela (Leningrad) **33**, 312 (1991) [Sov. Phys. Solid State **33**, 181 (1991)].

3. B. F. Borisov, T. Kraevskiĭ, A. K. Radzhabov, and E. V. Charnaya, Fiz. Tverd. Tela (St. Petersburg) **35**, 241 (1993) [Phys. Solid State **35**, 127 (1993)].

4. V. G. Eremenko and V. I. Nikitenko, Phys. Status Solidi A **14**, 317 (1972).

5. P. Pirouz, R. Chaim, and J. Samuels, Izv. Akad. Nauk SSSR, Ser. Fiz. **51**, 753 (1987).

6. S. F. Levitan, A. V. Prikhod'ko, and Yu. V. Sokolov, Ukr. Fiz. Zh. **35**, 1537 (1990).

7. I. M. Shmyt'ko, A. N. Izotov, N. S. Afonikova, *et al.*, Fiz. Tverd. Tela (St. Petersburg) **40**, 746 (1998) [Phys. Solid State **40**, 687 (1998)].

8. B. N. Nikolin, *Multilayer Structures and Polytypes in Metal Alloys* (Naukova Dumka, Kiev, 1984) [in Russian].

9. V. M. Babich, N. I. Bletskan, and E. F. Venger, *Oxygen in Single Crystals of Silicon* (Interpres, Kiev, 1997) [in Russian].

Translated by A. Kazantsev

ATOMIC STRUCTURE AND NONELECTRONIC PROPERTIES OF SEMICONDUCTORS

Phonon Scattering, Thermoelectric Power, and Thermal Conductivity Control in a Semiconductor–Metal Eutectic Composition

G. I. Isakov

Institute of Physics, National Academy of Sciences of Azerbaijan, Az-1143 Baku, Azerbaijan
e-mail: gudrat@physics.ab.az
Submitted May 31, 2004; accepted for publication November 25, 2004

Abstract—The thermoelectric power and thermal conductivity of a $GaSb–V_2Ga_5$ eutectic composition are studied. A characteristic feature of this composition is the formation of a V_2Ga_5 metal phase in the form of parallel whiskers in the GaSb semiconductor matrix during planar crystallization. New data are obtained on the scattering of long-wavelength phonons by metal whiskers and control of the thermoelectric power and thermal conductivity in semiconductor–metal eutectic compositions. © *2005 Pleiades Publishing, Inc.*

1. INTRODUCTION

The study of electron and phonon processes in semiconductors, their alloys, and compositions, as well as the control of these processes, is a fundamental problem of modern theoretical, experimental, and applied physics. Among the huge number of composite materials in existence, semiconductor–metal composites, in particular, III–V–metal ones, are of significant applied importance due to their potential applications as polarization filters of infrared (IR) radiation [1], galvanomagnetic [2] and thermomagnetic [3] sensors, and tensoresistors [4, 5].

In [5], we established that it is possible to control the tensometric parameters of semiconductor–metal eutectic compositions. It was later shown that the electrical properties of various samples taken from the same semiconductor–superconductor eutectic composition or of one sample are controllable in both a normal and a superconducting state [6, 7]. In [8], it was found that the thermal conductivity χ of $GaSb–V_2Ga_5$ and $InSb–NiSb$ eutectic compositions can be controlled by varying their growth rate. Such a study requires the growth of ingots with different compositions; moreover, it is important to control the thermoelectric power and thermal conductivity of these eutectic compositions using simple methods, as well as to simultaneously study the electron and phonon processes. One such method is based on varying the angle β between the heat flux direction Q and the direction of the parallel metal whiskers formed in the semiconductor matrix due planar crystallization.

The thermoelectric power and thermal conductivity in III–V–metal eutectic compositions was studied in [8–11]. However, the influence of metal phases on these parameters and processes, as well as the opportunity to control the thermoelectric power and thermal conductivity of semiconductor–metal eutectic compositions using simpler methods, was not explored.

Proceeding from the above-stated research, the aim of this study is control of the thermoelectric power α and thermal conductivity χ, and identification of the mechanism of phonon scattering in $GaSb–V_2Ga_5$ eutectic compositions for various angles β between the heat flux direction Q (temperature gradient direction ΔT) and the metal phase orientation X.

2. EXPERIMENTAL

The $GaSb–V_2Ga_5$ eutectic composition under study was prepared by direct alloying of GaSb that had first been purified by floating-zone melting (the hole concentration was $p = 1.3 \times 10^{17}$ cm^{-3} after purification) and by choosing the amount of V and Ga required to form the V_2Ga_5 compound. The alloying process was carried out in quartz cells pumped down to 10^{-5} Torr. The melt was subjected to vibration for 3 h at 800°C to attain complete homogeneity. Then, the composition melt was subjected to planar crystallization using the vertical Bridgman–Stockbarger method. A metallographic analysis using a MIM-8M microscope showed that the V_2Ga_5 metal phase in the GaSb matrix takes the form of whiskers of length $L \approx 200$–500 μm. Some of the V_2Ga_5 whiskers are of "infinite length"; i.e., they thread through the composition. The whisker diameter is $d \approx 1$–2 μm.

In order to measure the thermoelectric power and thermal conductivity, five samples in the shape of long parallelepipeds and $15 \times 3 \times 3$ mm in size were cut from the eutectic composition. The samples were cut so that angles β between the major axes Z of a parallelepiped and the crystallization (whisker) direction X were $\beta = 0°$, 20°, 45°, 70°, and 90°. When measuring the thermo-
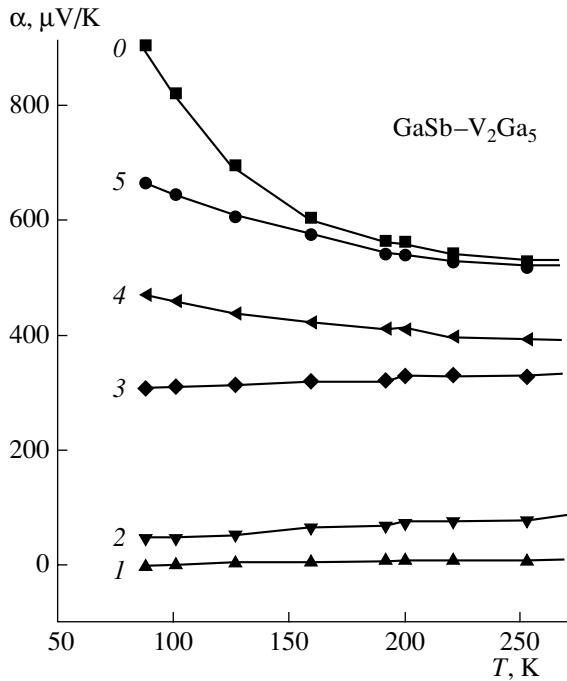
Fig. 1. Temperature dependences of the thermoelectric power α at the angles β = (*1*) 0°, (*2*) 20°, (*3*) 45°, (*4*) 70°, and (*5*) 90°; curve *0* corresponds to homogeneous GaSb.

electric power and thermal conductivity, the heat flux or temperature gradient direction should be parallel to Z ($Q \parallel Z$ and $\Delta T \parallel Z$).

Figures 1 and 2 show the temperature dependences of the GaSb–V$_2$Ga$_5$ thermoelectric power α and thermal conductivity χ, respectively, at various angles β. We can see that the thermoelectric power α and thermal conductivity χ of the GaSb–V$_2$Ga$_5$ eutectic composition can be controlled by varying the angle β between the heat flux direction Q and the metal-phase orientation Z:

$$\alpha_{\beta\,=\,0°} < \alpha_{\beta\,=\,20°} < \ldots < \alpha_{\beta\,=\,90°}, \tag{1}$$

$$\chi_{\beta\,=\,0°} > \chi_{\beta\,=\,20°} > \ldots > \chi_{\beta\,=\,90°}. \tag{2}$$

It can be seen in Fig.1 that α is controllable in the entire temperature range under study. However, the thermal conductivities (curves *1–5*) move closer to each other at $T > 300$ K. At $T = 400$ K, we have

$$\chi_1 = \chi_2 \ldots = \chi_5 \tag{3}$$

within the accuracy of thermal conductivity measurement ($\sigma \approx \pm 5\%$).

Figure 1 also shows the thermoelectric power of homogeneous GaSb with the hole concentration $p = 1.3 \times 10^{17}$ cm^{-3} (curve *0*, the hole concentration in GaSb–V$_2$Ga$_5$ is the same as in GaSb). We note that the thermal conductivity of GaSb–V$_2$Ga$_5$ (Fig. 2, curve *1*) is identical to that of GaSb (Fig. 2, curve *0*) at $\beta = 0°$ within the experimental error.
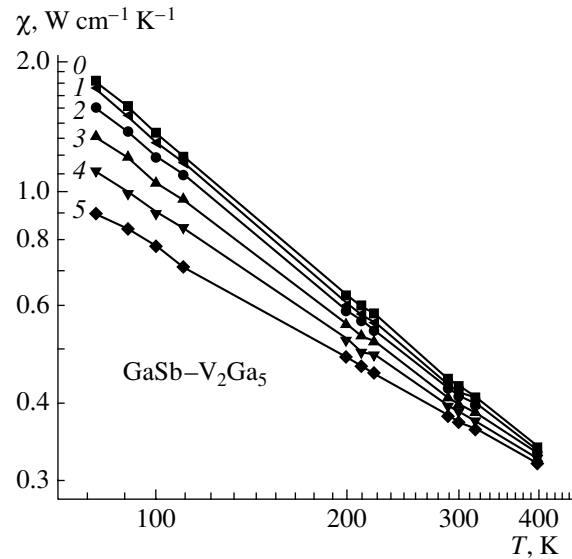
Fig. 2. Temperature dependences of the thermal conductivity χ at various angles β (the notation is the same as in Fig. 1).

3. DISCUSSION AND CONCLUSION

We can see in Fig. 1a that, below 200 K, as temperature decreases, the thermoelectric power increases in homogeneous GaSb (curve *0*) and in the GaSb–V$_2$Ga$_5$ eutectic composition when $\beta = 90°$ and 70° (curves *4*, *5*). This effect can be attributed to the drag of charge carriers by phonons.

The phonon-related fraction of the thermoelectric power is directly proportional to the relaxation time of long-wavelength phonons (see [12]),

$$\alpha_{ph} = \frac{1}{3}\frac{k_0}{e}\frac{m v^2}{k_0 T}\frac{\langle \tau_{ph} \rangle}{\tau_e}, \tag{4}$$

where $\langle \tau_{ph} \rangle$ is the average relaxation time of long-wavelength phonons, τ_e is the relaxation time of electrons, v is the velocity of sound in a crystal, and k_0 is the Boltzmann constant.

The average relaxation time of long-wavelength phonons is given by (see [12, 13])

$$\langle \tau_{ph} \rangle = \frac{1}{4k^4}\int_0^{2k} \tau_{ph} q^3 dq, \tag{5}$$

where

$$\tau_{ph}^{-1} = \frac{\hbar q}{\rho_0}\left(\frac{k_0 T}{\hbar v}\right)^4; \tag{6}$$

k and q are the electron and phonon wave vectors, respectively; and ρ_0 is the crystal density. By substitut-

ing expression (6) into formula (5), we derive the average relaxation time of long-wavelength phonons:

$$\langle \tau_{ph} \rangle = \frac{2\rho_0}{3\sqrt{2mk_0T}} \left(\frac{\hbar v}{k_0 T} \right)^4. \tag{7}$$

Using formula (7) for the mean free path of long-wavelength phonons, we obtain the following expression:

$$l = \frac{2\rho_0}{3\sqrt{2mk_0T}} \left(\frac{\hbar v}{k_0 T} \right)^4 v. \tag{8}$$

Calculations of the mean free path of long-wavelength phonons showed that $l = 2.4$ and $0.018\ \mu m$ at 100 and 300 K, respectively. Hence, the mean free path of long-wavelength phonons at low temperatures is comparable to the distance between metal inclusions, which intensively scatter long-wavelength phonons, $d \approx 1–5\ \mu m$. This fact explains the decrease in the phonon fraction of the thermoelectric power in GaSb–V_2Ga_5 at $\beta = 90°$ in comparison with homogeneous GaSb. It is known that the thermoelectric power consists of phonon and diffusion components:

$$\alpha = \alpha_{ph} + \alpha_d. \tag{9}$$

Considering that the scattering of long-wavelength phonons by metal phases should weaken as β decreases, α_{ph} should increase. However, the thermoelectric power α decreases as the angle β decreases due to the fact that, under these conditions, the electromotive force V_α is shunted in the temperature range $\alpha_d \gg \alpha_{ph}$. In this case, $V_{\alpha_{ph}}$ induced by dragged charge carriers is also shunted.

The generalized conductivity of heterogeneous systems was calculated by Odelevskiĭ in [14]. He derived corresponding formulas for the directions perpendicular and parallel to the second-phase inclusions. These formulas can also be used to calculate the thermal conductivity of heterogeneous systems. In this case, the formulas are written as

$$\chi_\perp = \chi_1 \left(1 + \frac{\psi}{\dfrac{1-\psi}{2} + \dfrac{\chi_1}{\chi_2 - \chi_1}} \right), \tag{10}$$

$$\chi_\parallel = \chi_2 \left(1 + \frac{\psi}{\dfrac{\chi_1}{\chi_2 - \chi_1}} \right), \tag{11}$$

where $\chi_\perp$ and $\chi_\parallel$ are the thermal conductivities of eutectic compositions at $\beta = 90°$ and $0°$; χ_1 and χ_2 are the thermal conductivities of the semiconductor matrix and metal phase; and $\psi = V_m/V_{sm}$ is the ratio of metal and semiconductor phase volumes, respectively. In GaSb–V_2Ga_5, $\psi = 0.04$. By substituting this value into formulas (10) and (11) and disregarding small terms, we obtain $\chi_\perp \approx \chi_1$ and $\chi_\parallel \approx \chi_1$; hence, $\chi_\perp \approx \chi_\parallel$. We obtained the equality $\chi_\parallel \approx \chi_0$ under experimental conditions. However, our results showed that $\chi_\perp \neq \chi_1$ and $\chi_\parallel \neq \chi_\parallel$ (see Fig. 2). Apparently, these inequalities, which allow the control of the parameter χ, are also related to the scattering of long-wavelength phonons by metal phases at $\beta \neq 0$. The equality $\chi_\parallel \approx \chi_1$ shows that the contribution of the metal phases to the generalized thermal conductivity at small ψ is negligible and its value is within the error of the thermal conductivity $\chi_\parallel$ measurement.

It should be noted that the phonons in metal phases can also be scattered by whisker tips at $\beta = 0°$. Therefore, the thermal resistance ΔW_1 can also manifest itself in the longitudinal direction. We note that the metal phases are also involved in heat transfer at $\beta = 0°$. If we assume that the thermal conductivity of a metal phase is larger than that of the semiconductor matrix, $\chi_2 > \chi_1$, this metal phase should additionally contribute to the generalized thermal conductivity. Nevertheless, the equality $\chi_\parallel \approx \chi_1$ shows that $\Delta W_\parallel$ is fully compensated by $\Delta \chi_2$, and $\Delta W_\parallel = 1/\Delta \chi_2$. However, the longitudinal size L of the metal phases are much larger than their lateral sizes, $L \gg d$ ($L/d = 50–\infty$). Hence, when the heat flux is perpendicular to the metal phases ($\beta = 90°$), they scatter phonons more intensively. In comparison with $\beta = 0°$, the additional thermal resistance $\Delta W_\perp \gg \Delta W_\parallel$ at $\beta = 90°$.

If the heat flux is parallel to the metal phases, the thermoelectric power is given by (see [15])

$$\alpha_\parallel = \alpha_1 + \frac{\rho_1(1+\psi)(\alpha_2 - \alpha_1)}{\rho_1(1+\psi) + \rho_2(1+\psi)/\psi}. \tag{12}$$

When the heat flux is perpendicular to the metal phases (see [11]),

$$\alpha_\perp = \alpha_1 + \frac{\rho_1 \left\{ \alpha_1 \left[1 - \left(\dfrac{\psi}{1+\psi} \right)^{\frac{1}{2}} + \alpha_2 \left(\dfrac{\psi}{1+\psi} \right)^{\frac{1}{2}} \right] - \alpha_1 \right\}}{1 - \left(\dfrac{\psi}{1+\psi} \right)^{\frac{1}{2}} \left(\rho_1 \left\{ \left[1 - \left(\dfrac{\psi}{1+\psi} \right)^{\frac{1}{2}} \right]^{-1} + 1 - \left(\dfrac{\psi}{1+\psi} \right)^{\frac{1}{2}} \right\} + \rho_2 \right)}, \tag{13}$$

where α_1 and α_2 are thermoelectric powers, and ρ_1 and ρ_2 are the resistivities of the semiconductor matrices and metal phases, respectively.

By substituting $\psi = 0.04$ into formulas (12) and (13) and disregarding small terms, we obtain $\alpha_\parallel \approx \alpha_2$ and $\alpha_\perp \approx \alpha_2$. These equalities show that the thermoelectric power in semiconductor–metal eutectic compositions with a low bulk content of metal phases is close to that of metals at $\beta = 0°$. At $\beta = 90°$, the value of $\alpha_\perp$ is close the thermoelectric power of the semiconductor matrix, as is experimentally confirmed. (See Fig. 1, curves *1* and *5*, respectively.) Based on the above, formulas for the control of the thermoelectric power and thermal conductivity of eutectic compositions at any β can be written as

$$\alpha_\beta \;=\; \alpha_\perp \sin^2\beta + \alpha_\parallel \cos^2\beta, \qquad (14)$$

$$\chi_\beta \;=\; \chi_\parallel \sin^2\beta + \chi_\perp \cos^2\beta. \qquad (15)$$

Thus, the possibility of controlling the thermoelectric power and thermal conductivity of semiconductor–metal eutectic compositions by varying the angle β between the heat flux Q and metal whiskers is established. It is shown that control of the thermal conductivity and weakening of the effect of carrier drag by phonons in semiconductor–metal eutectic compositions is due to a unified mechanism of long-wavelength phonon scattering by whisker crystals. The control of the thermoelectric power can be attributed to shunting of the voltage V_α by the metal whiskers.

ACKNOWLEDGMENTS

REFERENCES

1. B. Paul and H. Weiss, Solid-State Electron. **7**, 835 (1964).
2. G. N. Evstaf'eva, Élektron. Tekh., Ser. 6: Materialy **3** (118), 85 (1978).
3. O. Mosanov, E. Egennazarov, and O. Ismailov, Izv. Akad. Nauk Turkm. SSR, Ser. Fiz.–Tekh. Khim. Geol. Nauk **3**, 115 (1976).
4. M. I. Aliev, Z. A. Dzhafarov, and A. É. Agasiev, Prib. Sist. Upr., No. 2, 27 (1977).
5. G. I. Isakov, Pis'ma Zh. Tekh. Fiz. **22** (24), 71 (1996) [Tech. Phys. Lett. **22**, 1032 (1996)].
6. G. I. Isakov, Pis'ma Zh. Tekh. Fiz. **29** (19), 40 (2003) [Tech. Phys. Lett. **29**, 810 (2003)].
7. G. I. Isakov, Prikl. Fiz. **6**, 45 (2003).
8. M. I. Aliev, G. I. Isakov, É. A. Isaeva, and I. M. Aliev, Fiz. Tekh. Poluprovodn. (St. Petersburg) **30**, 1871 (1996) [Semiconductors **30**, 978 (1996)].
9. M. I. Aliev, S. G. Abdinova, and S. A. Aliev, Izv. Akad. Nauk SSSR, Neorg. Mater. **10**, 823 (1974).
10. M. I. Aliev and G. I. Isakov, Izv. Akad. Nauk SSSR, Neorg. Mater. **16**, 782 (1980).
11. M. I. Aliev, G. I. Isakov, and R. M. Dzhabbarov, in *Physical Properties of Compound Semiconductors* (Élm, Baku, 1982), p. 15 [in Russian].
12. A. I. Anselm, *Introduction to Semiconductor Theory* (Nauka, Moscow, 1978; Prentice-Hall, Englewood Cliffs, N.J., 1981).
13. V. M. Askerov, *Electronic Transport Phenomena in Semiconductors* (Nauka, Moscow, 1985) [in Russian].
14. B. I. Odelevskiĭ, Zh. Tekh. Fiz. **21**, 667 (1951).
15. W. K. Liebman and W. K. Miller, J. Appl. Phys. **34**, 2653 (1963).

Translated by A. Kazantsev

ATOMIC STRUCTURE AND NONELECTRONIC PROPERTIES OF SEMICONDUCTORS

The Influence of Oxygen on the Formation of Donor Centers in Silicon Layers Implanted with Erbium and Oxygen Ions

O. V. Aleksandrov*^, A. O. Zakhar'in**, and N. A. Sobolev**^^

*St. Petersburg State Electrotechnical University, St. Petersburg, 197376 Russia
^e-mail: Aleksandrov@svs.ru
**Ioffe Physicotechnical Institute, Russian Academy of Sciences, St. Petersburg, 194021 Russia
^^e-mail: nick.sobolev@mail.ioffe.ru
Submitted December 16, 2004; accepted for publication December 20, 2004

Abstract—A model of the formation of donor centers introduced by a combined implantation of Er^+ and O^+ ions into silicon with subsequent thermal annealing is developed. These centers are multiparticle erbium–oxygen complexes ErO_n with $n \geq 4$. The competing process of formation of electrically inactive oxygen clusters is taken into account. The model makes it possible to describe the dependence of the activation coefficient for the donor centers on the implantation dose of oxygen ions and, also, the effects of the oxygen ion implantation and annealing temperature on the concentration profiles of the donor centers. © 2005 Pleiades Publishing, Inc.

1. INTRODUCTION

Both optically active centers with a luminescence wavelength of 1.54 μm and donor centers are known to be formed in silicon as a result of an implantation of ions of the rare-earth element erbium with subsequent annealing (see reviews [1, 2]). The concentrations of both the erbium-containing optically active centers and the donor centers are higher in Czochralski grown silicon (Cz-Si) with a high oxygen concentration ($\sim 10^{18}$ cm^{-3}) than in silicon grown by the floating-zone method (fz-Si), in which case the oxygen concentration is low ($\leq 10^{16}$ cm^{-3}). The concentrations of both types of centers increase as a result an additional implantation of oxygen ions and correlate with each other, which indicates that oxygen atoms are involved in the formation of these erbium-containing optically active centers and donor centers [3, 4]. Emtsev *et al.* [5, 6] observed a variation in the activation energy of shallow-level donor centers as a result of the introduction of oxygen into silicon layers implanted with erbium ions. This variation is related to the formation of Er–O complexes and oxygen-containing quenched-in donors. The coefficient of activation f_a of the donor centers in the course of postimplantation annealing increases as the dose of oxygen ions increases and levels off at $f_a < 1$; in addition, the value of f_a decreases as the annealing temperature increases (the coefficient f_a is defined as $f_a = Q_a/Q_{Er}$, where Q_a is the integrated (sheet) electron concentration and Q_{Er} is the implantation dose of erbium ions) [7]. The structure of erbium–oxygen complexes has been studied using modern physical methods, i.e., an analysis of the extended X-ray absorption fine structure (EXAFS), electron-emission channeling, emission Mössbauer spectroscopy, and electron spin resonance [8–12]. It was established that erbium atoms are surrounded by interstitial oxygen atoms, whose number increases as the annealing duration and temperature increase [9, 12].

In one of our previous studies [13], we suggested a model of the activation of donor centers in silicon layers implanted with erbium and oxygen ions; in this model, it was assumed that the donor centers existed in the form of three types of erbium-containing complexes: erbium with oxygen Er–O, with a self-interstitial atom Er–I (I stands for self-interstitial atom), and with both oxygen and a self-interstitial atom Er–O–I. Multiparticle erbium–oxygen complexes and simultaneous clusterization of the oxygen atoms themselves, which proceeds at a high rate if radiation defects are present [14, 15], were disregarded. These shortcomings of the model meant that there was no way of explaining either the dependence of the activation coefficient for the donor centers on the oxygen-ion dose or the observed shift of the concentration profile of the donor centers towards the surface in the case of coimplantation of oxygen ions.

The objective of this study was to develop a model of the formation of erbium-containing donor centers in silicon (after an implantation of Er^+ and O^+ ions and subsequent thermal annealing) taking into account both the fact that the erbium–oxygen complexes can contain many oxygen atoms and the competing process of decomposition of the oxygen solid solution.

2. FORMULATION AND EQUATIONS OF THE MODEL

Various defects can be conducive to the decomposition of the oxygen solid solution in silicon layers implanted with erbium ions and doped with oxygen

during their growth and/or using coimplantation. This solution is supersaturated in Cz-Si even without an additional implantation of oxygen ions. The above defects primarily include erbium atoms that exhibit a pronounced oxygen affinity and can capture oxygen atoms [1, 2]. The resulting erbium–oxygen complexes are similar to oxygen-related quenched-in donors. These erbium–oxygen complexes, along with the oxygen-related quenched-in donors [16], introduce shallow donor levels with an ionization energy lower than 0.2 eV [5, 6] into the band gap. Both the quenched-in donors and the erbium–oxygen complexes [9, 12, 17] incorporate several oxygen atoms, whose number increases as the annealing temperature and duration increase. According to [18, 19], oxygen-related quenched-in donors are silicon clusters with a SiO_x composition, where the number of captured oxygen atoms x is no less than three to four. Similarly, we assume that erbium–oxygen complexes are electrically active erbium-containing donor centers and incorporate (as do the oxygen-related quenched-in donors) more than three oxygen atoms ($n \geq 4$).

The formation and growth of erbium–oxygen complexes ErO_n ($n = 1, 2, …, N$) is attained by adding free oxygen atoms to a free Er atom or to the previously formed complexes:

$$Er + O \longleftrightarrow ErO, \quad ErO + O \longleftrightarrow ErO_2, \dots$$
$$ErO_{n-1} + O \longleftrightarrow ErO_n. \qquad (1)$$
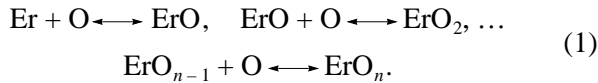
We disregard, in the model, the formation of clusters that incorporate several erbium atoms, since the diffusion length of erbium atoms does not exceed the mean distance between these atoms at the temperatures ($T \lesssim 900°C$) and durations ($t \lesssim 1$ h) of the annealing used to form optically active centers and donor centers.

Secondary radiation defects formed as a result of annealing can also be conducive to decomposition of the oxygen solid solution in implanted silicon layers. These defects include clusters of vacancies and interstitial atoms, dislocation loops, dislocations, microvoids, and disordered regions. It has been shown that decomposition of the oxygen solid solution is accelerated in silicon subjected to irradiation with high-energy electrons [14] and implantation with oxygen ions [15]. Accumulation of oxygen has been observed in silicon layers implanted with high-energy ions (F, Si, P, Ge, and As) and subjected to subsequent thermal annealing. This accumulation takes place not only in the region of the mean projected ion range R_p, where interstitial loops are located, but also at a depth that corresponds to $R_p/2$, where vacancy agglomerates are found [20, 21]. It is believed that the depth distribution of radiation defects corresponds to the distribution of both elastic energy losses and the number of displaced target atoms. Calculations [22] show that this distribution is shifted towards the surface with respect to the distribution of implanted ions; it is noteworthy that the peak in the distribution of radiation defects R_d depends on the ratio

between the masses of an ion and target atom and is located at a depth of $\sim 0.8 R_p$ for light ions (e.g., O^+) and $\sim 0.6 R_p$ for heavy ions (e.g., Er^+). It is important that the temperature T and duration t of the heat treatments typically used to form donor and optically active centers ($T = 700–900°C$ and $t = 0.5–1$ h) are insufficient for the formation of second-phase precipitates (e.g., SiO_2). Therefore, we assume that advanced precipitations are formed in the implanted layers. These precipitations consist of multiparticle oxygen clusters AO_m ($m = 1, 2, …, M$), where A are clusterization centers of radiation-related origin. The formation of larger precipitates occurs during the capture of free oxygen atoms by smaller precipitates; i.e.,

$$A + O \longleftrightarrow AO, \quad AO + O \longleftrightarrow AO_2, \dots,$$
$$AO_{m-1} + O \longleftrightarrow AO_m. \qquad (2)$$
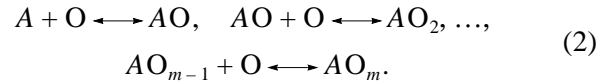
We assume that the oxygen clusters formed by the above mechanism at the centers of radiation-related origin are electrically inactive. It is worth noting that process (2) competes with process (1) for free oxygen atoms.

Since the diffusion coefficient for erbium atoms in silicon does not exceed 10^{-15} cm²/s at 900°C [2], which is three orders of magnitude smaller than the diffusion coefficient for oxygen atoms, the formation rate for erbium–oxygen complexes (as well as oxygen clusters) is controlled by the diffusion rate for oxygen atoms. This inference has been repeatedly proven for the decomposition of the oxygen solid solution in silicon (see, for example, review [23]). Therefore, the rate constants for direct reactions (1) and (2) can be written as

$$k_{fn} = 4\pi r_n D_{Ox}; \quad k_{fm} = 4\pi r_m D_{Ox},$$

where D_{Ox} is the diffusion coefficient for oxygen in silicon ($D_{Ox} = 0.13 \exp(-2.53 \text{ eV}/kT)$ [24]); k is the Boltzmann constant; T is temperature; and r_n and r_m are the radii of capture of oxygen atoms by erbium-containing complexes and oxygen clusters, respectively. We assume that the corresponding capture radii increase as the number of oxygen atoms in the erbium-containing complexes (n) and oxygen clusters (m) increases; specifically, we assume that

$$r_n = b(1+n)^{1/3}, \quad r_m = c(1+m)^{1/3},$$

where b and c are the capture radii when $n = 0$ and $m = 0$, respectively. The rate constants for the reverse reactions of those described by (1) and (2) are governed by the bonding energies of oxygen atoms in the erbium-containing complexes (E_W) and oxygen clusters (E_R), respectively; as a result, we have

$$k_{rn} = \nu_W \exp[-(E_W + E_D)/kT],$$
$$k_{rm} = \nu_R \exp[-(E_R + E_D)/kT],$$

where E_D is the activation energy for oxygen migration ($E_D = 2.53$ eV [24]), and ν_W and ν_R are the corresponding frequency factors.

In our previous model [13], we took into account formation of erbium-containing complexes involving self-interstitial silicon atoms produced as a result of annealing of radiation defects in the silicon lattice. However, the concentration of these complexes in Cz-Si, as well as in the case of coimplantation of oxygen ions, is much lower than the concentration in the erbium–oxygen complexes; therefore, complexes consisting of Er and interstitial Si atoms are disregarded in the model under consideration. It was established by Emtsev *et al.* [6] that a fraction of oxygen is involved in the formation of electrically inactive defects (most probably, oxygen precipitates) in the course of decomposition of the supersaturated oxygen solution in silicon. Therefore, in the model under consideration, we take into account the formation of electrically inactive oxygen clusters. As in the previous model [13], we disregarded the possible formation of both erbium–oxygen complexes that incorporate several erbium atoms and oxygen-related quenched-in donors.

The diffusion–kinetics equations of the model for free oxygen atoms, erbium–oxygen complexes, and oxygen clusters are written as

$$\frac{\partial C_{\text{Ox}}}{\partial t} = D_{\text{Ox}}\frac{\partial^2 C_{\text{Ox}}}{\partial x^2} - \sum_{n=1}^{N}(k_{fn}C_{\text{Ox}}C_{W\,n-1} - k_{rn}C_{Wn})$$
$$- \sum_{m=1}^{M}(k_{fm}C_{\text{Ox}}C_{R\,m-1} - k_{rm}C_{Rm}), \qquad (3)$$

$$\frac{\partial C_{Wn}}{\partial t} = k_{fn}C_{\text{Ox}}C_{W\,n-1} - k_{rn}C_{Wn}$$
$$- k_{f\,n+1}C_{\text{Ox}}C_{Wn} + k_{r\,n+1}C_{W\,n+1}, \qquad (4)$$

$$\frac{\partial C_{Rm}}{\partial t} = k_{fm}C_{\text{Ox}}C_{R\,m-1} - k_{rm}C_{Rm}$$
$$- k_{f\,m+1}C_{\text{Ox}}C_{Rm} + k_{r\,m+1}C_{R\,m+1}, \qquad (5)$$

where t is the annealing duration; x is the depth; C_{Ox} is the concentration of free (unbound) oxygen; C_{Wn} is the concentration of erbium-containing complexes ErO_n ($n = 1$–N); C_{Rm} is concentration of the oxygen clusters AO_m ($m = 1$–M); and C_{W0} and C_{R0} stand for the concentrations of free erbium and clusterization centers $C_A(x)$, respectively.

The Er atoms, their complexes ErO_n, and the oxygen clusters AO_m were assumed to be immobile. The initial concentrations of the erbium-containing complexes and oxygen clusters were assumed to be equal to zero. In accordance with the model, the coefficient of the donor-center activation was defined as $f_a = Q_a/Q_{\text{Er}}$, where Q_a is the integrated concentration of electrically active donor centers,

$$Q_a = \int \sum_{n=4}^{N} C_{Wn}dx,$$

and Q_{Er} is the integrated concentration of erbium in the form of free atoms and erbium-containing complexes,

$$Q_{\text{Er}} = \int \sum_{n=0}^{N} C_{Wn}dx.$$

Integration is performed over the entire region of interest, and the concentrations of all the components are low at the boundaries of this region. The largest possible number of oxygen atoms in the erbium-containing complexes N and oxygen clusters M was assumed to be equal to 20, since a further increase in N and M did not practically affect the solution.

3. RESULTS OF CALCULATIONS

System of Eqs. (3)–(5) was solved using the finite-difference method, specifically, the implicit difference scheme and sweep method for Eq. (3) and the Euler method for Eqs. (4) and (5). The solutions were sought taking into account the experimental conditions described in [7]. The implantation dose of erbium ions was $Q_{\text{Er}} = 10^{13}$ cm^{-2} and that of oxygen ions Q_{Ox} was varied from 10^{13} to 2×10^{14} cm^{-2}. The energies of the erbium ions (1 MeV) and oxygen ions (135 keV) were chosen so that the peaks of the concentration profiles for erbium and oxygen were located at the same depth $R_p \simeq 0.35$ μm. The annealing temperature was varied from 700 to 900°C, and the duration of the annealing was 30 min.

The initial oxygen profile was approximated by a Gaussian curve with the parameters $R_p = 0.35$ μm and $\Delta R_p = 0.09$ μm, where R_p is the mean projected range and ΔR_p is the projected-range standard deviation. In order to fit the experimental SIMS profile [7], we approximated the initial erbium profile using two half-Gaussian curves with the parameters $Q_1 = 0.72Q_{\text{Er}}$ and $\Delta R_{p1} = 0.09$ μm for $x \leq R_p$ and $Q_2 = 1.28Q_{\text{Er}}$ and $\Delta R_{p2} = 0.16$ μm for $x \geq R_p$ ($R_{p1} = R_{p2} = R_p = 0.35$ μm). The concentration profile $C_A(x)$ for the oxygen-clusterization centers in the implanted layer (this profile corresponded to the profile of residual radiation defects after implantation of the erbium and oxygen ions) was approximated by a Gaussian curve shifted towards the surface with respect to the profiles of the Er and O ions:

$$C_{A(x)} = \frac{Q_d}{\sqrt{2\pi}\Delta R_d}\exp\left[-\frac{(x - R_d)^2}{2\Delta R_d^2}\right]. \qquad (6)$$

Here, Q_d is the sheet concentration of residual intrinsic point defects; $Q_d = \chi_{\text{Er}}Q_{\text{Er}} + \chi_{\text{Ox}}Q_{\text{Ox}}$; χ_{Er} and χ_{Ox} are the

numbers of residual intrinsic point defects per incident erbium and oxygen ion, respectively; $\chi_{Er} = 3.1$ and $\chi_{Ox} = 1.25$ for the energies under consideration [25]; Q_{Er} and Q_{Ox} are the implantation doses of Er^+ and O^+ ions, respectively; and R_d and ΔR_d are the location of the peak and the width of the radiation-defects' distribution (we assumed that $R_d = 0.7 R_p$ and $\Delta R_d = \Delta R_p$).

We used the following values of the parameters in the calculation. The rate constants for direct and reverse reactions of oxygen clusterization (2) were determined from the requirement that the free-oxygen concentration in Cz-Si (the initial concentration was 10^{18} cm^{-3}) be equal to the concentration corresponding to the limiting oxygen solubility in silicon when equilibrium is established ($C_{eq} = 5.5 \times 10^{20} \exp(-0.89 \text{ eV}/kT)$ according to the data reported in [26]). We obtained $\nu_R = 3.6 \times 10^{14}$ s^{-1} if the values $E_R = 0.89$ eV (the enthalpy of the oxygen solubility) and $b = 4a$ ($a = 2.35$ Å is the interatomic distance in silicon) were used. An enhancement of decomposition of the oxygen solid solution in the implanted silicon layer [14, 15] was taken into account by increasing the constants of direct and reverse reactions (1) and (2) by an order of magnitude. The parameters to be determined were the capture radius and the rate constant for the reverse of reaction (1) relating to decomposition of erbium–oxygen complexes (donor centers); the concentration of these complexes were determined from the dose dependences of the activation coefficient for the donor centers at various temperatures.

In Fig. 1, we show the dependences of the activation coefficient for the donor centers on the implantation dose of O^+ ions at postimplantation annealing temperatures of 700, 800, and 900°C (the data reported in [7] were used). As can be seen from Fig. 1, the calculation based on the model and carried out using the parameters $c = 4a$, $\nu_W = 2.6 \times 10^{15}$ s^{-1}, and $E_W = 1.3$ eV makes it possible to describe both the increase in f_a and its leveling-off at a level lower than unity and the decrease in f_a as the annealing temperature increases. In the model under consideration, the leveling-off of the dose dependence of f_a at a level of $f_a < 1$ is attributed to the competing process of the capture of free-oxygen atoms by AO_m clusters rather than by the electrical inactivity of small erbium–oxygen clusters ErO_n with $n \le 3$. As the implantation dose of oxygen ions increases, ErO_n complexes in which the number n of oxygen atoms increases from three to four and oxygen clusters in which the number of oxygen atoms m increases from two to three are found to be prevalent after annealing at 700°C. As the annealing temperature increases to 900°C, the number of oxygen atoms is reduced to two or three in the ErO_n complexes and to two in the oxygen clusters. In all cases, the erbium–oxygen complexes ErO_n with $n = 4$ are the prevalent donor centers. A decrease in the activation coefficient f_a as the annealing temperature increases is attributed to the higher bonding
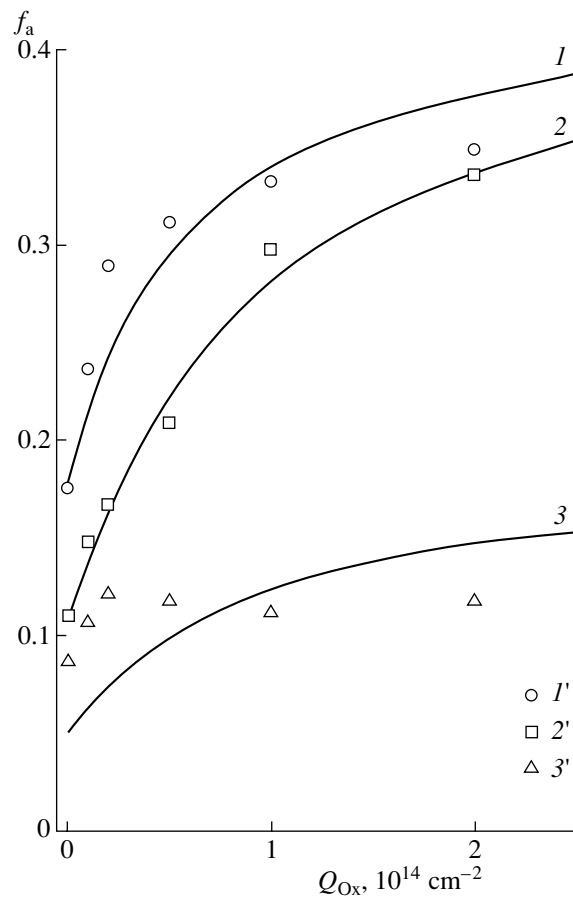

Fig. 1. Dependences of the activation coefficient for donor centers f_a on the implantation dose (Q_{Ox}) of O^+ ions. The annealing temperature is (*1*, *1'*) 700°C, (*2*, *2'*) 800°C, and (*3*, *3'*) 900°C. Solid lines *1–3* represent the results of calculation and symbols *1'–3'* correspond to the experimental data [7].

energy of the oxygen atoms in the ErO_n complexes (1.3 eV) than of those in the AO_m clusters (0.89 eV).

In the case of coimplantation of O^+ ions, not only is an increase in the concentration of donor centers at the peak of the distribution observed but also a shift of the profile of the donor centers from the region $x \gtrsim R_p$ towards the surface (Fig. 2a). Figure 2b illustrates the effect of coimplantation of oxygen ions on the concentration profiles of the donor centers after annealing at $T = 800$°C. As can be seen from Fig. 2b, the calculation makes it possible to describe the increase in the concentration of donor centers at the profile peak as the dose of oxygen ions increases as well as the shift of the profile of the donor centers towards the surface (to the region of the ion range R_p). This shift is related to the initial (at $Q_{Ox} = 0$) location of the profile of the donor centers beyond the region of R_p. In the context of the model, this position of the peak in the profile of the donor centers is attributed to a minimum in the distribu-
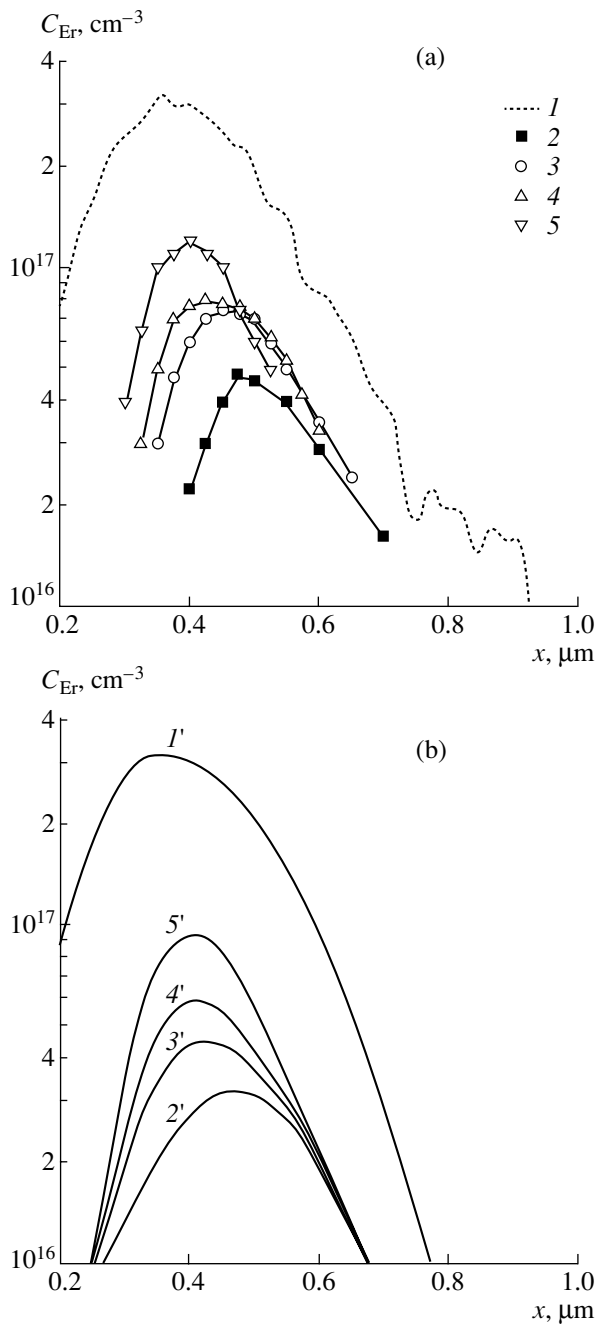
Fig. 2. (a) Experimental and (b) calculated concentration profiles of the Er atoms C_{Er} (curve *1* represents the data obtained by secondary-ion mass spectrometry and curve *1'* corresponds to the results of calculations) and donor centers C_a (curves *2–5, 2'–5'*). The coimplantation doses of O$^+$ ions are (*2, 2'*) 0, (*3, 3'*) 10^{13}, (*4, 4'*) 2×10^{13}, and (*5, 5'*) 5×10^{13} cm^{-2}. The annealing temperature is 800°C.

tion of free oxygen in the region where the radiation-induced centers of oxygen clusterization are located (at $x \simeq 0.7R_p$ in the case under consideration) (Fig. 3). After coimplantation of O$^+$ ions, the region in the vicinity of R_p becomes the source of free oxygen; as a result,
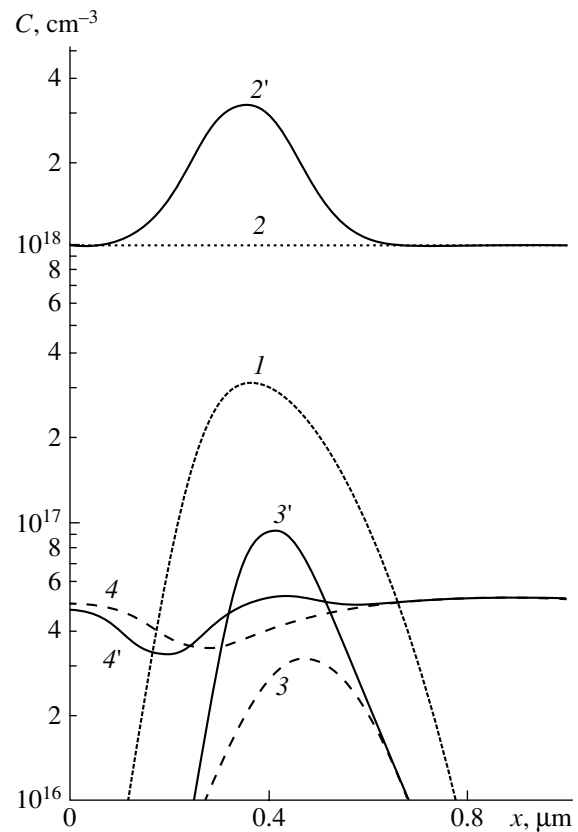
Fig. 3. Concentration profiles of (*1*) Er atoms and (*2, 2'*) oxygen atoms before annealing and of (*3, 3'*) donor centers and (*4, 4'*) oxygen atoms after annealing. The coimplantation doses of O$^+$ ions are (*2–4*) 0 and (*2'–4'*) 5×10^{13} cm^{-2}. The annealing temperature is 800°C.

the profile of the donor centers shifts towards this region (Figs. 2, 3).

In the model under consideration, it is assumed that the bonding energy E_W is independent of the number n of oxygen atoms in the ErO$_n$ complexes; this assumption is only an approximation. We can in fact expect a nonmonotonic (with a maximum) dependence of the bonding energy on the number of oxygen atoms in the erbium–oxygen complexes, as has previously been observed for oxygen clusters [18]. In this case, the obtained values of the bonding energy $E_W = 1.3$ eV and the frequency factor $\nu_W = 2.5 \times 10^{15}$ s^{-1} are effective and are more relevant to the complexes that have the largest number of oxygen atoms, i.e., to those with $n = 2$–4. If the bonding energy decreases at large values of n, we can expect a more pronounced tendency towards leveling-off of the dependence of the activation coefficient for the donor centers on the coimplantation dose of oxygen ions.

It is noteworthy that erbium diffusion is activated at annealing temperatures higher than 900°C; as a result, the formation of complexes that involve several

Er atoms, which is disregarded in the model under consideration, becomes possible.

4. CONCLUSION

We have developed a model of formation of donor centers in silicon layers coimplanted with Er^+ and O^+ ions. It is assumed that the donor centers are ErO_n complexes that contain more than three oxygen atoms. We take into account the fact that the donor centers in an implanted layer are formed simultaneously with electrically inactive oxygen clusters AO_m; secondary radiation defects play the role nucleation centers for these clusters. If the competing process of formation of oxygen clusters is taken into account, we can describe the leveling-off of the donor-center activation coefficient at values smaller than unity and the shift of the donors' concentration profile towards the surface (to the region of R_p) as the implantation dose of oxygen ions increases. A decrease in the activation coefficient as the annealing temperature increases is attributed to the fact that the bonding energy of oxygen atoms is higher in the ErO_n complexes (1.3 eV) than in the AO_m clusters (0.89 eV).

REFERENCES

1. N. A. Sobolev, Fiz. Tekh. Poluprovodn. (St. Petersburg) **29**, 1153 (1995) [Semiconductors **29**, 595 (1995)].

2. J. Michel, L. V. C. Assali, M. T. Morse, and L. C. Kimerling, Semicond. Semimet. **49**, 111 (1998).

3. F. Priolo, S. Coffa, G. Franzo, *et al.*, J. Appl. Phys. **74**, 4936 (1993).

4. N. A. Sobolev, A. M. Emel'yanov, Yu. A. Kudr'yavtsev, *et al.*, Solid State Phenom. **57–58**, 213 (1997).

5. V. V. Emtsev, V. V. Emtsev, Jr., D. S. Poloskin, *et al.*, Fiz. Tekh. Poluprovodn. (St. Petersburg) **33**, 1192 (1999) [Semiconductors **33**, 1084 (1999)].

6. V. V. Emtsev, Jr., C. A. J. Ammerlaan, B. A. Andreev, *et al.*, Solid State Phenom. **82–84**, 93 (2002).

7. O. V. Aleksandrov, A. O. Zakhar'in, N. A. Sobolev, and E. I. Shek, Izv. S.-Peterb. Gos. Élektrotekh. Univ., No. 516, 48 (1998).

8. D. L. Adler, D. C. Jacobson, D. J. Eaglesham, *et al.*, Appl. Phys. Lett. **61**, 2181 (1992).

9. A. Terrasi, G. Franzo, S. Coffa, *et al.*, Appl. Phys. Lett. **70**, 1712 (1997).

10. V. F. Masterov, F. S. Nasredinov, P. P. Seregin, *et al.*, Fiz. Tekh. Poluprovodn. (St. Petersburg) **32**, 708 (1998) [Semiconductors **32**, 636 (1998)].

11. J. D. Carrey, J. Phys.: Condens. Matter **14**, 8537 (2002).

12. U. Wahl, J. C. Correia, J. P. Araujo, *et al.*, Physica B (Amsterdam) **273–274**, 342 (1999).

13. O. V. Aleksandrov and A. O. Zakhar'in, Fiz. Tekh. Poluprovodn. (St. Petersburg) **36**, 1291 (2002) [Semiconductors **36**, 1209 (2002)].

14. T. Hallberg and J. L. Lindstrom, J. Appl. Phys. **72**, 5130 (1992).

15. H. Koyama, J. Appl. Phys. **51**, 3202 (1980).

16. V. V. Emtsev, Jr., G. A. Oganesyan, and K. Schmalz, Solid State Phenom. **47–48**, 259 (1996).

17. R. C. Newman, J. Phys.: Condens. Matter **12**, R335 (2000).

18. A. Ourmazd, W. Schroter, and A. Bourret, J. Appl. Phys. **56**, 1670 (1984).

19. M. Suezawa and K. Sumino, Phys. Status Solidi **82**, 235 (1984).

20. E. Chason, S. T. Picraux, J. M. Poate, *et al.*, J. Appl. Phys. **81**, 6513 (1997).

21. R. Krause-Rehberg, F. Borner, F. Redmann, *et al.*, Physica B (Amsterdam) **308–310**, 442 (2001).

22. I. A. Abroyan, A. N. Andronov, and A. I. Titov, *Physical Foundations of Electron- and Ion-Beam Technology* (Vysshaya Shkola, Moscow, 1984) [in Russian].

23. A. Borghesi, B. Pivac, A. Sassela, and A. Stella, J. Appl. Phys. **77**, 4169 (1995).

24. J. C. Mikkelsen, Mater. Res. Soc. Symp. Proc. **59**, 19 (1986).

25. L. Pelaz, G. H. Gilmer, M. Jaraiz, *et al.*, Appl. Phys. Lett. **73**, 1421 (1998).

26. W. Wijanarakula, Appl. Phys. Lett. **59**, 1185 (1991).

Translated by A. Spitsyn

ATOMIC STRUCTURE AND NONELECTRONIC PROPERTIES OF SEMICONDUCTORS

Stresses in Selectively Oxidized GaAs/(AlGa)$_x$O$_y$ Structures

S. A. Blokhin^, A. N. Smirnov, A. V. Sakharov, A. G. Gladyshev, N. V. Kryzhanovskaya, N. A. Maleev, A. E. Zhukov, E. S. Semenova, D. A. Bedarev, E. V. Nikitina, M. M. Kulagina, M. V. Maksimov, N. N. Ledentsov, and V. M. Ustinov

Ioffe Physicotechnical Institute, Russian Academy of Sciences, Politekhnicheskaya ul. 26, St. Petersburg, 194021 Russia
^e-mail: blokh@mail.ioffe.rssi.ru
Submitted December 7, 2004; accepted for publication December 22, 2004

Abstract—Raman scattering spectroscopy is used to study the process of selective oxidation of Al$_{0.97}$Ga$_{0.03}$As layers. Stresses arising in GaAs/(AlGa)$_x$O$_y$ layers as a result of selective oxidation under different conditions are determined. The effects of local heating of the samples with laser radiation during measurements of the Raman signals, photoresist hardening resulting from the oxidation, and overoxidation are analyzed. The instrumentation and method of selective oxidation are optimized; as a result, arrays of vertical-cavity surface-emitting lasers are fabricated. The active region of these lasers is based on two InGaAs quantum wells with top oxidized and bottom semiconductor distributed Bragg reflectors. © *2005 Pleiades Publishing, Inc.*

1. INTRODUCTION

The technology involved in selective oxidation of AlGaAs layers was first proposed more than ten years ago [1] and is now widely used in the fabrication of various optoelectronic devices based on III–V compounds, i.e., light-emitting diodes [2], metal–oxide–semiconductor transistors [3], optical waveguides [4], and vertical-cavity surface-emitting lasers (VCSELs) [5]. The unique feature of this technology is that it provides the opportunity to form buried insulating layers with a high structural quality and with the required electrical and optical parameters, which ensure not only efficient electronic confinement and an appreciable decrease in the internal optical losses in a VCSEL (in comparison to proton implantation) [6] but also make it possible to form distributed Bragg reflectors in a wide spectral range and reduce diffraction-related optical losses in the vertical microcavity [6].

However, there are still a number of unsolved problems related to the technology of selective oxidation. These include the problem of mechanical dependability and stability of the devices after oxidation. It is worth noting that selective oxidation of AlAs (at temperatures no higher than 500°C) leads to the formation of an (AlGa)$_x$O$_y$ amorphous matrix that is further partially transformed into γ-Al$_2$O$_3$ [7]. However, the appearing γ-Al$_2$O$_3$ phase is much denser than the initial AlAs, which gives rise to a linear compression of the layer after oxidation. Indeed, the volume occupied by an Al atom in AlAs is 3.57 Å^3, whereas this volume in γ-Al$_2$O$_3$ is about 2.85 Å^3, which corresponds to a linear compression of 20%. The specific degree of compression for the structure under consideration depends both on the thickness and composition of the layers and on the parameters of the oxidation process. In this context,

it is important to study the deformation of the structures under various conditions of selective oxidation.

It is well known that Raman spectroscopy makes it possible to quantitatively estimate stresses in semiconductors [8, 9]. Specifically, this method is widely used to study the local stresses that arise in silicon integrated circuits at various stages of their fabrication [10]. For example, in the case of a uniform biaxial stress in the *xy* plane (in the plane of an epitaxial structure) the stress tensor (for structures with a zinc blende lattice) features only the two nonzero components $\sigma_{xx} = \sigma_{yy} = \sigma$, while the strain tensor has the three nonzero components

$$\varepsilon_{xx} = \varepsilon_{yy} = \varepsilon_\parallel = (S_{11} + S_{12})\sigma$$
$$\text{and } \varepsilon_{zz} = \varepsilon_\perp = 2S_{12}\sigma,$$

where $S_{11} = 1.17 \times 10^{-2}$ GPa^{-1} and $S_{12} = -3.64 \times 10^{-3}$ GPa^{-1} are the elastic-compliance constants in GaAs at 300 K [11]. The shift $\Delta\omega_{LO}$ of the LO-phonon line in strained GaAs with respect to the LO-phonon line in unstrained GaAs (this shift arises owing to the stress σ) is given by

$$\Delta\omega_{LO}(\text{cm}^{-1})$$
$$= \omega_{LO}[pS_{12} + q(S_{11} + S_{12})]\sigma = -3.9\sigma(\text{GPa}),$$

where $p = -1.753$ and $q = -2.453$ are the phonon deformation potentials and $\omega_{LO} = 292$ cm^{-1} is the wave number of an LO phonon in unstrained gallium arsenide [10]. It is noteworthy that a biaxial compressive stress leads to an increase in the phonon frequency whereas a tensile stress leads to a decrease in this frequency.

Thus, Raman spectroscopy can be used to quantitatively estimate the stresses and strains that exist in the GaAs/(AlGa)$_x$O$_y$ structures under the condition that

selective oxidation gives rise to biaxial stresses in the plane of the epitaxial structure.

2. EXPERIMENTAL

The samples under study were grown by molecular-beam epitaxy (MBE) on a semi-insulating GaAs (100) substrate; a Riber 32P MBE system with a solid As source was used. First, a GaAs buffer layer and was grown; then, an $Al_{0.97}Ga_{0.03}As$ 227-nm-thick layer; and, finally, on top, a 94-nm-thick GaAs layer. The thicknesses of the layers were chosen so that they formed one period of an $(AlGa)_xO_y$/GaAs insulator-based distributed Bragg reflector for a region of 1.3 μm after oxidation. Using standard photolithography (an FP-9120 photoresist), in combination with a special method for hardening the photoresist and dry etching in a beam of Ar^+ ions (a MIM TLA 20 system for ion etching), we fabricated two types of mesa structures with stripe widths of 100 and 30 μm. The distance between the stripes was 350 μm, and the depth of etching was on the order of 1 μm. Selective oxidation of the test samples was carried out under various conditions after the formation of the mesa structures.

The Raman spectra were measured in the backscattering geometry $z(x, x)\bar{z}$ at room temperature. An Ar^+ laser with a radiation wavelength of 488 nm was used for pumping. The monochromator was calibrated using a Ne lamp. The characteristic absorption depth of the Ar^+-laser radiation (at the specified wavelength) in GaAs is on the order of 100 nm; therefore, we can disregard the contributions of the buffer and substrate to the detected signal.

3. RESULTS AND DISCUSSION

The conventional instrumentation for performing the processes involved in selective oxidation includes an open-type quartz reactor with either resistive or lamp-induced heating (Fig. 1a). The flow of carrier gas (typically, nitrogen) passes through a heated bubbler, where the gas is saturated with water vapors, and is then introduced into the reaction zone. The process of lateral oxidation of the AlGaAs layers occurs in this zone at characteristic temperatures of 350–450°C; the oxidation depth heavily depends not only on the composition and thickness of the layers but also on the initial state of the surface after dry etching [13]. In order to avoid surface damage and contamination from the dry etching, we carried out an additional chemical etching in a $NH_4OH : H_2O_2 : H_2O$ (1 : 2 : 50) solution for 4 s at room temperature immediately after the dry etching. However, preliminary studies showed that the state of the surface depends not only on the method used to treat it but also on the number of adsorbed water molecules. Therefore, preliminary heating of the samples at temperatures of 150–200°C in order to remove thes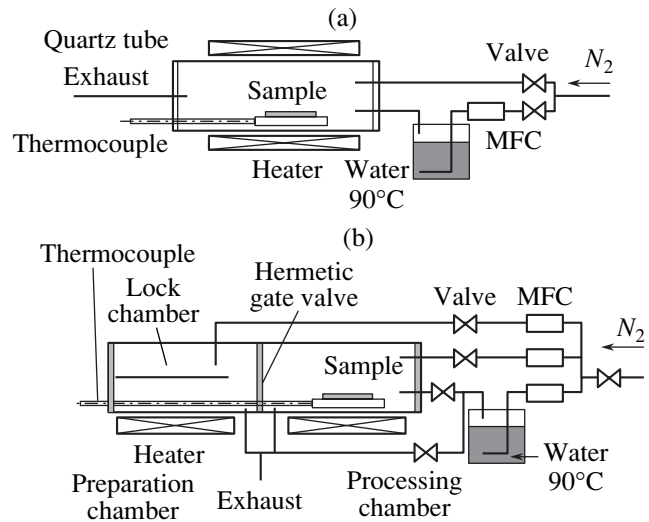e molecules is an important component of the selective-oxidation technology. In addition, a high-temperature annealing is required to increase the mechanical stability of the oxidized structures after the process is completed. This annealing ensures efficient removal of residual products from the oxidized layers [14].

Fig. 1. Schematic diagrams of the (a) standard and (b) developed setups for selective lateral oxidation of AlGaAs layers in water vapors. MFC stands for mass-flow controller.

To meet all of the above requirements for the process of selective oxidation, we designed and manufactured a two-chamber setup, whose schematic representation is shown in Fig. 1b. The availability of two independent chambers makes it possible to persistently maintain stable conditions in the working chamber (the carrier-gas flow, saturation with water vapors, and temperature), to rapidly complete the process by blowing dry nitrogen through this chamber, and to carry out both the high-temperature annealing of the samples in the dry-nitrogen atmosphere without exposure to air and the preliminary heating of the structures in the loading (preparatory) chamber. The experiments we conducted showed that this setup ensures high reproducibility and stability of the characteristics of selective oxidation.

We found, in the course of the conducted study, that oxidation under the conditions of saturation (in which case, the oxidation-reaction rate is independent of the rate of flow of water vapors into the chamber) and at moderate temperatures (400–440°C) is optimal from the standpoint of the quality and mechanical stability of the structure. However, if the duration of oxidation exceeds 30 min, the surface morphology degrades due to partial oxidation of the top GaAs layer, which, in turn, can lead to undesirable vertical oxidation of the surface layers (Fig. 2a) or defect-related oxidation (Fig. 2b).

In order to eliminate the mentioned effects, protective masks made of silicon nitride are usually used [6]. In this study, we used a photoresist as the mask. This approach made it possible to reduce the number of tech-
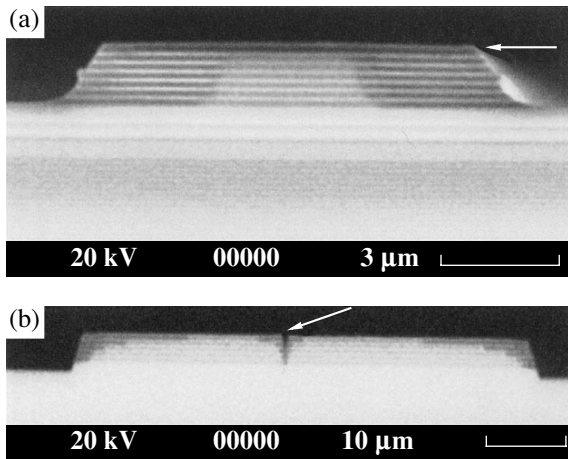
Fig. 2. Images of cleaved surfaces of the structures after selective oxidation. The arrows indicate undesirable (a) vertical oxidation and (b) defect-related oxidation. The images were obtained in a scanning electron microscope.
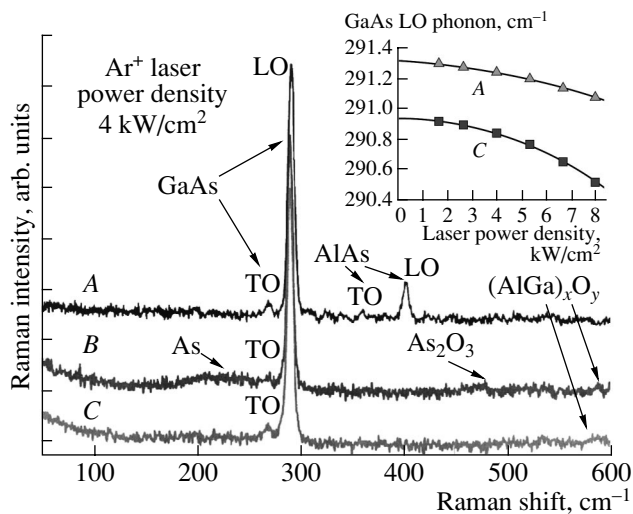

Fig. 3. Raman spectra of initial structure *A* and samples *B* and *C* (sample *C* underwent additional annealing after the completion of selective etching). Dependences of the position of the LO-phonon line for GaAs on the power density of the pump (an Ar^+ laser) for samples *A* and *C* are shown in the inset.

nological operations in comparison to the traditional technology used for VCSEL formation. As a result, the fabrication of VCSELs with a top oxidized reflector and oxidized apertures includes the process of etching off the first mesa (the smaller of the two) to the depth of the buried *p*-type contact layer and selective oxidation of this mesa under the protective photoresist for the formation of the upper reflector; the second mesa is then etched off to the depth of the buried *n*-type layer and the aperture layers are oxidized selectively [12]. Finally, *p*- and *n*-type ohmic contacts are formed, the device structure is passivated using an insulator, isolating

implantation is used, the contact windows are opened, and the contact areas are formed.

The main objective of this study was to estimate the stresses that arise as a result of selective oxidation of VCSEL structures. To this end, we prepared several series of test samples. Comparison was carried out against a sample (sample *A*) that constituted the initial structure; i.e., one that was not subjected to any treatment. In order to analyze the effect of high-temperature annealing on the mechanical stability of the oxidized samples, we used the first series of mesa structures, with the stripe width of 100 μm (samples *B* and *C*). All of these samples were subjected to lateral selective oxidation for 90 min at 420°C, and sample *C* was subjected to an additional annealing for 30 min at 420°C. The conditions of oxidation were chosen so as to ensure an oxidation depth of no less than 30 μm (the diameter of the focused laser-beam spot was no larger than 30 μm). In order to assess the stresses that arise owing to the hardening of the photoresist under oxidation conditions, we fabricated a second series of samples (samples *BA* and *CA*). These samples were similar to the first series but with dry nitrogen instead of water vapors introduced into the chamber; i.e., the oxidation process was simulated. The phenomenon of overoxidation is of profound practical interest. In order to study this phenomenon, we fabricated a third series of samples based on the mesa structures with the stripe width of 30 μm (samples *D*1, *D*2, and *D*3). These samples were subjected to selective oxidation at a temperature of 420°C for 45 min (sample *D*1), for 60 min (sample *D*2), and 75 min (sample *D*3); after that, all of the samples were subjected to an additional annealing for 30 min at 420°C. The entire $Al_{0.97}Ga_{0.03}As$ layer can be oxidized in 45 min in the chosen oxidation conditions; i.e., samples *D*2 and *D*3 were overoxidized.

In order to assess the stresses that arise in the structure as a result of oxidation correctly, we need to separate the possible stresses caused by photolithography, involving the special method for hardening the photoresist, from those caused by dry etching with the Ar^+ ion beam. The measurements of the Raman scattering carried out for the initial *A* structure and structure *AE*, subjected to the entire technological treatment (except for selective oxidation), indicate that the technological operations preceding oxidation do not introduce any appreciable stresses into the structure to within the experimental accuracy.

In Fig. 3, we show the Raman spectra for samples *A*, *B*, and *C*. The narrow peaks that can be seen at 292 and 403 cm^{-1} correspond to the LO phonons in GaAs and AlAs, respectively. The poorly pronounced peaks at 269 and 361 cm^{-1} correspond to the TO phonons in GaAs and AlAs, respectively (although the TO-phonon lines are forbidden in the backscattering geometry $z(x, x)\bar{z}$ according to the selection rules). After oxidation (structures *B* and *C*), the peaks related to AlAs disappear, which is indicative of complete transformation of AlAs

into (AlGa)$_x$O$_y$ (the poorly pronounced feature at 587 cm^{-1} [15]). In addition, in the Raman spectrum of structure B, we observe a poorly pronounced peak at 475 cm^{-1}, which is related to amorphous As$_2$O$_3$, and a broad feature in the range 180 to 280 cm^{-1}, which is a superposition of several peaks related to crystalline As (at 198 cm^{-1}), amorphous As (227 cm^{-1}), and the TO phonons in GaAs [16]. The presence of amorphous As$_2$O$_3$ suggests that diffusion from the oxide to the reaction front becomes the main mechanism limiting the oxidation rate, which, in particular, accounts for the observed parabolic time dependence of the oxidation depth for the samples studied.

The mechanical stability of the oxide layer depends heavily on the amount of residual (intermediate) products generated in the oxidation reaction [14]; in addition, the presence of residual As in the oxide leads to pinning of the Fermi level at the (AlGa)$_x$O$_y$–GaAs interface, which, in turn, affects the electrical properties of the oxide [15]. However, the effect of the structure of the oxide itself is of no less importance. As is well known, as a result of oxidation, AlGaAs transforms into amorphous (AlGa)$_x$O$_y$ that additionally contains AlO(OH) and Al(OH)$_3$ aluminum hydroxides. These compounds are metastable and can lead to continuation of the oxidation reaction for AlGaAs at room temperature [7, 16]. However, these hydroxides transform into γ-Al$_2$O$_3$ at temperatures higher than 350°C. In addition, residual As can interact with the hydroxides during annealing. This interaction brings about an appreciable reduction in the number of hydroxide groups in the (AlGa)$_x$O$_y$ layer [17]. Consequently, annealing of the structure results not only in removal of the residual reaction products but also in partial transformation of amorphous (AlGa)$_x$O$_y$ into the more stable γ-(AlGa)$_x$O$_y$ phase.

High-temperature annealing of the samples was carried out directly in the chamber (without either cooling or an exposure to air) in an atmosphere of dry nitrogen. Preliminary studies showed that the optimum (from the standpoint of mechanical stability) temperature of the annealing is the temperature used during oxidation. An annealing duration of about 30 min is sufficient for obtaining an oxidation depth of approximately 30 μm. An analysis of the Raman spectrum for structure C, annealed under optimum conditions, did not reveal any features related to As or As$_2$O$_3$. The procedures involved in rapid thermal annealing (simulation of alloying the contacts) after exposure of the structure to air did not apparently give rise to stratification of structure C, which suggests that the oxidized structure exhibits a high mechanical stability (Fig. 4a).

When analyzing the stresses in the structure, we have to take into account the possible heating of the sample by the laser radiation. It is well known that local overheating caused by a focused laser beam contributes to the shift of the phonon line for GaAs. In order to separate the effect of heating, we measured the dependence of the LO-phonon line position in the GaAs Raman
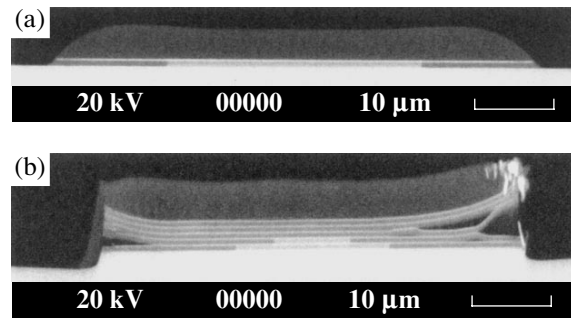

Fig. 4. Images of the cleaved surface of (a) the structure under study after selective oxidation at a temperature of 420°C and (b) a test structure after selective oxidation at a temperature of 450°C (the test structure was used to calibrate the oxidation rate in relation to the mole fraction of Al in the AlGaAs layers). The images were obtained in a scanning electron microscope.

spectrum on the power density of the pumping with an Ar$^+$ laser (see the inset in Fig. 3). The line shift due to overheating was equal to about 0.2 cm^{-1} for the initial structure (A), whereas a much larger shift (about 0.4 cm^{-1}) is observed for sample C. This fact is attributed to an appreciable difference in the heat-conductivity coefficients of AlGaAs and (AlGa)$_x$O$_y$ (amorphous (AlGa)$_x$O$_y$ is an insulator with low heat conductivity). Extrapolation of the experimental curves to zero laser power yields the true shift of the LO-phonon line in GaAs: $\Delta\omega_{LO} = -0.39$ cm^{-1}. This shift corresponds to extension in the structure plane (a negative shift of the phonon line). It is also worth noting that the top GaAs epitaxial layer is also somewhat stressed initially ($\sigma \approx 18$ MPa is the tensile stress). This behavior is caused by the fact that the lattice constant of AlAs is larger than the lattice constant of GaAs.

In order to correctly estimate the stresses introduced by selective oxidation of the AlGaAs layers with a high content of Al, we have to separately estimate the contribution producing the effect of hardening of the photoresist during oxidation. To this end, we simulated the oxidation process by introducing dry nitrogen (instead of water vapors) into the chamber. In Fig. 5, we show the results of measuring the Raman signal for samples A, BA, and CA. It can be seen that the contribution of the hardening of the photoresist to the stresses is relatively small ($\sigma \approx -18$ MPa) and corresponds to compression in the structure plane (a positive shift of the phonon line). All of the aforesaid evidently correlates with the fact that the photoresist is hardened and compressed at high temperatures (higher than 400°C). Thus, the photoresist also partially compensates for the stresses that appear in the surface layer due to oxidation. However, it is worth noting that, at oxidation temperatures exceeding 450°C, the photoresist compression becomes so high that the complete destruction (stratification) of a structure coated with this photoresist occurs (Fig. 4b).
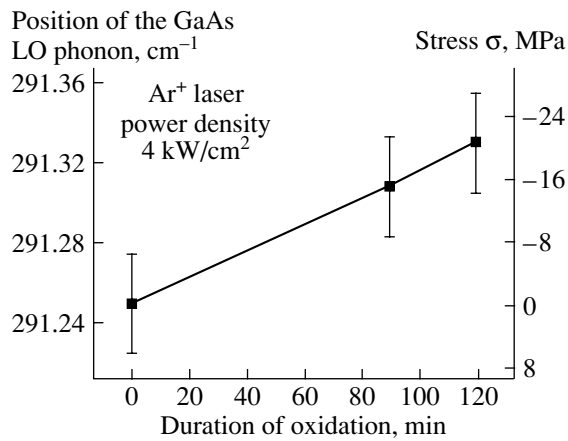
Fig. 5. Dependences of the position of the Raman line corresponding to the LO phonons in GaAs and the tensile stress σ on the duration of annealing in an atmosphere of dry nitrogen (simulation of selective oxidation).
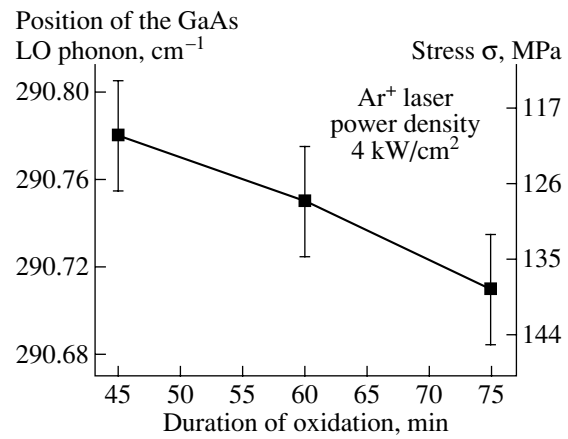

Fig. 6. Dependences of the position of the Raman line corresponding to the LO phonons in GaAs and the compressive stress σ on the duration of selective oxidation.

As a result, taking into account the effects of local overheating of the samples and hardening of the photoresist during oxidation, we find that the true shift of the phonon line is $\Delta\omega_{LO} = -0.46$ cm^{-1} and the corresponding tensile stress $\sigma = 118$ MPa. Thus, in the case under consideration, oxidation gives rise to the tensile strain $\varepsilon_{\parallel} = 9.38 \times 10^{-4}$ in the structure plane and the compressive strain $\varepsilon_{\perp} = -8.67 \times 10^{-4}$ in the direction of the structure growth. These results correlate with previously published data for GaAs/(AlGa)$_x$O$_y$ structures with 100-nm-thick AlAs and Al$_{0.98}$Ga$_{0.02}$As layers [18].

The effect of overoxidation (the situation in which the duration of the process exceeds that required for complete oxidation) on the stresses is illustrated in Fig. 6 (taking into account all the above effects). As a result of oxidation for 45 min, the AlGaAs layer becomes completely transformed into (AlGa)$_x$O$_y$. It can be seen that a further increase in the process duration reduces the mechanical stability of the structure, since the compression of the layers becomes too high. In addition, the overoxidation brings about a decrease in the reflection coefficient of the mirrors and a distortion of the reflection-spectrum shape due to degradation of the morphology and the presence of internal stresses [19].

We aimed, as a result of our studies, to optimize the reproducibility and stability of the parameters of selective oxidation and ensure the required mechanical stability of VCSEL structures. In this regard, we managed to fabricate 8×8 arrays of VCSELs with an active region based on InGaAs quantum wells. The individually addressed emitters exhibit continuous-wave lasing at room temperature with threshold currents of 1.0–2.5 mA at a wavelength of 960–965 nm, differential efficiency as high as 0.04 mW/mA, and their highest output power in excess of 2 mW [20].

4. CONCLUSION

Thus, in this study, we analyzed the stresses that appear in GaAs/(AlGa)$_x$O$_y$ structures as a result of selective oxidation of the AlGaAs layers. We showed that oxidation gives rise to tensile stresses in the GaAs layers. At the same time, the use of a photoresist as the protective mask during oxidation gives rise to compressive stresses as a result of hardening of the photoresist at high temperatures. We considered the effect of overoxidation on the mechanical stability of the structures. The developed and optimized technology of selective oxidation shows potential in relation to fabrication of individual WCSELs and arrays of emitters for high-speed systems of transmission and processing of information.

ACKNOWLEDGMENTS

REFERENCES

1. J. M. Dallesasse, N. Holonyak, A. R. Sugg, *et al.*, Appl. Phys. Lett. **57**, 2844 (1990).
2. D. L. Huffaker, C. C. Lin, J. Shin, and D. G. Deppe, Appl. Phys. Lett. **66**, 3096 (1995).
3. E. I. Chen, N. Holonyak, and S. A. Maranowski, Appl. Phys. Lett. **66**, 2688 (1995).
4. A. Fiore, V. Berger, E. Rosencher, *et al.*, Appl. Phys. Lett. **68**, 1320 (1996).
5. D. L. Huffaker, D. G. Deppe, K. Kummar, and T. J. Rogers, Appl. Phys. Lett. **65**, 97 (1994).
6. *Vertical Cavity Surface Emitting Lasers*, Ed. by L. A. Coldren, H. Temkin, and C. W. Wilmsen (Cambridge Univ. Press, Cambridge, 1999).

7. R. D. Twesten, D. M. Follstaedt, K. D. Choquette, and R. P. Schneider, Appl. Phys. Lett. **69**, 19 (1996).

8. F. Cerdeira, C. J. Buchenauer, F. H. Pollak, and M. Cardona, Phys. Rev. B **5**, 580 (1972).

9. S. C. Jain, M. Willander, and H. Maes, Semicond. Sci. Technol. **11**, 641 (1996).

10. Ingrid De Wolf, Semicond. Sci. Technol. **11**, 139 (1996).

11. G. Landa, R. Carles, C. Fontaine, *et al.*, J. Appl. Phys. **66**, 196 (1989).

12. N. A. Maleev, A. R. Kovsh, A. E. Zhukov, *et al.*, Fiz. Tekh. Poluprovodn. (St. Petersburg) **37**, 1265 (2003) [Semiconductors **37**, 1234 (2003)].

13. M. Creusen, F. de Btyun, F. Karouta, *et al.*, Electrochem. Solid-State Lett. **2**, 83 (1999).

14. H. Q. Jia, H. Chen, W. C. Wang, *et al.*, J. Cryst. Growth **223**, 484 (2001).

15. C. I. H. Ashby, J. P. Sullivan, P. P. Newcomer, *et al.*, Appl. Phys. Lett. **70**, 2443 (1997).

16. A. R. Sugg, N. Holonyak, J. E. Baker, *et al.*, Appl. Phys. Lett. **58**, 1199 (1991).

17. K. D. Choquette, K. M. Geib, C. I. H. Ashby, *et al.*, IEEE J. Sel. Top. Quantum Electron. **3**, 916 (1997).

18. J. P. Landesman, A. Fiore, J. Nagle, *et al.*, Appl. Phys. Lett. **71**, 2520 (1997).

19. V. A. Haisler, F. Hopfer, R. L. Sellin, *et al.*, Appl. Phys. Lett. **81**, 2544 (2002).

20. N. A. Maleev, A. G. Kuz'menkov, A. E. Zhukov, *et al.*, Fiz. Tekh. Poluprovodn. (St. Petersburg) **39**, 487 (2005) [Semiconductors **39**, 462 (2005)].

Translated by A. Spitsyn

ELECTRONIC AND OPTICAL PROPERTIES
OF SEMICONDUCTORS

Low-Temperature Instabilities of the Electrical Properties of $Cd_{0.96}Zn_{0.04}Te$:Cl Semi-insulating Crystals

A. V. Savitskiĭ^, O. A. Parfenyuk, M. I. Ilashchuk, K. S. Ulyanitskiĭ, S. N. Chupyra, and N. D. Vakhnyak

Fed'kovich State University, ul. Kotsyubinskogo 2, Chernovtsy, 58012 Ukraine
^e-mail: p_ebox@mail.ru
Submitted June 28, 2004; accepted for publication November 10, 2004

Abstract—The electrical properties in the temperature range 295–430 K and low-temperature (4.2 K) photoluminescence of $Cd_{1-x}Zn_xTe$:Cl semi-insulating crystals grown from melts with a variable impurity content ($C_{Cl}^0 = 5 \times 10^{17} - 1 \times 10^{19}$ cm^{-3}) are investigated. Nonequilibrium processes leading to a decrease in carrier concentration are observed in all the samples at low temperatures ($T = 330–385$ K). These changes are reversible. The activation energy of these processes E_a is found to be 0.88 eV. As with semi-insulating CdTe:Cl, the observed phenomena can be explained by a change in the charge state of background copper atoms: $Cu_{Cd} \longleftrightarrow Cu_i$. The introduction of Zn changes the ratio of the concentrations of shallow-level donors Cu_i and Cl_{Te} from their levels in the initial material. © 2005 Pleiades Publishing, Inc.

1. INTRODUCTION

Cadmium telluride and $Cd_{1-x}Zn_xTe$ alloys are potentially valuable for practical application and are currently under intense study in relation to the design of various devices. For most applications, bulk samples of high structural quality with very low concentrations of equilibrium carriers and stable parameters are required. In order to obtain such materials, crystals are doped with donor impurities, which compensate for intrinsic acceptor defects. The latter are considered to be isolated cadmium vacancies.

Hydrogen-like donor impurities (for example, Cl [1]) and elements inducing deep levels in the band gap (V, Ti, Ge, Sn, and Pb) [2] can be used as donor dopants. The best results in the development of X-ray and γ detectors have been obtained with CdTe crystals and $Cd_{1-x}Zn_xTe$ alloys.

Most studies of the properties of Cl-doped CdTe and CdZnTe consider the growth conditions and structural properties of bulk semi-insulating samples. However, little attention has been paid to transfer phenomena, especially for CdZnTe, or the determination of a possible correlation between the equilibrium parameters of crystals and the conditions of their preparation process.

When studying temperature dependences of the electrical properties (σ, R_H) of CdTe:Cl samples, reversible low-temperature variations have been found [3]. The purpose of this study is to examine the effect of Zn impurity on the magnitude and character of such variations for $Cd_{0.96}Zn_{0.04}Te$:Cl semi-insulating crystals. It is known [4] that the incorporation of Zn into the CdTe lattice increases the covalent bond component, which improves the structural quality of the material.

2. EXPERIMENTAL

The crystals under study were grown by the vertical Bridgman–Stockbarger method from a preliminarily synthesized material, to which a necessary amount of $CdCl_2$ salt was added. The chlorine concentration in the liquid phase was $C_{Cl}^0 = 5 \times 10^{17} - 1 \times 10^{19}$ cm^{-3}.

The resulting crystals had a large-block structure (a single block was 5–8 cm^3 in size). The total ingot volume was 50–60 cm^3. The samples to be used in electrical measurements ($1.5 \times 1.2 \times 12$ mm in size) were cut from the parts of the ingot grown at the initial (*I*), medium (*M*), and last (*L*) stages of the process (see Fig. 1). The sample preparation and contact deposition were carried out in a conventional manner. Direct current measurements of the temperature dependences of the electrical conductivity and Hall coefficient were carried out under both an increase and a decrease in temperature.

Low-temperature (4.2 K) photoluminescence (PL) was examined, according to the standard procedure, on freshly-cleaved surfaces. The resolution was no lower than 1 meV.

3. RESULTS AND DISCUSSION

All the crystals under study had *p*-type conductivity with resistivity (ρ) from 2.7×10^7 to 1.08×10^8 Ω cm and mobility μ_H in the range 58–80 cm^2/(V s) at 295 K (see table). A specific feature of the $Cd_{0.96}Zn_{0.04}Te$:Cl samples was that they were annealed at relatively low temperatures (330–385 K, Fig. 1) during the measurements. Measurements taken when temperature was

increasing revealed two straight-line segments with various slope angles at $T < 330$ K (region I) and $T > 385$ K (region II) that were separated by a transient region. As the temperature decreased, the measured values of R_H coincided with the values obtained in the first half of the measurement cycle (region II). With further cooling, these values exceeded those obtained during heating and thus formed region III.

The level ionization energies ΔE for various samples, which correspond to the conductivity in particular regions in the dependences $\log R_H = f(10^3/T)$, are given in the table. By comparing the values of ΔE_1, ΔE_2, and ΔE_3, we can see that the conductivity of all the annealed crystals is determined by deeper levels ($\Delta E_2 > \Delta E_1$) whereas, in region III, the activation energy remains the same or slightly increases ($\Delta E_3 \geq \Delta E_2$).

The observed variations are reversible. Keeping the samples at room temperature for several months restored their parameters to the initial values.

Analysis of the temperature dependences of the Hall mobility showed that scattering by thermal lattice vibrations is dominant in all the samples considered (see the inset in Fig. 1). A particular feature of the crystals is that, at temperatures exceeding the annealing temperature (region II in the dependence $\log R_H = f(10^3/T)$), the quantity $R_H \sigma$ sharply decreases. In this case, the slope angle in the dependence $\mu \propto T^{-\alpha}$ ranges from $\alpha \approx 1.4$ (region I) to $\alpha > 3.4$ (region II). The observed decrease in the mobility cannot be due to scattering by additionally charged point defects, since an estimation of the amount of defects necessary to produce it using the Brooks–Herring formula [5] leads to unrealistic values of N. This run of the dependence $\log(R_H \sigma) = f(\log T)$ can be explained by the fact that,
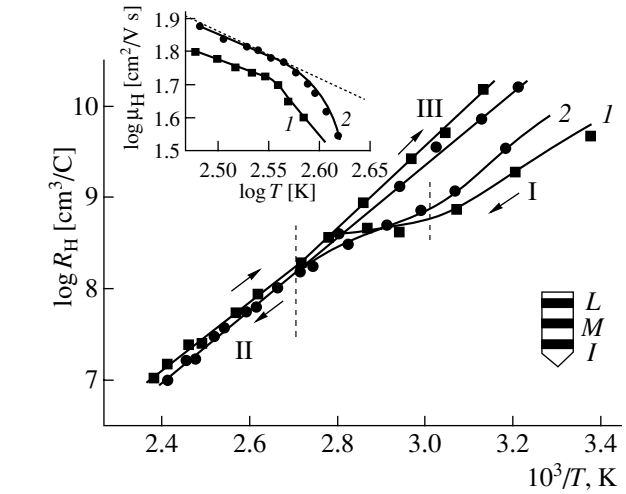

Fig. 1. Temperature dependences of R_H of the $Cd_{0.96}Zn_{0.04}Te:Cl$ samples: (*1*) sample *C-I* and (*2*) sample *E-M*. The arrows denote the sequence of measurements. The roman numerals denote various regions of the experimental dependences, and the vertical dashed lines separate the transient region (see text). The inset shows the temperature dependences of the Hall mobility for the same samples. The dashed line is the dependence $\mu_H(T)$ for scattering by optical phonons.

at temperatures corresponding to region II of the experimental dependence, the rigorous relation $p/n_i = (\mu_n/\mu_p)^2$, which should be satisfied for the impurity conductivity, is violated. Therefore, the conductivity becomes mixed. This fact was confirmed by measurements of R_H at higher temperatures. At $T \approx 200$ K, the sign of R_H changes and n-type conductivity emerges.

Equilibrium characteristics of the $Cd_{0.96}Zn_{0.04}Te:Cl$ samples prior to measurements (295 K) and the activation energies for different segments of the experimental dependences $\log R_H = f(10^3/T)$

| No. | Sample* | C_{Cl}^0, cm^{-2} | Prior to heating | | ρ/ρ_0, ** | ΔE, eV | | |
			ρ_0, Ω cm	μ_H, cm^2 V^{-1} s^{-1}		I ΔE_1	II ΔE_2	III ΔE_3
1	*A-I*	5×10^{17}	6.8×10^7	60	6.8	0.63	0.72	0.72
2	*A-M*	–	1.0×10^8	57	8.1	0.62	0.73	0.81
3	*A-L*	–	4.7×10^7	65	5.0	0.60	0.67	0.73
4	*B-M*	1×10^{18}	6.6×10^7	62	5.7	0.60	0.67	0.74
5	*B-L*	–	2.7×10^7	78	7.6	0.52	0.71	0.71
6	*C-I*	5×10^{18}	8.5×10^7	62	36	0.49	0.73	0.87
7	*C-M*	–	4.2×10^7	58	60	0.44	0.71	0.82
8	*C-L*	–	4.8×10^7	70	10.2	0.44	0.70	0.76
9	*D-M*	1×10^{18}	1.8×10^8	72	6.2	0.77	0.80	0.80
10	*E-M*	1×10^{19}	1.6×10^8	80	4.0	0.75	0.78	0.78

  * The first letter is the name of the ingot and the second letter indicates the part of the ingot the sample was cut from.

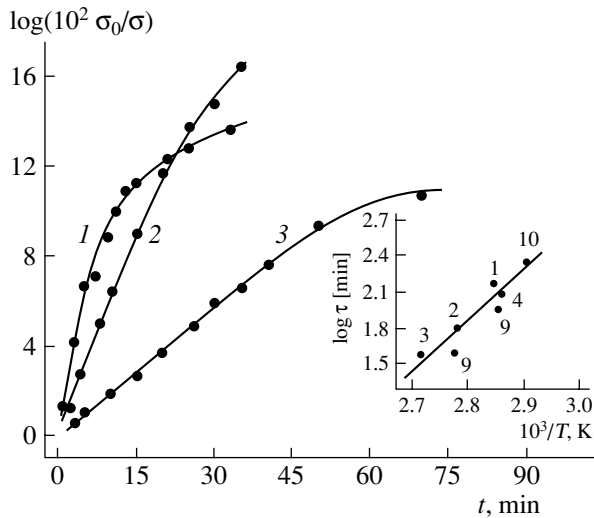 ** ρ is the resistivity after the measurement cycle.

Fig. 2. Typical isothermal relaxation dependences of the conductivity of the $Cd_{0.96}Zn_{0.04}Te:Cl$ semi-insulating samples at (*1*) 368, (*2*) 351, and (*3*) 344 K. The inset shows the temperature dependence of the relaxation time constant, which was obtained by studying various crystals. The numbers near the experimental points correspond to the sample enumeration in the table.

Fig. 3. Spectral dependences of the low-temperature PL of a $Cd_{0.96}Zn_{0.04}Te:Cl$ sample prior to annealing (dashed line) and after annealing at 373 K for 1 h (solid line).

Studies of the isothermal relaxation dependences of the sample conductivity at temperatures corresponding to the transient region showed that their initial segments can be described by the exponential dependence $\sigma = \sigma_0\exp(-t/\tau)$, where σ_0 is the sample conductivity under equilibrium conditions and τ is the relaxation time. By plotting the dependences $\log(\sigma_0/\sigma) = f(t)$, we were able to obtain the relaxation time from the slope of the resulting straight lines (see Fig. 2). The temperature dependence of τ of the samples can be described by the exponential law $\tau = \tau_0\exp(E_a/kT)$, where E_a is the activation energy of the process. The value of E_a was determined as 0.88 eV from the dependence $\log\tau = f(10^3/T)$ (see the inset in Fig. 2).

Typical PL spectra of the initial and thermally treated $Cd_{1-x}Zn_xTe$ samples are shown in Fig. 3. Differences between the PL spectra of particular samples are observed only in relation to the location of the peaks of separate emission bands, which is due to the different sample composition, and insignificant variations in the ratio of the peak intensities.[1]

In the exciton region of the spectrum (1.605–1.630 eV), lines of excitons bound at neutral donors (D^0, X) and acceptors (A^0, X) manifest themselves. The band (D^0, X) is rather narrow, with a half-width of ~2 meV, and has a peak at 1.6174 eV. The line (A^0, X)

is wider and is split into two components: (A_1^0, X) and (A_2^0, X), which have peaks at 1.6129 and 1.6117 eV, respectively. There are also two weaker lines resulting from recombination of free excitons from the upper (UPB) and lower (LPB) polariton branches. The corresponding energies are equal to 1.6209 and 1.6193 eV.

Starting from the energy location of the LPB and UPB bands and taking into account that the exciton bound energy in CdTe equals $E_{ex} = 10.3$ meV [7], the band gap of the samples is $E_g = 1.6304$ eV. This value of E_g corresponds to the Zn content $x = 0.07$, in accordance with the relation between the band gap and the composition for $Cd_{1-x}Zn_xTe$ alloys [8]: $E_g(Cd_{1-x}Zn_xTe) = E_g(CdTe) + 0.322x + 0.463x^2$.

The nature of the (A^0, X) band of CdTe has been studied by many researchers; however, there is no agreement on its origin (see [9]). In most publications on this topic, the view is expressed that this band has a complex nature and is formed with the participation of simple acceptors Cu_{Cd} and the associates $(V_{Cd}–D)$ or $(V_{Cd}–2D)$, where D are atoms of the donor background impurities. The broad maximum of the component (A_1^0, X) and signs of its definite structure indicate that the higher energy component in the spectra of the $Cd_{1-x}Zn_xTe$ crystals under study is due to excitons bound at complex acceptor defects, which include various shallow-level donors. The component (A_2^0, X) may be due to the recombination of excitons bound at the copper acceptors.

The PL intensity in the near-edge region (1.54–1.60 eV) is much lower. Here, we can distinguish two emission bands at 1.5915 and 1.5772 eV, as well as their first phonon replicas. This simultaneous manifestation of two types of transitions is typical of the PL of CdTe crystals in the near-edge spectral region. These

---

[1] The effective distribution coefficient of Zn in CdTe $\neq$ 1 and, according to the data of various researchers, is in the range 1.35–1.60 [6]. Therefore, the composition of the $Cd_{1-x}Zn_xTe:Cl$ samples depends on the part of the ingot that they were cut from.
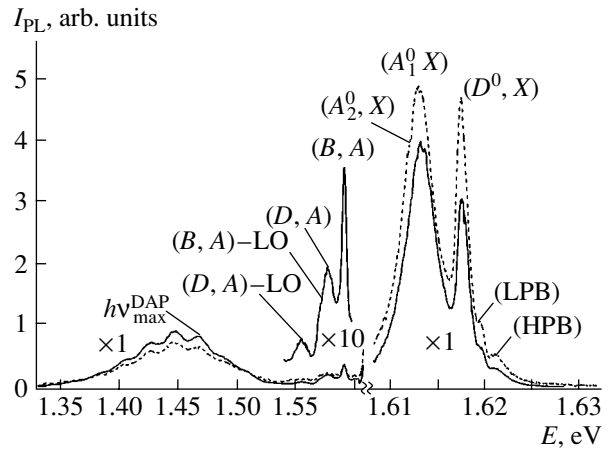
bands are attributed to transitions of the band electrons and electrons localized at shallow donor levels to shallow acceptor centers. Therefore, we can attribute the line peaked at 1.5915 eV to (B, A) emission, and the line peaked at 1.5772 eV to (D, A) transitions.

The activation energy of an acceptor defect E_a^{BA} involved in the (B, A) transitions can be found from the known formula

$$E_a^{BA} = E_g - h\nu_{max}^{BA} + \frac{kT}{2}.$$

Here, T is the electron temperature and $h\nu_{max}^{BA}$ is the energy location of the peak of the zero-phonon line. Using the values $E_g = 1.6304$ eV and $h\nu_{max}^{BA} = 1.5915$ eV, we obtain $E_a^{BA} = 0.039$ eV. Since the activation energies of the shallow-level acceptor impurities (Li, Na, N, and P) and V_{Cd} are larger in CdTe (0.05–0.06 eV [10]), the (B, A) band in the crystals under study cannot be due to transitions to isolated defects. This circumstance indicates that the level $E_a^{BA} = 0.039$ eV has a complex nature (donor–acceptor pairs, DAPs), and the ionization energy decreases due to Coulomb interaction between a pair's components. The crystals under study have a high concentration of donor defects (namely, background impurities and the Cl_{Te} doping impurity); therefore, the formation of such pairs is quite possible. The high concentration of donor defects manifests itself in the strong emission band of the excitons bound at neutral donors.

A broad emission band with a peak of the zero-phonon line $h\nu_{max}^{DAP}$ at 1.4689 eV (the DAP band), which is typical of CdTe, manifests itself in the donor–acceptor PL region (1.35–1.53 eV). This band is due to transitions to the acceptor centers in the energy range 0.12–0.17 eV. Such defects may be Cu atoms located in the Cd sites with the ionization energy $E_a = 0.146$ eV [10] or associates containing V_{Cd} vacancies and donors (A centers). In the general case, transitions can simultaneously occur to centers of various types. These transitions contribute to the formation of the DAP band, which considerably complicates its interpretation.

Let us assume that DAP emission is induced by electron transitions from the conduction band. In this case, the activation energies of the corresponding acceptor centers E_a^{DAP} can be determined from formula (1). Using the value $E_{max}^{DAP} = 1.4689$ eV, we obtain $E_a^{DAP} \approx 0.16$ eV. This activation energy of A centers is not characteristic of Cl-doped crystals (0.14 eV) [11]. Therefore, we can assume that the DAP band in the spectra of the $Cd_{1-x}Zn_xTe$:Cl crystals, as in the CdTe:Cl samples [9], is due to radiative transitions from shallow-level donors to acceptor defects. The value of E_a^{DAP} can be estimated

from the relation $h\nu_{max}^{DAP} = E_g - E_D - E_a^{DAP}$, where E_D is the activation energy of a shallow-level donor. Assuming E_D to be 0.014 eV [12], we obtain $E_a^{DAP} = 0.147$ eV, which coincides with the activation energies of a Cu acceptor in CdTe and an A center involving Cl.

The relaxation character of variations in the electrical parameters of the $Cd_{1-x}Zn_xTe$:Cl samples indicates that these variations are not associated with the approach of the system of point and structural defects to thermodynamic equilibrium at low temperatures, which is possible under certain growth conditions (high cooling rates, high concentrations of slightly soluble doping impurities, etc.).

An increase in the resistivity of the crystals at $T > 330$ K can be result from either a decrease in the total number of deep-level acceptor centers, which determine the conductivity of p-type crystals, or an increase in their degree of compensation. The nature of the levels in the midgap of the $Cd_{1-x}Zn_xTe$:Cl semi-insulating samples is still not completely understood. However, it is unlikely that their concentration can vary at such low temperatures. We believe that the cause of these variations is the formation of additional Cu_{Cd}^+ donors in accordance with the reaction $Cu_{Cd}^- \longleftrightarrow V_{Cd}^- + Cu_i^+ + e^-$ at $T > 330$ K. The concentration of copper (one of the main background impurities in CdTe) can be as high as 10^{16} cm^{-3}. Copper is, to some degree, involved in the processes of compensation in CdTe:Cl [13] and its interaction with intrinsic defects explains the relaxation processes observed in undoped CdTe [14]. Our suggestion of the considerable role of Cu in the processes under study is supported by the coincidence of the activation energy of the relaxation process (0.87 eV for CdTe:Cl) and the limits of the temperature range in which the variations are observed, as well as by the general character of the relaxation processes in the $Cd_{1-x}Zn_xTe$:Cl and CdTe:Cl samples [3].[2]

The PL measurements of the thermally treated $Cd_{1-x}Zn_xTe$:Cl crystals (Fig. 3) showed that annealing only slightly affects the shape of the emission spectrum. For all the crystals under study, the DAP band intensity slightly increased. This fact can be explained by the increase in the concentration of shallow-level donors, transitions from which cause the PL in this spectral region. The intensity of the PL lines after thermal treatment remains almost the same in the edge part of the spectrum and may slightly increase or decrease in the exciton region. In this case, the spectra of all the crystals measured prior to and after the thermal treatment contain a strong (D^0, X) PL band in addition to the (A^0, X) line.

[2] The validity of the suggestion of the decisive role of background Cu atoms in the relaxation processes occurring when semi-insulating CdTe:Cl is heated was substantiated in more detail in [3]. Therefore, we omit this information here.

Studies of the properties of the $Cd_{1-x}Zn_xTe:Cl$ and CdTe:Cl samples [3] show that both materials contain a large number of shallow-level donors (Cl_{Te}, Cu_i), which decrease the ionization energy of the shallow-level acceptors through the Coulomb interaction (for CdTe:Cl, E_a^{BA} = 0.03 eV [3]). Transitions to these defects form the (B, A) PL bands in the edge spectral region. Comparison of the effect of annealing on the dynamics of the variation in this emission line in CdTe:Cl [3] and $Cd_{1-x}Zn_xTe:Cl$ crystals shows that, in the alloy samples, Cu atoms play a lesser role in the formation of defects with the ionization energy E_a^{BA} and their concentration is lower than the concentration of Cl_{Te} shallow-level donors. In the spectra of Cl-doped CdTe, the (B, A) band arises only after thermal treatment.

The fact that variations in the properties of the CdTe:Cl [3] and $Cd_{1-x}Zn_xTe:Cl$ samples have the same character, revealed by electrical measurements, and that there are differences in the PL spectra of these materials agrees with the assumption that the relative amounts of Cu_i and Cl_{Te} donors are different. Since these defects are involved in the formation of the (B, A) PL band, its intensity only slightly varies due to the formation of a small amount of interstitial Cu upon heating ($[Cu_i] \ll [Cl_{Te}]$). However, even the generation of a small amount of additional donors may vary the degree of deep-level compensation and, correspondingly, the resistivity of the samples, since the equilibrium hole concentration at the beginning of the transient region ($T \geq 330$ K) is low: $p \leq 10^{10}$ cm^{-3}. The results obtained confirm the existing opinion that the incorporation of Zn atoms into the CdTe lattice substantially varies the system of intrinsic defects in CdTe [6].

4. CONCLUSIONS

Heating $Cd_{0.96}Zn_{0.04}Te:Cl$ semi-insulating crystals at fairly low temperatures ($T \geq 330$ K) leads to generation of additional donors, which, in turn, increase the material resistivity. The observed phenomena are reversible. As in the case of semi-insulating CdTe:Cl,

these processes are caused by variation in the charge state of Cu atoms: $Cu_{Cd} \longleftrightarrow Cu_i$. The introduction of Zn atoms changes the concentration ratio for shallow-level donor defects (Cu_i and Cl_{Te}) towards an increase in the amount of the latter.

REFERENCES

1. O. A. Matveev and A. I. Terent'ev, Fiz. Tekh. Poluprovodn. (St. Petersburg) **34**, 1316 (2000) [Semiconductors **34**, 1264 (2000)].
2. P. Moravec, M. Hage-Ali, L. Chibani, and P. Siffert, Mater. Sci. Eng. B **16**, 223 (1993).
3. A. Savitsky, O. Parfenuyk, M. Ilashchuk, *et al.*, Semicond. Sci. Technol. **15**, 263 (2000).
4. J. J. Kennedy, P. M. Amirthara, P. R. Boyd, *et al.*, J. Cryst. Growth **186**, 93 (1998).
5. *Physics and Chemistry of II–VI Compounds*, Ed. by M. Aven and J. S. Prener (North-Holland, Amsterdam, 1967; Mir, Moscow, 1970).
6. E. Weigel and G. Müller-Vogt, J. Cryst. Growth **161**, 40 (1996).
7. P. Hóschl, Yu. M. Ivanov, E. Belas, *et al.*, J. Cryst. Growth **184–185**, 1039 (1998).
8. W. Stadler, D. M. Hofmann, H. C. Alt, *et al.*, Phys. Rev. B **51**, 10619 (1995).
9. D. V. Korbutyak, S. G. Krilyuk, Yu. V. Kryuchenko, and N. D. Vakhnyak, Optoélektron. Poluprovod. Tekh. B **37**, 23 (2002).
10. E. Molva, J. L. Pautrat, K. Saminadayar, *et al.*, Phys. Rev. B **30**, 3344 (1984).
11. N. V. Agrinskaya, E. N. Arkad'eva, and O. A. Matveev, Fiz. Tekh. Poluprovodn. (Leningrad) **4**, 412 (1970) [Sov. Phys. Semicond. **4**, 347 (1970)].
12. J. M. Francou, K. Saminadayar, and J. L. Pautrat, Phys. Rev. B **41**, 12035 (1990).
13. B. Biglari, M. Samimi, M. Hage-Ali, *et al.*, J. Cryst. Growth **189**, 428 (1998).
14. A. V. Savitskiĭ, M. I. Ilashchuk, O. A. Parfenyuk, *et al.*, Ukr. Fiz. Zh. **41** (1), 82 (1996).

Translated by N. Korovin

Polarized Infrared and Raman Spectroscopy Studies of the Liquid Crystal *E*7 Alignment in Composites Based on Grooved Silicon

**E. V. Astrova[1]^, T. S. Perova[2], S. A. Grudinkin[1, 2], V. A. Tolmachev[1],
Yu. A. Pilyugina[1], V. B. Voronkov[1], and J. K. Vij[2]**

[1]*Ioffe Physicotechnical Institute, Russian Academy of Sciences, Politekhnicheskaya ul. 26, St. Petersburg, 194021 Russia*
^*e-mail: east@mail.ioffe.ru*
[2]*Department of Electronic and Electrical Engineering, University of Dublin, Trinity College, Dublin 2, Ireland*
Submitted September 6, 2004; accepted for publication September 17, 2004

Abstract—Alignment of liquid-crystal filler molecules and the electro-optical effect in composite photonic crystals based on grooved silicon are studied. It is found that the nematic liquid crystal molecules that fill the grooves are predominantly aligned in a planar configuration with respect to the silicon walls. The liquid crystal molecules are realigned homeotropically with respect to the groove walls under the influence of an electric field. The effect detected can be used to adjust the photonic band gap of a one-dimensional photonic crystal. © 2005 Pleiades Publishing, Inc.

1. INTRODUCTION

The concept of a tunable photonic crystal based on an insulating porous matrix filled with liquid crystal (LC) was first suggested in a theoretical study by Busch and John [1]. Since then, several experimental papers devoted to the development of composite photonic crystals of various dimensions and based on different insulating matrices have been published (see, e.g., [2, 3]). A photonic band shift of 70 nm was observed in two-dimensional composite photonic crystals based on silicon matrices such as macroporous silicon. This shift is caused by a change in the LC refractive index during the transition from a mesophase to an isotropic state upon heating [4]. Using the spectra measured in [4], Leonard *et al.* attempted to determine the initial alignment of molecules of nematic LC *E*7 in macroporous silicon channels. Their conclusion on an escaped-radial alignment of the LC was not confirmed in a later paper [5], where the nuclear spin resonance method showed that *E*7 molecules tend to be positioned along the channel axis on their long side. In this study, the thermooptical effect was used to reconstruct the photonic band gap of a two-dimensional PC.

The most important property from a practical point of view is adjustment of the photonic band gap using an electric field. In the case of composites based on macroporous silicon, it is not easy to apply an electric field to LC inside channels, since the corresponding Si matrix features high conductivity. Periodic structures of grooved silicon represent a more convenient silicon matrix and enable us to solve this problem. As has been shown previously, grooved silicon prepared by deep anisotropic etching of (110) silicon serves as a one-dimensional photonic crystal for light propagating perpendicular to the silicon edges in the wafer plane [6, 7]. Infiltration of this silicon by nematic *E*7 results in a shift of the observed photonic band gaps to the long-wavelength spectral region [8].

In this study, model structures of grooved silicon with insulated interdigital electrodes of various periods, together with composites based on them, were developed. Methodical problems related to the determination of LC director orientation in grooved silicon were considered and nematic *E*7 molecule alignment was studied in an initial state and under an external electric field.[1]

2. EXPERIMENTAL

Figures 1–3 show the basic types of samples under study, and Fig. 4 shows the cross section of interdigital structures used to attain an electro-optic effect. The initial material from which the samples were prepared was *n*-Si with a resistivity $\rho = 5 \, \Omega$ cm. Deep boron and aluminum diffusion to a depth $x_j = 160 \, \mu$m into 400-μm-thick ground (110) wafers was performed. A *p*-type layer was removed by grinding and polishing from the uppermost surface, leaving a final wafer thickness of 190 μm. Grooves were etched into this surface through an oxide mask in a heated KOH solution. The technology involved in producing the periodic structures of grooved silicon is described in more detail in [6]. The vertical planes of the silicon edges ((111) planes) are

---

[1] A director is the vector characterizing the predominant orientation of the long axes of LC molecules.
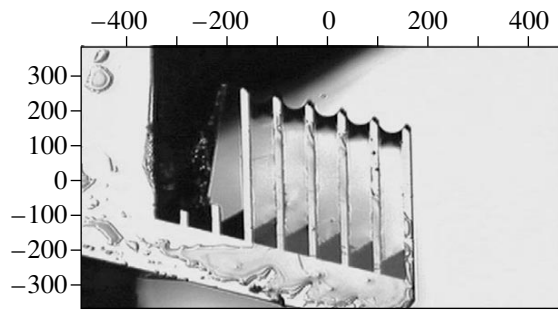
Fig. 1. Sample $D1$, filled with liquid crystal (optical microscope image).

Fig. 2. Sample D4-2, with a single groove (scanning electron microscope image): (a) the initial matrix and (b) the sample with electrodes after filling with liquid crystal.

optically smooth, while the groove bottom is rough. The grooves were etched to a depth $l = 50$ μm so that they penetrated the p-type region. The two silicon electrodes (*1* and *2*) (Fig. 3a) were electrically isolated from each other using a reversely biased p–n junction and provided voltage supply to nearby edges in the electrode overlap region. The uniform electric field configuration near the groove bottom can be slightly distorted. The height of such a region is on the order of the groove width w, and its effect can be disregarded in narrow and deep grooves if we assume that the field inside the groove is uniform. Each chip with interdigital electrodes had 17 grooves forming a "grating" with the periods $A = 32$, 16, and 8 μm. The silicon edge thickness d_{Si} and the groove width w in the final structure differed slightly from the width of the dark and light bands in the photomask and were identical within structures of the same type, $d_{Si} = w$. In addition to the periodic structures, test samples with a single groove of width $w = 50$ μm between electrodes were prepared (Fig. 2). Such samples were opaque in IR light due to the ground rear surface of the samples possessing a p–n junction and the high doping level of the lower region of the substrate. In order to carry out measurements in transmitted light, the rear side of the structures was etched with a CP-4 polishing etchant so as to remove 20–30 μm of silicon. Some of the samples were prepared without a p–n junction. Their rear surface was polished and had high transparency in the IR range (Fe03 sample). Samples that had through grooves (without bottoms) were also prepared (sample $D1$ in Fig. 1). They contained no interdigital electrodes and did not allow study of the electro-optic effect; however, they were convenient for studying the LC anisotropy in the visible region of the spectrum in transmitted light.

In order to measure the optical transmittance, all the samples were mounted onto a foil-clad Gertinax plate with a through semicircular hole at its edge. A metal wire that was 50 μm in diameter and silver paste were used to form a contact between a Si electrode and current-carrying path on the plate (see Fig. 2b). The grooves were filled with a liquid-crystal E7 mixture based on cyanobiphenyls (Merck Co., Germany) at
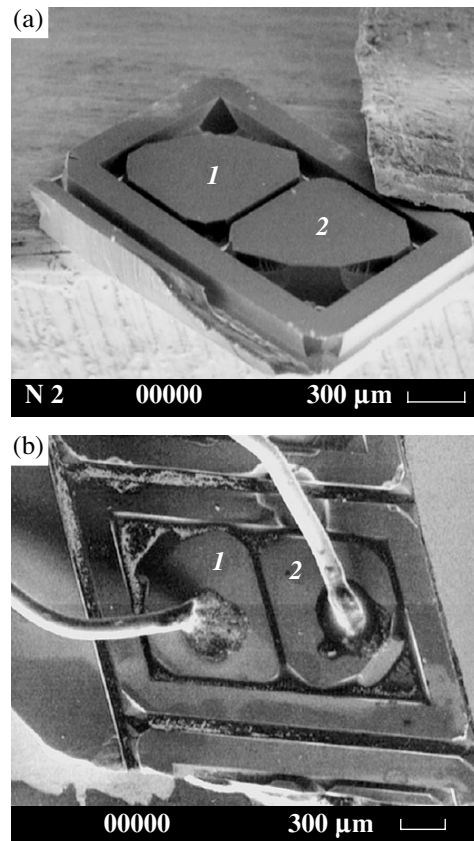
room temperature, i.e., in the nematic phase. Liquid crystal was inserted from a chip corner into a capacity formed by the outer frame and the electrodes. The filling of the grooves and the opposite corner of the capacity was observed using a microscope. The outer frame around the chip ruled out the possibility of LC leakage from the grooves. In sample $D1$ (with through grooves), the LC was confined between the Si walls due to surface tension. In order to compare IR absorption and Raman spectra, large-volume LC cells with BaF_2 windows that were transparent in the visible and IR spectral regions were prepared. To attain uniform planar LC alignment in these cells, the windows were coated with polyvinyl alcohol using a centrifuge, annealed at $T = 100°C$, and then rubbed with velveteen in one direction.

The IR absorption spectra were measured using a Digilab FTS6000 Fourier spectrometer equipped with a UMA-500 IR microscope. In order to measure the electro-optic effect, a rectangular aperture was used to cover either the electrode overlap region (see Fig. 3b) or a single groove (Fig. 2). In other cases, the entire composite area was exposed so as to determine the initial LC alignment. The grooved structures were studied
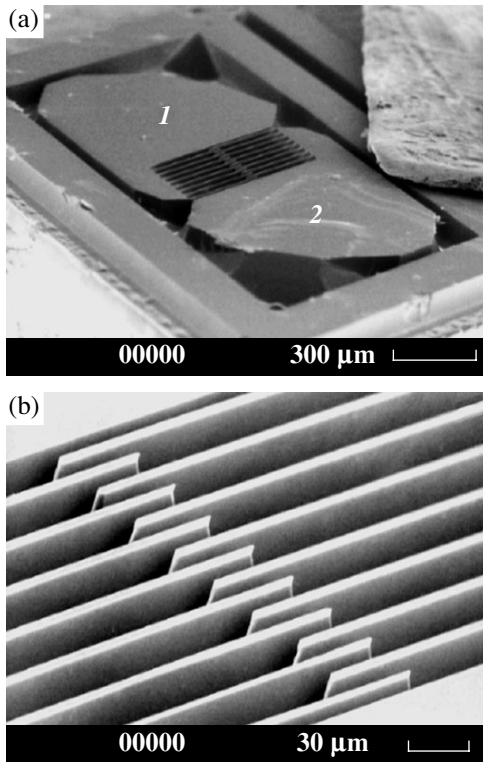
Fig. 3. Sample $D8$, with an interdigital electrode structure, before being filled with liquid crystal (the structure period is $A = 16$ µm and the groove width is $w = 8$ µm): (a) a general view of the chip and (b) a magnified image of the electrode overlap region.

Fig. 4. Schematic diagram of the cross section of a sample with interdigital electrodes insulated using a p–n junction.

when a sample was exposed perpendicularly to the substrate plane. Such a configuration allows separation of the director components along and across the long groove side, but it does not allow measurement of the photonic band gap and its shift under the effect of an electric field. The sample grooves were oriented parallel or perpendicularly to the light polarization vector (see Fig. 5a). It is known that $E7$ LC molecules have several IR absorption bands featuring dichroism [9]. For example, the directions of C≡N and C–C bond vibrations at frequencies $\nu_1 = 2226$ cm^{-1} and $\nu_2 = 1606$ cm^{-1}, respectively, are parallel to the long side of a rod-shaped LC molecule, and the vibration direction at $\nu_3 = 817$ cm^{-1} is perpendicular to the molecule axis. The ratio of the intensities of these bands for two orthogonal polarizations N_A can be used to determine the scalar order parameter S_A [10]. To measure the birefringence, the samples were placed between a polarizer (P) positioned at an angle of 45° with respect to the grooves (see Fig. 5b) and an analyzer (A). The spectra were measured for two analyzer positions: parallel $A \parallel P$ and perpendicular $A \perp P$ to the polarizer.

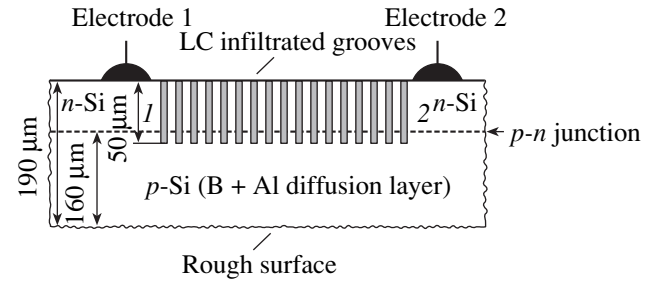The Raman spectra were measured using a Renishaw 1000 system in the backscattering geometry. This system made it possible to focus incident light from an argon laser ($\lambda = 514$ nm) to a spot ~1 µm in diameter. The laser beam power was 5 mW. The scattered-light component oriented in the direction of the incident light polarization was separated using an analyzer. In order to separate the transverse component of the scattered light, a $\lambda/2$ plate was placed in front of the analyzer. The experimental configuration is shown in Fig. 6. The polarization **E** of the incident laser light was always identical (in the horizontal direction in Fig. 6), while the sample was rotated by 90° so that the grooves were parallel or perpendicular to the light polarization vector **E**, i.e., horizontally (H) or vertically (V). Figure 7 shows that the incident light was focused onto the central region of a groove between the electrodes. After rotating the crystal from position H into position V, the exposed spot was fixed at the same position. In polarization RS spectroscopy, it is conventional to use a coordinate system rigidly attached to the sample. The scattered light intensity I_{ij} has two subscripts defining the polarization of scattered (i) and incident (j) light. In such notation, the depolarization ratios for the two sample orientations can be written as $R_H = I_{yx}/I_{xx}$ and $R_V = I_{xy}/I_{yy}$ [11]. The depolarization ratios are used to determine the LC orientation order parameters.

In order to examine the Freedericksz effect under an electric field, a dc or ac voltage with an amplitude $V = 14$–110 V was applied to the grooved sample electrodes. The ac voltage was in the form of rectangular pulses of both polarities with a frequency of 50 Hz.

3. RESULTS AND DISCUSSION

The most reliable data on the initial alignment of LC molecules were obtained from sample $D1$ (with through grooves) (Fig. 1). The LC optical anisotropy in the grooves was detected in the visible region using crossed polarizers of a polarization microscope in transmitted light. As the sample was rotated by 360°, the LC darkened four times when the grooves were parallel or perpendicular to the polarization vector of the incident light. The direction of the LC alignment was determined using IR measurements from the polarization dependence of the ν_1 absorption peak height. We can see in Fig. 8b that, for the polarization parallel $D_\parallel$
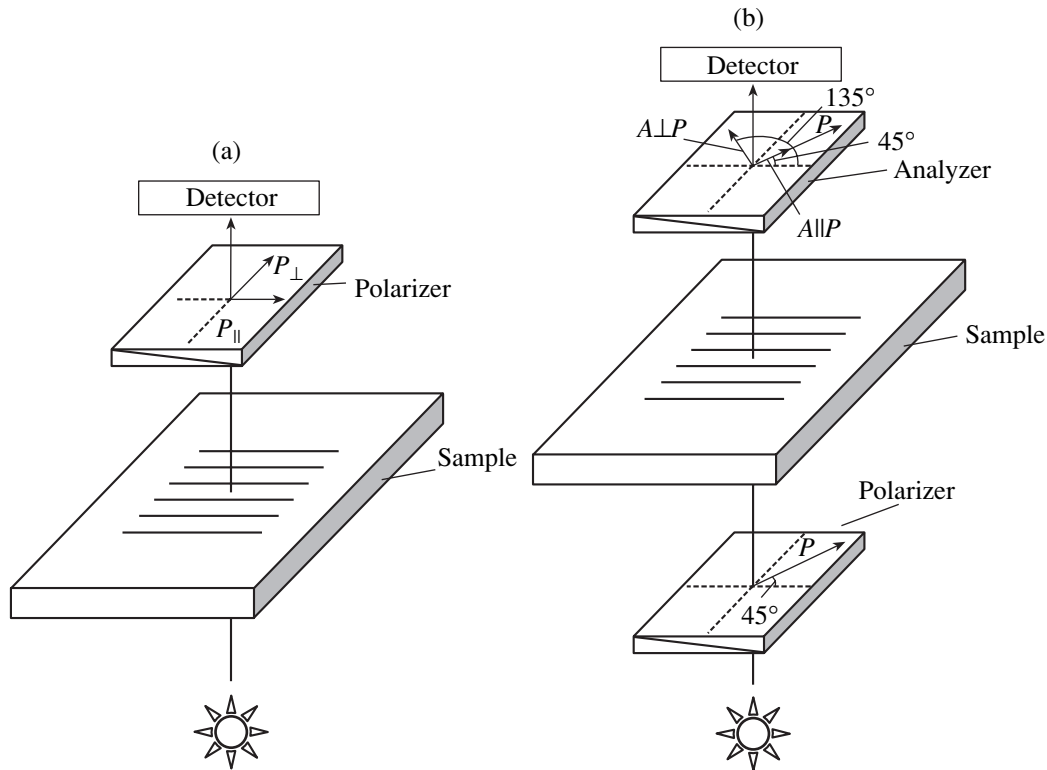
Fig. 5. Schematic diagram of the polarization measurements of the IR transmittance for (a) two orthogonal polarizations of light along and across the grooves and (b) a diagonal orientation of the polarizer and analyzer when measuring the birefringence.

and perpendicular $D_\perp$ to the grooves, the light absorption intensities are not identical. The dichroic ratio is $N_A = \dfrac{D_\parallel}{D_\perp} = 1.21$, which suggests that the predominant
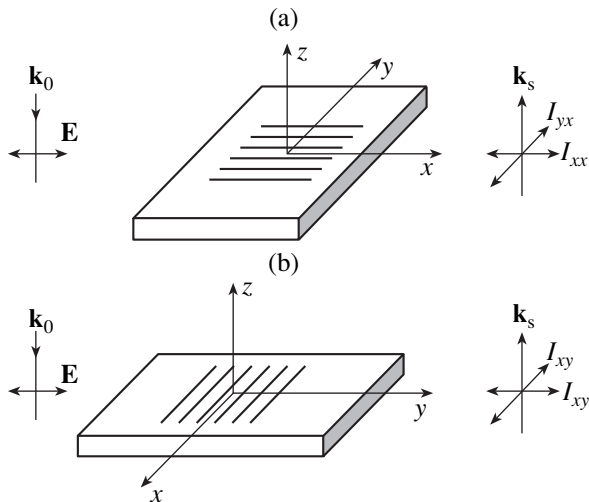

Fig. 6. Schematic diagram of the Raman scattering measurements: (a) horizontal position of the grooves H (parallel to the polarization vector $\mathbf{E}$ of incident light) and (b) vertical position of the grooves V (perpendicular to the polarization vector $\mathbf{E}$ of incident light); $\mathbf{k}_0$ and $\mathbf{k}_s$ are the wave vectors of incident and scattered light, respectively.

orientation of the LC director is along the grooves. The degree of order is not high and can be estimated using the expression (see [10])

$$S_A = \frac{N_A - 1}{N_A + 2} = 0.065. \tag{1}$$

The dichroic ratio for the samples with LC in grooves with bottoms is also small in comparison with that of the large-volume cells (see Table 1).

The birefringence experiment is at its most sensitive to optical anisotropy when a sample is placed between the polarizer and analyzer, positioned at 45° with respect to the optical axis. The spectra of sample $D1$, measured with the crossed $P \perp A$ and parallel $P \parallel A$ polarizer and analyzer, are shown in Fig. 9. In addition to characteristic LC absorption peaks, we can see periodic oscillations whose maxima and minima are out of phase for the two different analyzer positions. In this case, the difference Δn between the refractive indices of ordinary and extraordinary beams can be readily determined from the period of such oscillations, which is caused by the incursive phase difference between the ordinary and extraordinary beams at their exit from the anisotropic medium (see, e.g., [12]):

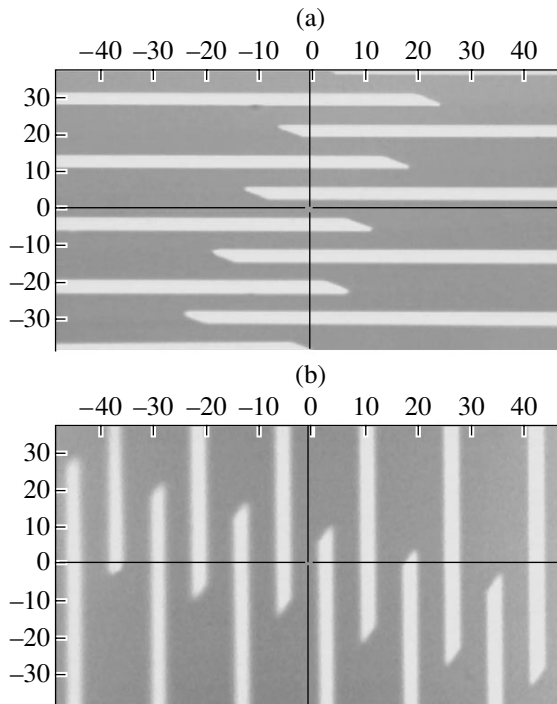$$\Delta n = \frac{10^4}{2l\Delta\nu} = 0.1. \tag{2}$$

Fig. 7. Region between the electrodes exposed to a laser when measuring Raman scattering (indicated by the cross) for (a) horizontal H and (b) vertical V orientations of the grooves with respect to the incident light polarization.

Fig. 8. Spectra of $E7$ liquid crystal in the through grooves of sample $D1$: (a) the intensities I_{xx} and I_{yy} of Raman scattering and (b) the absorptivity of IR light polarized parallel and perpendicularly to the grooves.

Here, $l = 45$ μm is the sample thickness, $\Delta\nu$ is the distance between the maximum at $\nu_{max} = 2100$ cm^{-1} and minimum at $\nu_{min} = 3200$ cm^{-1} in the spectrum when crossed polarizers are used.

A less common method for determining LC orientational ordering is Raman polarization spectroscopy (for the theoretical foundations of this method, see [11]). The Raman microprobe technique is well suited to studying composites based on grooved silicon, since it allows incident laser light to be focused onto a particular area under study. Moreover, the obtained intensities of scattered light are not distorted by having to pass through windows, as in the case of large-volume cells. In contrast to IR spectroscopy in transmitted light, where measurements may be impossible due to the absorption in a heavily doped layer and the scattering at a rough substrate surface, Raman spectra are measured in the backscattering geometry; hence, substrate transparency is of no importance.

The polarization spectra of IR absorption and Raman scattering for sample $D1$ are shown in Fig. 8. When studying the alignment of LC based on cyanobiphenyls using Raman scattering, the band at $\nu_2 = 1606$ cm^{-1}, resulting from C–C bending vibrations of the phenyl ring, is generally used. The vibration direction is also parallel to the long axis of the molecules [13, 14]. Raman scattering is an efficient method of investigation that yields information on the tensor of LC molecule polarizability. This method is used to determine the ori-
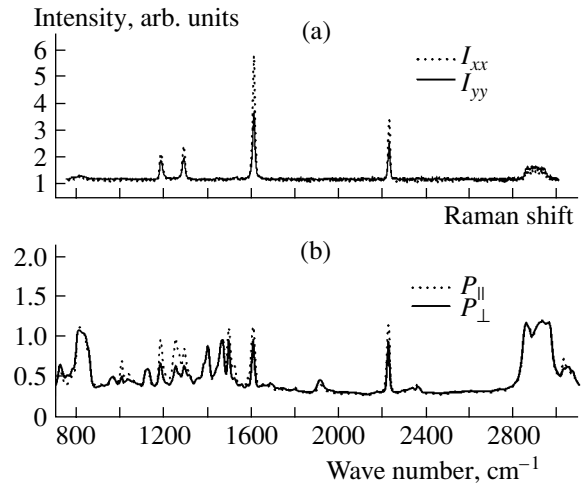
entational order parameters, including the higher degrees of expansion of the distribution function. However, accurate quantitative determination of the above-mentioned quantities is based on rather intricate calculations using input data in the form of experimentally measured depolarization ratios (R_H and R_V) [11, 13]. Therefore, when trying to ascertain the LC director orientation, we did not closely examine the solution to the equations required to obtain accurate parameters for the orientational ordering but used the RS technique to determine the polarization components of the scattered light intensity. Figure 8a shows the Raman spectrum for LC filling of the 48-μm-wide through grooves in sample $D1$. Its comparison with the IR absorption spectrum (Fig. 8b) shows that not all the vibrations are equally active in the IR absorption and Raman spectra. We can easily see the peaks at ν_1 and ν_2, caused by bond vibrations that are parallel to the molecule axis. It follows from the depolarization ratios R_H and R_V for C–C vibration ($\nu_2 = 1606$ cm^{-1}) that $R_V > 1$ (see Table 2). As was shown in [11, 13] and follows from our measurements

Table 1. Geometric parameters and dichroic ratio N_A in the absorption band $\nu_1 = 2226$ cm^{-1} for $E7$ liquid crystal in the grooved silicon samples and a cell with BaF$_2$ windows

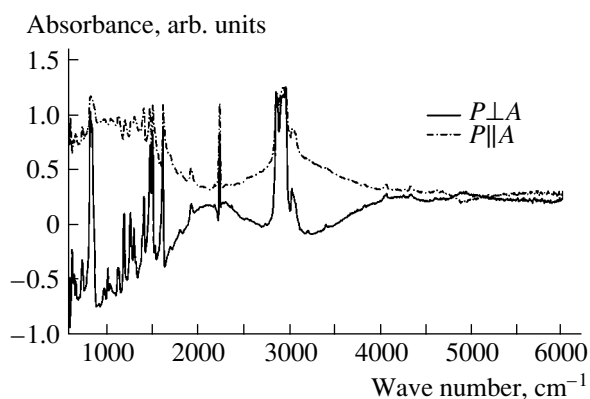| Sample	Structure period A, μm	Groove width w, μm	$N_A = D_\parallel/D_\perp$
$D5$	8	4	1.42
$Fe03$	–	50	1.18
$D4$-2	–	50	1.27
$D1$ (through grooves)	64	48	1.21
BaF$_2$ cell		8 (spacing thickness)	5.69

Absorbance, arb. units

Fig. 9. Optical absorption spectrum of sample *D*1, measured between two diagonally oriented polarizers *P* and *A* (see the diagram in Fig. 5b): $P \perp A$ (solid curve) and $P \parallel A$ (dash-dotted curve).
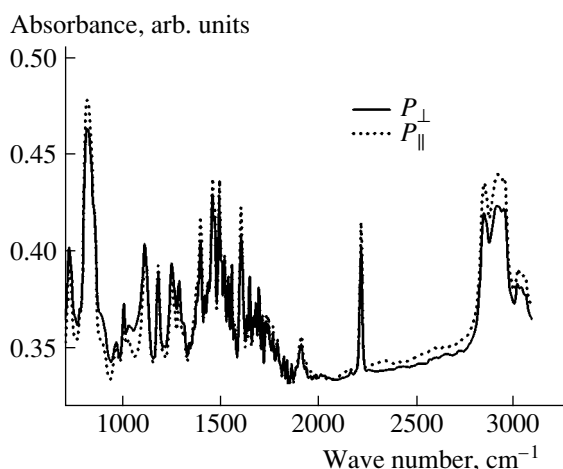
Absorbance, arb. units

Fig. 10. IR absorption spectrum of liquid crystal in sample *Fe*03, which had nonthrough grooves and was without a *p–n* junction.

This conclusion agrees well with the result obtained from the IR measurements. Let us compare the sensitivity of IR- and Raman-spectroscopy polarization methods for the same vibration at $\nu_1 = 2226$ cm^{-1}. The ratio of the intensities of scattered light (with the same polarization as that of the incident laser radiation) for the two mutually perpendicular sample positions *H* and *V* is $N_R(\nu_1) = I_{xx}/I_{yy} = 1.62$. This value is noticeably larger than the intensity ratio $N_A(\nu_1) = 1.21$, which was determined from the IR measurements. For the vibration at $\nu_2 = 1606$ cm^{-1}, the Raman-spectroscopy sensitivity to polarization is even higher, $N_R(\nu_2) = 1.83$, while $N_A(\nu_2) = 1.29$. Hence, the Raman-spectroscopy technique features a higher sensitivity when studying the LC alignment in the *xy* plane parallel to the substrate. In order to determine the *z* component of the director, which is perpendicular to the substrate, light should be incident laterally along the normal to the plane of the silicon edges. Since Si is opaque in the visible region used in Raman-spectroscopy studies, it is impossible to use RS spectroscopy in this configuration.

It was convenient to study the influence of the groove bottoms on the LC alignment using sample *Fe*03, which was without a *p–n* junction. The full range of the IR absorption spectrum for this sample is shown in Fig. 10. We can see that the peaks at $\nu_1 = 2226$ cm^{-1} and $\nu_2 = 1606$ cm^{-1} for parallel vibrations are small in comparison with the peak corresponding to transverse vibrations ($\nu_3 = 817$ cm^{-1}) for both polarizations. A comparison with the *E*7 spectra of the volume cells with planar and homeotropic orientations, as well as with the spectrum of sample *D*1 (possessing through channels) suggests that there exists a vertical director component normal to the substrate surface. The anisotropy in the plane parallel to the substrate is less pronounced than in the case of through grooves and depends on the groove width (at an unchanged groove depth). For example, the birefringence $\Delta n = 0.1$ was also reliably detected in sample *D*5, which had narrow grooves (4 μm wide), where the dichroic ratio for C≡N vibrations is at its largest (see Table 1). This value is almost the same as for sample *D*1 (with wide through grooves), while Δn for sample *K*2, which had 16-μm-wide grooves, is only 0.025.

using the BaF$_2$ cells with uniform planar orientation, $R_V > 1$ is the case where the incident light vector **E** is perpendicular to the LC director. Hence, it can be concluded that the LC director is parallel to the long side of the vertically oriented grooves (sample position *V*).

Table 2. Polarization components of RS from *E*7 liquid crystal in composites based on grooved silicon (with a band at $\nu_2 = 1606$ cm^{-1}), arb. units

Sample	Structure period A, μm	Groove width w, μm	I_{xx}	I_{yy}	$N_R = I_{xx}/I_{yy}$	$R_H = I_{yx}/I_{xx}$	$R_V = I_{xy}/I_{yy}$
*D*2	8	4	5980	1319	4.53	0.453	1.310
*D*8	16	8	2787	1947	1.43	0.513	0.907
*K*2	32	16	2319	1412	1.64	0.324	1.070
*D*1	64	48	4620	2520	1.83	0.425	1.158
BaF$_2$ cell		8 (spacing thickness)	14605	931	15.68	0.116	1.577

The RS data are listed in Table 2. The first point to note is that we can see qualitative agreement with the IR spectrometry data (Table 1). Second, the dependence of N_R and the depolarization ratios R_H and R_V on the groove width also manifests itself. The director orientation along the grooves is most pronounced for sample $D2$ (with a groove width of 4 μm), but this orientation is much weaker for grooves that are 8 and 16 μm wide. A comparison with sample $D1$, which has no groove bottoms and possesses wider grooves but retains the director orientation along them, allows us to conclude that a rough bottom distorts the director orientation. The influence of the bottoms becomes stronger as the groove depth-to-width ratio l/w decreases.

4. THE ELECTRO-OPTICAL EFFECT

The electro-optical effect can be visually observed in reflected polarized light under a microscope. As a dc, sawtooth, or pulsed voltage is applied under conditions in which crossed polarizers are used, the LC luminance in the strong-field region between the electrodes changed. The threshold voltage of the Freedericksz transition under the effect of an electric field for a sample with $w = 16$ μm was 14 V, whereas it was 2 V in the LC cells. This effect is apparently caused by a voltage drop across the contacts of the grooved structure. A further increase in the voltage strengthened the effect. At $V = 90$–110 V (depending on the signal frequency in the range 2–400 Hz), the LC in the grooves darkened over the entire structure length. This effect also took place in initially bright regions in the horizontal bottom region. In this case, the leakage current through the p–n junction was no higher than 200 μA in the best samples. We believe that it is possible to interpret the observed effect under voltages <30 V as a Freedericksz transition: First, Coulomb forces align the molecules, initially arranged along the grooves, in the horizontal plane parallel to the substrate. At higher voltages, the field transfers vertically oriented (homeotropically to the substrate) near-bottom molecules to the horizontal plane as well. In some of the samples, high voltages of ~100 V caused both high leakage currents (up to 5 mA) and structure heating up to 70°. In this case, the LC transformed into an isotropic state. Therefore, study of the electric-field effect required close control of the current flowing through the structure.

Figure 11 shows changes in the amplitude of the IR absorption band ν_1 as a voltage of 30 V is applied to an individual groove with a width of 50 μm. The change is most significant for light polarization perpendicular to the groove. In the samples with interdigital structures, where a smaller aperture in the electrode overlap region was required, we failed to detect changes in the peak height or Δn in the IR spectra. These changes were within the experimental error. In contrast, the RS measurements detected significant changes in the scattered light amplitude.

Figure 12 shows the RS spectra for sample $K2$. We can see that all the polarization components of scattered
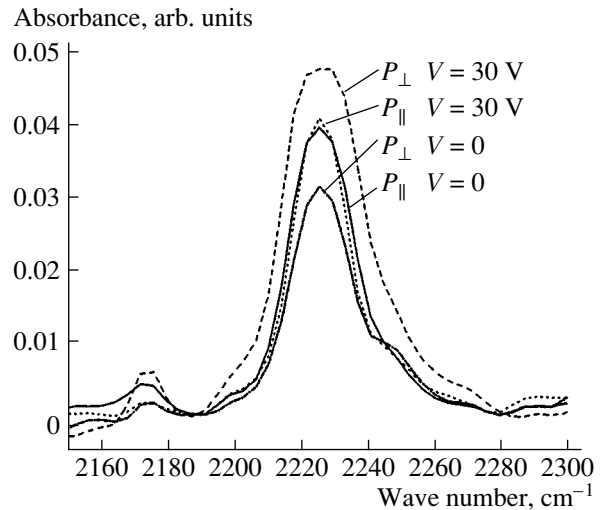

Fig. 11. Change in the height of the IR absorption peaks for light of various polarizations in sample $D4$-2 as an ac voltage $V = 30$ V is applied to the electrodes.
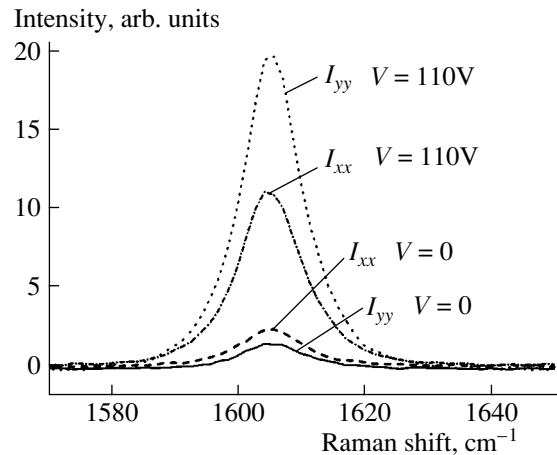

Fig. 12. Influence of an electric field on the polarization components of Raman-scattered light for sample K-2 ($V = 110$ V).

light significantly increase when rectangular pulses with an amplitude $V = 110$ V are applied to the electrodes (see Table 3). The amplitude I_{yy} increases most markedly (by a factor of 14) when the y component with polarization parallel to that of the incident light is separated from the scattered light and the incident light itself is polarized perpendicularly to the grooves (and perpendicularly to the initial director orientation).

The external electric field is directed along the y axis, and the LC molecules also tend to align in this direction. If the degree of orientational ordering is estimated using amplitude ratios at various voltages, $N_R(0) = I_{xx}/I_{yy}$ at $V = 0$ and $N_R(110) = I_{yy}/I_{xx}$ at $V = 110$ V, the director orientation varies from a planar orientation with respect to Si edge ($N_R(0) = 1.64$) to a homeotropic one ($N_R(110) = 1.79$). This variation affects the depolar-

Table 3. Influence of an ac electric field ($f = 50$ Hz, rectangular pulses) on the polarization components of the RS amplitude from liquid crystal in sample $K2$ ($v_2 = 1606$ cm^{-1})

Voltage, V	I_{xx}	I_{yy}	I_{yx}	I_{xy}	$R_H = I_{yx}/I_{xx}$	$R_V = I_{xy}/I_{yy}$
0	2319	1412	752	1544	0.324	1.07
110	11051	19756	1861	5057	0.168	0.256

Table 4. Dependence of the RS polarization components on the dc voltage applied to sample $D8$

Voltage, V	I_{xx}	I_{yy}	I_{yx}	I_{xy}	$R_H = I_{yx}/I_{xx}$	$R_V = I_{xy}/I_{yy}$
0	2787	1947	1429	1767	0.513	0.907
10	2895	1639	1479	1468	0.511	0.896
30	2984	1806	1558	1677	0.522	0.929
50	2915	2859	1635	2178	0.561	0.762
70	3711	3430	1986	2752	0.535	0.802

ization ratios as well. An increase in all the scattered light components apparently indicates director rotation to the plane parallel to the substrate.

Table 4 shows the variation in the scattered light amplitudes as the dc bias voltage between the sample $D8$ electrodes increases. The amplitude I_{yy}, as in the previ-
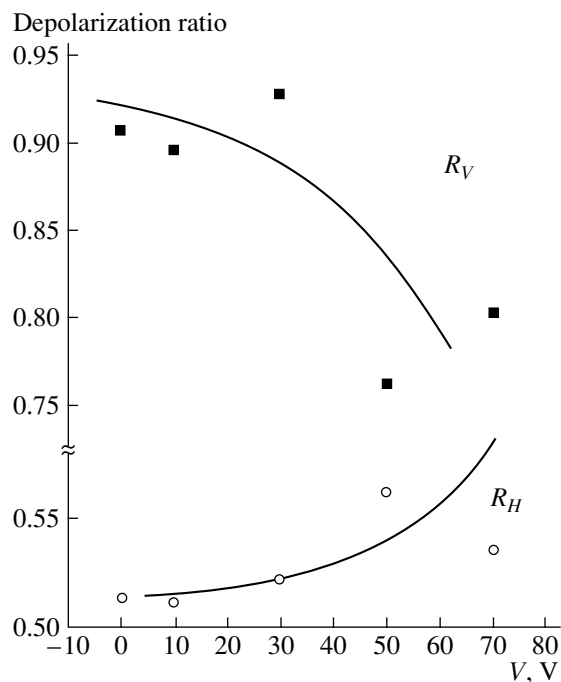
ous case, is most sensitive to the electric field. However, there is no more than a twofold change in this amplitude. Figure 13 shows the voltage dependences of depolarization ratios. The ratio R_V decreases, whereas R_H increases as the field strengthens, which indicates an increase in the fraction of molecules oriented along the field (perpendicular to the grooves).

5. CONCLUSION

In conclusion, we note that nematic $E7$ liquid crystal (LC) features weak adhesion to the vertical walls of grooved silicon; however, this LC is aligned mainly along the long groove sides (Fig. 14a). The groove bottom causes a more complex configuration of the director, since a fraction of the molecules are oriented homeotropically with respect to the substrate. An external electric field facilitates the transfer of LC molecules into a single plane and their alignment along the field lines (Fig. 14b). Polarization measurements showed that the most appropriate technique for studying LC alignment in grooved Si is RS microprobe spectroscopy. The electro-optical effect was observed in specially developed device structures, and it can be used to adjust the photonic band gap of grooved silicon–LC composites.
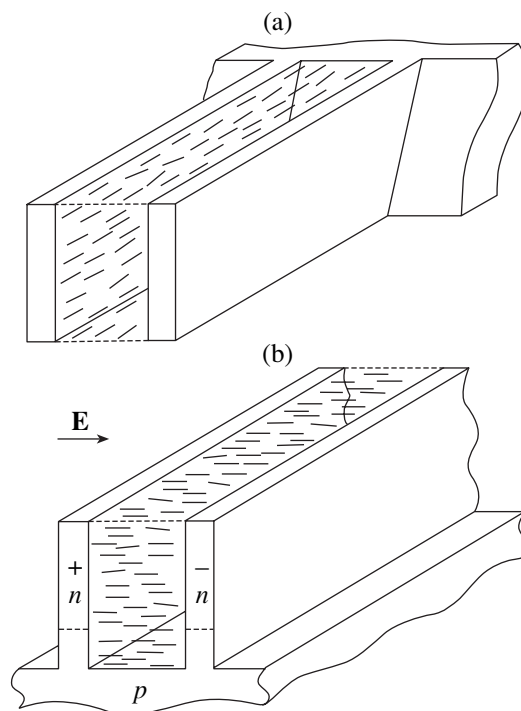

Fig. 13. Dependence of the depolarization ratios R_H and R_V on the applied dc voltage for sample $D8$.

Fig. 14. Schematic diagram of the orientation of the liquid crystal director in a silicon groove: (a) the initial orientation in a groove without a bottom and (b) the orientation in a groove with a bottom under the influence of an applied electric field (structure with insulated electrodes).

ACKNOWLEDGMENTS

REFERENCES

1. K. Busch and S. John, Phys. Rev. Lett. **83**, 967 (1999).

2. S. Gottardo, D. S. Wiersma, and W. L. Vos, Physica B (Amsterdam) **338**, 143 (2003).

3. G. Mertens, T. Röder, R. Schweins, *et al.*, Appl. Phys. Lett. **80**, 1885 (2002).

4. S. W. Leonard, J. P. Mondia, H. M. van Driel, *et al.*, Phys. Rev. B **61**, 2389 (2000).

5. G. Mertens, T. Röder, H. Matthias, *et al.*, Appl. Phys. Lett. **83**, 3036 (2003).

6. V. A. Tolmachev, L. S. Granitsyna, E. N. Vlasova, *et al.*, Fiz. Tekh. Poluprovodn. (St. Petersburg) **36**, 996 (2002) [Semiconductors **36**, 932 (2002)].

7. V. A. Tolmachev, T. S. Perova, and K. Berwick, Appl. Opt. **42**, 5679 (2003).

8. V. A. Tolmachev, T. S. Perova, E. V. Astrova, and R. M. Moore, in *Proceedings of 5th International Conference on Transparent Optical Networks* (Warsaw, 2003), Vol. 1, Tu.P.2.

9. S. T. Wu, Opt. Eng. **26**, 120 (1987).

10. L. M. Blinov, *Electro- and Magneto-Optics of Liquid Crystals* (Nauka, Moscow, 1978) [in Russian].

11. K. Miyano, J. Chem. Phys. **69**, 4807 (1978).

12. S. É. Frish and A. V. Timoreva, *Course of General Physics*, Vol. 3: *Optics. Atomic Physics* (Fizmatgiz, Moscow, 1961), p. 192 [in Russian].

13. S. Jen, N. A. Clark, and P. S. Pershan, J. Chem. Phys. **66**, 4635 (1977).

14. W. J. Jones, D. R. Thomas, D. W. Thomas, and G. Williams, J. Mol. Struct. **614**, 75 (2002).

Translated by A. Kazantsev

Hydrogen-Containing Donors in Silicon: Centers with Negative Effective Correlation Energy

Yu. M. Pokotilo^, A. N. Petukh, V. V. Litvinov, and V. G. Tsvyrko

Belarussian State University, Leningradskaya ul. 14, Minsk, 220050 Belarus
^e-mail: pokotilo@bsu.by
Submitted July 13, 2004; accepted for publication October 14, 2004

Abstract—The reconstruction of shallow-level hydrogen-containing donors in Si is studied. The donors are formed by implantation of low-energy (300 keV) hydrogen ions into the experimental samples and subsequent heat treatment at 450°C. The experiments are carried out for Ag–Mo–Si Schottky diodes and diodes with a shallow (~1 μm) p^+–n junction. The concentration and distribution of the donors are determined by applying the method of C–V characteristics at a frequency of 1.2 MHz. An analysis of the temperature dependence of the equilibrium electron concentration shows that the reconstruction of the hydrogen-containing donors can be described under the assumption of recharging of a center with negative effective correlation energy ($U < 0$). The transformation between two equilibrium configurations of a double hydrogen donor ($D_B^{++} \longleftrightarrow D_A^0$) proceeds with the Fermi level position $E_F = E_c - 0.30$ eV. The reconstruction of the donors from a neutral to a doubly charged state ($D_A^0 \longrightarrow D_B^{++}$) which is stimulated by the capture of minority carriers, is observed at room temperature. © 2005 Pleiades Publishing, Inc.

It is known that two types of hydrogen-containing donors are formed in hydrogen-implanted Si during heat treatment [1–3]. A short-term heat treatment of samples at 300–400°C leads to the formation of hydrogen double donors (HDDs), and their further heat treatment at 350–450°C leads to the emergence of shallow-level hydrogen donors (SHDs) with levels at $E_c -$ (0.020–0.035) eV [4]. It has been found that the SHD defects are bistable, and their concentration varies reversibly in the temperature range 90–300°C [5]. The limiting concentration of SHD centers (~10^{17} cm^{-3}) is attained at the Fermi level $E_c - 0.30$ eV. In combination with a slow conductivity relaxation at 100–200°C, this fact allowed Mukashev *et al.* [6] to assume that SHD centers have negative effective correlation energy ($U < 0$). In this study, we obtained more rigorous proof of this suggestion based on study of the temperature dependence of the equilibrium electron concentration during thermal reconstruction of SHDs and on the effect of minority charge carriers on this reconstruction.

In the experiment, we used Schottky diodes based on epitaxial P-doped n–n^+-Si structures with an n-type layer that had a resistivity of $\rho = 1.2$ Ω cm and shallow (~1 μm) p^+–n junctions with a high-resistivity ($\rho = 1$ kΩ cm) base on the basis of floating-zone Si. The samples were irradiated with H$^+$ ions at an energy of 300 keV and a 10^{15} cm^{-2} flux through the metal (Ag–Mo) contact of a Schottky diode or through the p^+-region of a junction. The irradiated samples were annealed in a quartz tube in air. The concentration profiles of the electron concentration in the diode bases were mea-

sured using a standard C–V method at a frequency of 1.2 MHz. Prior to the measurement, all the samples were thermally annealed for 20 min at 450°C, which corresponds to the accumulation mode of the highest SHD concentration [4].

The heat treatment of all the hydrogen-implanted samples led to an increase in the electron concentration in the diode bases and to residual nonequilibrium conductivity, which was caused by sample quenching from 280°C. Figure 1 shows the profiles of the electron concentration (n_0) in the base of an irradiated Schottky diode, which were measured after the sample had been quenched in water from 280°C and then kept at a fixed temperature in the range 100–280°C until the equilibrium value was attained. It can be seen that, at $X > 0.75$ μm, the measured value of n_0 corresponds to the P concentration in the epitaxial layer, while, at $X < 0.75$ μm, a sharp decrease in the electron concentration and a subsequent drop at the barrier interface is observed. A comparison of the profiles $n_0(X)$ with the distribution of implanted hydrogen ions, which was calculated using the TRIM code [7] (the solid curve in Fig. 1), allows us to suggest that the increase in the electron concentration is associated with the formation of hydrogen-containing donors.

Figure 2 shows the kinetics of variation in the electron concentration $n(t)$ at their distribution peak ($X \approx 0.4$ μm) after the samples had been quenched from 280°C in water and then kept at this temperature for a
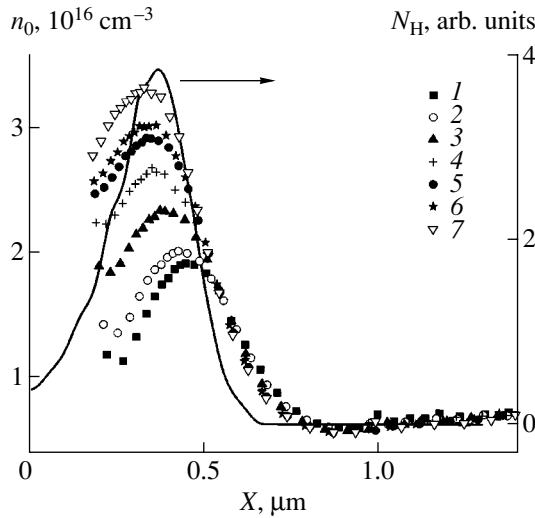
Fig. 1. Concentration profiles for electrons in the bases of Schottky diodes irradiated with hydrogen ions (at a dose of 10^{15} cm^{-2} and energy of 300 keV). The profiles were measured after quenching the samples from 280°C in water and then keeping them at a fixed temperature (T) until the equilibrium value was attained. The solid line shows the calculated concentration profile for implanted hydrogen N_H (the TRIM code [1]). $T = $ (1) 100, (2) 120, (3) 150, (4) 170, (5) 190, (6) 210, and (7) 280°C.
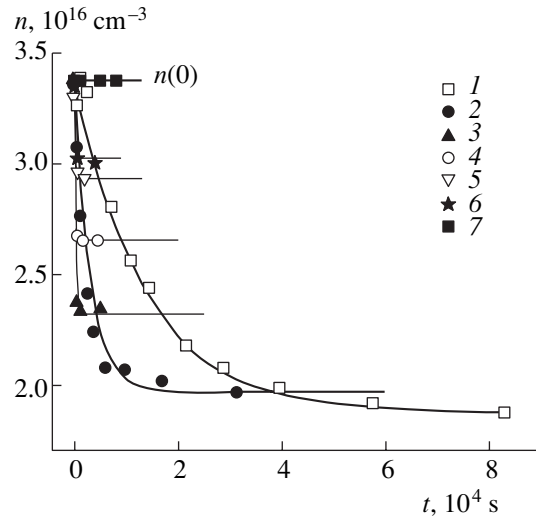

Fig. 2. Kinetics of variation in the electron concentration at the peak of its distribution ($X \approx 0.4$ μm) after quenching the samples from 280°C in water and then keeping them at temperature T. The numbering of the curves is the same as in Fig. 1.
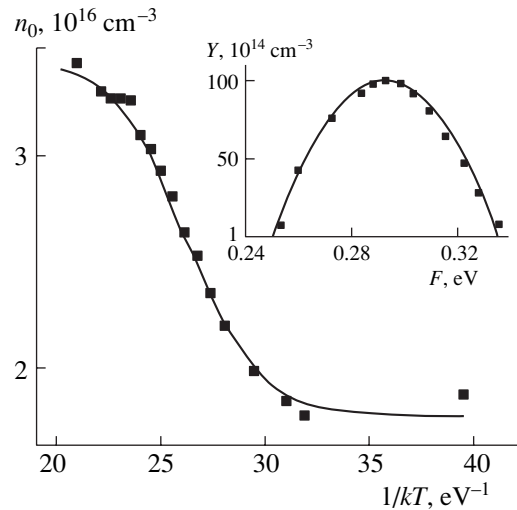

Fig. 3. Temperature dependence of the equilibrium electron concentration. The solid line represents the results of calculation by formula (3). The analysis of these data using the Hoffmann method is shown in the inset.

time t. It is found that the kinetics of the isothermal relaxation $n(t)$ at 90–200°C is described by the relation

$$n(t) = n_0 + [n(0) - n_0]\exp(-t/\tau). \qquad (1)$$

Here, $n(t)$, n_0, and $n(0)$ are the current, equilibrium, and initial (after quenching) electron concentrations at this temperature, respectively, and τ is the time constant, whose temperature dependence can be written as

$$\tau = 10^{-11}\exp(1.14/kT). \qquad (2)$$

Here, τ is expressed in seconds, and the activation energy $E = 1.14$ eV. It is noteworthy that the determined values of the parameters of slow conductivity relaxation are close to those reported in [8, 9] for the reconstruction of shallow-level hydrogen donors.

The temperature dependence of the equilibrium electron concentration n_0 is shown in Fig. 3. The values of n_0 were determined after keeping the samples for $t > 3\tau$, for example, for 15 months at room temperature (20°C), to attain the equilibrium state. Taking into account the slow establishment of the equilibrium concentration of SHD centers and the fact that shallow donor levels ($E_c - (0.020–0.035)$ eV) are related to these centers, we can explain the observed dependence $n_0(T)$ only under the assumption of reversible reconstruction of the SHD configuration. In this case, all the centers should be in a neutral state (configuration A) at temperatures lower than 90°C and in a shallow-level donor state (configuration B) at temperatures higher than 220°C. Such behavior is characteristic of bistable

oxygen-containing quenched-in donors in Si [10] and Ge [11].

By analogy with the quenched-in donors, let us assume that the SHDs are also double donors with negative effective correlation energy ($U < 0$). It can be shown [10, 11] that, in this case, the equilibrium defect configurations are D_A^0 and D_B^{++} while the concentration of defects with a single captured electron is close to zero; i.e., the total donor concentration $N \approx D_A^0 + D_B^{++}$. Taking into account this circumstance, the electroneutrality equation for the cases of single-electron and dou-
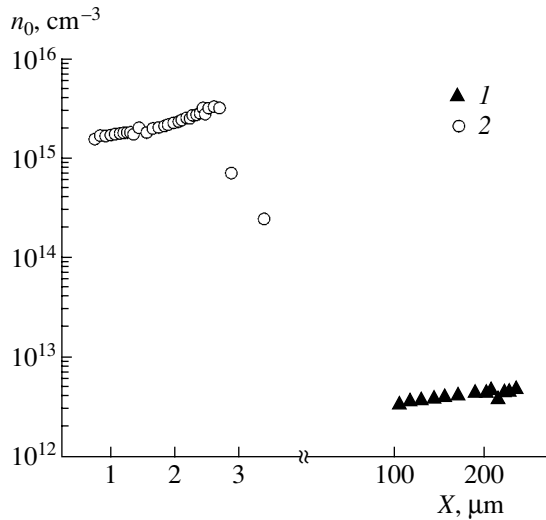
n_0, cm^{-3}

Fig. 4. Injection-induced reconstruction of the configuration of the SHD donors ($D_A^0 \longrightarrow D_B^{++}$) at room temperature. The data for the state D_A^0 (*1*) were obtained after keeping the bipolar diodes with introduced donors at $T = 100°C$ for 10 h, and the data for the state D_B^{++} (*2*) were obtained after injection of minority carriers at the forward current density $j = 10$ mA/cm^2 for 5 s.

ble-electron recharging of donors has the same form and can be written as

$$\left(\frac{n_0}{N_c}\right)^{\alpha} \frac{n_0(N_D - N_A)}{(N_D - N_A) + \alpha N} = g(\alpha)\left[\exp\left(-\alpha\frac{\Delta E^{(\alpha)}}{kT}\right)\right]. \quad (3)$$

Here, $\alpha = 1$ for a single donor, $g(1) = g^+/g^0$ is the spin degeneracy factor, $\Delta E^{(1)} = E_c - E(0/+)$ is the single-electron ionization energy of a donor, $\alpha = 2$ for a double donor with $U < 0$, $g(2) = g^{++}/g^0$, $\Delta E^{(2)} = E_c - E(0/++)$, $E(0/++) = (1/2)[E(0/+) + E(+/++)]$ is the double-electron occupancy level, $E(0/+)$ is the difference between donor energies in the neutral and singly positively charged states, $E(+/++)$ is the difference between donor energies in the singly and doubly positively charged states, and $N_D - N_A$ is the difference of the concentration of donors and acceptors. It follows from Eq. (3) that, when the Fermi level (F) is located lower than $E(0/++)$, a defect with $U < 0$ is in the state D_B^{++}, and, when $F > E(0/++)$, it is in the state D_A^0.

The experimental dependence $n_0(T)$ is described by Eq. (3) (the solid line in Fig. 1) under the assumption of both single-electron ($\alpha = 1$, case 1) and double-electron ($\alpha = 2$, case 2) ionization of the donors. However, in case 1, agreement between the calculated and experimental dependences is attained for the overestimated value $\Delta E^{(1)} = E_C - 0.63$ eV and physically unrealistic value of the spin degeneracy factor $g(1) = 6000$, while,

for a double donor with $U < 0$, agreement is attained for realistic values of the parameters: $E(0/++) = E_c - 0.30$ eV, $g^{++}/g^0 = 1$, and $N = 8.35 \times 10^{15}$ cm^{-3}. A differential analysis of the temperature dependences of n_0 using the Hoffmann method [12, 13] (see the inset in Fig. 3) also suggests double-electron recharging of the centers. Indeed, the presented dependence $n_0(T)$ in the coordinates $Y = kT(dn_0/dF)$ versus F looks like a spectral band that has a peak at the Fermi level $F = E_c - 0.293$ eV and half-width $\delta F = 1.8kT_m$, where T_m is the temperature at which the maximum value of Y is attained. According to Hoffmann [12], for conventional defects ($U > 0$), the peak $Y_m = (1/4)N$ at $F_m = \Delta E^{(1)}$ and the peak half-width $\delta F = 3.5kT_m$ while, for the defects with $U < 0$, $Y_m = N$, $F_m = \Delta E^{(2)}$, and $\delta F = 1.8kT_m$.

It also can be seen from Fig. 3 that the total concentration of the unreconstructed hydrogen donors minus that of the compensating acceptors ($N_D - N_A$) $\approx 1.2 \times 10^{16}$ cm^{-3} exceeds the concentration of the P dopant by almost a factor of 2. It is evident that there are several types of shallow-level hydrogen donors, and only some of them, in a similar way to quenched-in donors in Si [10] and Ge [11], feature reconstruction. This circumstance also agrees with the observation, via photoionization spectroscopy, of seven types of shallow-level hydrogen-containing defects (HD1–HD7) with close ionization-energy values (0.034–0.053 eV) [14].

According to the suggested model of two-electron recharging, the SHD centers are in the D_A^0 state at $F > E(0/++)$. In this case, minority carriers (holes), which are injected into the bases of the diodes, should be captured at the deep level $E(0/+) = 2E(0/++) - E(+/++) \approx E_c - 0.6$ eV. This phenomenon causes the configurational reconstruction $D_A^0 \longrightarrow D_B^{++}$ and an increase in the electron concentration, which is similar to the case of capture of photogenerated holes at reconstructing quenched-in donors [8, 9]. The experimental results shown in Fig. 4 completely confirm this model. A bipolar diode, which contained a shallow p^+–n junction and SHD centers incorporated into the base, was transformed into state *1* (see Fig. 4) with a low electron concentration as a result of being kept at $T = 100°C$ for 10 h. Then, the injection of minority carriers was carried out with the forward current density $j = 10$ mA/cm^2 for 5 s, which caused the transformation of the diode into state *2* with a high electron concentration. The nonequilibrium conductivity state and corresponding variation in the capacitance of the unbiased p^+–n junction within the range $100 \longrightarrow 3600$ pF was retained without injection at room temperature for several months. The experiment was repeated many times, and it indicated that the configuration reconstruction of the SHD centers was controlled by the change in their charge state.

The results of this study allow us to conclude that shallow-level hydrogen-containing donors (SHDs) in Si are centers with negative correlation energy ($U < 0$).

By analogy with quenched-in donors in Si and Ge, they can exist in the two equilibrium configurations D_B^{++} and D_A^0. A reversible transfer from one of these configurations to the other ($D_A^0 \longleftrightarrow D_B^{++}$), which occurs in the temperature range 100–200°C, is controlled by a change in the charge state for the Fermi level location near $E_c - 0.30$ eV. It is found that minority carriers injected into the base cause the transfer of the SHD centers from a neutral charge state to a double-positive state ($D_A^0 \longleftrightarrow D_B^{++}$) and, thereby, residual room-temperature conductivity.

REFERENCES

1. Y. Ohmura, Y. Zohta, and M. Kanazawa, Phys. Status Solidi A **15**, 93 (1973).

2. Yu. V. Gorelkinskii, V. O. Sigle, and Zh. S. Takibaev, Phys. Status Solidi A **22**, 55 (1974).

3. V. V. Kozlovskiĭ, *Modification of Semiconductors by Proton Beams* (Nauka, St. Petersburg, 2003) [in Russian].

4. Kh. A. Abdullin, Yu. V. Gorelkinskiĭ, and B. N. Mukashev, Fiz. Tekh. Poluprovodn. (St. Petersburg) **36**, 257 (2002) [Semiconductors **36**, 239 (2002)].

5. Yu. V. Gotelkinskii and N. N. Nevinnyi, Nucl. Instrum. Methods Phys. Res. **209**, 677 (1983).

6. B. N. Mukashev, Kh. A. Abdullin, and Yu. V. Gorelkinskiĭ, Usp. Fiz. Nauk **170**, 143 (2000) [Phys. Usp. **43**, 139 (2000)].

7. F. F. Komarov and A. F. Komarov, *Physical Processes During Ion Implantation in Solids* (Tekhnoprint, Minsk, 2001) [in Russian].

8. Yu. V. Gorelkinskii, Kh. A. Abdullin, and B. N. Mukashev, Mater. Sci. Eng. C **19**, 397 (2002).

9. Kh. A. Abdullin, Yu. V. Gorelkinskii, and B. N. Mukashev, Physica B (Amsterdam) **340–342**, 692 (2003).

10. L. F. Makarenko, V. P. Markevich, and L. I. Murin, Fiz. Tekh. Poluprovodn. (Leningrad) **19**, 1935 (1985) [Sov. Phys. Semicond. **19**, 1192 (1985)].

11. V. V. Litvinov and G. V. Palchik, Phys. Status Solidi A **108**, 311 (1988).

12. H. I. Hoffmann, Appl. Phys. A **27**, 39 (1982).

13. H. I. Hoffmann, Appl. Phys. A **27**, 307 (1982).

14. I. Hartung and I. Weber, Phys. Rev. B **48**, 14161 (1993).

Translated by N. Korovin

ELECTRONIC AND OPTICAL PROPERTIES OF SEMICONDUCTORS

Weak Ferromagnetism in InSe:Mn Layered Crystals

V. V. Slyn'ko*^, A. G. Khandozhko**, Z. D. Kovalyuk*, A. V. Zaslonkin*,
V. E. Slyn'ko*, M. Arciszewska***, and W. D. Dobrowolski***

*Institute of Material Sciences (Chernovtsy Branch), National Academy of Sciences of Ukraine,
ul. Zhovtneva 5, Chernovtsy, 58001 Ukraine
^e-mail: sel@chv.ukrpack.net
**Fed'kovich State University, ul. Kotsyubinskogo 2, Chernovtsy, 58012 Ukraine
***Institute of Physics, Polish Academy of Sciences, 02-668 Warsaw, Poland
Submitted October 5, 2004; accepted for publication October 19, 2004

Abstract—The electron spin resonance, magnetization, and dynamic magnetic susceptibility of $In_{1-x}Mn_xSe$ layered crystals ($x = 0.0125$) are studied. It is found that two different impurity subsystems independently coexist in the crystalline layer and in the interlayer spacing of unannealed samples. In both subsystems, ferromagnetic exchange interaction occurs between the Mn ions in the temperature range 300–140 K, and antiferromagnetic interaction occurs in the range 140–77 K. At temperatures below 77 K, a three-dimensional ferromagnetic order emerges. © 2005 Pleiades Publishing, Inc.

1. INTRODUCTION

In recent years, numerous studies have been devoted to investigation of a new class of semimagnetic semiconductors of the type $III_{1-x}–M_x–VI$, in which III–VI are layered crystals of the GaS group (GaSe, GaS, InSe, and GaTe) and M is a metal ion belonging to the transition group [1–6]. These systems are of interest because they possess nonlinear optical properties and, therefore, may be valuable for optoelectronic applications.

Similarly to II–VI semiconductors, the magnetic ions in the III–VI crystals are in a tetrahedral environment; however, their local environment is different, since each cation is surrounded by three anions and one cation. In addition, direct cation–cation bonds exist. Under these circumstances, the formation of pairs of direct interaction ($M–M$) in the layered crystals, in addition to standard indirect pairs of an $M–Se(S)–M$ type, is quite possible.

The formation of direct Mn–Mn pairs in a $Ga_{1-x}Mn_xSe$ alloy [5] and the absence of such pairs in a $Ga_{1-x}Mn_xS$ alloy [6] has been established via study of the temperature and field dependences of magnetization $M(T)$ and $M(H)$. The existence of strong direct interaction between the Mn ions in $Ga_{1-x}Mn_xSe$ crystals ($x = 0.012$) leads to the establishment of two-dimensional short-range antiferromagnetic order in the range 120–195 K. In $Ga_{1-x}Mn_xS$ crystals ($x = 0.11$, 0.066) in the same temperature range, only indirect antiferromagnetic interaction between the Mn ions is observed. At $T = 10.9$ K, an abrupt peak is observed in the dependence $M(T)$. This peak is thought to be associated with a transition to spin glass.

Making allowance for the substantial distinction in the state of the impurity systems in the $Ga_{1-x}Mn_xSe$

and $Ga_{1-x}Mn_xS$ layered crystals, it is of interest to study the magnetic properties of $In_{1-x}Mn_xSe$ alloys, which differ from the $Ga_{1-x}Mn_xSe$ alloys in the type of cations present. In this study, we examined the ESR spectra, magnetization curves, and dynamic magnetic susceptibility of $In_{1-x}Mn_xSe$ crystals. Based on these dependences, we analyzed the state of the impurity system in various temperature ranges.

2. EXPERIMENTAL

The $In_{1-x}Mn_xSe$ crystals were grown using the Bridgman–Stockbarger method and doped by adding 1 at % of Mn to the growth charge. X-ray fluorescent analysis showed that the impurity distribution along the ingot was nonuniform. In the initial part of the ingot (up to 0.6 of its length), the Mn content was no higher than 0.15 at %. In the end part, this content was as high as 3.5 at %.

The ESR spectra were recorded at a frequency of 10 GHz in the range 77–300 K using an ESR spectrometer with a digital signal integrator. The magnetic field was monitored with an NMR sensor accurate to ±1 G. As a standard, we used diphenyl pycryl hydrazil (DPPH) with a spin concentration of 5.0×10^{17} cm^{-3} and g factor of 2.0036.

In order to study the magnetization curves $M(H)$ and dynamic magnetic susceptibility $\chi_{ac}(T)$ of the samples, we used a Lake Shore 7229 AC Susceptometer/DC Magnetometer double-purpose system [7, 8]. The value of $\chi_{ac}(T)$ was measured in an ac magnetic field with an amplitude of ±20 Oe and frequency of 800 Hz in the temperature range 4.2–300 K. The magnetization curves $M(H)$ were obtained in the region of weak magnetic fields ($H = ±40$ Oe) at various temperatures.

3. RESULTS

The ESR spectra were measured for unannealed samples, which were cut along the growth axis of the ingot. A very weak ESR signal is detected for samples with the Mn content $N_{Mn} \leq 0.15$ at % (without any signs of a hyperfine structure). For samples with $N_{Mn} \approx 1$–2 at %, two-component ESR spectra are observed. A narrow line manifests itself against the background of a broad line. The intensity of the narrow line depends on the impurity distribution in the crystal.

The greatest separation between spectral components is observed in samples with $N_{Mn} = 1.25$ at % and the magnetic field **H** directed at an angle of 55° to the hexagonal axis c. Curve a in Fig. 1 shows that the ESR spectrum consists of two resonance lines, namely, a broad I line and a narrower L line. In is noteworthy that the L line virtually vanishes for a sample annealed in vacuum at $T = 593$ K for 28 h (Fig. 1, curve b). The data on ESR, χ_{ac}, and $M(H)$ obtained for unannealed samples with $N_{Mn} = 1.25$ at % are reported below.

The ESR spectrum was decomposed into I and L components using specially designed software. The width ΔH_I of the I line is ≈ 390 Oe, and the g factor equals 1.996. Both parameters are independent of the orientation of the magnetic field **H** relative to the axis **c**. In contrast, in the case of the L resonance, such a dependence is observed; specifically, ΔH_L varies from approximately 160 to 200 Oe, and the g factors are equal to 2.189 and 2.0998 at **H** ∥ **c** and **H** ⊥ **c**, respectively. Figure 2 shows the location of the L resonance as a function of the angle between the field **H** and the hexagonal axis c at $T = 293$ K. A similar angular dependence is also observed in a cleaved surface.

A substantial distinction between the I and L lines also manifests itself in the character of the temperature dependences of their widths. As the temperature decreases from 300 to 77 K, the I line monotonically broadens from ~400 to 700 Oe (Fig. 3, curve 1). In the case of the L line, the dependence ΔH_L is nonmonotonic. In particular, the L line narrows in the range 300–140 K and abruptly broadens at $T < 140$ K (Fig. 3, curve 2). However, the temperature dependences of the integrated intensities of both lines, $S_I(T)$ and $S_L(T)$, are nonmonotonic (Fig. 4). The intensities of the lines increase as T decreases from 300 to 140 K and decrease in the T range 140–77 K. In this case, the intensity of the I line is an order of magnitude higher than that for the L line.

The dynamic magnetic susceptibility of the crystals under study is a complex quantity: $\chi_{ac} = \chi_1 - i\chi_2$. The real component χ_1 and the imaginary component χ_2 nonmonotonically vary with temperature (Fig. 5). A clearly pronounced peak in curve χ_1 is observed at $T = 28$ K, and two more, which are much lower, are observed at 190.5 and 267 K. Curve χ_2 also includes three peaks. A high peak is observed at $T \approx 34$ K, a low peak is observed at 184 K, and a barely perceptible one is observed at 269 K. Note that the accuracy of the mea-
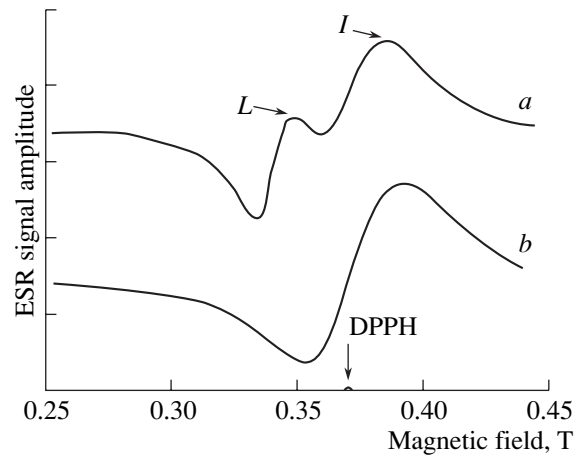
Fig. 1. ESR spectra of the $In_{1-x}Mn_xSe$ samples ($x = 0.0125$) at $T = 293$ K (a) prior to annealing, and (b) after annealing. The mark DPPH corresponds to the location of the reference line with $g = 2.0036$.
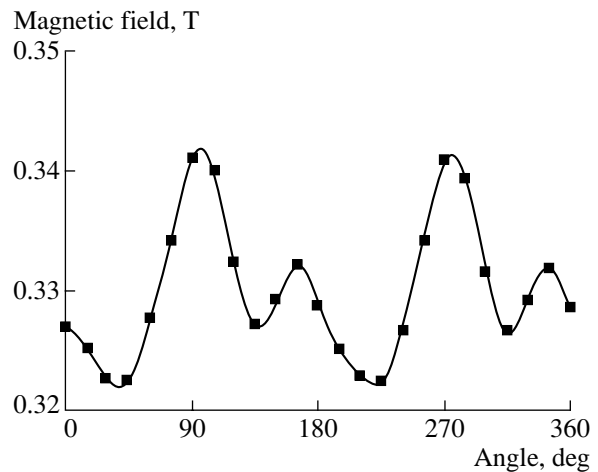

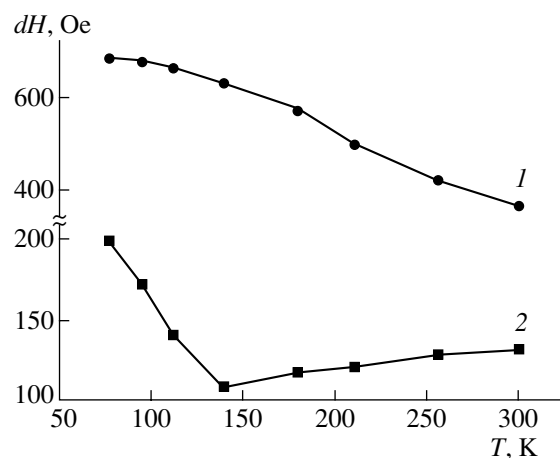**Fig. 2.** Center of the L resonance versus the angle between the field **H** and axis **c**.

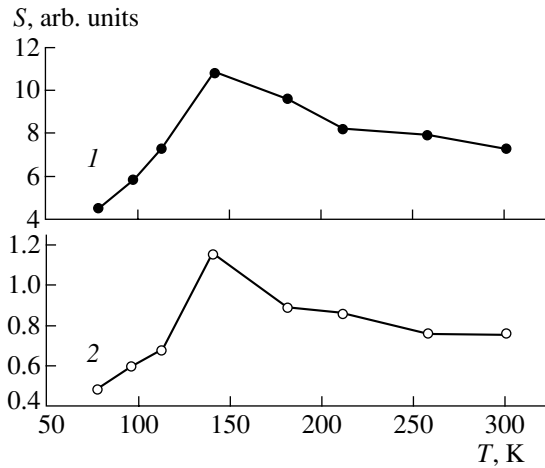**Fig. 3.** Width of the ESR lines versus temperature (1) for the I line and (2) for the L line.

S, arb. units

Fig. 4. Integrated intensity versus temperature for the *I* line (curve *1*) and for the *L* line (curve *2*).
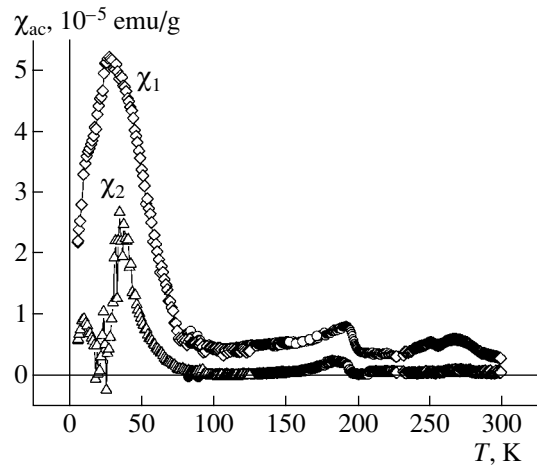
χ_{ac}, 10^{-5} emu/g

Fig. 5. Dynamic magnetic susceptibility versus temperature. The χ_1 curve corresponds to the real part of the magnetic susceptibility and the χ_2 curve corresponds to the imaginary part.
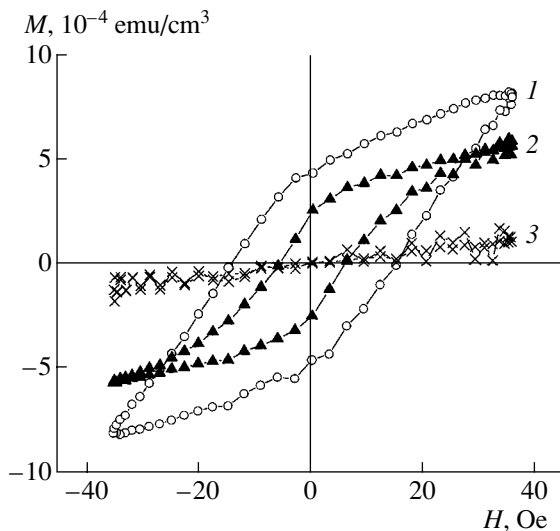
M, 10^{-4} emu/cm³

Fig. 6. Rayleigh hysteresis loops obtained at temperatures of (*1*) 20, (*2*) 50, and (*3*) 100 K.

surement of χ_{ac} is 10^{-7}. When studying the magnetization curves $M(H)$ in the region of weak magnetic fields ($H = \pm40$ Oe), we obtained Rayleigh hysteresis loops at $T = 20$ and 50 K. At $T = 100$ K, a linear dependence $M(H)$ is observed (Fig. 6).

4. DISCUSSION

The crystal structure of layered III–VI semiconductors can be thought of as fourfold layers packed in an anion–cation–cation–anion sequence. Predominantly, a covalent bonding is in effect in the layers themselves, and a weak Van der Waals bonding is observed between the layers. It is quite natural that, after doping these semiconductors, impurity atoms can both replace cations in a crystalline layer and be localized in the interlayer spacing. It seems likely that the latter mechanism is dominant, since its accomplishment requires considerably lower energy. It is known that intercalation of layered crystals, i.e., introduction of the impurity into the interlayer spacing, occurs even at room temperature [9].

The existence of two absorption lines with different parameters in the ESR spectrum (Fig. 1, curve *1*) unambiguously indicates that there are two different impurity subsystems in the $In_{1-x}Mn_xSe$ samples ($x = 0.0125$). It is reasonable to assume that the *I* component, which has a higher intensity, is associated with the Mn atoms located in the Van der Waals gap, while the *L* component is associated with the Mn atoms that replace the In atoms in the layer. In the context of this model, the absence of the *L* component in the ESR spectrum of the annealed samples becomes clear. In the course of annealing, the Mn ions diffuse from the crystalline layer into the interlayer spacing, which causes the *L* component to vanish.

The existence of an orientation dependence of the parameters of the *L* line and the nonexistence of such a dependence in the case of the *I* line indicates that there is a different symmetry of the local field that affects the Mn ions in the crystalline layers and in the interlayer spacing. It is known that the *g* factor is a tensor, which reflects the anisotropy of the intracrystalline field, and that the number of tensor components is associated with the symmetry of the local field in a crystal [10]. A cubic symmetry of the local field corresponds to an isotropic *g* factor. If there are two *g* factors, $g_\parallel$ and $g_\perp$, and the ESR spectrum exhibits axial symmetry in the *xy* plane, the symmetry of the local field is axial. If there are three *g* factors (g_x, g_y, and g_z), the symmetry is rhombic or even lower.

Consequently, the observation of the orientation dependence of the *L* line in two planes, namely, the *ac* plane and the cleavage plane, indicates that the symmetry of the local field in a crystalline layer is lower than axial symmetry. This suggestion agrees with the data presented in [11, 12], according to which InSe crystals grown using the Bridgman–Stockbarger method are usually related to the γ polytype and have a

rhombohedral (trigonal) crystalline structure. The absence of an angular dependence of the parameters of the I line (g factor is isotropic) indicates that a local field in the interlayer spacing of the $In_{1-x}Mn_xSe$ alloy ($x = 0.0125$) has a cubic symmetry.

The character of the temperature dependences of the width of the lines $\Delta H_I(T)$ and $\Delta H_L(T)$ and their integrated intensities $S_I(T)$ and $S_L(T)$ is mainly determined by the type of exchange pairs that exist in the interlayer space and at the midplane of a crystalline layer. In the latter case, in addition to the superexchange occurring in the pairs Mn–Se–Mn (and, possibly, Mn–In–Se–Mn), a direct exchange interaction can proceed in the Mn–Mn pairs (Fig. 1 in [5]). As for the interlayer spaces, where the Mn ions are most probably located in tetrahedral voids, which are formed by the neighboring Se monolayers, indirect exchange is possible only via the Se ions in the pairs Mn–Se–Mn.

The observed decrease in the intensities S_I and S_L as T decreases from 140 to 77 K (Fig. 4) and the simultaneous broadening of the I and L lines (Fig. 3) indicates that the exchange interaction between the Mn ions is antiferromagnetic in both impurity subsystems. In contrast, an increase in the intensities S_I and S_L in the range 300–140 K indicates ferromagnetic exchange interaction both in the interlayer spaces and in the crystalline layers.

The observed narrowing of the L line in the range 300–140 K (Fig. 3, curve 2), in contrast to the broadening of the I line (curve 1), may be caused by direct exchange in Mn–Mn pairs that exist only in the middle of the layers. According to [13], a very rapid direct exchange between paramagnetic ions leads to an averaging of the local fields that affect the paramagnetic ion; as a result, the ESR line is narrowed.

It was previously assumed [6] that a sharp peak in the dependence $M(T)$ for the $Ga_{1-x}Mn_xS$ alloy at $T = 10.9$ K is associated with a phase transition to the spin-glass state, which is characteristic of three-dimensional structures. This hypothesis is quite reasonable when we consider that the formation of Mn_1–S(Se)–Mn_2-type pairs is quite possible in quasi-two-dimensional crystals such as $Ga_{1-x}Mn_xS$ and $In_{1-x}Mn_xSe$. In this case, the Mn_1 ions are localized in the interlayer spaces, while the Mn_2 ions are localized in the layers. The indirect exchange interaction occurring in such pairs combines neighboring crystalline layers, which causes the emergence of three-dimensional magnetic order.

The character of the temperature dependence $\chi_{ac}(T)$ (Fig. 5), as well as the existence of magnetic hysteresis loops in the Rayleigh region (Fig. 6), provides direct evidence of existence of three-dimensional ferromagnetic order in the $In_{1-x}Mn_xSe$ crystals in the region $T < 77$ K. Taking into account the magnitude of the effects observed, we can assume that the ferromagnetic ordering does not enclose the entire crystal bulk. Rather, this ordering is established in separate regions of the bulk, i.e., in clusters of impurity ions. Therefore, the exist-

ence of magnetic hysteresis loops suggests a domain structure of ferromagnetically ordered clusters.

Similarly to the case of conventional magnetic hysteresis [14], Rayleigh hysteresis loops are associated with irreversible magnetization in a weak magnetic field. In this case, the dependence of the magnetization M on the magnetic field H in the initial portion of the magnetization curve is described by the Rayleigh formula [13, 14]

$$M = \chi_a H \pm nH^2, \qquad (1)$$

where χ_a is the initial magnetic susceptibility, b is the Rayleigh constant, and the signs + and – correspond to the magnetic field direction. The constant b is related to the residual magnetization M_R and the saturation field H_m [13]:

$$b = \frac{2M_R}{H_m^2}. \qquad (2)$$

The hysteresis-loop area increases as the temperature decreases (Fig. 6). This effect is associated with an increase in hysteresis losses, which is characteristic of typical ferromagnets. Using experimental values of M_R and H_m (Fig. 6), we can determine hysteresis losses in the case of a Rayleigh loop [13]:

$$W_h = \frac{1}{4\pi}\oint HdM = \frac{bH_m^3}{3\pi} = \frac{2M_R H_m}{3\pi}. \qquad (3)$$

The imaginary component χ_2 of the magnetic susceptibility (Fig. 5) is also associated with hysteresis losses, since measurements of $\chi_{ac}(T)$ are carried out in a low-frequency field [14]. Eddy current losses can be disregarded because of the low concentration of free carriers (about 10^{12}–10^{13} cm^{-3}).

Poorly pronounced peaks in the curves $\chi_1(T)$ and $\chi_2(T)$ are observed in the temperature range ~300–150 K (Fig. 5). In this range, the ferromagnetic exchange interaction is in effect in both impurity subsystems (Fig. 4). In this case, the mentioned peaks are absent in the range 140–77 K, which corresponds to the antiferromagnetic exchange interaction between the Mn ions in the subsystems (Fig. 4). Since magnetic susceptibility is an integrated characteristic of the crystal, it is quite probable that the origin of the emergence of the mentioned peaks is the same as at a low temperature. The only distinction is that ferromagnetic ordering is established in clusters whose size is close to critical.

5. CONCLUSION

The results of our examination of the ESR spectra indicate that two different quasi-two-dimensional impurity subsystems exist in the unannealed $In_{1-x}Mn_xSe$ samples ($x = 0.0125$), both in the crystalline layers and in the interlayer spaces. In the temperature range 300–140 K, the exchange interaction (in both subsystems) between Mn ions is ferromagnetic, while, in the range

140–77 K, it is antiferromagnetic. The existence of magnetic hysteresis loops and the form of the temperature dependence of the dynamic magnetic susceptibility indicate the emergence of three-dimensional ferromagnetic ordering at $T < 77$ K. It is possible that ferromagnetically ordered clusters form at a range of relatively high temperatures (300–140 K), and their size is close to critical.

REFERENCES

1. A. Segura, J. Bouvier, M. V. Andres, *et al.*, Phys. Rev. B **56**, 4075 (1997).

2. L. T. Vinh, M. Eddrief, J. E. Mahan, *et al.*, J. Appl. Phys. **87**, 7289 (1997).

3. S. Nüsse, P. H. Bolivar, H. Kurz, *et al.*, Phys. Rev. B **55**, 4620 (1997).

4. M. A. Alzhdanov, M. D. Nadzhafzade, and X. Yu. Seidov, Phys. Status Solidi **41**, 20 (1999).

5. T. M. Pekarek, B. C. Crooker, I. Miotkowski, and A. K. Ramdas, J. Appl. Phys. **83**, 6557 (1998).

6. T. M. Pekarek, M. Duffy, J. Garner, *et al.*, Appl. Phys. **87**, 6448 (2000).

7. J. K. Krause and J. R. Bergen, Supercond. Industry **3**, 23 (1990).

8. F. Gömöry, Rev. Sci. Instrum. **62**, 2019 (1991).

9. I. I. Grigorchak, Z. D. Kovalyuk, and S. P. Yurtsenyuk, Izv. Akad. Nauk SSSR, Neorg. Mater. **17**, 412 (1981).

10. W. Low, *Paramagnetic Resonance in Solids* (Academic, New York, 1960; Inostrannaya Literatura, Moscow, 1962), Chap. 2.

11. P. A. Likforman, D. Carre, J. Etienne, and B. Bachet, Acta Crystallogr. B **31**, 1252 (1975).

12. J. Rigoult, A. Rimsky, and A. Kuhn, Acta Crystallogr. B **36**, 916 (1980).

13. S. V. Vonsovskiĭ, *Magnetism* (Nauka, Moscow, 1971; Wiley, New York, 1974), Chap. 23.

14. S. Chikasumi, *The Physics of Ferromagnetism: Magnetic Characteristics and Engineering Applications* (Syokabo, Tokyo, 1984; Mir, Moscow, 1987), Chap. 7.

Translated by N. Korovin

ELECTRONIC AND OPTICAL PROPERTIES
OF SEMICONDUCTORS

Dispersion of the Refractive Index in Tl$_{1-x}$Cu$_x$GaSe$_2$ ($0 \le x \le 0.02$) and Tl$_{1-x}$Cu$_x$InS$_2$ ($0 \le x \le 0.015$) Crystals

A. N. Georgobiani*^, A. Kh. Matiev^^, and B. M. Khamkhoev****

*Lebedev Physical Institute, Russian Academy of Sciences, Moscow, 117924 Russia
^e-mail: georg@sci.lebedev.ru
**Ingush State University, Magas, 386100 Russia
^^e-mail: Ing_gu@southnet.ru
Submitted November 23, 2004; accepted for publication November 25, 2004

Abstract—The dispersion of the refractive index in Tl$_{1-x}$Cu$_x$GaSe$_2$ ($0 \le x \le 0.02$) and Tl$_{1-x}$Cu$_x$InS$_2$ ($0 \le x \le 0.015$) crystals is studied by measuring their intrinsic interference patterns. Anomalous dispersion regions are found to exist in the crystals at wavelengths slightly exceeding those corresponding to exciton peaks. It is ascertained that, by analyzing the intrinsic interference patterns, it is possible to detect excitons in these crystals at room temperature. A modulation of the interference patterns is observed and an explanation of this phenomenon is suggested. © 2005 Pleiades Publishing, Inc.

The study of exciton states in semiconductors with an anisotropic crystalline structure is associated with the possibility of testing the validity of calculations performed within a two-dimensional exciton model. In this context, the study of the optical properties of semiconductors crystallizing in layered structures is of both scientific and applied interest. In particular, the exciton states of III–VI binary compounds (GaSe, GaS, etc.) and the solid solutions based on them have been extensively studied using the method of transmitted light interference [1].

In this paper, we report the results of our experimental studies of the refractive index dispersion in Tl$_{1-x}$Cu$_x$GaSe$_2$ ($0 \le x \le 0.02$) and Tl$_{1-x}$Cu$_x$InS$_2$ ($0 \le x \le 0.015$) crystals in the range of the absorption band edge.

We grew single crystals of these compounds using the Bridgman–Stockbarger method. Such crystals belong to the monoclinic system, are layered, and their lattices are of a TlGaSe$_2$ type [2, 3]. Due to these properties, thin plane-parallel plates can be cleaved from a single crystal ingot.

The dispersion of the refractive index of the Tl$_{1-x}$Cu$_x$GaSe$_2$ ($0 \le x \le 0.02$) and Tl$_{1-x}$Cu$_x$InS$_2$ ($0 \le x \le 0.015$) crystals was studied by measuring the interference patterns in the region of the intrinsic absorption band edge of these crystals [1, 4]. The sample thickness was varied within the range 5–20 μm. The interference fringes were measured on an SDL-2 spectral–computing complex specially adapted for these purposes. As an example, Fig. 1 shows an interference pattern of transmission maxima and minima of TlGaSe$_2$ at $T = 300$ K.

Figure 2 presents the corresponding dependences of *nd* on λ plotted according to the formulas [1, 4]

$$n = \sqrt{\sin^2 i + \frac{\lambda_1^2 \lambda_2^2 (\Delta M)^2}{4 d^2 (\lambda_1 - \lambda_2)^2}}, \qquad (1)$$

$$n = \sqrt{\sin^2 i + \frac{\lambda_1^2 \lambda_2^2}{16 d^2 (\lambda_1 - \lambda_2)^2}}. \qquad (2)$$

Here, ΔM is the phase difference between neighboring interference maxima, λ_1 and λ_2 are the wavelengths of adjacent extrema (a maximum and the minimum closest to it), d is the thickness of a single crystal plate, and n is the refractive index.

It can be seen from Fig. 2 that each dependence $n = f(\lambda)$ is a unconventional kind of averaging of the fre-
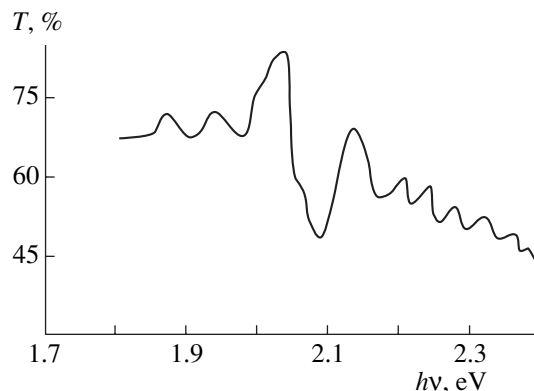

Fig. 1. Interference pattern resulting from the transmission of TlGaSe$_2$ crystals at $T = 300$ K.
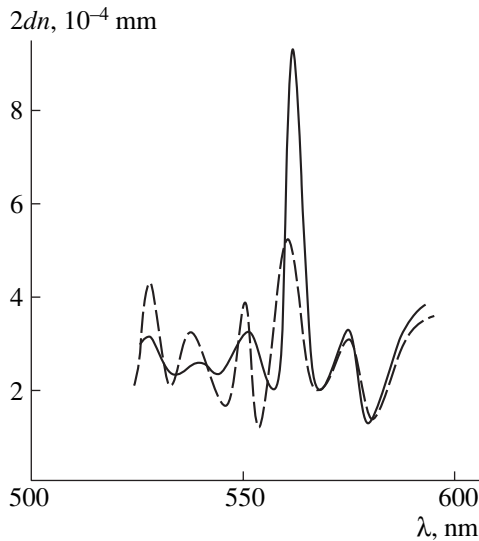
Fig. 2. (*1*, *2*) Dispersion curves of the refractive index of TlGaSe$_2$ crystals at $T = 300$ K plotted according to formulas (1) and (2), respectively.
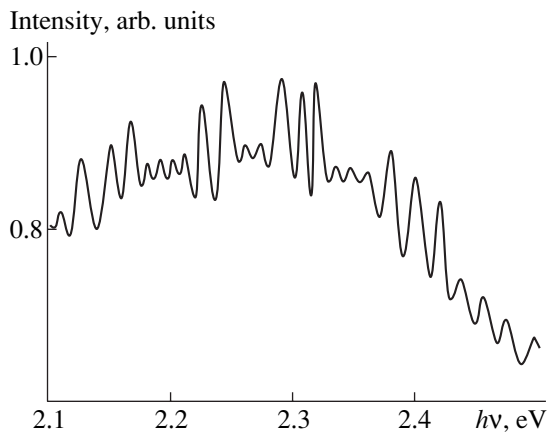

Fig. 3. Modulation of the intensity of transmitted light in TlGaSe$_2$ crystals at $T = 300$ K.

quency dependence of the refractive index. Apart from regions of anomalous dispersion located in the immediate vicinity of each exciton peak, regions of sharp changes in the refractive index (i.e., of anomalous dispersion) that are not associated with free excitons are also observed. All the regions of anomalous dispersion are associated with a particular absorption mechanism. The anomalous dispersion regions that, judging from their location, are not associated with excitons possessing different quantum numbers can be attributed to the occurrence of excitons of different types, polariton states, or the long-wavelength absorption edge.

The occurrence of polariton states in III–VI layered crystals was ascertained in [5]. Clearly, calculation of the refractive index performed using formula (2) is in fact an averaging over the wavelength range corre-

sponding to adjacent extrema. Nevertheless, this averaged pattern reflects the real trend of the dispersion. The observed regions of sharp changes in *n* are regular, and they make it possible to judge the character of the dispersion in a substance. Similar results were obtained when studying the dispersion of the refractive index in the Tl$_{1-x}$Cu$_x$GaSe$_2$ ($0 \leq x \leq 0.02$) and Tl$_{1-x}$Cu$_x$InS$_2$ ($0 \leq x \leq 0.015$) crystals. As was noted above, the occurrence of this region of anomalous dispersion can be attributed to excitons. Exciton absorption lines in the absorption spectra of the Tl$_{1-x}$Cu$_x$GaSe$_2$ ($0 \leq x \leq 0.02$) and Tl$_{1-x}$Cu$_x$InS$_2$ ($0 \leq x \leq 0.015$) crystals are observed only at low temperatures. However, it is likely that the sensitivity of the intrinsic interference method made it possible to detect excitons at room temperature.

In the study of interference in TlGaSe$_2$ and TlInS$_2$ layered semiconductors, as well as in GaS crystals [6], there occur cases in which variations in the intensity of light passed through a sample are modulated; i.e., the amplitude of variations in the light intensity periodically alternates. Such an interference pattern is shown in Fig. 3 for TlGaSe$_2$. Similar interference patterns are also observed for crystals of the solid solutions Tl$_{1-x}$Cu$_x$GaSe$_2$ ($0 \leq x \leq 0.02$) and Tl$_{1-x}$Cu$_x$InS$_2$ ($0 \leq x \leq 0.015$). Interference patterns of this type differ significantly from the ordinary interference patterns shown in Figs. 1 and 2. Analogous interference patterns were also observed in [6–8] for Bi$_2$S$_3$, In$_2$Se, and GaS. In the opinion of the authors of these studies, the reason for the appearance of interference patterns with "beats" can be attributed to either natural or artificial birefringence.

In [8], modulation of the interference pattern observed for GaAs:Se was attributed to the effect of photoelasticity [9]. The authors of [8] believed that, due to residual stress, the crystals exhibit birefringence; i.e., ordinary and extraordinary rays appear. We can assume that rays of both types give rise to interference patterns, but these patterns somewhat differ from each other. Ordinary and extraordinary rays do not interfere with each other. However, the presence of two different interference patterns leads to a situation in which the energy of the transmitted light varies with the wavelength and results in the interference pattern becoming modulated. If this explanation of the modulation of interference patterns holds, then, in the case of polarized light, the modulation amplitude should depend on the orientation of the plane of polarization of incident light. Apart from this explanation, an assumption that the coupling between some layers inside a crystal can become broken also seems to apply. In this case, emerging rays can mentally be divided into two beams, which both satisfy the formula [1, 4]

$$T = (l - R)^2 [1 - 2R^2 \cos 2\delta + R^4]^{-1}, \qquad (3)$$

where R is the reflectance of a surface and δ is the change in the phase due to a single reflection.

For one of these beams of rays, the phase difference depends on the thickness of a sample d:

$$\delta = \frac{2\pi}{\lambda} n d. \tag{4}$$

For the other beam, which arises due to reflection from a detached layer, the phase difference is determined by the thickness of this detached layer d_1:

$$\delta = \frac{2\pi}{\lambda} n d_1. \tag{5}$$

If the modulation is caused by layer detachment, then the shape of the interference pattern should not depend on whether the beam emerging from a sample passes through a polarizer or not. In contrast, if the modulation is caused by birefringence, the shape of the interference pattern should depend on the orientation of the polarizer. Experiments conducted according to the scheme sample $\longrightarrow$ analyzer $\longrightarrow$ detector showed that the above-described modulation of the interference pattern takes place in TlGaSe$_2$ and TlInS$_2$ crystals. The analyzer had no effect on the radiation emerging from the Tl$_{1-x}$Cu$_x$GaSe$_2$ $(0 \leq x \leq 0.02)$ and Tl$_{1-x}$Cu$_x$InS$_2$ $(0 \leq x \leq 0.015)$ crystals or, therefore, on the interference pattern. Consequently, we can state that, in our case, the modulation of the interference pattern is associated with layer detachment in the samples.

REFERENCES

1. S. G. Abdulova, G. L. Belen'kiĭ, and N. T. Mamedov, Fiz. Tekh. Poluprovodn. (Leningrad) **15**, 943 (1981) [Sov. Phys. Semicond. **15**, 540 (1981)].

2. D. Muller and H. Hahn, Z. Anorg. Allg. Chem. **438**, 258 (1978).

3. A. U. Mal'sagov, Izv. Akad. Nauk SSSR, Neorg. Mater. **25**, 25 (1989).

4. Yu. A. Ukhanov, *Optical Properties of Semiconductors* (Nauka, Moscow, 1977), Chap. 2, p. 68 [in Russian].

5. L. N. Kurbatov, L. I. Dirochka, and V. A. Sosin, Fiz. Tekh. Poluprovodn. (Leningrad) **13**, 75 (1979) [Sov. Phys. Semicond. **13**, 43 (1979)].

6. A. M. Malik, Z. D. Kovalik, and G. B. Dzhevskiĭ, Izv. Vyssh. Uchebn. Zaved., Fiz. **3**, 144 (1975).

7. A. N. Borets and I. M. Stakhira, Ukr. Fiz. Zh. **9**, 1074 (1964).

8. I. B. Bandrivchak and M. N. Bylyĭ, Opt. Spektrosk. **40**, 1078 (1976) [Opt. Spectrosc. **40**, 621 (1976)].

9. T. S. Narasimhamurty, *Photoelastic and Electro-Optic Properties of Crystals* (Plenum, New York, 1981; Mir, Moscow, 1984), Chap. 5.

Translated by V. Rogovoĭ

ELECTRONIC AND OPTICAL PROPERTIES OF SEMICONDUCTORS

The Effect of Neutron Irradiation on the Properties of *n*-InSb Whisker Microcrystals

I. A. Bolshakova*^, V. M. Boĭko**, V. N. Brudnyĭ***^^^, I. V. Kamenskaya***,
N. G. Kolin**^^, E. Yu. Makido*, T. A. Moskovets*, and D. I. Merkurisov**

*Lviv National Polytechnical University, Lviv, 290013 Ukraine
^e-mail: inessa@mail.lviv.ua
**Karpov Institute of Physical Chemistry (Obninsk Branch), Obninsk, Kaluga oblast, 249033 Russia
^^e-mail: ngkolin@mail333.com
***Kuznetsov Physicotechnical Institute, Tomsk State University, Tomsk, 634050 Russia
^^^e-mail: brudnyi@ic.tsu.ru
Submitted November 3, 2004; accepted for publication November 25, 2004

Abstract—The results of studying the effect of irradiation with fast neutrons in an IBR-2 reactor on the characteristics of magnetic-field sensors based on n^+-InSb whisker microcrystals are reported (the measurements were carried out in the course of the irradiation). The optimum concentration of free electrons n for providing the highest possible radiation resistance of the InSb sensors is estimated ($n \approx (6–7) \times 10^{17}$ cm^{-3}). The contributions of two competing processes to variation in the electrical properties of InSb under neutron irradiation (transmutation-related doping of InSb with a Sn shallow-level donor impurity and compensation of the initial n^+-InSb conductivity as a result of generation of deep-level acceptor-type radiation defects) are determined separately. © 2005 Pleiades Publishing, Inc.

1. INTRODUCTION

Magnetic-field sensors based on semiconductors are used for mapping magnetic fields and have applications related to exposure to hard radiation in charged-particle accelerators, in atomic power-engineering plants, aboard spacecraft, and so on. This circumstance imposes the requirements of high radiation resistance and long-term stability on the output characteristics of the active components of the sensors under exposure to high-energy radiation [1]. The most important characteristic of a magnetic-field sensor is its sensitivity $K = U_{out}/B$ (U_{out} is the output voltage and B is the magnetic induction), which is related to the electrical parameters of the material used. The main contribution to variation in the value of K is made by variation in the charge-carrier concentration in the material in the case of irradiation with low doses of high-energy particles. Therefore, in order to ensure the stability of the output parameters of magnetic-field sensors, it is necessary to attain as small as possible a variation in the concentration of free charge carriers in a semiconductor under exposure to hard radiation.

Among Group IV semiconductors and III–V compounds, the InSb compound has attracted particular attention as a suitable material for fabrication of the active elements of sensors, owing to the high mobility of free electrons within it. However, exposure of these sensors to high-energy radiation gives rise to donor- and acceptor-type radiation defects in the InSb crystal lattice, which affects the charge-carrier concentration,

mobility, and lifetime [2–5]. All these effects cause instability in the output parameters of InSb-based magnetic-field sensors under exposure to hard radiation.

2. EXPERIMENTAL

In this paper, we report the results of studying the effect of irradiation with reactor neutrons on the parameters of both the material itself and magnetic-field sensors based on *n*-InSb whisker microcrystals in relation to the level at which these microcrystals were initially doped. The *n*-InSb whisker microcrystals, obtained by free crystallization from a gaseous phase [6], were doped with several impurities simultaneously (Sn, Al, and Cr) during their growth. The main donor impurity (Sn) provided the required free-electron concentration (n_0), whereas Al and Cr impurities were used to stabilize the characteristics of InSb under the effect of irradiation. It was assumed that Al and Cr give rise to strain in the InSb crystal lattice [7] and, thus, form additional sinks for mobile radiation defects during irradiation, which should increase the resistance of InSb to hard radiation. The doping level of the starting material was varied within the range $n_0 = 3 \times 10^{16}–1 \times 10^{18}$ cm^{-3} and the Hall mobility varied from 52 400 to 22 300 cm^2/(V s) at 290 K. The dimensions of the samples under study were $0.7 \times 0.07 \times 0.03$ mm^3. It is worth noting that there is very little data on the irradiation of heavily doped *n*-InSb with reactor neutrons in the available publications.
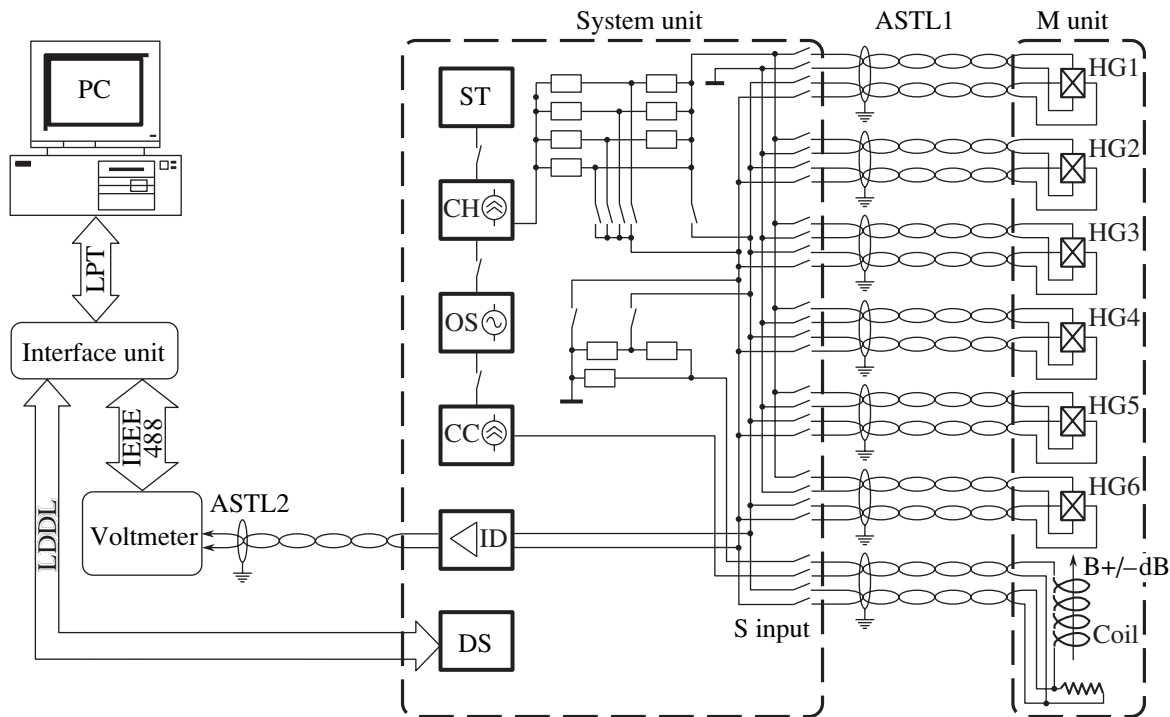
Fig. 1. Block diagram of an MMSI setup: HG1–HG6 denote the samples under study; ST, the voltage stabilizer; CH and CC, the current sources; OS, the reference-voltage generator; ID, the input amplifier; DC, the command decoder; and ASTL1 and ASTL2 are the transmission lines for the signals.

The samples were irradiated with neutrons in an IBR-2 pulsed reactor at the Laboratory of Neutron Physics at the Joint Institute for Nuclear Research (Dubna, Russia). The fluence of fast neutrons (with energies $E > 0.1$ MeV) was as high as $F_{fn} = 3.1 \times 10^{16}$ cm^{-2} at a flux density $\varphi = 9 \times 10^9$ cm^{-2} s^{-1} and the average reactor-neutron energy $E \approx 1.35$ MeV. A special feature of the experiment under consideration was that the sensors' parameters were measured in a reactor channel during the irradiation, which improved the accuracy of dose-related measurements when the same sample was used and reduced the duration of the experiment [1, 8–10].

The samples under study were positioned in the gap between the poles of a SmCo$_5$-based permanent magnet ($B = 290$ mT) that was mounted in a horizontal channel of the reactor. The measurements were carried out remotely using a precision automated measuring system designed and assembled at the Laboratory of Magnetic Sensors at Lviv National Polytechnical University (Lviv, Ukraine). This system made it possible to measure relative variations in the electrical parameters of the samples to an accuracy of 0.01%, the temperature in the vicinity of the samples to an accuracy of 0.1 K, and the induction of a magnetic field generated by the SmCo$_5$-based permanent magnet mounted in the reactor channel to an accuracy of 0.1% [11]. A block diagram of the setup for measuring the parameters of the magnetic-field sensors during irradiation is shown in

Fig. 1. The samples under study, permanent magnet, and measuring instrumentation were accommodated in three different zones. The permanent magnet and the samples (the M_unit) were placed in the first zone (the reactor zone). The main measuring instrumentation (the System_unit) was mounted in a technical room at a distance of 10 m from the reactor channel. The third zone (a room for personnel), at a distance of 30 m from the reactor channel, accommodated the measuring voltmeter, interface unit, and personal computer. Recording of the results of measurements and correction of the measuring-instrumentation function were performed automatically; the number of measurements was as large as 3×10^6 [12].

3. RESULTS

In Fig. 2, we show the dependences of relative variations $\Delta K/K$ in the sensitivity coefficient of the magnetic-field sensors, whose parameters are listed in the table. In the range of neutron fluences F_{fn} under consideration, we can see virtually linear fluence dependences of $\Delta K/K$ for all the samples involved in this study. Both positive and negative values of $\Delta K/K$ are observed, depending on the initial doping level of n-InSb. For sample 2 ($n_0 = 6 \times 10^{17}$ cm^{-3}), the variation in $\Delta K/K$ does not exceed 0.05% if the sample is irradiated with a fast-neutron fluence $F_{fn} = 1.7 \times 10^{15}$ cm^{-2} and does not exceed 1% at a neutron fluence as high as 3×10^{16} cm^{-2}. This observation means that sample 2 exhibits the high-
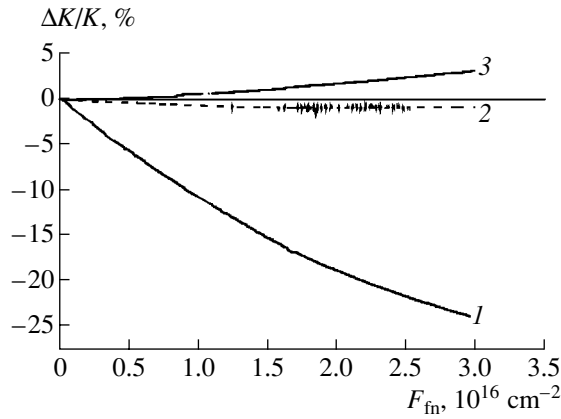
Fig. 2. Dose dependences of relative variation in the sensitivity $\Delta K/K$ of magnetic-field sensors based on *n*-InSb whisker microcrystals (samples 1, 2, and 3; see table) and exposed to neutron radiation. The temperature of the measurements is 290 K.

Fig. 3. Dependence of the rate of variation in the charge-carrier concentration ($\Delta n/\Delta F_{\text{fn}}$) for *n*-InSb microcrystals on the initial charge-carrier concentration in samples irradiated with fast neutrons: (a) samples 1, 2, and 3 (see table) after irradiation with a fluence of 3×10^{16} cm^{-2} of fast neutrons and (b) additional samples (not included in the table) after irradiation with a fluence of 1.7×10^{15} cm^{-2} of fast neutrons.

est radiation resistance among the samples under study after irradiation in the above conditions.

In Fig. 3, we show the dependences of the rate of variation in the charge-carrier concentration under irradiation with fast neutrons ($\Delta n/\Delta F_{\text{fn}}$) in *n*-InSb microcrystals on the initial charge-carrier concentration n_0 in irradiated samples for the neutron fluences of 1.7×10^{15} and 3×10^{16} cm^{-2}. As can be seen from Fig. 3, a virtually linear dependence of the charge-carrier removal rate on the initial charge-carrier concentration is observed in irradiated *n*-InSb. In order to explain the physical processes that occur in InSb under irradiation with reactor neutrons quantitatively, we should take into account the following two most important factors: (i) formation of radiation defects in InSb exposed to irradiation with fast neutrons, the γ-ray component of the reactor spectrum, and recoil atoms; and (ii) formation of doping-impurity atoms (~98% Sn) as a result of nuclear reactions that occur due to the interaction of
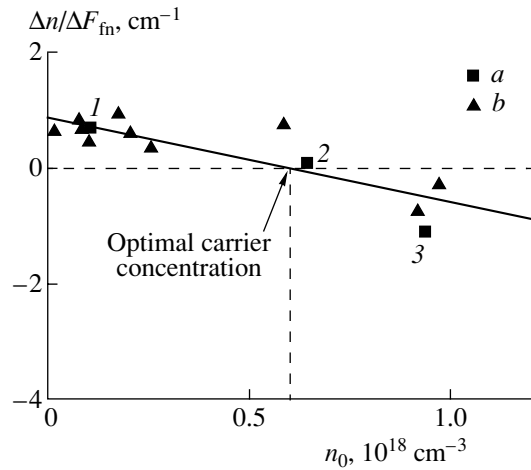
thermal and intermediate-energy neutrons with the atoms of the main material.

As is well known, formation of Sn atoms in InSb depends on the reactor parameters and neutron fluence and is independent of the charge-carrier concentration in the initial material. The level at which InSb is doped with Sn under irradiation with neutrons can be estimated from the expression $\alpha = \sigma N_{\text{In}}$, where σ is the cross section for formation of Sn atoms under irradiation with neutrons and N_{In} is the concentration of In atoms in InSb. For low neutron doses, the rate of variation in the charge-carrier concentration in the irradiated InSb samples can be represented by a linear dependence as

$$\Delta n/\Delta F_{\text{fn}} \approx \alpha - \beta n. \tag{1}$$

Here, β is the cross section for the production of radiation defects $N_{\text{RA}} - N_{\text{RD}}$, where N_{RD} (N_{RA}) are the concentrations of radiation-induced donors (acceptors); and n is the concentration of charge carriers in the irradiated samples. It can be seen from Fig. 3 that, for the microcrystalline InSb samples, the cross section for the production of radiation defects ($N_{\text{RA}} - N_{\text{RD}}$) is equal to $\beta \approx 1.5 \times 10^{-18}$ cm^2 at 295 K. By choosing the initial doping level, we can ensure that $\alpha \approx \beta n$, which corresponds to $\Delta n/\Delta F_{\text{fn}} \approx 0$. It is the additional doping with tin that leads to this situation in the case of irradiation of *n*-InSb with reactor neutrons. It is important that the specific critical concentration n needed to ensure $\Delta n/\Delta F_{\text{fn}} \approx 0$ depends on the reactor-neutron spectrum in the vicinity of a sample.

Previous data [13] on irradiation of InSb samples with high fluences of full-range spectrum of reactor

The parameters of Hall sensors based on whisker *n*-InSb crystals at 295 K

Parameters	Sample no.		
	1	2	3
Charge-carrier concentration n_0, cm^{-3}	8×10^{16}	6×10^{17}	1×10^{18}
Magnetic sensitivity K at the nominal current, mV/T	40	14	10
Nominal current I, mA	30	40	60
Input resistance R_{in}, Ω	5.0	2.3	1.2
Output resistance R_{out}, Ω	2.0	1.8	1.0
Residual voltage at the nominal current U_0, mV	0.07	0.03	0.02
Temperature range T, K	4.2–350	4.2–350	4.2–350

neutrons for the purpose of transmutational doping indicate that the major fraction of the impurity atoms introduced into InSb (in the case under consideration, this is the Sn impurity) is in an electrically active state immediately after irradiation (without subsequent heat treatments). This state governs, to a great extent, the main electrical characteristics of irradiated samples. Even irradiation of InSb in a Cd container [10] does not lead to complete elimination of the transmutation-doping effect. In order to estimate the value of α, we determined the flux densities for slow and moderate-energy neutrons in the neutron spectrum of the IBR-2 pulsed reactor taking into account the experimental data obtained using sensors that detect neutrons with energies $E > 0.4$ MeV (see [14]). Taking into consideration the fact that the fraction of moderate-energy neutrons ($E = 5 \times 10^{-4}$–100 keV) amounts to ~20% of the fast-neutron fluence [15] and $\varphi(E = 0.1$ MeV$) = 3 \times 10^9$ cm^{-2} s^{-1} MeV$^{-1} = 3 \times 10^3$ cm^{-2} s^{-1} eV^{-1}, we obtained the following description for the spectrum of the moderate-energy neutrons (we performed sewing at 0.1 MeV and selected the exponent, $E^{-0.89}$):

$$\varphi(E) = \varphi_{epi} dE/E^{0.89},$$

$$\varphi_{epi} = 0.84 \times 10^8 \text{ cm}^{-2} \text{ s}^{-1} \text{ eV}^{-0.11}.$$

The absolute values of the exponent when smaller than unity are characteristic of the spectrum of neutrons formed by metals (liquid sodium is the heat-transfer agent in the IBR-2 reactor). The differential spectrum of the neutrons in the irradiation zone of the IBR-2 reactor is shown in Fig. 4. The calculations performed taking into account the neutron energy spectra made it possible to determine the fraction of moderate-energy and slow-neutron fluxes in the total neutron flux as 20 and 25%, respectively, relative to the integrated fast-neutron flux. Since the sizes of the InSb microcrystals were small, we also took into account the resonance absorption of 1.46-eV neutrons at In atoms (the absorption cross section $\sigma_0 \approx 4 \times 10^4$ b and the half-width $\Gamma = 75$ meV). The obtained coefficient is equal to 0.56 cm^{-1} for the introduction of Sn by thermal neutrons and equal to 0.19 cm^{-1} in the case of moderate-energy neutrons (taking into account the maximal resonance); as a result, the total introduction coefficient for Sn $\alpha = 0.75$ cm^{-1} (the coefficient is normalized per fast neutron). The value of the coefficient α estimated from the experimental data in Fig. 3 is equal to ~0.9 cm^{-1} for the lightly doped samples, which is in satisfactory agreement with the value obtained from calculations based on an analysis of the IBR-2 reactor spectrum. All of the above information makes it possible to estimate the concentration of Sn impurity introduced into InSb owing to nuclear reactions with involvement of In atoms [16, 17–20].

It is worth noting that, in spite of a large volume of experimental data on radiation defects in InSb, the data on variations in the electrical properties of this material
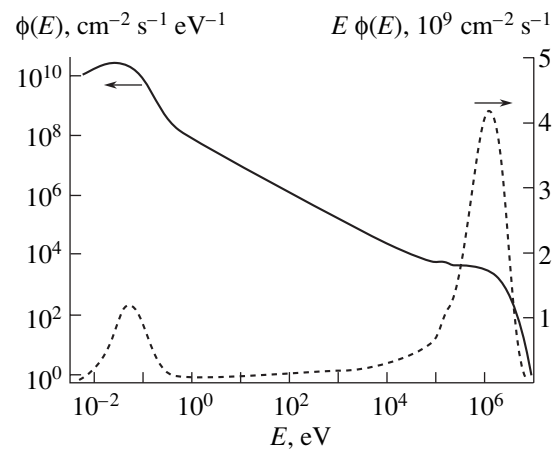

Fig. 4. Dependences of differential flux density of neutrons $\varphi(E)$ and the quantity $E\varphi(E)$ on the neutron energy E for the IBR-2 reactor.

under irradiation are very controversial and, in the case of heavily doped InSb, there is almost no data available. According to the published data, the parameters of irradiated InSb largely depend on the irradiation conditions, i.e., the type of incident particles, their energy, and the temperature of a sample during irradiation. For example, irradiation of InSb with fast neutrons, protons, or high-energy electrons (with energies of several tens of megaelectronvolts) invariably produces n-InSb irrespective of the sample temperature during irradiation [21–24]. At the same time, irradiation with electrons with energies lower than 10 MeV at temperatures $T \leq 200$ K produces p-InSb, whereas similar irradiation at a temperature of about 295 K produces either n-InSb or p-InSb, depending on the radiation dose and the temperature region where the parameters of irradiated samples are measured [21, 25–28]. This behavior of InSb when exposed to high-energy radiation is related both to the characteristics of the prevalent radiation defects and to the generally low stability of radiation defects in InSb. It has been assumed that acceptor-type defects are prevalent at low temperatures, whereas donor-type radiation defects are predominantly accumulated at higher temperatures. Presumably, this circumstance brings about a shift of the Fermi level from the lower half of the band gap to the upper half and, consequently, the conversion of the conductivity type as the temperature increases. It is worth noting that the lack of experimental room-temperature data on heavily doped n-InSb irradiated with fast neutrons makes it difficult to analyze the results of this study. It should also be mentioned that the available experimental data on the properties of irradiated InSb are, in general, inconsistent with the corresponding data for other semiconductors. It is typical of the majority of semiconductors that the parameters of an irradiated material depend only slightly on the irradiation conditions and the material's history and are, to greater extent, intrinsic characteristics of the crystal. Indeed, according to contemporary
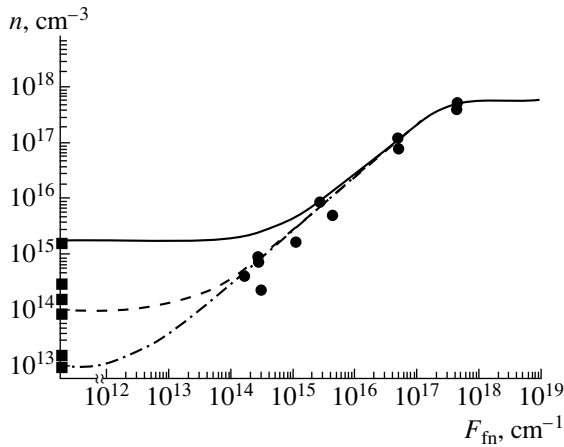
Fig. 5. Dependences of the free-electron concentration at 77 K in bulk *n*-InSb crystals grown by the Czochralski method and irradiated with full-spectrum neutrons (the ratio between the fluxes of fast and slow neutrons is $\varphi_{fn}/\varphi_{sn} \approx 1$) in a VVR-ts water-cooled and water-moderated reactor on the fluence of fast neutrons. The circles correspond to experimental data, and the curves represent the results of calculations using formula (3) for samples with different initial charge-carrier concentrations (squares on the vertical axis) for $\alpha \approx 2.9$ cm^{-1} and $\beta \approx 4.8 \times 10^{-18}$ cm^2.

theoretical models and experimental studies, what is occurring in radiation-induced modification of the electrical parameters of a semiconductor is in fact the reduction its electrical activity, as a result of which the degree of mutual compensation of the material by the radiation-induced donors and acceptors approaches unity as the radiation dose increases. Ultimately, when the concentration of radiation defects exceeds that of the initial doping impurity, this circumstance leads to pinning of the Fermi level at a certain characteristic limiting position F_{lim} for each specific semiconductor [29]. In turn, this position corresponds to a limiting charge-carrier concentration $n_{lim}(p_{lim})$ in an irradiated semiconductor. According to the models suggested Brudnyi *et al.* [29], the limiting electrical parameters of InSb after high-energy irradiation should correspond to those of a material with *p*-type conductivity and to pinning of the Fermi level in the lower half of the semiconductor's band gap [27]. Taking into account this reasoning and the available experimental data, we can conclude that radiation-induced donors should be more efficient if initial *p*$^+$-InSb is irradiated, whereas radiation-induced acceptors should be prevalent in the case of initial *n*$^+$-InSb. Indeed, the measurements carried out at 77 K indicate that the initial conductivity of InSb is compensated by various types of radiation. At the same time, the measurements performed at 295 K indicate that the electrical properties of InSb are affected insignificantly by even high doses of particles. Although the data on *n*$^+$-InSb are scarce, these data confirm the high efficiency of the compensation of the *n*-type conductivity in this material due to the introduction of acceptors

by irradiation with 50-MeV electrons at temperatures close to 295 K [30]. The data obtained in this study are also indicative of the highly efficient formation of acceptor-type radiation defects in *n*$^+$-InSb irradiated with reactor neutrons at a temperature near 300 K.

The results of this study can also be used in an analysis of the performance of magnetic-field sensors based on *n*-InSb if these sensors are employed in other reactors. Indeed, in the case of constant values of α and β, expression (1) can be written as

$$n \approx (n_0 - \alpha/\beta)\exp(-\beta F_{fn}) + \alpha/\beta. \qquad (2)$$

This formula transforms into the following expression if $F_{fn} \longrightarrow \infty$:

$$n \approx (n_0 - n_\infty)\exp(-\beta F_{fn}) + n_\infty,$$
$$\text{where} \quad n_\infty \approx \alpha/\beta. \qquad (3)$$

If the parameters α and β are known, this expression can be used to estimate the initial doping level of InSb ($n_\infty \approx \alpha/\beta$) required to attain the highest possible radiation resistance of sensors based on *n*-InSb to neutron radiation. For example, Fig. 5 shows experimental data on variations in the electron concentration in bulk *n*-InSb crystals subjected to irradiation with neutrons in a VVR-ts water-cooled and water-moderated reactor at the Karpov Institute of Physical Chemistry (Obninsk Branch) [10, 13]. Processing these data according to expressions (1)–(3) for $\alpha \approx 2.9$ cm^{-1} and $\beta \approx 4.8 \times 10^{-18}$ cm^2 yields $n_\infty \approx 6 \times 10^{17}$ cm^{-3} if initial *n*-InSb is chosen (all curves in Fig. 5).

4. CONCLUSION

Thus, the results of in situ experimental studies of magnetic-field sensors based on *n*-InSb whisker microcrystals and subjected to irradiation with fast neutrons can be adequately described on the assumption that there are two competing processes: formation of acceptor-type radiation defects and doping of InSb with a shallow-level Sn donor impurity as a result of nuclear reactions that involve In atoms. It is this circumstance that makes it possible to ensure the stability of the output parameters of sensors based on *n*$^+$-InSb whisker microcrystals with respect to the neutron dose by choosing the initial doping level of the material in the relation to the irradiation conditions. We estimated the optimal level of initial doping of *n*-InSb as $n_0 \approx (6$–$7) \times 10^{17}$ cm^{-3} for the production of radiation-resistant magnetic-field sensors (with the optimum sensitivity of ~14 mV/T at a nominal current of 40 mA) if these sensors operate in the horizontal channel of the IBR-2 reactor. These studies can be used as a basis for choosing the initial *n*-InSb for fabrication of magnetic-field sensors that can operate not only in fields of neutron radiation but also in accelerators of high-energy ions if we take into account the efficiency of transmutational doping of the material under irradiation and the estimate of the rate of radiation-defect production.

REFERENCES

1. I. Bolshakova, Sens. Actuators A **106**, 344 (2003).

2. F. A. Zaitov, F. K. Isaev, A. Ya. Polyakov, and A. V. Kuz'min, *Influence of Penetrating Radiation on the Properties of Indium Arsenide and Indium Antimonide* (ÉLM, Baku, 1984) [in Russian].

3. V. V. Butkov and A. V. Voĭtsekhovskiĭ, Izv. Vyssh. Uchebn. Zaved., Fiz. **24** (12), 102 (1981).

4. V. N. Brudnyĭ and I. V. Kamenskaya, Izv. Vyssh. Uchebn. Zaved., Fiz. **34** (7), 99 (1991).

5. V. N. Brudnyi, I. A. Bolshakova, I. V. Kamenskaya, and N. G. Kolin, in *Proceedings of 12th International Conference on Radiation Physics and Chemistry of Inorganic Materials* (Tomsk. Politekh. Univ., Tomsk, 2003), p. 235.

6. F. Terra, G. Fahim, I. A. Bol'shakova, *et al.*, Izv. Vyssh. Uchebn. Zaved., Fiz. **46** (6), 67 (2003).

7. E. I. Givargizov, *Growth of Whisker and Scaly Crystals from Vapors* (Nauka, Moscow, 1977) [in Russian].

8. N. I. Yarmolyuk, V. N. Vigdorovich, N. G. Kolin, *et al.*, Fiz. Tekh. Poluprovodn. (Leningrad) **14**, 1311 (1980) [Sov. Phys. Semicond. **14**, 773 (1980)].

9. G. A. Vikhliĭ, A. Ya. Karpenko, I. G. Megela, and L. I. Tarabrova, Ukr. Fiz. Zh. **27**, 1104 (1982).

10. N. G. Kolin, D. I. Merkurisov, and S. P. Solov'ev, Fiz. Tekh. Poluprovodn. (St. Petersburg) **33**, 927 (1999) [Semiconductors **33**, 847 (1999)].

11. I. A. Bolshakova, R. Holyaka, and C. Leroy, IEEE Trans. Appl. Supercond. **12**, 1655 (2002).

12. M. Kumada, I. Bol'shakova, and R. Holyaka, Izv. Vyssh. Uchebn. Zaved., Fiz. **46** (6), 98 (2003).

13. N. G. Kolin, D. I. Merkurisov, and S. P. Solov'ev, Fiz. Tekh. Poluprovodn. (St. Petersburg) **33**, 774 (1999) [Semiconductors **33**, 712 (1999)].

14. A. D. Galanin, *Introduction to the Theory of Thermal-Neutron Reactors*, 2nd ed. (Énergoatomizdat, Moscow, 1990) [in Russian].

15. V. V. Golikov, G. Ya. Kaskanov, E. N. Kulagin, V. V. Kukhtin, E. L. Florman, C. Leroy, V. I. Lushchikov, A. P. Cheplakov, and E. P. Shabalin, *Installation for Irradiation of Large-Dimensional Objects Using Beam No. 3 of the IBR-2 Reactor* (Ob. Inst. Yad. Fiz., Dubna, 1996) [in Russian].

16. K. H. Beckurts and K. Wirtz, *Neutron Physics* (Springer, Berlin, 1964; Atomizdat, Moscow, 1968).

17. J. W. Cleland and J. H. Crawford, Jr., Phys. Rev. **95**, 1177 (1954).

18. W. G. Clark and R. A. Isakson, J. Appl. Phys. **38**, 2284 (1966).

19. F. Kuchar, E. Fantner, and G. Bauer, Phys. Status Solidi A **24**, 513 (1974).

20. N. G. Kolin, D. I. Merkurisov, and S. P. Solov'ev, Physica B (Amsterdam) **307**, 258 (2001).

21. L. K. Vodop'yanov and N. I. Kurdiani, Fiz. Tverd. Tela (Leningrad) **7**, 2749 (1965) [Sov. Phys. Solid State **7**, 2224 (1965)].

22. I. Fujisawa, Jpn. J. Appl. Phys. **19**, 2137 (1980).

23. F. A. Zaitov, O. V. Gorshkova, A. Ya. Polyakov, *et al.*, Izv. Akad. Nauk SSSR, Neorg. Mater. **18** (1), 8 (1982).

24. N. A. Vitovskiĭ, T. V. Mashovets, O. V. Oganesyan, and N. Kh. Pambukhchyan, Fiz. Tekh. Poluprovodn. (Leningrad) **12**, 1861 (1978) [Sov. Phys. Semicond. **12**, 1106 (1978)].

25. S. Myhra, Phys. Status Solidi A **9**, 985 (1978).

26. V. P. Skipetrov, V. V. Dmitriev, V. F. Zaitov, *et al.*, Fiz. Tekh. Poluprovodn. (Leningrad) **20**, 1787 (1986) [Sov. Phys. Semicond. **20**, 1120 (1986)].

27. V. N. Brudnyĭ, V. M. Boĭko, I. V. Kamenskaya, and N. G. Kolin, Fiz. Tekh. Poluprovodn. (St. Petersburg) **38**, 802 (2004) [Semiconductors **38**, 769 (2004)].

28. L. W. Aukerman, Phys. Rev. **115**, 1125 (1959).

29. V. N. Brudnyi, S. N. Grinyaev, and N. G. Kolin, Physica B (Amsterdam) **348**, 213 (2004).

30. G. A. Vikhliĭ, A. Ya. Karpenko, I. G. Megela, and L. I. Tarabrova, Izv. Akad. Nauk SSSR, Neorg. Mater. **21**, 1279 (1985).

Translated by A. Spitsyn

The Electrooptic Effect and Anisotropy of the Refractive Index in $Tl_{1-x}Cu_xGaSe_2$ ($0 \leq x \leq 0.02$) Crystals

A. N. Georgobiani*^, A. Kh. Matiev**^^, and B. M. Khamkhoev**

*Lebedev Physical Institute, Russian Academy of Sciences, Moscow, 117924 Russia
^e-mail: georg@sci.lebedev.ru
**Ingush State University, Magas, 386100 Russia
^^e-mail: Ing_gu@southnet.ru
Submitted November 23, 2004; accepted for publication November 26, 2004

Abstract—The electrooptic effect and anisotropy of the refractive index in $Tl_{1-x}Cu_xGaSe_2$ ($0 \leq x \leq 0.02$) crystals are studied. It is found that, as the intrinsic absorption band of each crystal is approached, the crystal refractive index increases. It is ascertained that, if an external electric field is directed along the crystallographic c axis and light propagates along this axis, the electrooptic effect is quadratic; however, if the field is perpendicular to the c axis and the light propagates along it, the electrooptic effect is linear. © 2005 Pleiades Publishing, Inc.

The compound $TlGaSe_2$ is known to crystallize according to the monoclinic system; however, its unit cell exhibits two particular features: $a = b$ (in the monoclinic system, $a \neq b$) and the angle β differs very little from 90° [1]. Single crystals of $Tl_{1-x}Cu_xGaSe_2$ ($0 \leq x \leq 0.02$), grown from a melt using the Bridgman–Stockbarger method, also belong to the monoclinic system, are solid solutions, and their lattices are of a $TlGaSe_2$ type [2]. Since these crystals are layered, there is a high probability that they possess anisotropic properties. In this respect, study of the optical properties of $Tl_{1-x}Cu_xGaSe_2$ ($0 \leq x \leq 0.02$) crystals along directions perpendicular and parallel to the plane of a layer is important. For this purpose, light should be directed parallel and perpendicularly to the cleavage plane. Since it is almost impossible to obtain samples with a large area of surface perpendicular to the cleavage plane, we studied the anisotropy of optical properties under conditions in which the angle of incidence of plane-polarized light was varied. Samples with good optical quality and the same thickness were obtained by cleaving plane-parallel plates from a single crystal ingot. By directing linearly polarized light toward a sample at different angles, we determined the transmittance of the sample using an SDL-2 spectral–computing complex specially adapted for these purposes. The refractive index was determined according to the procedure used in [3, 4] on a setup equipped with a computer. When studying the optical constants, the structure of the $TlGaSe_2$-type crystalline samples was considered to be pseudotetragonal.

In this paper, we present the results of our experimental studies of the refractive-index anisotropy α and quadratic electrooptic effect in $Tl_{1-x}Cu_xGaSe_2$ ($0 \leq x \leq 0.02$) crystals. The absorptance of a crystal near the intrinsic absorption band edge should not depend on the angle of

incidence of light; nevertheless, we found that the ratio $\alpha_{\parallel}/\alpha_{\perp} = 3$–$5$. The absorptance $\alpha_{\parallel}$ was determined under the conditions $\mathbf{E} \perp L$ and $\mathbf{V} \perp L$, while the absorptance $\alpha_{\perp}$ was found at $\mathbf{E} \perp L$ and $\mathbf{V} \parallel L$ (here, the symbol L denotes the cleavage plane, $\mathbf{E}$ is the electric field vector, and $\mathbf{V}$ is the direction of light propagation).

Figures 1a and 1b show, respectively, dispersion curves of the refractive index $n_0 = n_{\perp}$ ($\mathbf{E} \perp L$, $\mathbf{V} \perp L$) and $n_0 = n_{\parallel}$ ($\mathbf{E} \perp L$, $\mathbf{V} \parallel L$), where n_0 is the refractive index of light propagating along the c axis. It follows from Fig. 1 that, in the wavelength range $\lambda = 0.6$–0.66 μm, $n_0 = n_{\perp} < n_{\parallel}$ and both refractive indices increase as they approach the intrinsic absorption band ($E_g' = 2.03$ eV) [5].

The data presented can be described fairly well using the one-term Sellmeier relation, which retains the physical meaning of the parameters of an oscillator [6]:

$$n^2(\lambda) - 1 = S_0 \lambda_0^2 \left[1 - \left(\frac{\lambda_0}{\lambda} \right)^2 \right]^{-1}. \quad (1)$$

Here, λ_0 and S_0 are the average position and average strength of an oscillator, respectively.

Using the dependence of $(n_0 - 1)^{-1}$ on λ^2 (Fig. 1), we can determine the parameters S_0 and λ_0 for a given direction of light propagation. In our case, two pairs of these parameters are determined: $S_{0\perp}$, $\lambda_{0\perp}$, $S_{0\parallel}$, and $\lambda_{0\parallel}$. They refer to the refractive indices in directions perpendicular ($n_0 = n_{\perp}$) and parallel ($n_0 = n_{\parallel}$) to the c axis of a crystal. The values of the parameters $S_{0\perp}$, $\lambda_{0\perp}$, $S_{0\parallel}$, and $\lambda_{0\parallel}$ determined from Fig. 1 are listed in the table.

The electrooptic properties of the $Tl_{1-x}Cu_xGaSe_2$ ($0 \leq x \leq 0.02$) crystals were studied at room temperature in alternating and constant electric fields using the conventional polarization–optical method [3, 6]. With this method, we can measure only birefringence Δn, which
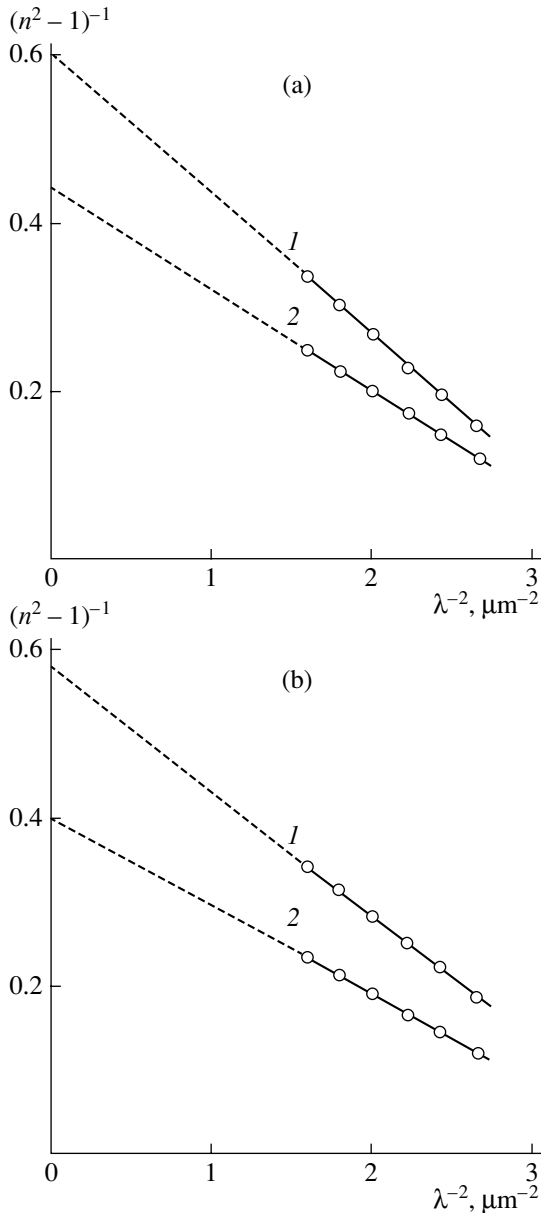
Fig. 1. Dispersion dependences of the refractive indices
(*1*) $n_\parallel$ and (*2*) $n_\perp$ for the (a) TlGaSe$_2$ and (b) Tl$_{0.98}$Cu$_{0.02}$GaSe$_2$
crystals.

Fig. 2. Dependences of Δn on (*1–3*) the electric field
strength at $\lambda = 0.63$ μm and (*4–6*) the wavelength at $E =$
3.5 kV/cm. Curves: (*1, 4*) TlGaSe$_2$, (*2, 5*) Tl$_{0.98}$Cu$_{0.02}$GaSe$_2$,
and (*3, 6*) Tl$_{0.99}$Cu$_{0.01}$GaSe$_2$.

gives no way of determining the sign of the electrooptic
coefficients r_{ijk} and R_{ijkl}. When studying induced bire-
fringence in the Tl$_{1-x}$Cu$_x$GaSe$_2$ ($0 \leq x \leq 0.02$) crystals,
light and an external low-frequency (up to $\sim 10^4$ Hz)
electric field **E** were directed perpendicularly to the lay-
ers. The value of the quantity $\Gamma(I)$ arising in a plate
under the action of the external electric field is given by

$$\Gamma(I) = \frac{2\pi(n_1 - n_2)}{\lambda}d = 2\pi d\frac{\Delta n}{\lambda}. \qquad (2)$$

Here, d is the optical path length of the light in a
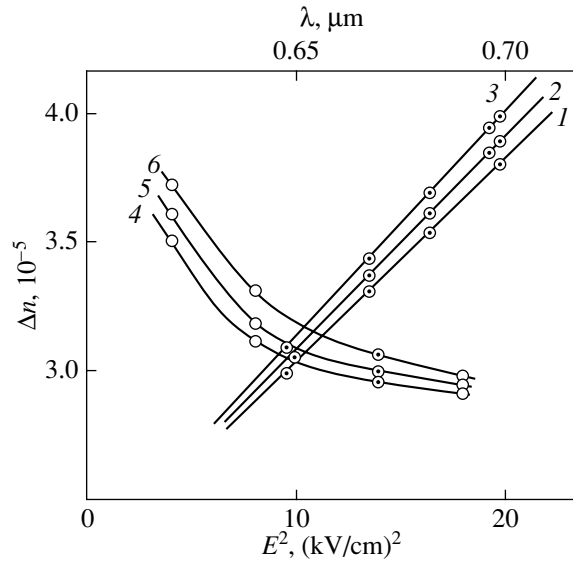sample, λ is the wavelength, and Δn is the change in

birefringence. The induced birefringence of the
Tl$_{1-x}$Cu$_x$GaSe$_2$ ($0 \leq x \leq 0.02$) crystals remains qua-
dratic in character at least in the range of the electric
fields studied ($\mathbf{E} \lesssim 5$ kV/cm), which can clearly be seen
from Fig. 2 (curves *1*, *2*). Using the dependence of Δn
on the electric field strength for the above-mentioned
geometrical conditions of the experiment, we calcu-
lated the quantity $n_0^3 r_{13} - n_e^3 r_{33}$, where r_{ij} are electroop-
tic coefficients that are nonzero for the given experi-
mental geometry. This quantity proved to be equal to
2×10^{-9} esu.

Then, we studied the dependence of Δn on λ. Our
measurements showed that, as the wavelength of inci-
dent light decreased and approached the absorption
edge, Δn increased, with this dependence being steeper
for greater x (Fig. 2, curves *4–6*).

Measurements of the induced birefringence showed
that the values of Δn determined in the constant field
differed from those obtained in the alternating field,
with this difference increasing as the optical absorption
edge was approached. (This result is probably related to
the fact that, in the case of a constant electric field, the
field distribution over a crystal is nonuniform.) The
occurrence of a photoeffect in these crystals at $\lambda \approx$
0.63 μm testifies to the possibility of accumulating
space charges at the periphery of the light beam.

Electron–hole pairs arising under the action of light
can form large space charges at the periphery of a beam
that decrease the internal field in crystals [7]. It should
be noted that, according to the data presented in [1], the
point symmetry group of TlGaSe$_2$ crystals is C_c,

The parameters $S_{0\perp}$, $\lambda_{0\perp}$, $S_{0\parallel}$, and $\lambda_{0\parallel}$

	$S_{0\perp}$, 10^{-8} cm^{-2}	$\lambda_{0\perp}$, 10^{5} cm^{-5}	$S_{0\parallel}$, 10^{-8} cm^{-2}	$\lambda_{0\parallel}$, 10^{5} cm^{-5}
$TlGaSe_2$	8.18	0.711	6.00	0.713
$Tl_{0.99}Cu_{0.01}GaSe_2$	9.00	0.711	6.92	0.714
$Tl_{0.98}Cu_{0.02}GaSe_2$	9.62	0.710	7.03	0.715

whereas, in accordance with the results in [8], this group is $P2_1/m$. These crystals have a pseudotetragonal monoclinic structure. The linear electrooptic effect identified in them is characteristic of the monoclinic system. For the class of compounds under consideration (of the $TlGaSe_2$ type), $a = b$ and the β electrooptic effect differs little from the quadratic effect (90°). Therefore, we can assume that, along some crystallographic direction (e.g., along the c axis), the quadratic effect is more likely to occur.

REFERENCES

1. D. Muller and H. Hahn, Z. Anorg. Allg. Chem. **438**, 258 (1978).
2. G. D. Guseĭnov, A. U. Mal'sagov, I. M. Berfirer, and A. A. Abdullaev, Izv. Vyssh. Uchebn. Zaved., Fiz. **3**, 124 (1984).
3. A. A. Agasiev, A. Kh. Zeĭnalov, A. A. Mamedov, and N. K. Éfendiev, Fiz. Tekh. Poluprovodn. (Leningrad) **6**, 649 (1972) [Sov. Phys. Semicond. **6**, 560 (1972)].
4. G. A. Akhundov, S. A. Musaev, A. É. Bakhyshov, *et al.*, Fiz. Tekh. Poluprovodn. (Leningrad) **9**, 142 (1975) [Sov. Phys. Semicond. **9**, 94 (1975)].
5. A. É. Bakhyshev, L. G. Musaeva, A. A. Lebedev, and M. A. Yakobson, Fiz. Tekh. Poluprovodn. (Leningrad) **9**, 1548 (1975) [Sov. Phys. Semicond. **9**, 1021 (1975)].
6. A. A. Arabidze, D. D. Khalilova, and V. D. Kokoeva, Soobshch. Akad. Nauk Gruz. SSR **50**, 59 (1968).
7. I. I. Andrianova, A. A. Berezhnoĭ, and Yu. V. Popov, Opt. Spektrosk. **90**, 957 (1971).
8. T. J. Issaev, J. Appl. Crystallogr. **6**, 413 (1973).

Translated by V. Rogovoĭ

ELECTRONIC AND OPTICAL PROPERTIES
OF SEMICONDUCTORS

Stimulation of Negative Magnetoresistance by an Electric Field and Light in Silicon Doped with Boron and Manganese

M. K. Bakhadyrkhanov^, O. É. Sattarov, Kh. M. Iliev, K. S. Ayupov, and Tuérdi Umaĭer

Beruni State Technical University, Tashkent, 700095 Uzbekistan

^e-mail: tstu@uzpak.uz

Submitted November 15, 2004; accepted for publication December 9, 2004

Abstract—It is experimentally ascertained that light stimulates the negative magnetoresistance observed in a high electric field in silicon doped with boron and manganese. The optimum conditions (the electric field, temperature, illumination, and resistivity of the material) for observation of the largest magnitude of negative magnetoresistance in (Si:B):Mn are determined. The dependence of the negative magnetoresistance on the concentration of compensating impurity is established. © 2005 Pleiades Publishing, Inc.

The effect of negative magnetoresistance in semiconductors in high electric fields was studied by Ashe *et al.* [1] and later considered in [2]. This effect is observed mainly at 77 K and attains its largest magnitude (~28%) at an electric-field strength of about 500 V/cm. In contrast, we observed negative magnetoresistance at room temperature and in relatively low electric fields in *p*-Si doped with boron and manganese. In this context, the aim of the present study was to clarify the optimum conditions for the existence of negative magnetoresistance.

Compensated silicon doped with manganese was obtained by diffusion of manganese into silicon from a gaseous phase using the technology we developed in [3]. As the starting material, we used single-crystal *p*-Si:B with a resistivity $\rho_{st} = 1$–10 Ω cm; the boron concentration N_B varied from $\approx 2 \times 10^{16}$ to 2×10^{15} cm^{-3}, respectively. The oxygen concentration in the materials under study was nearly constant and was equal to $N_O \approx (5$–$7) \times 10^{17}$ cm^{-3}.

The temperature and duration of the diffusion were chosen so as to obtain compensated *p*-Si:(B, Mn) or overcompensated *n*-Si:(B, Mn) materials uniformly doped with manganese and with a resistivity $\rho \approx 10^2$–10^5 Ω cm at room temperature. The dimensions of the samples were identical ($0.4 \times 0.2 \times 0.05$ cm) in all the experiments, and contacts were deposited onto the side surfaces (with an area of 0.2×0.05 cm^2) of the samples.

In order to form ohmic contacts to the *p*-Si:(B, Mn) samples, we used a chemical deposition of nickel. To improve the nickel's adhesion, we lapped the samples using an M-9 micropowder and treated them in a solution of hydrofluoric acid (HF : H$_2$O = 1 : 3) to remove any oxide before the nickel-plating. The electrolyte for the nickel-plating was prepared according to the method described in [4]. The electrolyte was first heated to 86–90°C; ammonia and sodium hypophosphite were then added to the solution; and, finally, the

samples were immersed in the solution. The duration of the nickel-plating was 40 ± 20 s. After the process was completed, the sample surface exhibited a light-yellow coloring and was coated uniformly with nickel. The ohmic properties of the coating were checked by measuring the current–voltage (*I*–*V*) characteristics of the samples. The quality of the samples was assumed to be appropriate if the corresponding *I*–*V* characteristics were linear in the electric-field range under consideration. The samples were then tin-plated in preparation for a subsequent soldering of leads with the use of a rosin flux. For the tin-plating, we used solders with a relatively low melting temperature T_m: a POSK 50 solder ($T_m \approx 150$°C) and a POSK 61 solder ($T_m \approx 180$°C).

When measuring the magnetoresistance $\Delta\rho/\rho$, we varied the magnetic-field strength H in the range from 0 to 2 T. The direction of the field was perpendicular to both the direction of the current and the (111) plane (the face of a sample with an area of 0.4×0.05 cm^2). A reversal of the magnetic-field direction did not affect the value of $\Delta\rho/\rho$, whereas this value changed by 4–5% as a result of an electric-field reversal. These values were averaged in calculations of the magnetoresistance.

The experimental results show that the magnitude of the negative magnetoresistance and its variations depend heavily on the electric field applied to a sample. Therefore, we studied the electric-field dependence of the negative magnetoresistance in *p*-Si:(B, Mn) samples with $\rho \approx 6.2 \times 10^3$ Ω cm at room temperature and at $H = 1.5$ T (Fig. 1). As can be seen, the negative-magnetoresistance magnitude attains a maximum at $E_{max} = 90$–100 V/cm, decreases as E increases further, and tends to zero at $E \gtrsim 200$ V/cm. The domain of existence for the negative magnetoresistance corresponds to $E < 200$ V/cm in the samples under study.

A small positive-magnetoresistance effect is always observed in the overcompensated *n*-Si:(B, Mn) samples irrespective of their resistivity, and the magnitude of
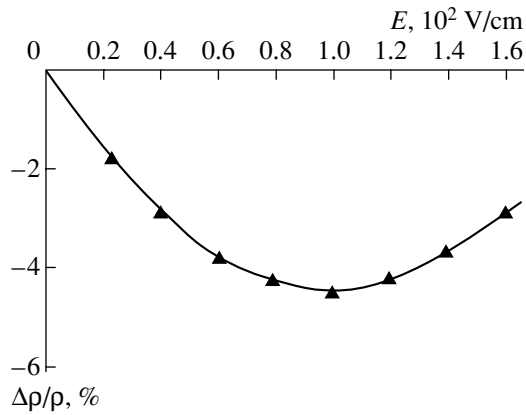
Fig. 1. Dependence of the magnetoresistance on the electric-field strength in a p-Si:(B, Mn) sample with the resistivity $\rho \approx 6.2 \times 10^3$ Ω cm in the dark, at room temperature, and in a constant magnetic field $H = 1.5$ T.

Fig. 2. Dependences of the magnetoresistance on the magnetic field for various values of the resistivity of the p-Si:(B, Mn) samples (in the dark, at room temperature, and at $E = 100$ V/cm): $\rho = $ (*1*) 2.5×10^2, (*2*) 6.2×10^2, (*3*) 6.3×10^3, (*4*) 1.5×10^4, (*5*) 6.5×10^4, and (*6*) 2×10^5 Ω cm.

Fig. 3. Dependences of the magnetoresistance on the magnetic-field strength for the p-Si:(B, Mn) samples with the resistivity $\rho \approx 6.2 \times 10^3$ Ω cm at room temperature, the constant electric field $E = 100$ V/cm, and the illumination intensity $L = $ (*1*) 8, (*2*) 32, (*3*) 80, (*4, 7*) 150, (*5*) 320, and (*6*) 450 lx. Dependences *1–6* correspond to samples that were obtained from initial p-Si:B samples with $\rho = 10$ Ω cm, and dependence *7* corresponds to a sample obtained from initial p-Si:B with $\rho = 1$ Ω cm.

this effect increases as the resistivity of the samples increases. It is worth noting that, although variations in the positive magnetoresistance in the overcompensated InSb samples do not differ from those in uncompensated (without manganese) Si:B samples with the same resistivity, the magnitude of the positive-magnetoresistance effect in n-Si:(B, Mn) is somewhat smaller than in the uncompensated samples.

In Fig. 2, we show the relative variations in the resistivity of compensated p-Si:(B, Mn) samples with several values of resistivity at room temperature in relation to the magnetic-field strength in the dark (at $E = 100$ V/cm). The results indicate that small-magnitude positive magnetoresistance is always observed in samples with $\rho \lesssim 5 \times 10^2$ Ω cm. As the resistivity of the p-Si:(B, Mn) samples increases, the magnetoresistance sign changes and negative magnetoresistance appears. The magnitude of the negative magnetoresistance increases with ρ and attains a maximum for samples with $\rho = (6–7) \times 10^3$ Ω cm. A further increase in the resistivity of the samples brings about a decrease in the negative-magnetoresistance magnitude, while the magnetoresistance changes its sign again and becomes positive for samples with $\rho \gtrsim (5–6) \times 10^4$ Ω cm.

We obtained interesting results when studying the magnetoresistance of p-Si:(B, Mn) samples exposed to white light. Both sides of the samples were illuminated uniformly, and the illumination intensity was controlled using a calibrated mesh. The direction of the incident light coincided with the magnetic-field direction. We found that illumination stimulated the negative magnetoresistance in p-Si:(B, Mn) appreciably. In Fig. 3, we show the dependences of the negative magnetoresistance on the magnetic field for p-Si:(B, Mn) samples that had $\rho \approx 6.2 \times 10^3$ Ω cm and were exposed to illumination of various intensities. As can be seen from Fig. 3, the negative-magnetoresistance magnitude increases as the
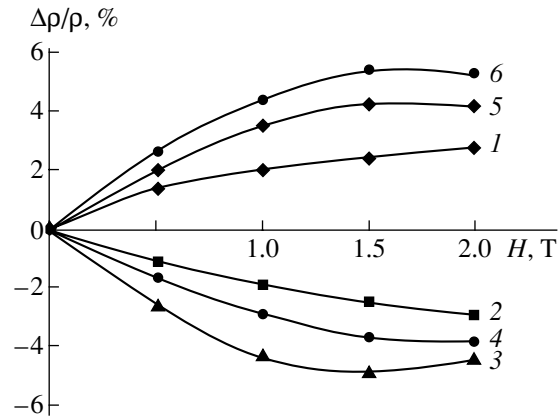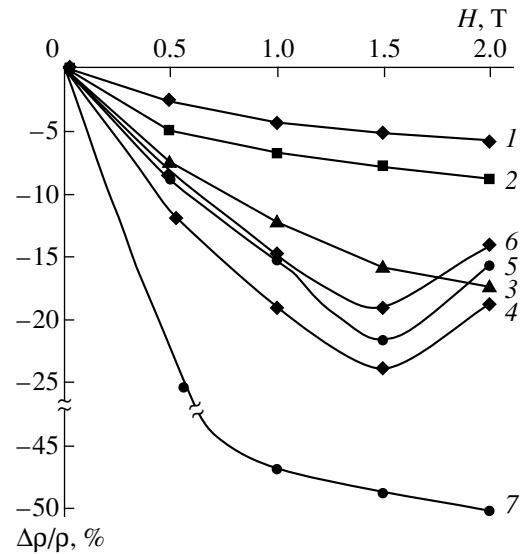
illumination intensity L is increased and attains a maximum at $L = 150$ lx. If the illumination intensity is increased still further, the negative-magnetoresistance magnitude decreases. The experimental results show that the magnetoresistance changes its sign at $L \approx 1000$ lx; i.e., it transforms into positive magnetoresistance. Thus, it is established that negative magnetoresistance stimulated by illumination is observed in the samples studied in the range of illumination intensities

0 lx $< L <$ 1000 lx, and the maximum magnitude of the negative magnetoresistance is observed at L = 150–180 lx.

We also studied the dependence of the magnetoresistance for p-type samples with $\rho \approx 6.3 \times 10^3$ Ω cm on the magnetic field at various temperatures (Fig. 4). The experimental results show that there is always small-magnitude positive magnetoresistance in these samples at T = 77 K in the magnetic-field range under consideration and that the magnitude of this magnetoresistance increases as H increases according to the law $\Delta\rho/\rho \propto H^2$ (curve 1). As the temperature is increased, the magnitude of the positive magnetoresistance decreases, and small-magnitude negative magnetoresistance is observed at T = 130–140 K. The negative-magnetoresistance magnitude increases with a further increase in temperature and attains a maximum at T = 290–300 K. After this point, increasing the temperature brings about a decrease in the negative-magnetoresistance magnitude.

Curve 7 in Fig. 3 represents the magnetic-field dependence of the negative-resistance magnitude for a p-Si:(B, Mn) sample with $\rho \approx 6.2 \times 10^3$ Ω cm obtained from starting silicon with a resistivity $\rho \approx 1$ Ω cm. In this sample, the concentration of electrically active Mn atoms is $N_{Mn} \approx 2.1 \times 10^{16}$ cm^{-3}, which exceeds that in the samples whose data are represented by curves 1–6. As can be seen from Fig. 3, the negative-resistance magnitude increases more than twofold as the concentration of compensating-impurity atoms increases under fixed conditions (L, E, T, and ρ). These data indicate that one can control the negative-magnetoresistance magnitude in p-Si:B by varying the diffusion-induced Mn concentration. The limitation of the manganese concentration by $N_{Mn} \approx 2.1 \times 10^{16}$ cm^{-3} is related to the solubility of Mn atoms in Si.

Thus, our studies show that the optimum conditions for observation of the largest magnitude of negative magnetoresistance in silicon doped with boron and manganese consist specifically in the requirement that the initial p-Si:B material has the resistivity ρ_{st} = 1–10 Ω cm. After the manganese diffusion, the samples
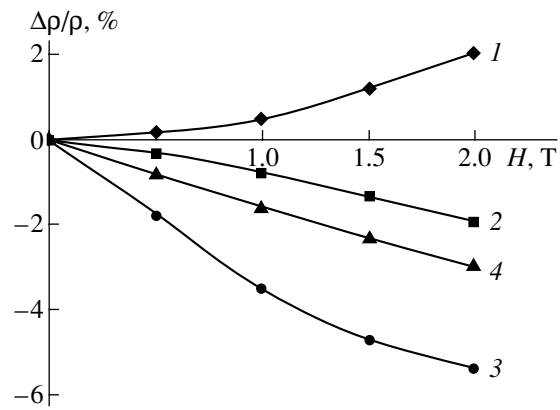

Fig. 4. Dependences of the magnetoresistance on the magnetic-field strength for p-Si:(B, Mn) samples with the resistivity $\rho = 6.3 \times 10^3$ Ω cm in the dark, at E = 100 V/cm, and at temperatures T = (1) 77, (2) 135, (3) 290, and (4) 320 K.

should still be p-type when the resistivity $\rho = (6–7) \times 10^3$ Ω cm, electric-field strength E = 80–100 V/cm, intensity of integrated illumination L = 130–150 lx, and optimum temperature T = 290–300 K.

REFERENCES

1. M. Ashe, Yu. G. Zav'yalov, and O. G. Sarbeĭ, Pis'ma Zh. Éksp. Teor. Fiz. **13**, 401 (1971) [JETP Lett. **13**, 285 (1971)].

2. K. Seeger, *Semiconductor Physics* (Springer, Berlin, 1974; Mir, Moscow, 1977).

3. B. I. Boltaks, M. K. Bakhadyrkhanov, S. M. Gorodetskiĭ, and G. S. Kulikov, in *Compensated Silicon*, Ed. by B. I. Boltaks (Nauka, Leningrad, 1972), pp. 12–24 [in Russian].

4. M. Shalkauskas and A. Vashkyalis, *Chemical Metallization of Plastics* (Khimiya, Moscow, 1977), pp. 133–134 [in Russian].

Translated by A. Spitsyn

SEMICONDUCTOR STRUCTURES, INTERFACES, AND SURFACES

Specific Features of the Physical Properties of a Modified CdTe Surface

V. P. Makhniy

Fed'kovich State University, ul. Kotsyubinskogo 2, Chernovtsy, 58012 Ukraine
e-mail: oe-dpt@chnu.cv.ua

Abstract—Specific features of the optoelectronic properties of CdTe substrates with a modified layer and surface-barrier diodes based on them are revealed and explained by quantum confinement effects in the nanocrystalline structure of the modified layer. The formation of the modified layer is confirmed by study of its surface using atomic-force microscopy and is attributed to the processes of self-organization, which is dominant under specific annealing conditions. © 2005 Pleiades Publishing, Inc.

Surface-barrier diodes (SBDs) based on single-crystal CdTe can be used as efficient detectors of various types of radiation, including solar radiation [1, 2]. Their main photoelectric parameters are determined, in many respects, by the material itself, the method used to form the rectifying contact, and the technique chosen for treatment of the base substrate. The technology involved in the fabrication of SBDs, which includes preliminary annealing (modification of the surface) of single-crystal n-CdTe wafers in air, has demonstrated great potential. In particular, this method has made it possible to fabricate Au–CdTe contacts with a photoconversion efficiency of ~(13–15)% at 300 K under solar illumination (AM1.5 source) [3, 4]. Subsequent, more detailed, studies of such samples have revealed the presence of a number of specific features, the most important of which are as follows:

(i) The dependences of short-circuit current (J_{sc}) and open-circuit voltage (V_{oc}) on the process conditions of SBD fabrication are rather complex. However, there exist an optimal temperature T_a and time t_a of substrate annealing and optimal electrical parameters of the substrate at which the highest photoconversion efficiency is attained [5].

(ii) SBDs fabricated on substrates with a modified surface have a higher photosensitivity S_ω in the high-energy spectral region as compared with a gold–base-crystal contact (the reference sample). In addition, the cutoff in the photon energy axis (Fig. 1, curve *2*) gives the energy $\hbar\omega \approx 1.3$ eV. This value is much lower than the expected value of 1.5 eV, which corresponds to the band gap E_g of CdTe at 300 K (Fig. 1, curve *1*).

(iii) In some cases, the experimentally observed short-circuit current density for SBDs with a modified surface [6] substantially exceeds the theoretically possible value of this parameter under the same illumination conditions [2].

(iv) Irrespective of the type and magnitude of conductivity, CdTe crystals annealed under optimal conditions (annealing time and temperature) exhibit their highest photoluminescence (PL) efficiency at 300 K [7]. It is noteworthy that, under the same excitation conditions, the PL edge of the base substrates is unobservable near room temperature. Moreover, emission has not been observed from annealed samples after removal of the modified surface layer in a polishing etchant.

(v) Illumination of the modified surface, prepared at the optimal values of T_a and t_a, by a nitrogen laser results in PL, whose spectrum is shown by curve *3* in Fig. 1. The most characteristic spectral feature is the presence of a wide A band covering the photon energy range 1.7–3.5 eV. The intensity of this band decreases with time, while the band peak shifts to low energies. Note that the steady-state values of the peak intensity
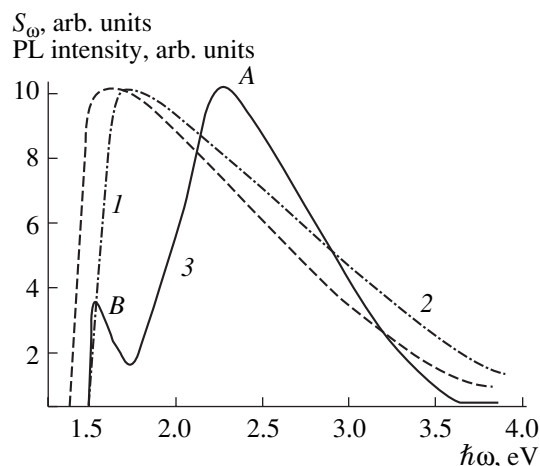

Fig. 1. Photosensitivity spectra of gold contacts with a (*1*) conventional and (*2*) modified CdTe surface, and (*3*) the PL spectrum of the modified layer.

and energy are attained within several minutes of switching on the laser excitation, and the PL spectrum shown in Fig. 1 was measured precisely under these conditions. The PL band *A* under consideration may be due to a quantum-confinement effect, since its behavior is characteristic of the high-energy emission of low-dimensional systems such as Si nanocrystals [8]. Let us consider this question in more detail.

First of all, note that the modified surface is visually dull as compared with the mirror surface of the initial substrates. A microprofile study using a Nanoscope IIIa atomic-force microscope in a periodic contact mode shows that the surface of the annealed samples is characterized by a grain structure with a lateral grain size of 10–50 nm. These grains can condense into larger ones (100–300 nm) (Fig. 2). Small grains are in fact nanocrystals that form the PL band *A*. The peak spread and the large spectral width can be explained by the size and shape dispersion of the smaller CdTe nanocrystals. Note that the *A* band cannot be attributed to the luminescence of the CdO film that, in principle, can be formed after annealing. This statement is confirmed by several experimental observations. First, the PL spectra of samples with a specially grown CdO film possessing a mirror surface show no significant emission in the visible range. Second, the reflection spectrum of such samples, measured with wavelength modulation, contains a peak corresponding to the CdO band gap. This peak is absent in the similar spectra of the modified surface. Finally, the high-energy wing of the *A* band is cut at energies that greatly exceed the CdO band gap width [9]. It is quite possible that the CdO film can be involved in the passivation of surface bonds and the effect of dielectric amplification; however, this issue requires additional examination.

In conclusion, note that the proposed model of the modified surface also adequately explains the observed specific features of the photoelectric properties of Au–*n*-CdTe contacts. The existence of fairly strong edge emission (the *B* band in Fig. 1) indicates a considerable decrease in the surface recombination velocity. In addition, the surface of the annealed samples has a more developed profile, thus providing a larger effective photocell area and, as a result, a higher short-circuit current. Due to multiple reflections, the photon absorption coefficient also increases (especially for low-energy photons), which leads to the observed shift of the photosensitivity edge. This effect, as in a textured photocell [2], also causes an increase in J_{sc}, V_{oc}, and high-energy photosensitivity.

Thus, the results obtained show that the modified surface layer has a nanocrystalline structure in which quantum-confinement effects are observed. The formation of this structure is apparently caused by the processes of self-organization, whose manifestation is quite probable in view of the specific features of the annealing conditions. First of all, we should note the rather narrow
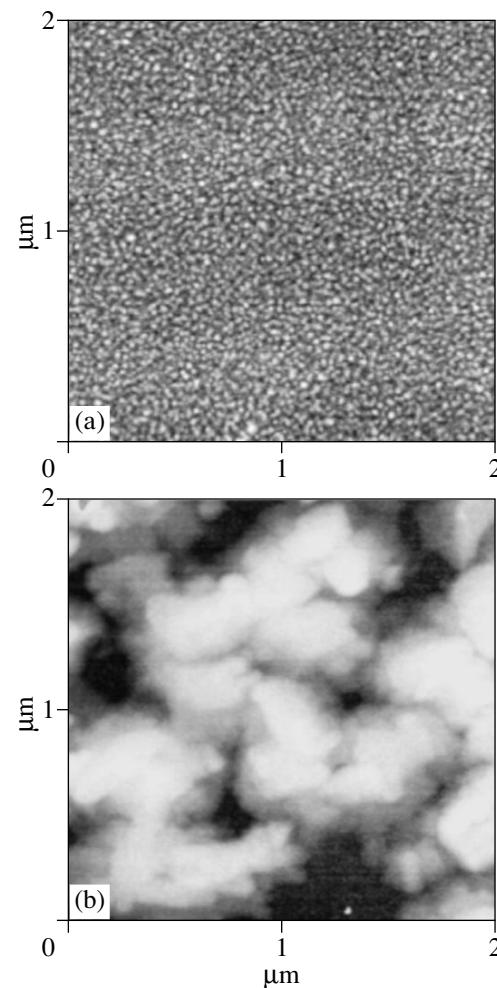
Fig. 2. Structure of the surfaces of (a) base and (b) annealed CdTe crystals.

temperature and time annealing ranges [7]. In addition, when these parameters are used under different conditions (vacuum or inert atmosphere), the desired result is not obtained. In this context, the final solution to the problem of the involvement of self-organization processes in the formation of the nanocrystalline structure can be obtained only by performing additional experimental and theoretical studies, which are beyond the remit of this paper.

ACKNOWLEDGMENTS

REFERENCES

1. D. V. Korbutyak, S. V. Mel'nichuk, S. V. Korbut, *et al.*, *Cadmium Telluride* (Ivan Fedorov, Kiev, 2000) [in Ukrainian].

2. A. L. Fahrenbruch and R. H. Bube, *Fundamentals of Solar Cells* (Academic, New York, 1987; Énergoatommash, Moscow, 1987).

3. R. Ciach, M. V. Demich, P. M. Gorley, *et al.*, J. Cryst. Growth **197**, 675 (1999).

4. K. Pranab and P. Raychaudhuri, J. Appl. Phys. **62**, 3025 (1987).

5. M. V. Demich, P. M. Gorleĭ, V. P. Makhniĭ, *et al.*, Nauk. Visn. Chernivets. Derzh. Univ.: Fiz. **30**, 124 (1998).

6. P. M. Gorley, M. V. Demich, V. P. Makhniy, *et al.*, Thin Solid Films **30**, 124 (2002).

7. V. P. Makhniĭ, M. V. Demich, and M. M. Sl'otov, Ukr. Patent No. 5010A (April 22, 2003).

8. É. B. Kaganovich, É. G. Manoĭlov, I. R. Bazylyuk, and S. V. Svechnikov, Fiz. Tekh. Poluprovodn. (St. Petersburg) **37**, 353 (2003) [Semiconductors **37**, 336 (2003)].

9. K. L. Chopra and S. R. Das, *Thin Film Solar Cells* (Plenum, New York, 1983; Mir, Moscow, 1986).

Translated by N. Korovin

SEMICONDUCTOR STRUCTURES, INTERFACES, AND SURFACES

The Effects of Interface States on the Capacitance and Electroluminescence Efficiency of InGaN/GaN Light-Emitting Diodes

N. I. Bochkareva*^, E. A. Zhirnov, A. A. Efremov***, Yu. T. Rebane*,
R. I. Gorbunov*, A. V. Klochkov*, D. A. Lavrinovich*, and Yu. G. Shreter***

*Ioffe Physicotechnical Institute, Russian Academy of Sciences, Politekhnicheskaya ul. 26, St. Petersburg, 194021 Russia
^e-mail: n.bochkareva@mail.ioffe.ru
**Department of Physics, Bath University, Bath, BA2 7AY, UK
***St. Petersburg State Technical University, Politekhnicheskaya ul. 29, St. Petersburg, 194251 Russia
Submitted November 3, 2004; accepted for publication November 25, 2004

Abstract—The capacitance–voltage characteristics and external quantum efficiency of electroluminescence in blue GaN light-emitting diodes (LEDs) with an InGaN quantum well have been investigated in the temperature range 77–300 K. The results obtained are interpreted taking into account the effect of the InGaN/GaN interface states of structural defects and impurities on the capacitance of the GaN LEDs. The nonlinearity of the $C^{-2}(U)$ characteristics observed at low forward bias is attributed to an increase in the interface charge resulting from tunneling of free electrons and their trapping at the interface states. According to estimates, states with a density of about 3×10^{12} cm^{-2} are present at the interface. A recombination current in the interface region suppresses the injection of charge carriers into the quantum well and decreases the electroluminescence efficiency at high forward bias. Degradation of the optical power of the LEDs, accompanied by an increase in the measured capacitance, is attributed to an increase in the density of charged interface states and changes in their distribution in the band gap. © 2005 Pleiades Publishing, Inc.

1. INTRODUCTION

The capacitance–voltage characteristics of InGaN/GaN light-emitting diodes (LEDs) based on p–n heterostructures with quantum wells are usually analyzed within the Anderson model of an ideal heterojunction [1], which assumes the absence of localized interface states. In this case, the shape of the $C^{-2}(U)$ characteristics of these LEDs is understood as being related to the dopant profile [2]. However, phases with different lattice constants are matched at the interfaces in InGaN/GaN LEDs. For example, the lattice mismatch between the GaN and In$_x$Ga$_{1-x}$N phases in blue LEDs is about 4% [3]. Such a mismatch should lead to a high density of interface states [4, 5]. The localized states at the interface between the n and p regions of the LED structure may also be due to structural defects and impurities segregated at the inner surfaces of the heterostructure, i.e., at heterointerfaces and grain boundaries in the GaN layers. Localized states at the phase boundaries in the InGaN quantum well also serve as interface states. It is well known that dislocations and grain boundaries in GaN are negatively charged [6]. It is also known that oxygen and hydrogen segregate at extended defects in this material [7, 8]. It has been shown that oxygen, which forms complexes with gallium vacancies, gives rise to deep acceptor states at dislocations in GaN [9]. In InGaN/GaN structures, the interfaces also contain polarization charges [10], whose screening by free charge carriers should lead to a change in the electric field distribution as the forward bias increases [11]. The charged states localized between the n and p regions may lead to significant band bending. In this case, the energy band diagram and electrical characteristics of an n-GaN/InGaN/p-GaN heterostructure depend not only on the doping level of the n-GaN and p-GaN layers but also on the magnitude of the charge localized at the interface [12].

In this paper, we report the results of measurements of the $C(U)$ characteristics of LEDs with an InGaN/GaN quantum well in the temperature range 77–300 K and temperature measurements of the external quantum efficiency of electroluminescence carried out before and after optical power degradation. The data are analyzed taking into account the effect of states localized at the InGaN/GaN interfaces on the LED capacitance and electroluminescence efficiency. The shape of the $C(U)$ characteristics is related to the distribution of the density of interface states in the band gap. Degradation phenomena are explained by an increase in the density of states at the InGaN/GaN interfaces and a change in their distribution in the band gap during the LED degradation.
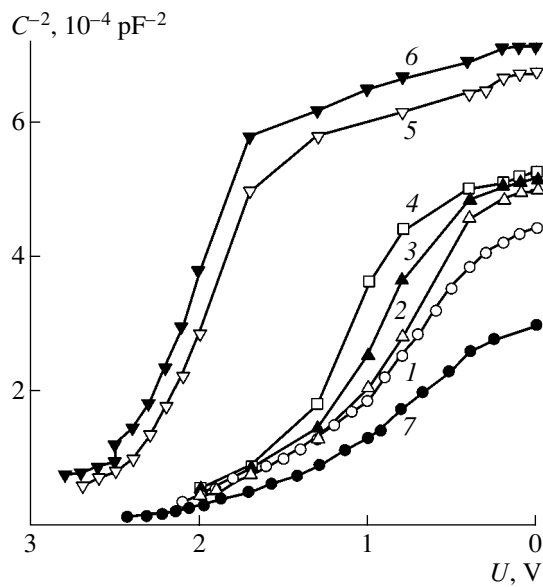
Fig. 1. Capacitance–voltage $C^{-2}(U)$ characteristics of (*1–6*) an operating LED and (*7*) a LED after operation for a year. $T = (1, 7)$ 300, (*2*) 250, (*3*) 230, (*4*) 200, (*5*) 150, and (*6*) 90 K.
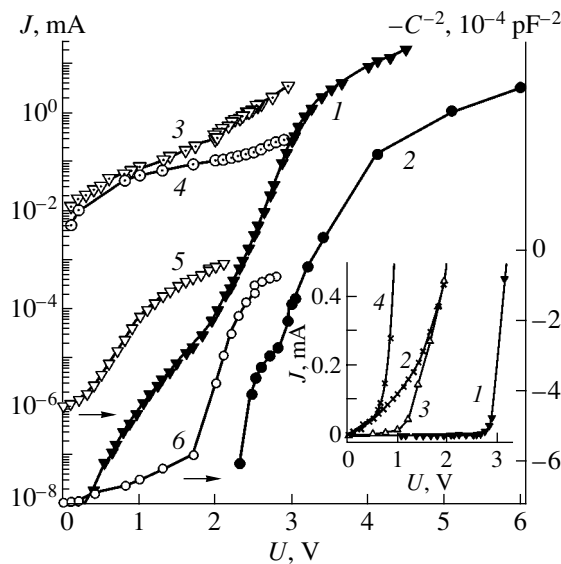

Fig. 2. (*1, 2*) Static $J(U)$ and (*3, 4*) high-frequency $J_\sim(U)$ current–voltage characteristics and (*5, 6*) the capacitance–voltage characteristic of a LED. $T = (1, 3, 5)$ 300 and (*2, 4, 6*) 77 K. The inset shows (*1*) the $J(U)$ and (*2*) $J_\sim(U)$ characteristics of an operating LED and (*3, 4*) the change in the J–U characteristic during degradation.

2. EXPERIMENTAL

We investigated blue LEDs based on n-GaN/InGaN/p-GaN heterostructures (with an area $S = 6 \times 10^{-4}$ cm^2) containing a 30-Å InGaN quantum well. The heterostructures were prepared by metal–organic chemical vapor deposition [11, 12] (for a detailed description of the LED structure, see [11, 12]).

The capacitance–voltage characteristics were measured at frequencies ranging from 10 kHz to 1 MHz at temperatures of 77–300 K using an immittance bridge, a 232B Unipan lock-in nanovoltmeter, a BCI-280 box-car integrator, and a 590 Keithley $C(U)$ analyzer. The electroluminescence efficiency $\eta_{EL} \equiv L/J$ (L is the electroluminescence intensity and J is the current through a LED) was measured using a Si photodiode. In order to measure the current–voltage $J(U)$ and electroluminescence-intensity–voltage $L(U)$ characteristics, a Keithley 238 source measurement unit and a B7-40/1 voltmeter were employed.

3. RESULTS

Figure 1 shows the capacitance–voltage characteristics of the LEDs under study in the $C^{-2}(U)$ coordinates at different temperatures and at low forward bias. The dependences obtained are nonlinear. At room temperature, the capacitance sharply increases (by 80–130 pF) with an increase in the forward bias from ~0.5 to ~1 V. When approaching the cutoff voltage, the slope of the $C^{-2}(U)$ curves decreases. With a decrease in temperature to 150–90 K, the most significant change in the capacitance is observed near 1.7 V.

In the LEDs under consideration, we also observed small-signal high-frequency conductance $G(U)$. The high-frequency active current

$$J_\sim(U) = \int_0^U G(U)\,dU,$$

calculated from the experimental data on $G(U)$, is shown in Fig. 2 as a function of bias at 300 and 77 K (curves *3, 4*). Figure 2 also shows the static characteristics $J(U)$ (curves *1, 2*). The nonlinearity of the static $J(U)$ and high-frequency $J_\sim(U)$ characteristics is typical of charge carrier trapping [11, 12].

Figure 3 shows the bias dependences of the electroluminescence efficiency of the LEDs. The dependences $\eta_{EL}(U)$ measured at 300 and 77 K attain a maximum at about 3.2 V.

The temperature dependences of the capacitance $C_0(T)$ measured at zero bias are shown in Fig. 4. Let us first consider curve *1* (measurement before LED degradation). It can be seen that the capacitance changes stepwise with temperature. The sharpest changes are observed in the temperature ranges 100–150 and 225–300 K. A small step in the dependences capacitance $C_0(T)$ is also observed at ~260 K. A sharper increase in the current and the electroluminescence efficiency is observed in approximately the same temperature ranges (Fig. 4, curves *3, 4*).

In addition, Fig. 4 shows the temperature dependences of the capacitance and efficiency of a LED whose electroluminescence intensity decreases by a factor of more than 100 after degradation. The temper-

ature dependences of the capacitance and efficiency become more monotonic (curves *2*, *5*). The capacitance of a low-intensity LED at temperatures above 200 K (Fig. 4, curve *2*) increases (see, also, Fig. 1, curve *7*). The $J(U)$ characteristic of the low-intensity LED shifts to lower biases and is similar to the dependence $J_\sim(U)$ of an operating LED (inset in Fig. 2, curves *2*, *3*). The LED current only weakly depends on temperature. With further degradation, the $J(U)$ characteristic shifts even closer to zero bias (curve *4*).

4. DISCUSSION

In the LEDs under study, the *n*-GaN layers are much more heavily doped ($N_d = 10^{18}$ cm^{-3}) than the *p*-GaN layers ($N_a = 2 \times 10^{17}$ cm^{-3}). With due regard to the large effective hole mass in GaN, $2.2m_0$ (m_0 is the free electron mass) [13], we previously proposed [12] a tunnel recombination model of the current transmission in a GaN LED. This model takes into consideration the tunneling of electrons through the potential barrier in the *n* region to the states localized at the InGaN/GaN interfaces and the thermal activation of holes above the potential barrier in the *p* region. Taking into account that a change in the charge of the interface states resulting from an increase in bias in nonideal *p–n* heterojunctions generally has the same sign as in the depleted layer of the more heavily doped junction region [5] and that dislocations and grain boundaries in GaN are negatively charged [6, 14], we assume that the states localized near the InGaN/GaN interfaces are acceptor-like ones. To simplify the analysis, we also assume that the states are localized in the same plane, i.e., at the InGaN/*p*-GaN interface.

4.1. Capacitance and Shape of the C(U) Characteristic of a p–n Heterostructure with Localized Interface States

In the absence of interface states, the field of contact potential difference between the *n* and *p* regions of the barrier structure is screened by charges of ionized impurities (Q_n and Q_p, respectively). In this case, the diffusion potentials in the *n* and *p* regions of the *p*-GaN/InGaN/*n*-GaN heterostructure are determined by the level of doping of the *n*-GaN and *p*-GaN layers, and $Q_n = -Q_p$. In the presence of interface states, the field of the contact potential difference is partially screened by the total charge of these states $Q_i = \sum_j Q_j(U)$ (Q_j is the charge density in the *j*th band of the interface states), and $Q_n = -(Q_p + Q_i)$. Taking into account that $Q_n = (2q\varepsilon N_d U_n)^{1/2}$ and $Q_p = -(2q\varepsilon N_a U_p)^{1/2}$, we find that $Q_i = (2q\varepsilon)^{1/2}[(N_a U_p)^{1/2} - (N_d U_n)^{1/2}]$. Here, q is the elementary charge; ε is the permittivity; $U_{bi} - U = U_n + U_p$; U_{bi} is the built-in voltage in the *p–n* heterostructure; and U_n and U_p are the parts of the potential $U_{bi} - U$ in the *n* and *p* regions, respectively. Using these
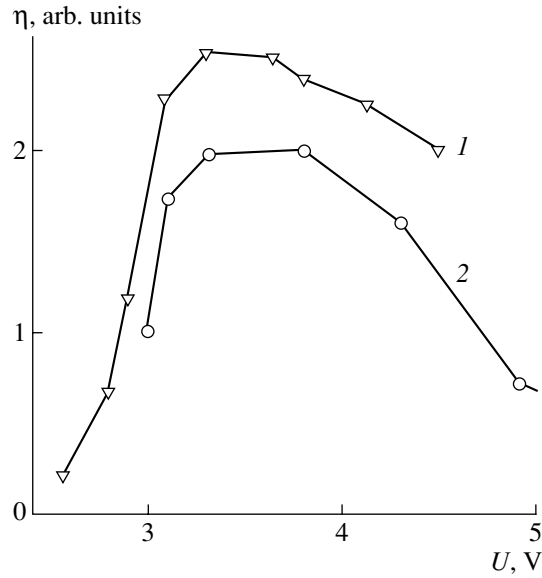
Fig. 3. Dependence of the LED quantum efficiency on bias at (*1*) 300 and (*2*) 77 K.
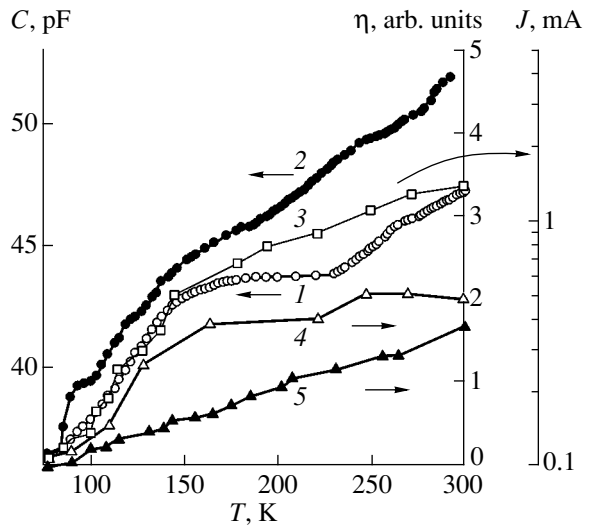
Fig. 4. Temperature dependences of the (*1*, *2*) capacitance and (*3*) current at $U = 3.05$ V and (*4*, *5*) the efficiency at the operation current $J = 20$ mA (*1*, *3*, *4*) before and (*2*, *5*) after degradation of the LED optical power. The η axis scale for curve *5* is increased by a factor of 100.

relations, we can obtain an expression for the differential capacitance of the heterostructure: $C = dQ_n/dU = dQ_n/dU_n(dU_n/dU)$, which is similar to the expression for the capacitance of a nonideal *p–n* heterojunction [5] but, in contrast to [5], assumes that the *p* and *n* regions of the heterostructure have the same permittivity. When $N_d \gg N_a$, the expression for the capacitance as a function of the impurity concentrations in the *n*-GaN and

p-GaN layers and the charge at the InGaN/GaN interface can be compactly written as

$$C = \left(\frac{\varepsilon q N_a}{2\left(U_{bi} - \dfrac{Q_i^2(U)}{2\varepsilon q N_d} - U \right)} \right)^{1/2} \left(1 + \frac{Q_i(U)}{\varepsilon q N_d} \frac{dQ_i}{dU} \right). \quad (1)$$

The effect of the charge of the interface states on the capacitance of an asymmetric *p–n* heterostructure is determined by the dopant concentration in the heavily doped layer. With an increase in the density of interface states and the interface charge, the heterostructure capacitance is determined to an even greater extent by the interface charge and to a lesser extent by the doping level. In the presence of interface states, the barrier capacitance, as well as the slope of the $C(U)$ characteristic, increases:

$$\frac{\partial(C^{-2})}{\partial U} = -\frac{2}{\varepsilon q N_a}\left(1 + \frac{Q_i(U)}{\varepsilon q N_d} \sum_j \frac{\partial Q_j(U)}{\partial U} \right). \quad (2)$$

As follows from (1), the density of charged interface states is normalized to the space charge density in the depletion region at $U_n = 1$ V: $Q_0 \equiv Q_n^2/U_n = 2\varepsilon q N_d$. This relation makes it possible to estimate the characteristic density of interface states at $N_d = 10^{18}$ cm^{-3}, which are responsible for the significant increase in the heterostructure's capacitance, as $N_i = 3 \times 10^{12}$ cm^{-2}. It follows from (2) that the change in the slope of the $C^{-2}(U)$ characteristic depends on the distribution of the interface states in the band gap. Thus, a sharp change in the slope can be observed for the pinning of the Fermi level at the interface and $dQ_n/dU \gg Q_0$.

In the case of total filling of the interface state band, when the quasi-Fermi level crosses the top of this band and the hole density at the interface is still low, the increase in the capacitance due to increasing forward bias slows and the slope of the characteristic begins to be determined by the doping levels and, hence, decreases. Thus, the slope of the $C(U)$ characteristic in the $C^{-2}(U)$ coordinates increases as the charge Q_i increases (with increased bias) and decreases when the interface state band is completely filled. These considerations suggest that the changes in the slope of the $C^{-2}(U)$ characteristic observed near 0.5 and at 1.5 V (Figs. 1, 2) may be related to the filling of two groups of states.

In the model of tunnel transport of charge carriers through the space charge region in the presence of interface states, the dependences $\log J(U)$ and $-C^{-2}(U)$ are nonlinear: $\log J \propto U - U_{bi} + \alpha Q_i(U)$ and $-C^{-2} \propto U - U_{bi} + \alpha Q_i(U)$, where $\alpha = (2q\varepsilon(N_d + N_a))^{-1}$. Thus, in the presence of interface states, the nonlinear dependences $-C^{-2}(U)$ and $\log J(U)$ should be similar. These curves are compared at 300 (*1, 5*) and 77 K (*2, 6*) in Fig. 2. As can be seen, their shape is similar, which confirms the proposed mechanism of current transmission and formation of the *J–U* and *C–U* characteristics.

4.2. High-Frequency Conductance

Capacitance measurements of GaN-based LED heterostructures have also revealed the presence of high-frequency conductance G [2, 11, 12]. Under these circumstances, large conductance and the specific features of the temperature and frequency dependences of the capacitance were attributed to a finite rate of charge exchange between the energy bands and the states in the band gap formed by the main dopant [2]. However, when electrons tunnel to the states localized at the interface, the charge exchange rate of the interface states is determined by the electron tunnel current. The following equivalent scheme of the structure can be considered: two capacitances, C_n and C_p, connected in series with parallel connected resistances of depleted layers, R_n and R_p, in the *n* and *p* regions. The characteristic time required for charge exchange at the interface states can be written as $\tau = (R_n R_p/R_n + R_p)(C_n + C_p)$. The delay in the charge exchange at the interface states by the tunnel current explains the occurrence of the high-frequency conductance. The charge exchange is nonexponential in time, since a change in the interface charge is accompanied by a change in the barrier height and, respectively, all the resistances and capacitances of the equivalent scheme.

In addition, note that when conducting channels through the depletion region are formed in the *p–n* heterostructure (for example, when a local p^+–n^+ junction is formed), a grain boundary with segregated impurities can play the role of a channel gate. The capture of electrons at the grain boundary narrows the channel, which compensates for the initial increase in the conductivity resulting from an increase in the forward bias. This process may increase the measured LED capacitance and conductivity.

4.3. Electroluminescence Efficiency in a Heterostructure with Localized Interface States

As can be seen in Fig. 2, with an increase in bias to ~3 V, the static current gradually approaches the value of the active component of the high-frequency current. Figure 3 demonstrates that the maximum electroluminescence quantum efficiency is observed in this bias range. This circumstance suggests that the interface traps are completely filled at the total-filling bias $U_{TFL} \approx 3.2$ V and the concentration of charge carriers injected into the quantum well increases.

With an increase in the concentration of holes, their tunneling and recombination with electrons captured at the localized interface states controls the forward bias distribution in the structure, which leads to the suppression of charge carrier injection into the quantum well and decreases the electroluminescence efficiency at $U >$

U_{TFL} [12]. As a result, the efficiency, which attains its maximum at relatively low currents (~1–3 mA), significantly decreases, even at operation currents of 20 mA.

At low temperatures and $U = U_{TFL}$, the thermally activated hole current is low. As a result, even at low currents, the electroluminescence efficiency begins to decrease as the bias decreases at low temperatures. When there is a constant current through a LED, its efficiency decreases as the temperature decreases (Fig. 4, curve *4*). The observed correlation between the dependences $\eta_{EL}(T)$, $C(T)$, and $J(T)$ suggests that the decrease in the electroluminescence efficiency upon cooling is caused by temperature changes in the band bending and the density of charged interface states.

A degraded LED sample demonstrated an increase in leakage currents to the value of an active high-frequency current in an operating LED (i.e., the tunnel current to the interface states) and a decrease in efficiency. A correlation between the temperature dependences of the efficiency and the capacitance was also observed after degradation. The dependences $\eta_{EL}(T)$ and $C(T)$ are more monotonic in this case (Fig. 4, curves *5*, *2*). This fact suggests that the density of charged interface states increases during degradation and their distribution in the band gap changes.

5. CONCLUSIONS

Analysis of the capacitance–voltage measurements of blue GaN LEDs showed that states localized at the InGaN/GaN interface, formed by structural defects and impurities, significantly affect the LEDs' capacitance. According to estimates, states with a density of about 3×10^{12} cm^{-2} are present at the interface. The nonlinearity of the $C^{-2}(U)$ characteristics observed at low forward bias is attributed to an increase in the density of charged interface states resulting from the tunneling and trapping of free electrons. The Fermi level pinning at the interface leads to a decrease in the electroluminescence efficiency as the forward bias increases. The observed correlation between the temperature dependences of the efficiency and the capacitance suggests that the reason for the decrease in the electroluminescence efficiency upon cooling is temperature changes in the band bending and the density of charged interface states. The degradation of optical power, accompanied by an increase in the measured LED capacitance, is attributed to an increase in the density of interface states and a change in their distribution in the band gap.

REFERENCES

1. R. L. Anderson, Solid-State Electron. **5**, 341 (1962).
2. Y. Zohta, H. Kuroda, R. Nii, and S. Nakamura, J. Cryst. Growth **189–190**, 816 (1998).
3. O. Ambacher, J. Phys. D: Appl. Phys. **31**, 2653 (1998).
4. W. G. Oldham and A. G. Milnes, Solid-State Electron. **7**, 153 (1964).
5. J. P. Donnelly and A. G. Milnes, IEEE Trans. Electron Devices **14**, 63 (1967).
6. J. Oila, K. Saarinen, A. E. Wickenden, *et al.*, Appl. Phys. Lett. **82**, 1021 (2003).
7. K. S. A. Butcher, H. Timmers, Afifuddin, *et al.*, J. Appl. Phys. **92**, 3397 (2002).
8. I. Arslan and N. D. Browning, Phys. Rev. Lett. **91**, 165 501 (2003).
9. J. Elsner, R. Jones, M. I. Heggie, *et al.*, Phys. Rev. B **58**, 12571 (1998).
10. T. Takeuchi, C. Wetzel, S. Yamaguchi, *et al.*, Appl. Phys. Lett. **73**, 1691 (1998).
11. Y. T. Rebane, N. I. Bochkareva, V. E. Bougrov, *et al.*, Proc. SPIE **4996**, 113 (2003).
12. N. I. Bochkareva, E. A. Zhirnov, A. A. Efremov, *et al.*, Fiz. Tekh. Poluprovodn. (St. Petersburg) **39**, 627 (2005) [Semiconductors **39**, 594 (2005)].
13. J. S. Im, A. Moritz, F. Steuber, *et al.*, Appl. Phys. Lett. **70**, 631 (1997).
14. G. Koley and M. G. Spencer, Appl. Phys. Lett. **78**, 2873 (2001).

Translated by Yu. Sin'kov

SEMICONDUCTOR STRUCTURES, INTERFACES, AND SURFACES

The Properties of Structures Based on Oxidized Porous Silicon under the Effect of Illumination and a Gas Environment

D. I. Bilenko^, O. Ya. Belobrovaya, É. A. Zharkova, D. V. Terin, and E. I. Khasina

Research Institute of Mechanics and Physics, Saratov State University, Saratov, 410026 Russia

^e-mail: bil@sgu.ru

Submitted December 16, 2004; accepted for publication December 16, 2004

Abstract—The effect of illumination and adsorption of polar molecules on the properties of structures based on oxidized porous silicon has been investigated. The specific features of these structures are fluctuations and a change in the sign of open-circuit voltage under the influence of long-term photoexcitation, time-related instabilities of the current in media with a high content of hydrogen sulfide, long periods of photocurrent decay after switching off the illumination, and the occurrence of negative photoconductivity in structures with space-charge-limited currents. The results obtained are explained by the presence of multiply charged traps of different types in oxidized porous silicon, their charge exchange, and the tunneling of charge carriers between silicon nanocrystallites. © 2005 Pleiades Publishing, Inc.

1. INTRODUCTION

The effect of a gas environment on the electrical and photoelectrical properties of porous silicon (*por*-Si) and structures based it is of interest both for understanding the physical processes occurring in these *por*-Si structures and for practical application, in particular, the development of highly sensitive sensors. The effect of a gas environment on the properties of *por*-Si has been investigated in a number of studies [1–6]. However, the properties of structures with partially oxidized *por*-Si layers have not been studied in detail.

Anomalous behavior of the current–voltage (*I–V*) characteristics of samples with oxidized *por*-Si layers at low biases (nonzero current at zero bias) has previously been observed both by us [7–9] and in other studies [10, 11]. Our early investigations showed that the specific features of such structures are the presence of open-circuit voltage V_{oc} in the initial state, which changes after adsorption of polar molecules, and high sensitivity of their electrical properties to hydrogen sulfide and acetone [7–9]. The effect of humidity on the open-circuit voltage in Au–*por*-Si–*n*-Si structures was investigated in [12].

It is of interest to analyze the effect of illumination and adsorption of polar molecules on the electrical properties of Pd–(oxidized *por*-Si)–*p*+-Si–Al structures.

2. EXPERIMENTAL

Oxidized *por*-Si layers were prepared by electrochemical etching of *p*-Si single-crystals with $\rho = 0.03\ \Omega$ cm and subsequent anodic oxidation using the technique described in [8, 9]. The thickness *d* of the *por*-Si layers and their porosity *q* were monitored during their formation. Samples with $d = 2–10\ \mu m$ and $q =$ 0.6–0.85 were selected for further investigation. Pd–(oxidized *por*-Si)–*p*+-Si–Al structures were formed by deposition of an aluminum ohmic contact on a *p*+-Si substrate in vacuum ($P \approx 10^{-5}$ Torr) at a substrate temperature of 120°C with subsequent alloying. Then, a palladium electrode was deposited in vacuum onto an oxidized *por*-Si layer. The thickness of the Pd layers, controlled during the deposition, varied within 50–60 nm.

The effect of illumination on the oxidized *por*-Si structures was studied under steady-state conditions. We used light with an intensity of ~80 mW/cm² from a source with a spectrum similar to that of AM-1. Acetone, nitrogen, and nitrogen–hydrogen sulfide mixtures were used as gaseous media. The samples were placed in a chamber during a reversible change of a gaseous medium. Measurements of the *I–V* characteristics in air and the above gases were performed in darkness and under illumination. The current kinetics was measured with a step of 2–10 s at fixed biases. The open-circuit voltage V_{oc} was measured by an electrometer millivoltmeter (with a measurement duration of 1–2 s and a time of 15–60 s between measurements).

3. RESULTS AND DISCUSSION

In our earlier research, we showed that Pd–(oxidized *por*-Si)–*p*+-Si–Al structures have *I–V* characteristics of two types, which are typical of Schottky barrier structures and structures with space-charge-limited currents. The first type of structures have a higher sensitivity to the adsorption of polar molecules (hydrogen sulfide and acetone).

Further investigations showed that illumination affects the properties of Schottky barrier structures and structures with space-charge-limited currents differently. Figure 1 shows the *I–V* characteristics of a Schot-
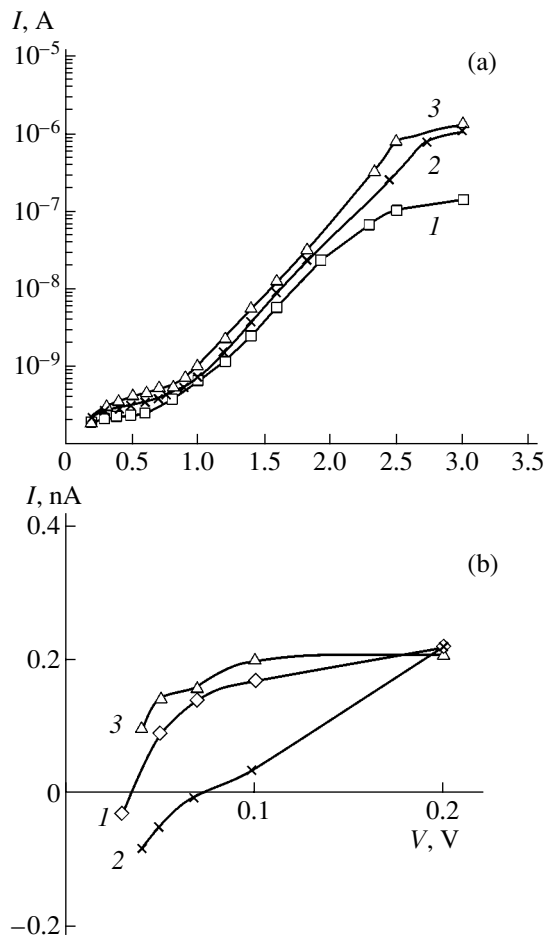
Fig. 1. Reverse current–voltage characteristics (positive voltage at Pd) of a Pd–(oxidized *por*-Si)–p^+-Si–Al structure at (a) $V_+ > V_{oc}$ and (b) $V_+ \leq V_{oc}$ ($V_{oc} \approx 170$ mV): (*1*) in air, (*2*) in acetone vapor ($C \approx 1000$ ppm), and (*3*) in acetone vapor under illumination.

Fig. 2. Kinetics of the reverse current through a Pd–(oxidized *por*-Si)–p^+-Si–Al structure upon photoexcitation. (a) A Schottky barrier structure at $V_+ = $ (*1*) 0.2, (*2*) 0.4, (*3*) 0.5, (*4*) 1, and (*5*) 1.6 V; (b) a structure with space-charge-limited currents at $V_+ = $ (*1*) 2 and (*2*) 2.5 V. The instants when the illumination was switched on and switched off are indicated by arrows.

tky barrier structure in its initial state (in air) and in acetone vapor in darkness and under illumination for two ranges of reverse bias V (positive voltage at Pd): $V > V_{oc}$ (Fig. 1a) and $V < V_{oc}$ (Fig. 1b). As can be seen in Fig. 1a, in the range of biases exceeding the open-circuit voltage, all the curves tend to constant values. In the presence of acetone vapor and under illumination, the current increases by a factor of 1.5–2; in this case, the shape of the I–V characteristic remains almost the same.

In the bias range $V \leq V_{oc}$ (Fig. 1b), the current changes direction. As was noted in [9], this phenomenon is related to the presence of a positive charge on the Pd electrode, which gives rise to a current direction opposite to the current from an external source when the structure has a reverse bias (positive voltage at Pd). The adsorption of polar acetone molecules decreases the current magnitude and expands the bias range of the negative current. Illumination of the sample in acetone vapor results in the opposite effect: the I–V characteristic shifts to positive currents.
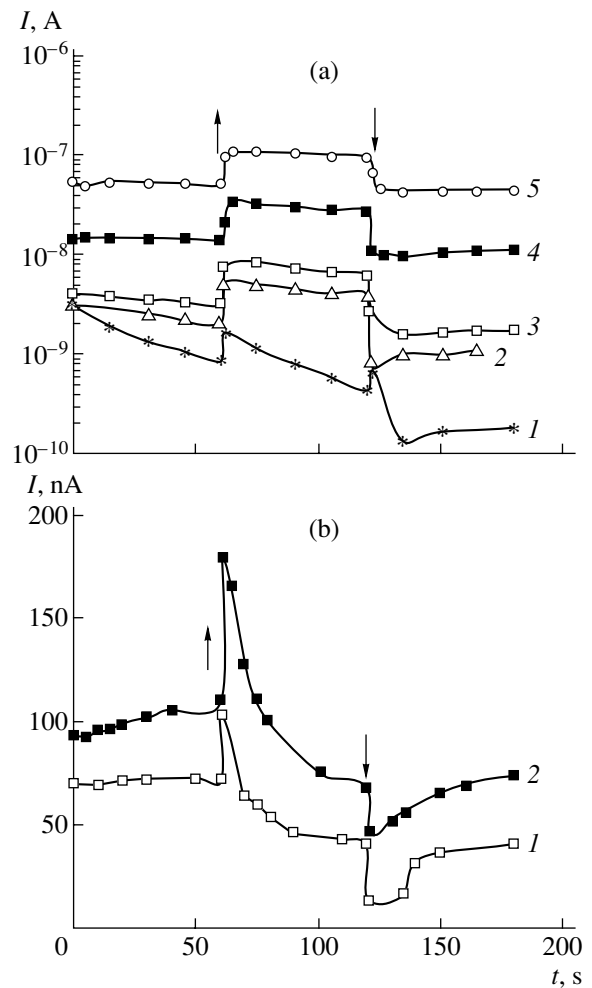
The characteristic current kinetics in a Schottky barrier structure at fixed biases is shown in Fig. 2a. Measurements were performed in two ranges: $V > V_{oc}$ and $V \leq V_{oc}$. At biases $V > V_{oc}$, dark current I_d and photocurrent I_{ph} decrease by 10–30% (curves *2*, *3*). The higher the bias, the more stable the current is. Illumination leads to an increase in the current by a factor of 2–7. At values of V close to V_{oc} (curve *1*), I_d and I_{ph} decrease over time and the current changes only when the illumination is switched on or switched off. At $V < V_{oc}$, the negative values of the current (Fig. 1b) remain, even when photoexcitation occurs.

In structures with space-charge-limited currents (Fig. 2b), in the entire range of forward and reverse biases under consideration (0.2–2.5 V), an increase in the current is observed only when a light pulse is switched on. The current increases for $t \leq 10$ s. Then,
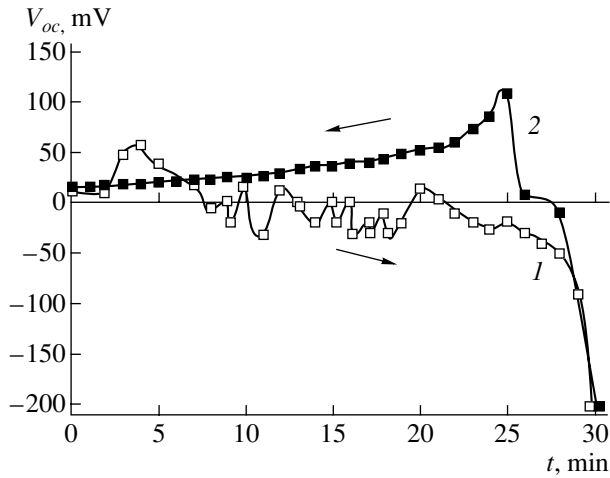
Fig. 3. Experimental time dependence of the open-circuit voltage in a Pd–(oxidized *por*-Si)–p^+-Si–Al structure (*1*) under continuous illumination and (*2*) in darkness after illumination.
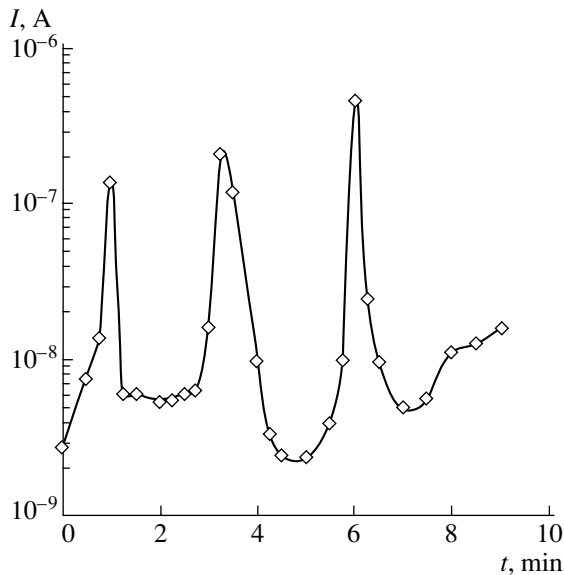

Fig. 4. Oscillations of current through a Pd–(oxidized *por*-Si)–Pd structure in the presence of a high content of hydrogen sulfide: $C_{H_2S} \approx 10^4$ ppm; $V_+ = 8$ V.

under illumination, I_{ph} decreases for 40 s until it reaches a constant value, which is smaller than the initial current I_d (Fig. 2b). This effect is similar to the phenomenon of negative photoconductivity, when the dark conductivity exceeds the photoconductivity.

Measurements of the open-circuit voltage in a Pd–(oxidized *por*-Si)–p^+-Si–Al structure subjected to long-term steady-state illumination (Fig. 3) revealed aperiodic oscillations of the magnitude and sign of V_{oc} during a gradual change from positive to negative charge on the Pd electrode. After switching off the illu-

mination, the built-in charge changes sign to become a positive charge of approximately the same value and V_{oc} monotonically returns to the initial value for ~30 min. Measurements of the open-circuit voltage after several days and even years showed a finite value of V_{oc}, which changes little for a specific sample stored in darkness but depends strongly on the adsorption of polar molecules [8, 9]. Thus, V_{oc} is not a residual photovoltage in the initial state.

As was noted in [9], in structures with oxidized *por*-Si layers, the current is unstable over time under the effect of adsorption of molecules. Further analysis revealed the occurrence of aperiodic current oscillations with the ratio $I_{max}/I_{min} \approx 10^2$ in a structure with two Pd–(oxidized *por*-Si) Schottky barriers formed at the same side and exposed to a nitrogen–hydrogen-sulfide mixture with a high content of hydrogen sulfide ($C \approx 10^4$ ppm) at reverse biases of 8–10 V (Fig. 4). The time taken for the current to rise and then drop again was ~15–30 s. Replacement of the gas mixture with nitrogen in the chamber containing the sample led to the recovery of the initial constant value of the current. In the case of one Pd–(oxidized *por*-Si) Schottky barrier, we also observed current instabilities at values of V close to the breakdown voltage and smaller oscillation amplitudes (~5–10%). It should be noted that, at low hydrogen sulfide contents ($C \approx 0.08$ ppm), the current is relatively stable and retains its value within 20–40% for 6 h of continuous operation. In [13], current self-oscillations in Pt–*por*-Si–$n(p)$-Si structures in an ether atmosphere at reverse biases in the range of negative differential conductivity were also observed.

Our study of the effect of illumination and adsorption of polar molecules on the electrical properties of structures with oxidized *por*-Si layers revealed the following features:

(i) structures with space-charge-limited currents in air show a decrease in photocurrent as compared with the dark current;

(ii) the period of photocurrent decay after switching off illumination is rather long (more than 30 s);

(iii) the open-circuit voltage oscillates and changes sign under the effect of long-term photoexcitation in air;

(iv) the current is unstable over time in a medium with a high content of hydrogen sulfide;

(v) the effect of acetone adsorption on the *I–V* characteristics of Schottky barrier structures in the range of biases lower than the initial value of V_{oc} manifests itself as an increase in the magnitude of the negative current and, accordingly, an increase in V_{oc};

(vi) illumination of structures in a gaseous medium containing acetone leads to a change in the sign of the current and a decrease in V_{oc}.

The nature of the positive charge observed near the metal–(oxidized *por*-Si) interface in darkness is unclear. At present, no one mechanism can be suggested to explain this phenomenon. It is difficult to

explain the existence of V_{oc} only in relation to the presence of a residual electrolyte and ionic conductivity. Several cycles of thermal heating of the samples in vacuum ($P \approx 10^{-5}$ Torr) at $T \approx 150°C$ barely changed the value of V_{oc}, although such treatment should affect the content of the residual electrolyte. In addition, the value of V_{oc} depends strongly on the electrode material [9]. Ablova *et al.* [11], who investigated the *I–V* characteristics of structures with thermally oxidized *por*-Si, suggest that the nonzero current observed at zero bias is related to the presence of shallow quantum wells in oxidized *por*-Si. The dependence of the open-circuit voltage V_{oc} in Au–*por*-Si–*n*-Si on humidity (50% and higher) and the absorption of various hydrogen-containing molecules was explained in [12] as the effect of dipoles formed by decomposition of the adsorbed molecules.

Obviously, the noted regular features of the photoconductivity and instabilities of the current and V_{oc} indicate the existence of deep multiply charged trapping centers of an acceptor and donor type near the Fermi level in oxidized *por*-Si, their charge exchange under the effect of photoexcitation and adsorption of polar molecules, and avalanche ionization of the carriers at deep levels. As was shown in [9], the concentration of traps N_t in these structures is about $(10^{17}–10^{18})$ cm^{-3} eV^{-1}, while the levels are spaced from the conduction band by 0.5–0.7 eV.

The oxidized *por*-Si structures under study contain a Pd–(oxidized *por*-Si) Schottky barrier and an isotype (oxidized *por*-Si)–p^+-Si heterojunction. The asymmetry of these junctions forms an internal field, which facilitates the accumulation of majority carriers (holes) at the Pd–(oxidized *por*-Si) interface. Under long-term exposure of a sample to light in the intrinsic-absorption region of *por*-Si, the relative change in the conductivity occurs mainly in the oxidized *por*-Si layer, since the substrate is heavily doped. The generated nonequilibrium electron–hole pairs drift in the internal field, and the holes are captured in the oxidized *por*-Si layer by acceptor-like traps. Since the concentration of traps N_t significantly exceeds that of the electron–hole pairs generated by illumination ($N_{ph} = 10^{13}–10^{14}$ cm^{-3}), in the course of time, the accumulated charge of excess electrons leads to a change in the sign of V_{oc} and an increase in its magnitude. When the light is switched off, the holes return from the traps to the valence band, the nonequilibrium electron–hole pairs recombine, and some electrons are captured by donor-like traps. The resulting open-circuit voltage V_{oc} changes sign and decreases in magnitude, gradually (for the time $\Delta t \approx 30$ min) returning to the initial state.

The oxidized *por*-Si layers form a nanocomposite medium containing segments of *c*-Si quantum wires and quantum dots in a SiO$_2$ matrix when the oxide thickness ranges from 0.1 to 10 nm. Along with the above-considered photogeneration in a structure with a thick oxide, charge carriers tunnel from the metal to the nanocrystallites and between the nanocrystallites through the oxide interlayers, whose thickness is suffi-

ciently small for free charge carriers to tunnel through. Under illumination, an excess charge is formed both at the oxide–nanocrystallite interface Δq_{ss} and in the space-charge layer Δq_s in a nanocrystallite, which changes the voltage across the oxide ΔV_i and the space-charge layer ΔV_{dl}. As a result, there is open-circuit voltage, similar to that observed in [14] in Schottky barrier solar cells with an oxide thickness of 10–20 Å:

$$V_{oc} = \Delta V_i + \Delta V_{dl}.$$

When the barrier permeability is estimated by the expression $\sqrt{\dfrac{m^*\chi_n}{\hbar^2}\delta^2}$, the open-circuit voltage has the form [14]

$$V_{oc} = \left(1 + \frac{\delta}{W}\frac{\varepsilon_s}{\varepsilon_i}\right)\frac{KT}{q}\ln\left[\frac{J_{sc}}{J_{n0}}\exp\left\{\sqrt{\frac{m^*\chi_n}{\hbar^2}\delta^2}\right\} + 1\right] + \frac{\delta}{\varepsilon_i}\Delta q_{ss}, \tag{1}$$

where δ is the oxide layer thickness; W is the width of the space-charge layer; ε_s and ε_i are the permittivities of the semiconductor and insulator, respectively; J_{sc} is the short-circuit current; χ_n is the height of the potential barrier for electrons at the semiconductor–oxide interface, $J_{n0} = qv_n n_0 \exp(-qV_D/KT)$; v_n is the thermal velocity of electrons; n_0 is the equilibrium electron concentration; and V_D is the voltage drop on the space-charge region in a nanocrystallite.

The excess charge Δq_s in a space-charge layer of thickness W is determined as

$$\Delta q_s = \frac{\varepsilon_s}{W}\frac{KT}{q}\ln\left[\frac{J_{sc}}{J_{n0}}\exp\left\{\sqrt{\frac{m^*\chi_n}{\hbar^2}\delta^2}\right\} + 1\right]. \tag{2}$$

The experimental values of V_{oc} and J_{sc} make it possible to estimate Δq_s and Δq_{ss} for the illuminated samples.

In order to solve this problem, a data processing program was developed that allowed us to determine changes in the built-in charges of the structure under study in the open-circuit mode using relation (1). The width of the space-charge layer W was assumed to be equal to the nanocrystallite size: 50–100 Å. In accordance with the data of [15, 16], the concentration of charge carriers in oxidized *por*-Si was taken to be $10^{11}–10^{13}$ cm^{-3}. The oxide thickness δ varied from 8 to 20 Å.

Under long-term illumination (30 min), the ranges of variation in V_{oc} and the short-circuit current were 14–370 mV and 1.3–14 nA, respectively. The calculated values of Δq_{ss} at the oxide thickness $\delta = 8$ Å ranged from 4.7×10^{-8} to 1.2×10^{-6} C/cm^2. In this case, the space charge in a nanocrystallite hardly changed and remained several orders of magnitude lower than the built-in charge at the interface.

4. CONCLUSIONS

The illumination of structures based on oxidized *por*-Si, as well as the adsorption of polar molecules, lead to a number of unusual changes in current transport. The observed instabilities of the current, photocurrent, and open-circuit voltage are related to the presence of multiply charged acceptor and donor traps in oxidized *por*-Si. The model of charge carrier tunneling allowed us to estimate the illumination-induced redistribution of excess charges in the oxide and segments of Si quantum wires. The observed dependence of V_{oc} on a large number of parameters, related to the both process conditions and external effects, calls for further investigation to reveal the nature of the open-circuit voltage V_{oc}.

A necessary condition for the application of oxidized *por*-Si in highly sensitive sensors in a wide range of gas concentrations is a solution to the problem of stabilizing the properties of oxidized *por*-Si structures.

REFERENCES

1. M. Ben-Chorin and A. Kux, Appl. Phys. Lett. **64A**, 481 (1994).
2. D. Stivenard and D. Deresmes, Appl. Phys. Lett. **67**, 1570 (1995).
3. S. V. Slobodchikov, Kh. M. Salikhov, and E. V. Russu, Fiz. Tekh. Poluprovodn. (St. Petersburg) **31**, 15 (1997) [Semiconductors **31**, 11 (1997)].
4. P. K. Kashkarov, E. A. Konstantinova, and V. Yu. Timoshenko, Fiz. Tekh. Poluprovodn. (St. Petersburg) **30**, 1479 (1996) [Semiconductors **30**, 778 (1996)].
5. S. V. Slobodchikov, D. N. Goryachev, Kh. M. Salikhov, and O. M. Sreseli, Fiz. Tekh. Poluprovodn. (St. Petersburg) **33**, 340 (1999) [Semiconductors **33**, 339 (1999)].
6. R. Angelucci, A. Poggi, L. Dori, *et al.*, Sens. Actuators A **74**, 95 (1999).
7. D. Bilenko, O. Belobrovaja, E. Jarkova, *et al.*, Sens. Actuators A **62**, 621 (1997).
8. D. Bilenko, O. Belobrovaja, E. Jarkova, *et al.*, Sens. Actuators A **79**, 147 (2000).
9. D. I. Bilenko, O. Ya. Belobrovaya, É. A. Zharkova, *et al.*, Fiz. Tekh. Poluprovodn. (St. Petersburg) **36**, 490 (2002) [Semiconductors **36**, 466 (2002)].
10. M. Ben-Chorin, F. Möller, and F. Koch, J. Appl. Phys. **77**, 4482 (1995).
11. M. S. Ablova, M. V. Zamoryanskaya, V. I. Sokolova, and R. I. Khasanov, Pis'ma Zh. Tekh. Fiz. **29** (11), 41 (2003) [Tech. Phys. Lett. **29**, 459 (2003)].
12. T. D. Dzhafarov, C. Oruc, and S. Aydin, J. Phys. D **37**, 404 (2004).
13. A. N. Laptev, A. V. Prokaznikov, and N. A. Rud', Pis'ma Zh. Tekh. Fiz. **26** (24), 47 (2000) [Tech. Phys. Lett. **26**, 1049 (2000)].
14. G. P. Srivastava and P. K. Bhatnagar, Solid-State Electron. **22**, 581 (1979).
15. D. I. Bilenko, N. P. Aban'shin, Yu. N. Galishnikova, *et al.*, Fiz. Tekh. Poluprovodn. (Leningrad) **18**, 2090 (1983) [Sov. Phys. Semicond. **18**, 1302 (1983)].
16. S. P. Zimin, Fiz. Tekh. Poluprovodn. (St. Petersburg) **34**, 359 (2000) [Semiconductors **34**, 353 (2000)].

Translated by Yu. Sin'kov

<div align="center">

LOW-DIMENSIONAL
SYSTEMS

</div>

Optical Transitions in a Quantized Cylindrical Layer in the Presence of a Homogeneous Electric Field

V. A. Arutyunyan*^, S. L. Arutyunyan*, G. O. Demirchyan*, and G. Sh. Petrosyan**

*Armenian State Engineering University, Gyumri Branch, Gyumri, 377503 Armenia
^e-mail: volhar@mail.ru
**Artsakhi State University, Stepanakert, 374430 Nagornyǐ Karabakh Republic
Submitted July 20, 2004; accepted for publication November 15, 2004

Abstract—Variations in the charge carrier energy spectrum in the presence of a transverse electric field in a cylindrical semiconductor layer are considered using the one-electron approximation. The explicit dependences of the Stark shift on an external field and on nanoradial sample dimensions are obtained. The absorption factors are calculated and the selection rules are obtained for both interband and intraband–intersubband optical transitions in the presence of an external electric field. © 2005 Pleiades Publishing, Inc.

1. INTRODUCTION

In recent times, in addition to numerous low-dimensional semiconductors, various quasi-one-dimensional structures in the form of axially symmetric nanocrystalline layers (called quantum tubes), cylindrical heterostructures with a nanoradial period, superlattices based on cylindrical quantum dots, etc., have also been intensively studied (see, for example, [1–6]). In this context, the study of the effect of static fields on the properties of a confined electronic subsystem in an isolated cylindrical layer is of interest. This interest is primarily related to the fact that this type of layer combines a number of physical features of both quantum wires and quantized films; due to the combination of their unique properties, such a layer can find applications both in its "pure form" and as a component of more complicated quantum confined structures, which are very promising materials with respect to the fabrication of new elements for modern optoelectronics.

In this study, we theoretically consider reconstruction of the energy spectrum of one-electron states in the presence of a homogeneous electric field in a cylindrical layer with quantum confinement and, accordingly, the optical transitions in this layer in the presence of the field.

2. ONE-ELECTRON STATES IN A LAYER

We represent the structure under study as a core–layer–medium composition and assume a strong confinement in the layer; i.e., we assume that the Coulomb binding energy of a 3D exciton in the layer is much smaller than the radial confinement energy,

$$L^2 \ll a_L^2. \tag{1}$$

Here, L is the layer thickness and a_L is the Bohr radius of a 3D exciton in the material of the layer. Furthermore, to ensure technical feasibility, we assume that the layer lies fairly far from the symmetry axis,

$$L^2 \ll R_1^2, R_2^2. \tag{2}$$

Here, R_1 and R_2 are the inner and outer radii of the layer.

We assume that the system is infinite in the direction of the symmetry axis Z, just as in the case of a "usual" quantum wire. When choosing the model potential in the (ρ, φ) plane, in addition to conditions (1) and (2), we also assume that the band gap of the layer material is small compared to that of the bulk material (medium) and that the band offset energy at the interface when materials that are in contact with each other have overlapping band gaps is much greater than the energies of quantized charge-carrier motion in the layer. In this respect, the CdS/HgS/CdS composition is typical (see Tables 1, 2).

Table 1. Characteristics of CdS and HgS crystals

Material	a_0, nm	ε_0	E_g, eV	$\dfrac{\mu_c}{m_0}$	$\dfrac{\mu_v}{m_0}$	U^c, eV	U^v, eV	ΔU^c, eV	ΔU^v, eV	a_{ex}, nm
CdS	0.5818	9.1	2.5	0.2	0.7	–3.8	–6.3	–	–	3
HgS	0.5851	18.2	0.5	0.036	0.044	–5	–5.5	1.2	–0.8	50

Table 2. Energy parameters for transverse carrier motion

R_1, nm	L, nm	$\dfrac{L^2}{a_{ex}^2}$	$\dfrac{L^2}{R_1^2}$	E_{conf}^c, meV	E_{conf}^v, meV	E_{rot}^c, meV	E_{rot}^v, meV	$\dfrac{E_c^{(0)}}{\Delta U^c}$	$\dfrac{E_v^{(0)}}{\Delta U^v}$
15	5	10^{-2}	1/9	42.4	34.7	4.7	3.9	0.04	0.048
30	10	4×10^{-2}	1/9	10.6	8.7	1.2	0.96	0.01	0.012

Then, by analogy with fullerene [7], a model of a quantum well rolled into a tube is physically quite adequate for the case under consideration:

$$U(\rho) = \begin{cases} 0 & \text{for } R_1 < \rho < R_2 \\ \infty & \text{for } \rho \le R_1; \quad \rho \ge R_2. \end{cases} \quad (3)$$

Within the framework of this model, using an approximation of isotropic effective mass μ, we obtain the following expression for the energy and envelope wave functions of nonperturbed transverse charge carrier motion in the layer:

$$E_{n,m}^{(0)} \cong \frac{\pi^2 \hbar^2 n^2}{2\mu L^2} + \frac{\hbar^2(4m^2 - 1)}{8\mu R_0^2}$$

$$\equiv E_1^{(0)} n^2 + \frac{\hbar^2(4m^2 - 1)}{8I} \equiv E_{conf}^{(0)} + E_{rot}^{(0)} \quad (4)$$

$$(n = 1, 2, 3, \ldots; \ m = 0, \pm 1, \pm 2, \ldots),$$

$$\Psi_{n,m}^{(0)}(\rho, \varphi) \cong \frac{\exp(im\varphi)}{\sqrt{2\pi}} \sqrt{\frac{2}{L\rho}} \sin\frac{\pi n}{L}(\rho - R_1)$$

$$\equiv \Phi_n^{(0)}(\rho) \frac{\exp(im\varphi)}{\sqrt{2\pi}}. \quad (5)$$

Here, the effective rotational radius R_0 is defined by

$$\frac{1}{R_0^2} = \frac{1}{2}\left(\frac{1}{R_1^2} + \frac{1}{R_2^2}\right). \quad (6)$$

3. THE EXTERNAL FIELD AS A PERTURBATION

If an external homogeneous field is directed along the X axis, $\mathbf{F} = \mathbf{F}(F, 0, 0)$, then the electrostatic energy of a particle confined in the layer is given by [8]

$$w(\boldsymbol{\rho}) = q\left(B\rho + \frac{C}{\rho}\right)\cos\varphi, \quad (R_1 \le \rho \le R_2), \quad (7)$$

where q is the particle charge. Generally, when the permittivities of the core (ε_1), layer (ε_2), and medium (ε_3) are different, we may use the boundary conditions for the potential and its derivatives and find the constants B and C:

$$B = FR_2^2$$

$$\times \frac{2(\varepsilon_{2,1} + 1)}{(\varepsilon_{2,3} + 1)(\varepsilon_{2,1} + 1)R_2^2 - (\varepsilon_{2,3} - 1)(\varepsilon_{2,1} - 1)R_1^2} \equiv FB_0, \quad (8)$$

$$C = FR_2^2$$

$$\times \frac{2(\varepsilon_{2,1} - 1)R_1^2}{(\varepsilon_{2,3} + 1)(\varepsilon_{2,1} + 1)R_2^2 - (\varepsilon_{2,3} - 1)(\varepsilon_{2,1} - 1)R_1^2} \equiv FC_0. \quad (9)$$

Here, $\varepsilon_{2,3} = \dfrac{\varepsilon_2}{\varepsilon_3}$, $\varepsilon_{2,1} = \dfrac{\varepsilon_2}{\varepsilon_1}$.

From the most general arguments, it is clear that the external field can be considered as a perturbation if the energy $\Delta E(F)$ transferred by the field to the particles is much smaller than the distance between the neighboring levels of energy substructure (4):

$$\Delta E(F) \ll \Delta E_{n,m}^{(0)}. \quad (10)$$

As can clearly be seen, the diagonal elements of operator (7) that are formed from wave functions (5) vanish; i.e., there is no linear Stark effect in the system under study. Since (with respect to the azimuthal number m) only the matrix elements $V_{m, m \pm 1} = \dfrac{1}{2}$ are nonzero, a second-order correction to the energy of any state $|n, m\rangle$ can generally be written as

$$\Delta E_{n,m}^{(2)} = \frac{|V_{n,n}|^2}{4}\left\{\frac{1}{E_{n,m}^{(0)} - E_{n,m-1}^{(0)}} + \frac{1}{E_{n,m}^{(0)} - E_{n,m+1}^{(0)}}\right\}$$

$$+ \frac{1}{4}\sum_{n \ne n'} |V_{n,n'}|^2\left\{\frac{1}{E_{n,m}^{(0)} - E_{n',m-1}^{(0)}} + \frac{1}{E_{n,m}^{(0)} - E_{n',m+1}^{(0)}}\right\}, \quad (11)$$

where the matrix elements $V_{n, n'}$ constructed using radial functions (5) and taking into account conditions (1) and (2) are given by

$$V_{n,n} \cong qFR_0\left(B_0 + \frac{C_0}{R_0^2}\right), \quad (n = n'), \quad (12)$$

$$V_{n,n'} \cong \frac{8qFL}{\pi^2}\frac{nn'}{(n^2 - n'^2)^2}\left(\frac{C_0}{R_0^2} - B_0\right), \quad (n \ne n'). \quad (13)$$

The specific character of spectrum (4) requires special analysis of the effect of the field on the levels of states with $m \neq 0$ and $m = 0$.

1. $m \neq 0$. In this case, general condition (10) is reduced to the condition

$$\Delta E(F) \ll \Delta E_{rot}^{(0)} \approx E_{rot}^{(0)}; \tag{14}$$

as a result, the correction to energy (11) is rewritten as

$$\Delta E_{n,m}^{(2)}(FR_0, \mu) \cong \frac{\mu R_0^2 (qFR_0)^2}{\hbar^2 (4m^2 - 1)}\left(B_0 + \frac{C_0}{R_0^2}\right)^2$$
$$\equiv \frac{I(qFd)^2}{\hbar^2 (4m^2 - 1)} \quad \text{for } |m| \neq 1, \tag{15}$$

$$\Delta E_{n,m}^{(2)}(FR_0, \mu) \cong \frac{5\mu R_0^2 (qFR_0)^2}{6\hbar^2}\left(B_0 + \frac{C_0}{R_0^2}\right)^2$$
$$\equiv \frac{5I(qFd)^2}{6\hbar^2} \quad \text{for } m = +1, \tag{16}$$

$$\Delta E_{n,m}^{(2)}(FR_0, \mu) \cong -\frac{\mu R_0^2 (qFR_0)^2}{6\hbar^2}\left(B_0 + \frac{C_0}{R_0^2}\right)^2$$
$$\equiv -\frac{I(qFd)^2}{6\hbar^2} \quad \text{for } m = -1. \tag{17}$$

2. $m = 0$. In this case, the radial motion is perturbed and inequality (10) is reduced to the condition

$$\Delta E(F) \ll \Delta E_{conft}^{(0)} \approx E_{conf}^{(0)}. \tag{18}$$

For the energy correction, we now obtain

$$\Delta E_{n,0}^{(2)}(FL, \mu) \cong \frac{(qFL)^2}{48n^2 E_n^{(0)}}\left[B_0 - \frac{C_0}{R_0^2}\right]^2 f_n, \tag{19}$$

where

$$E_n^{(0)} = \frac{\pi^2 \hbar^2 n^2}{2\mu L^2} \equiv E_{conf}^{(0)}, \quad f_n = \frac{1}{2}\left(1 - \frac{15}{\pi^2 n^2}\right).$$

For the perturbed part of the wave function at $m \neq 0$ and $m = 0$, we have

$$\Psi_{n,m}^{(1)}(\rho, \varphi) \cong \Phi_n^{(0)}(\rho)\frac{I}{4\hbar^2}\frac{V_{n,n}}{\sqrt{2\pi}}$$
$$\times \exp(im\varphi)\left\{\frac{\exp(-i\varphi)}{2m-1} - \frac{\exp(i\varphi)}{2m+1}\right\} \tag{20}$$

and

$$\Psi_{n,0}(\rho, \varphi) \cong \frac{1}{\sqrt{2\pi}}\frac{\cos\varphi}{E_1^{(0)}}\sum_{n \neq n'}\frac{V_{n,n'}\Phi_{n'}^{(0)}(\rho)}{n^2 - n'^2}$$
$$\left(E_1^{(0)} = \frac{\pi^2 \hbar^2}{2\mu L^2}\right), \tag{21}$$

respectively.

4. OPTICAL TRANSITIONS IN THE PRESENCE OF AN ELECTRIC FIELD

For the perturbation $\hat{U}$ related to the optical wave, we have

$$\hat{U} = \frac{|e|}{m_0 c}(\hat{\mathbf{A}}, \hat{\mathbf{P}}), \tag{22}$$

where e is the elementary charge, c is the speed of light in free space, $\hat{\mathbf{A}}$ is the vector potential of a weak wave, and $\hat{\mathbf{P}}$ is a three-dimensional momentum operator. Furthermore, to be specific, we assume that an incident wave of frequency ω is linearly polarized along the X axis.

4.1. Interband Transitions

Generally, we can write the matrix element for transitions from the valence band (v) to the conduction band (c) in the form

$$M_{c,v} = U_{c,v}\int[\Psi_c^{(0)}(\boldsymbol{\rho}) + \Psi_c^{(1)}(\boldsymbol{\rho})]^*$$
$$\times[\Psi_v^{(0)}(\boldsymbol{\rho}) + \Psi_v^{(1)}(\boldsymbol{\rho})]d\boldsymbol{\rho}, \tag{23}$$

where $U_{c,v}$ is the matrix element of operator (22) constructed from Bloch amplitudes of the v and c bands. After simple calculations we obtain the following expression for $M_{c,v}$ at $m \neq 0$:

$$M_{c,v} \cong U_{c,v}\left\{\delta_{n_c,n_v}\delta_{m_c,m_v}\right.$$
$$\left. + \frac{V_{n,n}(I_v - I_c)}{\hbar^2}\delta_{n_c,n_v}\frac{\delta_{m_c,m_v \pm 1}}{2m_v \pm 1}\right\} \equiv M_{c,v}^{(0)} + M_1^{(1)}. \tag{24}$$

Here, $I_v = m_v R_0^2$, $I_c = m_c R_0^2$, and $\delta_{i,k}$ is the Kronecker delta.

It is clear from (24) that, when calculating the absorption coefficient, there are no "interference" terms in the expression $|M_{c,v}|^2 = |M_{c,v}^{(0)} + M_{c,v}^{(1)}|^2$ and the interband absorption coefficient may also be represented as the sum

$$\alpha(\omega) = \alpha^{(0)}(\omega) + \alpha^{(1)}(\omega). \tag{25}$$

For the threshold frequencies of each of the transitions in (24) and (25), we have, respectively,

a) the transitions $n_c = n_v \equiv n$ and $m_c = m_v \equiv m$;

$$\hbar\omega_{n,m} = E_g + \frac{\pi^2\hbar^2 n^2}{2\mu_{c,v}L^2} + \frac{\hbar^2(4m^2 - 1)}{8\mu_{c,v}R_0^2} \qquad (26)$$

$$+ \Delta E_{n,m}^{(2)}(FR_0, \mu_v) + \Delta E_{n,m}^{(2)}(FR_0, \mu_c) \equiv \Delta_{n,m}^g,$$

where $\mu_{c,v}^{-1} = \mu_c^{-1} + \mu_v^{-1}$;

b) the transitions $n_c = n_v \equiv n$ and $m_c = m_v \pm 1$ ($m_v \equiv m$);

$$\hbar\omega_{n,m\pm 1} = E_g + \frac{\pi^2\hbar^2 n^2}{2\mu_{c,v}L^2}$$

$$+ \frac{\hbar^2(4m^2 - 1)}{8\mu_v R_0^2} + \frac{\hbar^2(4(m+1)^2 - 1)}{8\mu_c R_0^2} \qquad (27)$$

$$+ \Delta E_{n,m}^{(2)}(FR_0, \mu_v) + \Delta E_{n,m\pm 1}^{(2)}(FR_0, \mu_c) \equiv \Delta_{n,m\pm 1}^g.$$

Now, using the standard relation between $M_{c,v}$ and $\alpha(\omega)$ for structures with one degree of freedom (see, for example, [9]), we obtain, for the interband absorption band at $m \neq 0$,

$$\alpha^{(0)}(\omega) \approx \sum_{n,m}|U_{c,v}|^2(\hbar\omega - \Delta_{n,m}^g)^{-\frac{1}{2}}\Theta(\hbar\omega - \Delta_{n,m}^g), \quad (28)$$

$$\alpha^{(1)}(\omega) \approx \sum_{n,m}|U_{c,v}|^2\frac{|V_{n,n}(I_v - I_c)|^2}{\hbar^4(2m\pm 1)^2}$$

$$\times (\hbar\omega - \Delta_{n,m\pm 1}^g)^{-\frac{1}{2}}\Theta(\hbar\omega - \Delta_{n,m\pm 1}^g), \qquad (29)$$

where $\Theta(x)$ is the step function.

In the case $m = 0$, for corresponding quantities, we obtain

$$M_{c,v} = U_{c,v}\delta_{n_c,n_v}, \qquad (30)$$

$$\hbar\omega_{c,v} = E_g + \frac{\pi^2\hbar^2 n^2}{2\mu_{c,v}L^2} - \frac{\hbar^2}{8\mu_{c,v}R_0^2} \qquad (31)$$

$$+ \Delta E_{n,0}^{(2)}(FL, \mu_v) + \Delta E_{n,0}^{(2)}(FL, \mu_c) \equiv \Delta_{c,v}^g,$$

$$\alpha^{(0)}(\omega) \approx \sum_n |U_{c,v}|^2(\hbar\omega - \Delta_{c,v}^g)^{-\frac{1}{2}}\Theta(\hbar\omega - \Delta_{c,v}^g). \quad (32)$$

4.2. Intraband and Intersubband Transitions

For the transitions between discrete levels $|n_i, m_i\rangle \longrightarrow |n_f, m_f\rangle$ in the same band with $m \neq 0$, we obtain the following selection rules with respect to the azimuthal number:

a) $\Delta m = \pm 1$ for a zeroth-order matrix element;

b) $\Delta m = 0$ for a first-order matrix element.

Calculations of the matrix elements and the corresponding threshold frequencies now yield the following results:

a) the transitions $m_f = m_i \pm 1$ and $n_f = n_i$ ($m_i \equiv m$);

$$M_{f,i}^{(0)} \cong i\hbar\frac{|e|A_0}{4m_0 cL}(2m \pm 1)\ln\frac{R_2}{R_1}, \qquad (33)$$

$$\hbar\omega_1^0 = \hbar^2\frac{(1 \pm 2m)}{2\mu R_0^2} + \Delta E_{n,m\pm 1}^{(2)}(FR_0, \mu)$$

$$- \Delta E_{n,m}^{(2)}(FR_0, \mu); \qquad (34)$$

b) the transitions $m_f = m_i \pm 1$ and $n_f \neq n_i$ ($m_i \equiv m$);

$$M_{f,i}^{(0)} \cong i\hbar\frac{|e|A_0}{m_0 cL}\frac{n_i n_f}{n_f^2 - n_i^2} \text{ for odd-numbered } n_f \pm n_i,$$

$$M_{f,i}^{(0)} \equiv 0 \text{ for even-numbered } n_f \pm n_i, \qquad (35)$$

$$\hbar\omega_2^0 = \frac{\pi^2\hbar^2}{2\mu L^2}(n_f^2 - n_i^2) + \frac{\hbar^2(1 \pm 2m)}{2\mu R_0^2}$$

$$+ \Delta E_{n_f,m\pm 1}^{(2)}(FR_0, \mu) - \Delta E_{n_i,m}^{(2)}(FR_0, \mu); \qquad (36)$$

c) the transitions $\Delta m = 0$ with odd-numbered $n_f \pm n_i$,

$$M_{f,i}^{(1)} \cong i\hbar\frac{|e|A_0}{m_0 cL}\frac{V_{n,n}}{\hbar^2}\frac{n_f n_i}{n_f^2 - n_i^2}\frac{I}{4m^2 - 1}, \qquad (37)$$

$$\hbar\omega_1^1 = \frac{\pi^2\hbar^2}{2\mu L^2}(n_f^2 - n_i^2). \qquad (38)$$

For the transitions $\Delta m = 0$ with $n_f = n_i$ and even-numbered $n_f \pm n_i$, the matrix element $M_{f,i}$ vanishes.

For the matrix element and the threshold frequency of intraband transitions at $m = 0$, we obtain

$$M_{f,i} \cong i\hbar\frac{|e|A_0}{m_0 cL}\frac{qFL}{\pi^2 E_1^{(0)}}\left(B_0 - \frac{C_0}{R_0^2}\right)\frac{n_f^2 + n_i^2}{n_f^2 - n_i^2}\frac{1}{n_f n_i} \qquad (39)$$

and

$$\hbar\omega_{f,i} = \frac{\pi^2\hbar^2}{2\mu L^2}(n_f^2 - n_i^2) + \Delta E_{n_f,0}^{(2)}(FL, \mu)$$

$$- \Delta E_{n_i,0}^{(2)}(FL, \mu), \qquad (40)$$

respectively.

To avoid unnecessary complications, we do not explicitly write the intraband absorption coefficient, since expressions (32)–(40) provide a complete representation of these transitions.

5. DISCUSSION

Now, we apply the above model approach to a CdS/HgS/CdS structure. Table 1 gives the physical characteristics of β modifications to CdS and HgS

direct-gap semiconductor crystals (the data are taken from [6, 10, 11]) and Table 2 gives the energy parameters for charge-carrier transverse motion. We use the following notation: m_0 is the free-electron mass; E_g is the band gap of a bulk semiconductor composed of the layer material; U^c and U^v are the band energies measured from a vacuum level for the c and v bands, respectively; a_0 is the lattice constant; a_{ex} is the Bohr radius of a bulk exciton; and ε_0 is the static permittivity.

By comparing the data in Tables 1 and 2, we can readily see that, for the structure under consideration, conditions (1) and (2) are satisfied and, in all cases, for the given composition but for not highly excited states, the approximations of our model are indeed satisfied with sufficient accuracy.

Since the radial and rotational motions are separated, they are each "separately" perturbed by an external field. Furthermore, for $m \neq 0$, level splitting is observed in the $2m$th order of perturbation theory; therefore, the level with $|m| = 1$ is split into two sublevels (16) and (17) and the levels with $|m| > 1$ are simply displaced by the field and retain their double degeneracy in m.

Using the characteristic system dimensions from Tables 1 and 2, for $\varepsilon_{1,2} = \varepsilon_{2,3} = 2$, we obtain the following estimates for the external field when it is considered as a perturbation.

If the layer thickness varies in the range $L = 5$–10 nm and the inner radius varies in the range $R_1 = 15$–30 nm, an external field in the range $F = 10$–10^2 V/cm may, to a high accuracy, be considered as a perturbation if the rotational motion is perturbed (condition (14)).

For the same dimensions of the system, the perturbation of the radial motion (condition (18)) can be considered as weak in the following range of external field intensities:

$$F = 10^2\text{–}10^3 \text{ V/cm}.$$

In Tables 3 and 4, the corresponding Stark shifts determined from (15)–(17) and (19) are listed.

With regard to the dependence of the shift on the number of an energy level, it can clearly be seen from expressions (15)–(17) and (19) that the correction $\Delta E_{n,m}^{(2)}$ decreases very rapidly as both the azimuthal and the radial quantum numbers rise; thus, only the lowest states are of real physical interest. In the limit $\dfrac{L}{R_1} \longrightarrow 0$, using the example of the ground state, we can easily see that the correction to the energy of radial motion $\Delta E_{1,0}^{(2)}(FL, \mu)$ (see (19)) transforms into an expression similar to that describing the Stark effect for a "conventional" film with quantum confinement [12]:

$$\Delta E_{1,0}^{(2)}(FL, \mu) \cong \frac{(qFL)^2}{96 E_1^{(0)}}\left(1 - \frac{15}{\pi^2}\right).$$

Table 3. Stark shift of the rotational-motion energy

L, nm	R_1, nm	F, V/cm	$\Delta E_{n,m}^{(2)}$, meV $m = 2$	$\Delta E_{n,m}^{(2)}$, meV $m = +1$	$\Delta E_{n,m}^{(2)}$, meV $m = -1$
5	15	5×10^2	0.8×10^{-2}	10.4×10^{-2}	2.08×10^{-2}
10	30	5×10	0.13×10^{-2}	1.7×10^{-2}	0.28×10^{-2}

Table 4. Stark shift of the energy of radial motion

L, nm	R_1, nm	F, V/cm	$\Delta E_{n,m}^{(2)}$, meV $n = 1, m = 0$
5	15	1.2×10^3	43.2×10^{-2}
10	30	1.4×10^2	9.7×10^{-2}

For interband transitions, the absorption band consists of two nonoverlapping series: a basic one, provided by (28), and a field "satellite," as in (29); the latter is modulated by a field factor that decreases as the azimuthal quantum number m rises. For $m = 0$, transitions (30) have a purely "film" character [12], and the presence of a field does not affect absorption. However, for each of series (28), (29), and (32), the presence of a field results in an effective change in the band gap $\Delta_{i,k}^g$, which is determined by the external field and the geometrical dimensions of the sample, namely, by the effective rotational radius for $m \neq 0$ and the layer thickness for $m = 0$. The same quantities also determine the threshold frequencies for intraband transitions (33)–(40).

We note that, for intraband transitions that are diagonal with respect to the radial number, an external field produces a relative shift of the frequencies of absorption and emission by $\hbar\Delta\omega = \Delta E_{n,m+1}^{(2)}(FR_0, \mu) + \Delta E_{n,m-1}^{(2)}(FR_0, \mu)$, whereas, in the absence of the field, the resulting absorption should be observed at the frequencies $\omega_m = \dfrac{\hbar m}{2\mu R_0^2}$. Furthermore, for both interband and intraband transitions, the presence of a field results in the explicit dependence of the absorption on the charge-carrier effective mass for each of the bands.

In summary, we conclude that the results of this study make it possible to change the optical energy characteristics of the layer by varying the external field and the sample dimensions in a controlled way; furthermore, the explicit dependence of the absorption parameters on the carrier effective mass can be used to experimentally determine the "optical" effective mass.

ACKNOWLEDGMENTS

REFERENCES

1. S. Ijima, Nature **354**, 56 (1991).

2. T. W. Ebessen, H. J. Lezec, H. Hiura, *et al.*, Nature **382**, 54 (1996).

3. S. Roche, F. Triozon, A. Rubio, and D. Mayou, Phys. Rev. B **64**, R121401 (2001).

4. N. Tkach, J. Phys. Stud. **3**, 377 (2001).

5. N. V. Tkach and V. A. Golovatskiǐ, Fiz. Tverd. Tela (St. Petersburg) **43**, 350 (2001) [Phys. Solid State **43**, 365 (2001)].

6. N. V. Tkach, A. M. Makhanets, and G. G. Zegrya, Fiz. Tekh. Poluprovodn. (St. Petersburg) **36**, 543 (2002) [Semiconductors **36**, 511 (2002)].

7. V. V. Rotkin and R. A. Suris, Mol. Mater. **5**, 87 (1994).

8. W. R. Smythe, *Static and Dynamic Electricity*, 2nd ed. (McGraw-Hill, New York, 1950; Inostrannaya Literatura, Moscow, 1954).

9. V. V. Mitin, V. A. Kochelap, and M. A. Stroscio, *Quantum Heterostructures, Microelectronics, and Optoelectronics* (Cambridge Univ. Press, Cambridge, 1999).

10. A. Mews, A. V. Kadavanich, U. Banin, and A. P. Alivisatos, Phys. Rev. B **53**, 13 242 (1996).

11. *Tables of Physical Quantities: A Reference Book*, Ed. by I. K. Kikoin (Nauka, Moscow, 1976) [in Russian].

12. D. A. B. Miller, S. Schmitt-Rink, and D. S. Chemia, Adv. Phys. **38**, 89 (1989).

Translated by I. Zvyagin

Nonohmic Quasi-2D Hopping Conductance and the Kinetics of Its Relaxation

B. A. Aronzon*^, D. Yu. Kovalev*, and V. V. Ryl'kov**

*Russian Scientific Center, Kurchatov Institute, Moscow, 123182 Russia

^e-mail: aronzon@imp.kiae.ru

**Institute for Radio Engineering and Electronics, Russian Academy of Sciences, Fryazino, Moscow oblast, 141120 Russia

Submitted November 9, 2004; accepted for publication November 25, 2004

Abstract—The nonohmic properties of a quasi-2D hopping-conductance channel are studied. The channel is formed in a p-Si layer by a field effect in the region where the Fermi level crosses the impurity band. It is shown that the dependence of conductance σ on a longitudinal electric field E has a threshold character and obeys the law $\ln\sigma(E) \propto E^{1/2}$. The dependences of the conductance of the quasi-2D channel on temperature and the electric field are satisfactorily explained using the concepts of nonlinear screening and of nonohmic properties of disordered systems with a random Coulomb potential. This mechanism of nonlinearity is confirmed by specific features of the mesoscopic fluctuations in the off-diagonal component of resistance, which reflect the reconstruction of a percolation cluster under the action of the longitudinal electric field. A long-term relaxation in conductance is observed during transition from a nonohmic to ohmic mode, which indicates that the system exhibits properties corresponding to electronic glass and that the current paths are significantly modified in a strong electric field. © 2005 Pleiades Publishing, Inc.

1. INTRODUCTION

Nonohmic hopping conductivity via states in the vicinity of the Fermi level has previously been studied in amorphous semiconductors, in which the conductivity σ frequently increases as the electric field E increases according to the law (see [1] and the references therein)

$$\sigma(E) = \sigma(0)\exp\left(\frac{CeEr_h}{kT}\right), \qquad (1)$$

where e is the elementary charge, r_h is the average hopping length, and C is a numerical coefficient. However, it is worth noting that, for these conditions, the existing theoretical models predict not only law (1) but also another type of $\sigma(E)$ dependence:

$$\ln\sigma(E) \propto E^2 \quad \text{or} \quad \ln\sigma(E) \propto E^{1/2}.$$

Numerical simulation also describes the experimental situation only qualitatively, which can be accounted for by the complex and diverse nature of localized states in amorphous materials (defects, composition fluctuations, impurities, etc.) and by the insufficient information available on the density of their distribution in the band gap of a semiconductor [1].

Nonohmic hopping conductance via states in the vicinity of the Fermi level can also be observed in thin films of a doped semiconductor under the conditions of a field effect [2]. In this case, the position of the Fermi level near the surface of the semiconductor relative to the impurity band can be controlled by a voltage V_g applied to a gate electrode, separated from the semiconductor by an insulating layer, under variation of the filling of the impurity band by charge carriers (Fig. 1). It is particularly remarkable that, starting from some $V_g > V_t$, a quasi-two-dimensional (quasi-2D) hopping-conductance channel is formed in the region where the Fermi level crosses the impurity band. In this case conduction occurs via the band of states near the Fermi level (Fig. 1, region II), in which the number of empty and occupied states is approximately the same. In contrast, filled or empty states dominate in regions situated nearer to the interface (Fig. 1, region I) or farther from it (Fig. 1, region III), resulting in the conductance in these regions being virtually zero. At gate voltages $V_g > V_t \approx 2$ V, when the quasi-2D hopping-conductance channel has already formed, the conductance in this channel is virtually independent of the gate voltage, since, under uniform doping, the effect of V_g is limited to a shift of the channel into the semiconductor bulk whereas the density of states and the relative amounts of filled and empty states remain unchanged. The stability of $\sigma(V_g)$ at $V_g > 2$ V is demonstrated in the inset in Fig. 1. It has also been shown [3] that a significant contribution to the formation of the channel in question is made by fluctuations in the Coulomb potential of ionized impurities in the surface region of the semiconductor, where the impurity band is completely filled and does not contribute to conductance (Fig. 1, region I). In this case, the scatter of states over energy is defined by a well-known mechanism, namely, the Coulomb fluctuation potential. It is noteworthy that the hopping conductivity in the band of states near the Fermi level has only been theoretically studied [4] in the context of the
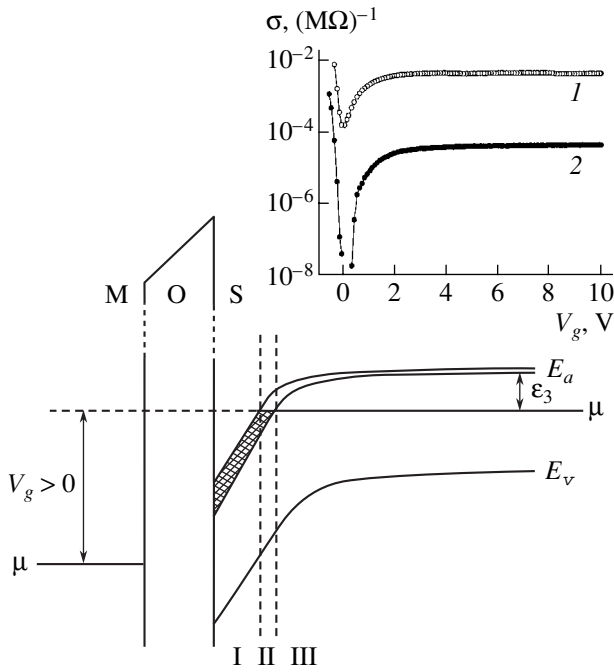
Fig. 1. Band diagram of a MOSFET structure based on weakly compensated doped *p*-Si. (I) a region of negatively charged acceptors; (II) an intermediate region where the quasi-2D hopping-conductivity channel in the impurity band is formed; and (III) the region of the impurity band, which is almost completely filled by holes and empty for electrons. E_a, μ, and E_v are the energy positions of the acceptor levels, Fermi level, and valence band edge, respectively; ε_3 is the activation energy for impurity conductivity in the electrically neutral region. Inset: the conductance of the structure as a function of the gate voltage at the temperatures (*1*) 10 and (*2*) 4.2 K.

known problem of existence of a constant activation energy ε_3 when the hopping energy, $|\varepsilon_i - \varepsilon_j|$, is close to $|\mu - \varepsilon_{j,\,i}|$, which is the energy spacing between the Fermi energy μ and the energies of localized states.[1] Calculations [4] have shown that, in this case, the temperature dependence of conductivity is governed by a variable-range hopping mechanism at temperatures below some T_c. However, the activation energy is constant at $T \gtrsim 2T_c$ and is related to the energy scatter of states by a simple expression [4]:

$$\varepsilon_3 = \frac{5}{6}\Delta\varepsilon, \qquad (2)$$

$$T_c = 0.29\Delta\varepsilon(N^{1/3}r_B)/k. \qquad (3)$$

Here, $\Delta\varepsilon$ is the half-width of the impurity band, N is the number of states in the unit volume, and r_B is the Bohr radius of these states.

---

[1] In doped semiconductors, usually, $|\mu - \varepsilon_{j,\,i}| \gg |\varepsilon_i - \varepsilon_j|$ and the activation energy coincides with the Fermi level position with respect to the density-of-states peak [4].

In this study, we present the results of our investigation into nonohmic hopping conductance in the band of states in the vicinity of the Fermi level using weakly compensated doped Si:B layers as an example. It is shown that, in this case, the dependence of conductance on a longitudinal electric field has a threshold character and, starting from a certain value of the field, obeys a law similar to the Frenkel–Poole law: $\ln\sigma(E) \propto E^{1/2}/kT$ (in contrast to amorphous semiconductors, where $\ln\sigma(E) \propto E/kT$).

It is found also that, under the effect of a sharp decrease in the field, a long-term relaxation of conductance can be observed in the kinetics of the transition from a nonohmic to ohmic mode. This behavior is typical of glass systems.

First, we discuss the temperature behavior of the conductance in the structures under study and show that it indeed demonstrates all the specific features of hopping conductivity in the band of states near the Fermi level [4] formed by Coulomb potential fluctuations. It is necessary to note that the transport properties of these structures have previously been studied only at relatively high temperatures $T > 7$ K [2, 3, 5].

2. SAMPLES AND TEMPERATURE DEPENDENCE OF CONDUCTANCE IN WEAK FIELDS

Under study were thin (0.5 μm) *p*-Si layers with a boron concentration $N_a = 10^{18}$ cm^{-3} and two p^+ contacts. The layers were formed by ion implantation of boron on a (100) *n*-Si substrate with $N_d = 10^{15}$ cm^{-3}. A degenerate poly-Si gate contact of 100×100 μm in area was insulated from *p*-Si by a thermal oxide of 62 nm in thickness.

The conductance of the *p*-Si layers in a weak longitudinal electric field (~10 V/cm) was measured as a function of the gate voltage V_g in the temperature range 4.2–20 K (study of the Hall effect has shown that, at $T > 20$ K, free holes make a significant contribution to conductivity [5]). The inset in Fig. 1 shows typical $\sigma(V_g)$ dependences at different temperatures. These dependences demonstrate the formation, under the effect of the gate voltage V_g (the field effect), of a surface accumulation layer at $V_g < V_{min}$. In the depletion mode, at $V_{min} < V_g < V_{in}$, a quasi-2D channel of hopping transport via the boron impurities is formed [2]. Here, V_{min} is the flat-band voltage corresponding to the minimum $\sigma(V_g) = \sigma_{min}$ and, thereby, to the contribution of the bulk conductance in a *p*-Si layer and V_{in} is the inversion voltage, which is about 10 V in our case. It is necessary to note that an estimate in the Schottky approximation shows that, close to inversion, the depletion layer thickness is 0.04 μm, which is far less than the thickness of a *p*-Si layer (0.5 μm).

As can be seen in the inset in Fig. 1, the surface hopping conductance first increases, and then, at $V_g > V_t \approx$

2 V, remains almost constant right up to the inversion voltage. In other words, in our samples, the hopping transport channel is formed at $V_g \approx 2$ V. The channel conductance σ_c can be determined by subtracting, from the total conductance, $\sigma(V_g)$ of the structure in the region of the plateau of the bulk conductance of a p-Si layer, i.e., σ_{min}: $\sigma_c = [\sigma(V_g) - \sigma_{min}]$, where $V_g \gtrsim 2$ V [2, 3]. Figure 2 shows the temperature dependence of the quasi-2D hopping conductance $\sigma_c(T)$ obtained using this method. For comparison, Fig. 2 also shows the temperature dependence of the structure conductance at the minimum $\sigma_{min}(T)$, that is, in the flat-band mode. An activation dependence of the conductance $\sigma_{min}(T)$ is observed with the activation energy $\varepsilon_3^f = 8.1$ meV, which coincides with the activation energy ε_3 of the hopping conductivity in the p-Si bulk at the same doping level [6]. In addition, a range of constant activation energy can be seen in the $\sigma_c(1/T)$ plot at relatively high temperatures, but its value, $\sigma_3^c = 3.9$ meV, is significantly (about twice) less than ε_3^f. At $T \lesssim 6$ K, the dependence $\sigma_c(1/T)$ starts to level-off, which indicates a transition to a variable-range hopping mode. Now, we can estimate the temperature T_c of the transition to variable-range hopping conductance using Eqs. (2) and (3) and the experimental value $\varepsilon_3 = \varepsilon_3^c = 3.9$ meV. Taking into account that the localization length of light holes at boron atoms in Si is $r_B = 23$ Å [6], we obtain $T_c = 3.5$ K. According to [4], the transition to conductance with a constant activation energy must occur at $T \geq 2T_c$, that is, at $T \geq 7$ K in our case, which agrees well with the experimental data.

We now discuss the specifics of the energy broadening of the impurity band. As was mentioned above, this broadening is caused by a fluctuation potential induced by ionized boron atoms in the surface region of the semiconductor, where the impurity band is completely filled (Fig. 1) [3]. Assuming that the random potential is screened only by free carriers in the bulk, with a density equal to the concentration of compensating donors ($N_d = 10^{15}$ cm^{-3}), its amplitude, when calculated in terms of the theory of nonlinear screening [4], should be $V_0 \approx 100$ meV. However, the experiment indicates that the amplitude $V_0 \approx 2\varepsilon_3^c$ must be 8 meV. This contradiction is eliminated under the following natural assumption. Near the boundary of region I, which separates the regions of the completely filled and nearly empty impurity band (see Fig. 1), the electrons at boron atoms are mobile and, on one hand, form the quasi-2D channel of hopping transport and, on the other hand, screen the fluctuation potential. In order to determine the amplitude of this potential, we can use an analogy with the problem of screening of the fluctuation potential of donors, which are uniformly distributed in the
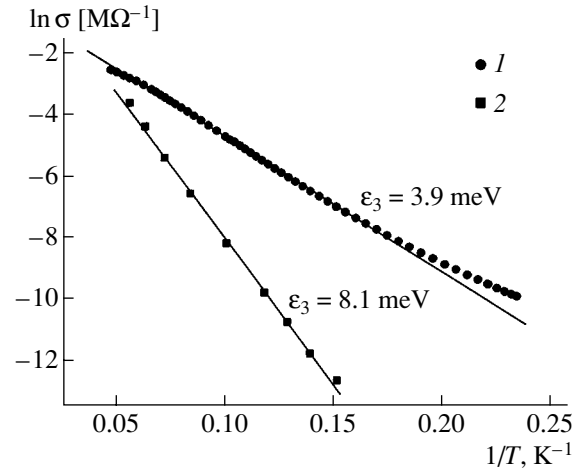

Fig. 2. Temperature dependences of (*1*) quasi-2D hopping conductance σ_c and (*2*) conductance σ_{min} of the structure under flat-band conditions at a gate voltage corresponding to the minimum value of σ.

space surrounding an electron layer, by a 2D electron gas [7, 8]. In this case,

$$V_0 = Ae^2N_i/\kappa n, \qquad (4)$$

where A is a coefficient on the order of unity, N_i is the concentration of ionized centers, κ is the dielectric constant of the semiconductor, and n is the surface density of carriers in the 2D channel. In our case, $N_i = N_a$, and n is also determined by the concentration of acceptors within a monolayer [2]: $n \approx N_a^{2/3}$. Therefore, the amplitude of a random potential is $V_0 \approx 2\varepsilon_3^c \approx Ae^2N_a^{1/3}/\kappa$. It is necessary to note that the activation energy of hopping conductivity in the bulk of a weakly compensated p-type semiconductor is $\varepsilon_3 = \varepsilon_3^f = 0.99e^2N_a^{1/3}/\kappa$ [4]. As can be seen from a comparison with the preceding relation, a linear relation must exist between ε_3^c and ε_3^f: $2\varepsilon_3^c \approx A\varepsilon_3^f$. Taking into account the experimentally determined values of ε_3^c and ε_3^f, we obtain $A \approx 1$, which seems reasonable.

Hence, the above analysis of the temperature dependence of quasi-2D hopping conductance σ_c indicates that, in our case, the hopping transport occurs in the band of states in the vicinity of the Fermi level and the energy scatter of these states is caused by a random Coulomb potential. Below, we discuss the range of high electric fields, in which this circumstance is strongly manifested. In particular, we show that the principal features of the σ_c behavior in a longitudinal electric field can be satisfactorily understood in terms of the Shklovskiĭ model of nonohmic conductivity in percolation systems with a random Coulomb potential [9].
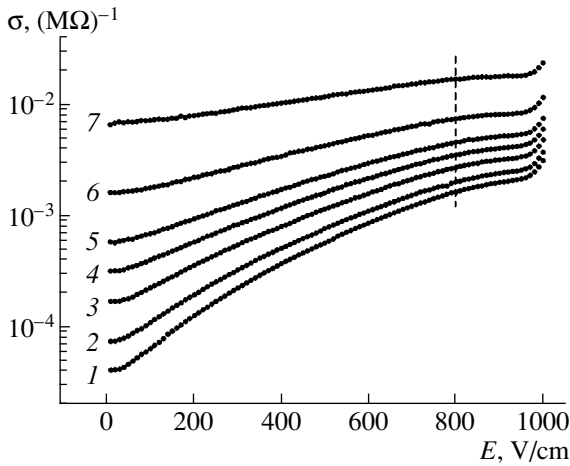
σ, (MΩ)⁻¹

Fig. 3. The structure conductance vs. the longitudinal field at a fixed gate voltage $V_g = 9.5$ V. Temperature: (*1*) 4.22, (*2*) 4.7, (*3*) 5.4, (*4*) 6.0, (*5*) 6.6, (*6*) 7.8, and (*7*) 10 K.

3. NONOHMIC QUASI-2D HOPPING CONDUCTANCE AND THE KINETICS OF ITS RELAXATION

As is well known, the nonlinearity of current–voltage (*I–V*) characteristics in classical 2D systems with an inversion-type or built-in conductivity channel is usually attributed to carrier density effects [10]. Indeed, in such systems, an increase in the driving longitudinal voltage V_d applied to the drain electrode is followed by a decrease in the carrier density near the drain and redistribution of an electric field E along the channel, which results in sublinear behavior of the *I–V* characteristic [10]. A similar carrier density effect may also occur in the current situation, but with the difference being that it must arise in a threshold mode when the potential difference between the gate and drain of the structure $\Delta V = (V_g - V_d) \lesssim 2$ V, i.e., when the quasi-2D hopping conductance channel is depleted at the drain. At the same time, at $\Delta V \gtrsim 2$ V, the longitudinal field can be considered as uniform and equal to $E = V_d/l$, where l is the distance between the current contacts. In these structures, this distance is determined by a gate length of 100 μm. It can be easily shown that, in fact, this follows from the independence of the conductance σ_c from the width of the space charge region at $V_g \gtrsim 2$ V. It is important that this condition allows us to study the nonohmicity of quasi-2D hopping conductance in a rather wide range of fields uniformly distributed along the channel, in particular, at a gate voltage close to the inversion value ($V_g \approx 10$ V) and up to fields $E \approx 800$ V/cm.

It is necessary to draw attention to another circumstance that facilitates the study of nonohmic hopping conductivity under the conditions of transport along a quasi-2D channel. As follows from the data presented in Fig. 2, the conductance σ_c of the surface channel significantly exceeds that of a *p*-Si layer in the entire temperature range under study (at $T < 8$ K, by more than

two orders of magnitude). Furthermore, experimental data [11] show that, in *p*-Si samples with similar doping level, the increase in hopping conductivity is not higher than a factor of several tens at these temperatures. Therefore, we also disregard the effect of parallel conductance of the *p*-Si layers on the nonohmic properties of the structures.

Figure 3 shows dependences of the hopping conductance on the longitudinal field, which were obtained at different temperatures and fixed gate voltage $V_g = 9.5$ V (below the inversion voltage). The dependences demonstrate a significant nonlinearity. The vertical dashed line in Fig. 3 ($E \approx 800$ V/cm) separates the range corresponding to a uniform electric field. Within this range, the hopping conductance at $T = 4.2$ K increases by the factor of 50. At the drain voltage $V_d \gtrsim 8$ V ($E \gtrsim 800$ V/cm), the $\sigma(E)$ dependence first levels off, owing to depletion of the quasi-2D hopping conductance channel at the drain, and then increases again, due to accumulation of holes in the drain region. We draw attention to the fact that, near liquid-helium temperature, the $\sigma(E)$ dependence demonstrates square-root-type behavior in the range of uniform fields ($E \lesssim 800$ V/cm). This behavior becomes even clearer for $\sigma(E, T)$ curves plotted as $\ln[\sigma(E)/\sigma_0]$ vs. $E^{1/2}/T$, where σ_0 is the conductance in the weak-field limit (Fig. 4a). In these coordinates, scaling invariance is achieved; i.e., all the curves show the same run up to the fields corresponding to accumulation, and, starting from some value σ_0, the curves in Fig. 4a have nearly the same slope ($\alpha \approx 0.75$ (V/cm)⁻¹/² K). For comparison, Fig. 4b shows $\sigma(E, T)$ dependences in the form $\ln[\sigma(E)/\sigma_0]$ vs. E/T, which, as can be seen, do not exhibit a satisfactory scaling invariance. Figure 5 shows temperature dependences of the conductance in strong fields, specifically, at $E = 490$ and 750 V/cm. These curves additionally confirm the fact that, in the situation under study, conductance obeys the law

$$\sigma(E, T) = \sigma_0 \exp\left(\alpha \frac{E^{1/2}}{T}\right).$$

The coefficient α obtained from these dependences varies within the range 0.68–0.73 (V/cm)⁻¹/² K; i.e. it is virtually field-independent and coincides with the coefficient determined from the scaling curve in Fig. 4a. It is noteworthy that, under the conditions of a standard Frenkel–Poole effect in extrinsic semiconductors, the exponent also equals $\alpha \frac{\sqrt{E}}{T}$, where $\alpha = \frac{1}{k}\sqrt{4e^3/\kappa} = 2.57$ (V/cm)⁻¹/² K, which is significantly higher than in our case. Furthermore, for the samples under study, the field effect manifests itself in the threshold mode at $E^{1/2}/T \gtrsim 2$ (V/cm)¹/² K⁻¹, whereas, in accordance with the standard Frenkel–Poole relation, it should arise at indefinitely small values of $E^{1/2}/T$.

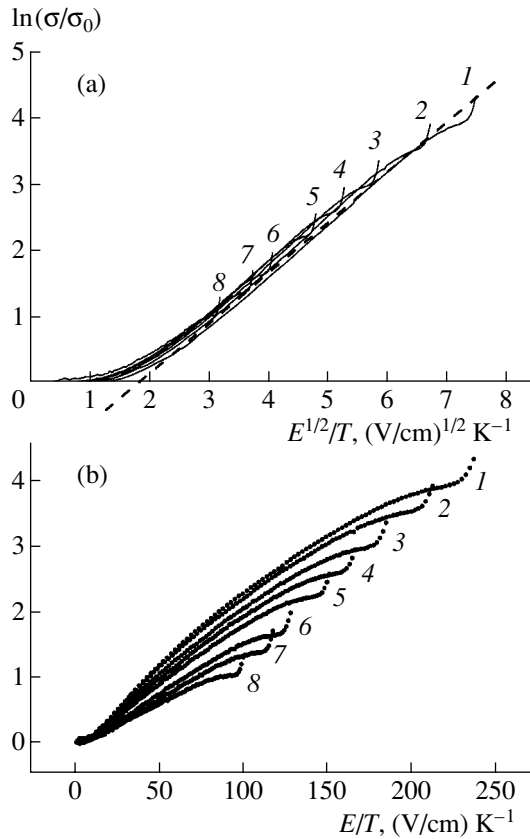Now, we analyze the specific features of the field dependence of hopping conductance, beginning with a

Fig. 4. Field dependences of the structure conductance at different temperatures in the coordinates (a) $\ln[\sigma(E)/\sigma_0]$ vs. $E^{1/2}/T$ and (b) $\ln[\sigma(E)/\sigma_0]$ vs. E/T. σ_0 is the conductance in the weak-field limit. Temperature: (*1*) 4.22, (*2*) 4.7, (*3*) 5.4, (*4*) 6.0, (*5*) 6.6, (*6*) 7.8, (*7*) 8.5, and (*8*) 10 K.

model of the nonlinear properties of percolation systems with a random Coulomb potential [9]. The effect of an electric field on the conductance at the percolation level is discussed in [9], and the role of the field is shown to be limited to lowering the activation energy, which can be interpreted as a lowering of percolation threshold independently of the mean free path for energy loss by carriers; in other words, the results of [9] can be extended to include hopping conductivity and, in particular, as was mentioned in [9], to the case of the ionic conductivity of glass. In these systems, the nonlinear *I–V* characteristic has the form

$$J = J_0 \exp \frac{(CeEaV_0^\nu)^{\frac{1}{1+\nu}}}{kT} \qquad (5)$$

under the condition that the inequality

$$eEa > kT\left(\frac{kT}{V_0}\right)^\nu \qquad (6)$$

is valid. Here, *a* is a characteristic spatial scale of the random potential, ν is the critical index in percolation
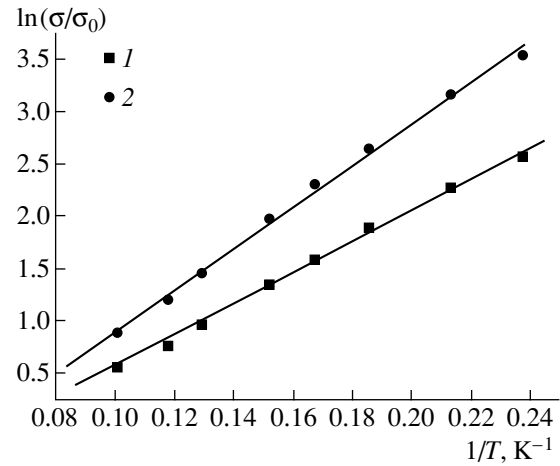
Fig. 5. Temperature dependences of the normalized conductance of the structure at the gate voltage $V_g = 9.5$ V in a strong longitudinal field *E*: (*1*) 490, (*2*) 750 V cm^{-1}.

theory, and *C* is a numerical coefficient. If we disregard the difference between the index ν and unity, we obtain, from (5), a law similar to the Frenkel–Poole law [9]:

$$J = J_0 \exp\left(\alpha \frac{E^{1/2}}{T}\right), \qquad (7)$$

where

$$\alpha = \frac{(CeaV_0)^{1/2}}{k}.$$

In our case, the amplitude of the random potential $V_0 \approx e^2 N_a^{1/3}/\kappa$ (see Section 2), and its characteristic spatial scale is determined, according to [7, 8], by the nonlinear screening length $R_s = a = N_i n^{-2} \approx N_a^{-1/3}$; therefore, we obtain $aV_0 \approx e^2/\kappa$.[2] By substituting this product and the experimentally determined value of α into (7), we find the coefficient $C \approx 0.3$, in agreement with [9], where $C = 0.25$. In the situation under study, condition (6) for the onset of exponential nonohmicity takes the form

$$\frac{E^{1/2}}{T} > k\left(\frac{e^3}{\kappa}\right)^{-1/2} \approx 1 \ (V/cm)^{1/2} \ K^{-1}, \qquad (8)$$

which is also in reasonable agreement with the experimental data (see Fig. 4a).

___

[2] This estimation of the screening length corresponds to the condition $n^3 = N_i^2$; i.e., it is obtained at the applicability limit of the theory [8] developed for the case $n^3 < N_i^2$. It is necessary to note, however, that the model of nonlinear screening describes a number of experimental facts in the conditions well when there is a single source of potential fluctuations per electron (for example, principal specific features of the metal–insulator transition in compensated InSb [12]).
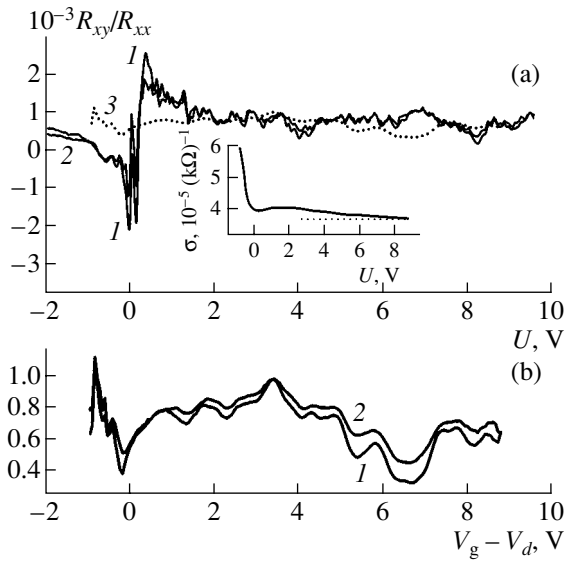
Fig. 6. (a) Ratios of transverse to longitudinal resistance (R_{xy}/R_{xx}) vs. the gate voltage V_g in a weak longitudinal field ($E = 8$ V cm^{-1}) at the temperatures (*1*) 18 and (*2*) 19.6 K. (*3*) R_{xy}/R_{xx} vs. the drain voltage V_d at a fixed $V_g = 8.9$ V and $T = 18$ K. $U = V_g$ is plotted along the abscissa axis for R_{xy}/R_{xx} recorded with V_g scanning (curves *1, 2*) and $U = V_g - V_d$ is plotted for R_{xy}/R_{xx} recorded with (*3*) V_d scanning. Inset: the conductance $\sigma = 1/R_{xx}$ vs. $U = V_g - V_d$ at $V_g = 8.9$ V. (b) R_{xy}/R_{xx} vs. $V_g - V_d$ at $V_g = 8.9$ V at the temperatures (*1*) 18, and (*2*) 19.6 K.

It is necessary to note that the substitution of the critical index $\nu = 1.33$, which corresponds to a 2D situation [4], into (5) yields an exponent of 0.43 in the field dependence of the activation energy, which contrasts with the value of 0.5 used in our calculations. However, in our case, this exponent leads to poorer scaling than it does, e.g., in a description of the nonohmic conductivity of 2D electron gas localized on the fluctuation potential [13]. The reason for this circumstance remains unclear, but a possible explanation is that the discussed hopping-conductance channel formed under the field effect takes an intermediate position between the 3D ($\nu = 0.82$–0.94 [4]) and 2D cases. It is also necessary to remember that the relation for $J(E)$ obtained in [9] is valid for the case of strong nonlinearity, when the exponent is much higher than unity. In our case this exponent is only 4, and it seems probable that, in this case, the field dependence of the preexponential factor, which was disregarded in [9], must be taken into account.

In our opinion, an important conclusion to be drawn from [9] is that, if condition (6) is satisfied, the decrease in activation energy is accompanied by a decrease in the correlation length L (cell size) of a percolation cluster. In particular, at $\nu = 1$, we obtain

$$L(E) = (aV_0/CeE)^{1/2}. \tag{9}$$

This dependence offers a new opportunity to verify the assumption that the nonohmic behavior of conductivity in the situation under study occurs according to the Shklovskiĭ mechanism [9] and is related to reconstruction of a percolation cluster under the action of the electric field. The existence of an $L(E)$ dependence has been confirmed in a study of the mesoscopic fluctuations in voltage arising between the Hall probes in samples shaped in the form of a double Hall cross (with the length $l = 150$ μm and width $w = 50$ μm). Earlier, such fluctuations were studied in a weak longitudinal field as functions of the gate potential V_g [5]. The origin of these fluctuations is as follows: even in a zero magnetic field and for a symmetrical position of the Hall probes, a potential difference can arise between these probes due to a percolation cluster inhomogeneity of scale ~L. The corresponding potential difference between the Hall probes is on the order of $\delta V_{xy} \approx 2LE$, and it changes randomly as the quasi-2D hopping-conductance channel is shifted (for its spatial position changes, see Fig. 1) under the action of V_g due to reconstruction of a percolation cluster [5].[3] In this case, the ratio between the amplitudes of fluctuations in the voltage across the Hall probes δV_{xy} and the longitudinal drain voltage V_d is directly determined by the size L of a percolation cluster cell [5]:

$$\delta V_{xy}/V_d = \delta R_{xy}/R_{xx} \approx 2L/l. \tag{10}$$

Here, R_{xy} and R_{xx} are the Hall and longitudinal resistances, respectively. In this context, it is interesting to compare mesoscopic fluctuations arising in the case of V_g variation in a weak electric field with fluctuations measured with V_d varied at a fixed V_g, for which the effect of the longitudinal field on the value of L should be manifested.

Figure 6a shows the dependences of R_{xy}/R_{xx} on V_g (solid curves). It can be seen that these dependences demonstrate fluctuation-type behavior and are reproduced well in repeated measurements, which confirms their above-described mesoscopic nature. Figure 6b shows the same quantity but as function of V_d. It can be seen that the fluctuations in R_{xy}/R_{xx} vs. V_d are also mesoscopic. For convenience of comparison, the data in Fig. 6b are plotted as functions of $U = V_g - V_d$, with V_d being varied. The inset in Fig. 6a, which shows the dependence of R_{xy}/R_{xx} on V_d, demonstrates the qualitative similarity of a curve presented in this way to the $\sigma(V_g)$ dependence (see the inset in Fig. 1). Here, our prime interest is in the $L(V_d)$ dependence, which, according to (10), can be determined from a compari-

---

[3] These voltage fluctuations are a manifestation of noncoherent mesoscopy and, in contrast to conductivity (current) fluctuations [14], can be observed in samples of macroscopic dimensions. For example, recently [15], we observed δV_{xy} fluctuations in nanocomposite Fe/SiO$_2$ samples of millimeter size in which a random variation in current percolation paths was due to the action of a magnetic field and the temperature, especially under the conditions of thermally stimulated metal–insulator transition.

son of the amplitudes of fluctuations as V_d and V_g are scanned. Along with the solid lines (V_g sweep), Fig. 6a shows a dotted line (V_d scanning), plotted as a function of $U = V_g - V_d$. It can be seen that, as the abscissa tends to zero, the amplitude of the solid lines increases much more strongly than that of the dotted line. Real fluctuations of voltage across the Hall probes depend on the potential difference between the gate and the channel at the Hall probes. In our case, the Hall probes are situated at a distance of $0.32l$ from the source, and, if the driving field is uniform, the corresponding potential difference is $V_H = V_g - 0.32V_d$. Figure 7 shows the ratio R_{xy}/R_{xx} as a function of the last quantity for which V_d was scanned as well as, for comparison, the $R_{xy}/R_{xx} = f(V_g)$ curve. It can be seen that the character of the fluctuations in the range $V_H = 7$–9 V ($V_d = 0$–6 V) is the same in both cases, which confirms their common origin related to shift of the quasi-2D hopping-conductance channel [5]. However, at higher driving fields, the amplitude of the fluctuations obtained by V_d scanning shows a tendency to decrease as compared to $R_{xy}/R_{xx} = f(V_g)$.[4]

Under depletion of the quasi-2D hopping-transport channel ($V_g < 2$ V), the amplitude of the R_{xy} fluctuations strongly increases as V_g decreases (Fig. 6a), which is related to the increasing size of a percolation cluster cell due to a decrease in the density of states at the Fermi level [5]. At the same time, no evident increase of the fluctuation amplitude is observed in the R_{xy}/R_{xx} dependence on V_d. This observation implies that, in this case, this increase in the correlation length of a percolation cluster, related to a decrease in the density-of-states at the Fermi level, is compensated by a decrease due to the rise in the longitudinal field (see Eqs. (9) and (10)). A comparison of the relative amplitudes of the R_{xy} fluctuations for different scanning modes shows that, in the range of depletion of the quasi-2D hopping-conductance channel, at small V_d, the amplitude of $R_{xy}/R_{xx} = f(V_g)$ is about four times larger than the amplitude of $R_{xy}/R_{xx} = f(V_d)$. The nonohmicity of quasi-2D hopping conductance in the temperature range under study arises at the drain voltage $V_d \approx 1$ V (see the inset in Fig. 6a). Therefore, based on the Shklovskiĭ model [9] (see (9)), we can expect the following:

(i) As V_d increases, the amplitude of the $R_{xy}/R_{xx} = f(V_g)$ fluctuations must exceed that for $R_{xy}/R_{xx} = f(V_d)$. This effect starts from some definite value of V_d (in our case, $V_d \approx 6$ V (see above)) at which the change in the cluster related to $L(E)$ dependence [9] (see (9)) becomes comparable with its reconstruction resulting from the shift of the channel position [5].

Fig. 7. (1) R_{xy}/R_{xx} vs. $V_H = V_g - 0.32V_d$, recorded at $V_g = 8.9$ V with V_d scanning in the range 0–6 V, and (2) R_{xy}/R_{xx} vs. V_g at $E = 8$ V cm^{-1}. Temperature $T = 18$ K.

(ii) A decrease in the correlation length of the percolation cluster by a factor of 3–5 at $V_d \approx 9$ V (the lower bound is obtained by assuming a uniform field distribution in the channel, while the upper bound is obtained for a nonuniform field).

These conclusions correlate well with the experimental data. A more detailed analysis of the dependence of mesoscopic fluctuations on the longitudinal field will be presented elsewhere.

The structures under study are systems with a strong fluctuation potential and, thereby, their phase space contains multiple local minima of energy. The behavior of such systems with hopping conductivity is similar to that of glass systems, and the removal of a system from a state of thermodynamic equilibrium or a "frozen pseudo ground state" [16] is accompanied by a long-term relaxation towards equilibrium or new pseudo ground state. As the driving electrical field increases, the correlation length of a percolation cluster decreases and the sample is homogenized; therefore, when the longitudinal field decreases sharply, the system tends to pass from an excited to an equilibrium state. Under experimental conditions, this process should be manifested as a long-term relaxation of conductivity.

The relaxation current arising upon a sharp decrease in the field was recorded using an automatic system based on an HP 3457A nanovoltmeter, which allowed the sampling of the signal at a 20-Hz frequency. The signal from the samples was recorded using a current–voltage converter with the response time of ~0.1 s, a sensitivity of several picoamperes, and a dynamic range up to 10^4 pA. Figure 8a shows the current relaxation curves obtained at different temperatures and in different initial fields (the final field was the same and was 30 V cm^{-1} in all the measurements). Portions of fast and slow current decrease are observed in these curves. The

---

[4] At $V_d \gtrsim 9$ V and the chosen $V_g = 8.9$ V, the resistance of the channel near the drain decreases owing to formation of a hole accumulation channel, which results in an additional increase in the field near the Hall probes. Our estimates of the field distribution in the samples show that, at a driving voltage up to 10 V, the accumulation region may come close to the Hall probes.
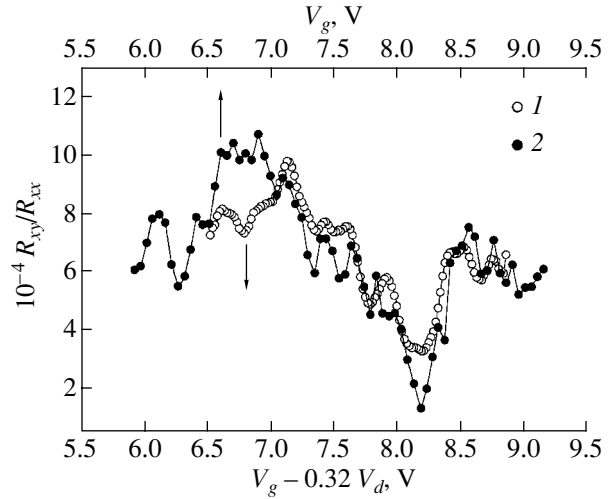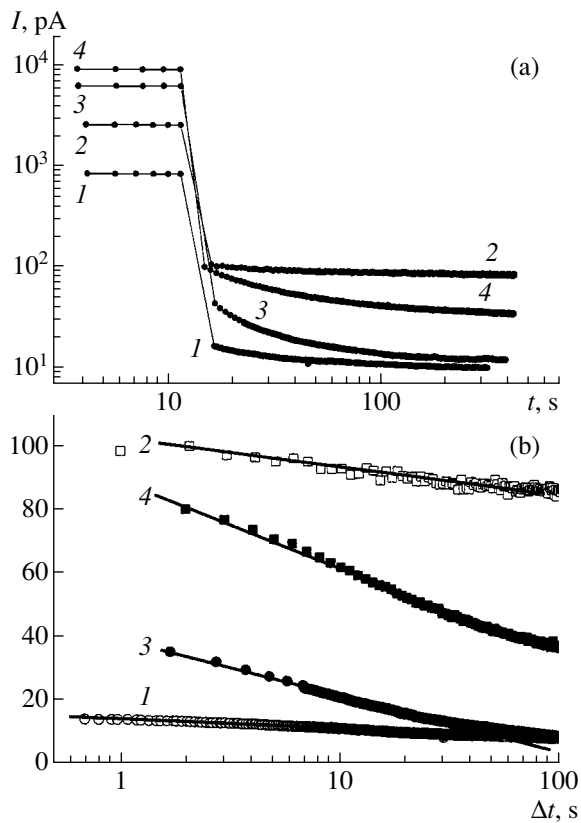
Fig. 8. (a) Curves of current relaxation after a step reduction of the longitudinal field recorded at the temperatures (*1*, *3*) 4.4, (*2*) 6.0, and (*4*) 5.2 K. Initial field, E_0: (*1*, *2*) 300 and (*3*, *4*) 600 V cm^{-1}. The final field was 30 V cm^{-1}. (b) Relaxation of the slow component of the current on a semi-log scale. The curve numbers correspond to those in (a).

fast-decrease region is beyond the time resolution limit of the digital signal-processing system. The slow component is resolved well: the ratio of its magnitude to the steady-state current, $(I_0 - I_\infty)/I_\infty$, increases as the field drop becomes more pronounced and the temperature is lowered. It is noteworthy that the slow component is not related to capacitance processes, since the product of capacitance and channel resistance in our experiments does not exceed 0.1 s, which is much shorter than the characteristic decay time of the slow component (~100 s).

Several possible mechanisms of hopping conductivity relaxation have been discussed in the literature. Similar long-term relaxation was observed under the injection of free carriers in disordered semiconductors (in systems with dispersive transport) [17]. In this case, the current relaxation follows a power law if the energy distribution of traps is nearly uniform and extends deep into the band gap from the band edges, i.e., under the conditions of multiple capture of carriers when the characteristics times of their thermal escape are distributed over an exponentially wide range. In our case, the spectrum of the time distribution of carrier exchange with traps (dead and/or isolated ends of a percolation cluster) is also broad; therefore, it might give rise to relaxations similar to those observed in systems with dispersive transport. However, this type of reconstruction of a percolation cluster, when a number of carriers are trapped in the dead (isolated) ends of the cluster, must occur also under variation of the gate voltage. Nevertheless, no long-term conductivity relaxations were was observed upon a step change in the gate voltage V_g. Another possible mechanism of long-term conductivity relaxation in systems with large-scale fluctuation potential is related to the slow exchange of carriers between a percolation cluster and the regions isolated from it. In these regions, the electrons do not contribute to conductivity but exert influence on it via nonlinear screening effects [18]. However, even in this case, relaxation should occur upon a step change in V_g.

The slow relaxation of conductivity that occurs in the Anderson insulator, which behaves in a similar manner to electronic glass, is attracting a great deal of attention at present (see [19] and the references therein). In this case, a logarithmic decay, followed by a power-law decay, of conductivity is observed upon a sharp change in the state of the system in a limited, but sufficiently wide, time range [19]. In these experiments, a nonequilibrium state was produced by changing the gate voltage.

Figure 8b shows the same relaxation curves as Fig. 8a but plotted on the semi-log scale, with the time counted off from the onset of the slow decrease in conductivity. It can be seen that the relaxation of the slow component of the current obeys the logarithmic law, and its rate only weakly depends on temperature in the studied range but rather strongly depends on the initial driving field. It is also necessary to note that long-term relaxation is observed in the temperature range $T \lesssim 6$ K (see Fig. 2), which corresponds to the transition to the variable-range hopping conductivity and indicates that the glass-type properties of these systems are manifested. All these facts point to the similarity between the system under study and those studied in [19], in which similar relaxation was explained in terms of the many-electron effects responsible for features in the density of states near the Fermi level. However, the difference is that, in our case, the strongest deviation from equilibrium is presumably reached not upon a change in the gate voltage but due to reduction of the size of a percolation cluster under the action of longitudinal field [9], which leads to natural homogenization of the medium.

At the same time, the possibility of describing the observed relaxation by the power law does not allow us to utterly exclude the mechanism discussed in [17].

4. CONCLUSION

The concepts of nonlinear screening [7, 8] and the nonohmic properties [9] of disordered systems with a random Coulomb potential make it possible to consistently describe a mechanism of formation of quasi-2D

hopping conductivity under a field effect in the impurity band of weakly compensated doped silicon and its observed dependences on the electric field and temperature. Long-term relaxations of hopping conductivity in the transition from the nonohmic to ohmic mode are indicative of the glass-type properties of the system under study and of a significant modification of the current paths under the action of the electric field. The last assertion is confirmed by the specific features observed in the behavior of mesoscopic fluctuations of the off-diagonal component of resistance (in the Hall effect configuration), which reflect the reconstruction of a percolation cluster under the action of a longitudinal field.

ACKNOWLEDGMENTS

REFERENCES

1. E. I. Levin and B. I. Shklovskiĭ, Fiz. Tekh. Poluprovodn. (Leningrad) **18**, 856 (1984) [Sov. Phys. Semicond. **18**, 534 (1984)].

2. A. S. Vedeneev, A. G. Gaivoronskii, A. G. Zhdan, *et al.*, Appl. Phys. Lett. **64**, 2566 (1994).

3. A. S. Vedeneev, A. G. Gaĭvoronskiĭ, A. G. Zhdan, *et al.*, Pis'ma Zh. Éksp. Teor. Fiz. **60**, 457 (1994) [JETP Lett. **60**, 475 (1994)].

4. B. I. Shklovskiĭ and A. L. Éfros, *Electronic Properties of Doped Semiconductors* (Nauka, Moscow, 1979; Springer, New York, 1984).

5. B. A. Aronzon, V. V. Rylkov, A. S. Vedeneev, and J. Leotin, Physica A (Amsterdam) **241**, 259 (1997); B. A. Aronzon, A. S. Vedeneev, and V. V. Ryl'kov, Fiz. Tekh. Poluprovodn. (St. Petersburg) **31**, 648 (1997) [Semiconductors **31**, 551 (1997)].

6. J. A. Chroboczek, F. H. Pollak, and H. F. Staunton, Philos. Mag. B **50**, 113 (1984).

7. V. A. Gergel' and R. A. Suris, Zh. Éksp. Teor. Fiz. **75**, 191 (1978) [Sov. Phys. JETP **48**, 95 (1978)].

8. B. I. Shklovskiĭ and A. L. Éfros, Pis'ma Zh. Éksp. Teor. Fiz. **44**, 520 (1986) [JETP Lett. **44**, 669 (1986)].

9. B. I. Shklovskiĭ, Fiz. Tekh. Poluprovodn. (Leningrad) **13**, 93 (1979) [Sov. Phys. Semicond. **13**, 53 (1979)].

10. S. Sze, *Physics of Semiconductor Devices*, 2nd ed. (Wiley, New York, 1981; Mir, Moscow, 1984).

11. D. I. Aladashvili, Z. A. Adamiya, K. G. Lavdovskiĭ, *et al.*, Fiz. Tekh. Poluprovodn. (Leningrad) **23**, 213 (1989) [Sov. Phys. Semicond. **23**, 132 (1989)].

12. B. A. Aronzon and I. L. Drichko, Fiz. Tekh. Poluprovodn. (St. Petersburg) **26**, 1446 (1992) [Sov. Phys. Semicond. **26**, 811 (1992)].

13. I. L. Drichko, A. M. D'yakonov, I. Yu. Smirnov, and A. I. Toropov, Fiz. Tekh. Poluprovodn. (St. Petersburg) **34**, 436 (2000) [Semiconductors **34**, 422 (2000)].

14. A. O. Orlov, M. É. Raĭkh, I. M. Ruzin, and A. K. Savchenko, Zh. Éksp. Teor. Fiz. **96**, 2172 (1989) [Sov. Phys. JETP **69**, 1229 (1989)].

15. V. V. Ryl'kov, B. A. Aronzon, A. B. Davydov, *et al.*, Zh. Éksp. Teor. Fiz. **121**, 908 (2002) [JETP **94**, 779 (2002)]; B. Raquet, M. Goiran, N. Negre, *et al.*, Phys. Rev. B **62**, 17144 (2000).

16. S. D. Baranovskii, B. L. Gelmont, B. I. Shklovskii, and A. L. Efros, J. Phys. C **12**, 1023 (1979); D. Menashe, O. Biham, B. D. Laikhtman, and A. L. Efros, Phys. Rev. B **64**, 115209 (2001).

17. I. P. Zvyagin, *Kinetic Phenomena in Disordered Semiconductors* (Mosk. Gos. Univ., Moscow, 1984) [in Russian].

18. A. B. Davydov and B. A. Aronzon, Fiz. Tekh. Poluprovodn. (St. Petersburg) **38**, 693 (2004) [Semiconductors **38**, 666 (2004)].

19. A. Vaknin, Z. Ovadyahu, and M. Pollak, Phys. Rev. B **65**, 134208 (2002).

Translated by D. Mashovets

The Transition from Thermodynamically to Kinetically Controlled Formation of Quantum Dots in an InAs/GaAs(100) System

**Yu. G. Musikhin[1]^, G. E. Cirlin[1, 2], V. G. Dubrovskiĭ[1], Yu. B. Samsonenko[1, 2],
A. A. Tonkikh[1, 2], N. A. Bert[1], and V. M. Ustinov[1]**

[1]*Ioffe Physicotechnical Institute, Russian Academy of Sciences, Politekhnicheskaya ul. 26, St. Petersburg, 194021 Russia*
^*e-mail: musikhin@mail.ioffe.ru*
[2]*Institute of Analytical Instrument Making, Russian Academy of Sciences, Rizhskiĭ pr. 26, St. Petersburg, 190103 Russia*
Submitted November 9, 2004; accepted for publication November 25, 2004

Abstract—The results of experimental and theoretical studies of quantum dot formation in an InAs/GaAs(100) system in the case of a subcritical width of the deposited InAs layer (1.5–1.6 monolayers) are presented. It is shown that, in the subcritical range of InAs thicknesses (smaller than 1.6 monolayers), regardless of the deposition rate, the density of quantum dots increases and their size decreases in response to an increase in surface temperature. In the overcritical range of InAs thicknesses (more than 1.8 monolayers), the density of quantum dots increases and their size decreases in response to a decrease in temperature and an increase in the deposition rate. The observed behavior of quantum dot morphology is attributed to the transition from a thermodynamically to kinetically controlled regime of quantum dot formation near the critical thickness. © 2005 Pleiades Publishing, Inc.

1. INTRODUCTION

The unique properties of semiconductor heterostructures based on quantum dots (QDs) are related to the atomic-like spectrum of QD energies and make these heterostructures very promising for various applications in modern optoelectronics and microelectronics [1–3]. One of the major challenges related to the physics and technology of direct fabrication of QDs by molecular beam epitaxy (MBE) is the study of their formation mechanisms, which is necessary for controlled growth of QD arrays with the desired properties. Until recently, it was universally believed [2] that the formation of elastically strained QDs in semiconductor systems with lattice parameter mismatch (for example, in an InAs/GaAs(100) system with a lattice mismatch of $\varepsilon_0 = 7\%$) is only possible if the total thickness H_0 of the material deposited on the surface exceeds some critical thickness of H_c. This critical thickness decreases as the lattice mismatch increases, and, in a InAs/GaAs(100) system, it is approximately equal to 1.7 monolayers (MLs) at typical growth temperatures [4–7]. However, in a few earlier studies (for example, in [8]), InAs QDs were experimentally detected at the subcritical thickness of InAs (less than 1.6 MLs). Understanding the nature of critical thickness is important, in particular, for settling the issue of whether the structural properties of experimentally observed QD arrays are thermodynamically or kinetically controlled [9–15].

This study is a continuation of our experimental [11–13] and theoretical [12–15] investigations into the potential for and laws of QD formation. In [11, 12], the formation of subcritical InAs QDs on a GaAs (100) surface was experimentally detected by reflection high-energy electron diffraction (RHEED) and photoluminescence. In the present study, in order to perform a systematic analysis of subcritical QDs, we supplement the previous results with data obtained using transmission electron microscopy (TEM). Then, the obtained experimental data are analyzed from the standpoint of the kinetic theory of formation of coherent islands in mismatched heteroepitaxial systems [12–15].

2. EXPERIMENTAL

The samples under study were grown by MBE using an EP1203 installation. Single-crystalline semi-insulating gallium arsenide wafers with a (100) surface orientation were used as substrates. The samples were grown in the following way. An InAs layer (with a thickness of 1.6 MLs for the first series of samples and 1.5 MLs for the second series) was deposited onto a GaAs buffer layer grown at a temperature of 580°C. The growth temperatures at which the InAs layer was deposited did not exceed 485°C. For all the samples under study, the InAs deposition rate was 0.05 MLs/s. After the deposition of InAs, the substrate surface was exposed for a certain period of time to an As_4 flux; then, a covering GaAs layer with a thickness of 5 nm was deposited on it at the same substrate temperature. Following this deposition, the substrate temperature was increased to 585°C and a 50-nm GaAs layer was grown. Thus, two

series of samples were obtained. In the first series, InAs was deposited on the GaAs surface at the temperatures 485, 450, and 420°C, and the thickness of the InAs layer was 1.6 MLs. In the second series, InAs was deposited at the same temperatures, but the layer thickness was 1.5 MLs. We note that, for each sample, the exposure time of the surface after the InAs deposition stage was different. The exposure stage was necessary to produce an elastically strained array of InAs islands from the initial film, which had a low degree of metastability. The appearance of InAs islands on the surface of the structure was observed due to characteristic changes in the RHEED patterns.

Table 1 lists the main parameters and the results of measurements for the samples under study. Let us use the following example in our discussion of the features of formation of InAs QDs at the subcritical thickness of the deposited material. In situ observations of the RHEED patterns showed that, immediately after depositing an InAs layer with a thickness of 1.5–1.6 MLs, no islands are formed on the surface. In this case, the diffraction patterns remained linear and only main $(0n)$ reflections were visible. The stage following the deposition of InAs, involving exposure in an As_4 stream, resulted (in most cases) in a drastic change in the RHEED patterns. We observed the appearance of bulk diffraction reflections characteristic of island growth [4]. After the appearance of these bulk reflections, the surface of the samples was kept for a further period of time in the As_4 flux, which led to the appearance of inclined linear reflections that originated in the bulk reflections and corresponded to diffractions of electrons from the lateral sides of the islands. We assumed that the instant at which point reflections appear is the typical moment of QD formation, and, with the instant at which additional inclined reflections appear, we estimated the time required for the islands to attain a quasi-stationary size [12]. The deposition of the covering GaAs layer began immediately after the appearance of the additional inclined reflections in the diffraction pattern. An analysis of the data (see Table 1) on the substrate-temperature dependence of the times of QD formation for the structures with 1.5 and 1.6 InAs MLs allows us to make the following conclusions. First, the formation of islands occurs both for the greater thickness of the deposited material (1.6 MLs) and for the smaller thickness (1.5 MLs). It was repeatedly noted in earlier publications [4–7] and in our experimental studies [11, 12] that both these values are smaller than the critical thickness for QD formation according to the Stranski–Krastanov mechanism. Second, for the structures with 1.5 InAs MLs, QDs are formed much later than for the samples with 1.6 InAs MLs. Furthermore, for the deposition thickness of 1.5 MLs and substrate temperature of 485°C, no formation of QDs was observed after an exposure time of 90 s.

The TEM studies were performed using a Philips EM2420 transmission electron microscope with an accelerating voltage of 100 kV. The samples (with

Table 1. Parameters of the samples under study

Sample	InAs thickness, MLs	T, °C	Formation time, s
1a	1.6	485	13
1b	1.6	450	4
1c	1.6	420	2
2a	1.5	485	>90
2b	1.5	450	20
2c	1.5	420	15

regard both to the geometry of the cross section and to the planar geometry) were prepared using ionic sputtering, which was performed using 4-keV argon ions in a Gatan DOU Mill 600™ setup. In order to visualize elastically strained coherent inclusions, bright-field images were obtained using a (220)-type reflection.

3. RESULTS AND THEIR THEORETICAL INTERPRETATION

The electron microscopy studies showed that the formation of InAs QDs on the GaAs (100) surface occurs during the deposition of InAs both at a thickness of 1.6 MLs (Fig. 1) and 1.5 MLs (Fig. 2). Surface contrast, characteristic of elastically coherent inclusions, is clearly seen in the TEM patterns. An analysis of TEM patterns shows that the density of inclusions is GaAs $\sim 10^{10}$ cm^{-2}, which corresponds to typical values of the InAs QD density in the GaAs matrix. After the deposition of 1.6 InAs MLs, the InAs QD densities for all the samples were greater than at 1.5 MLs. Thus, the density of QDs at a fixed surface temperature increases with the amount of deposited InAs. The temperature depen-
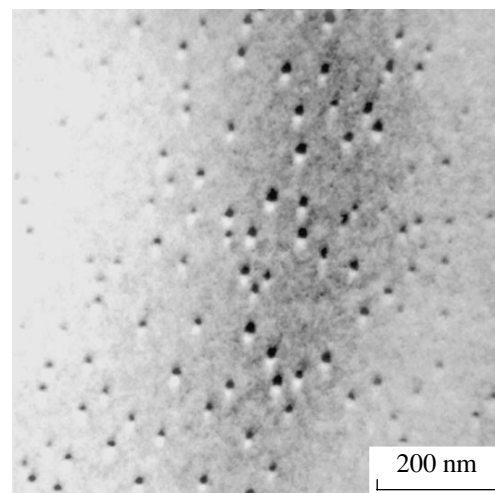

Fig. 1. Bright-field TEM image for a sample with 1.6 InAs MLs deposited at the substrate temperature $T = 485$°C in the planar geometry; the image was obtained using (220) reflection.

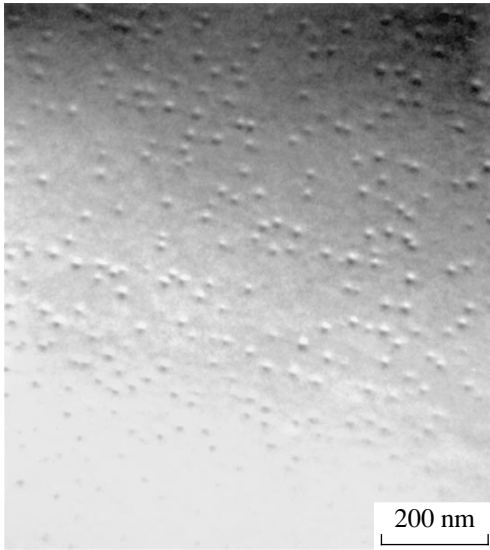**Fig. 2.** Bright-field TEM image for a sample with 1.5 InAs MLs deposited at the substrate temperature T = 450°C in the planar geometry; the image was obtained using (220) reflection.

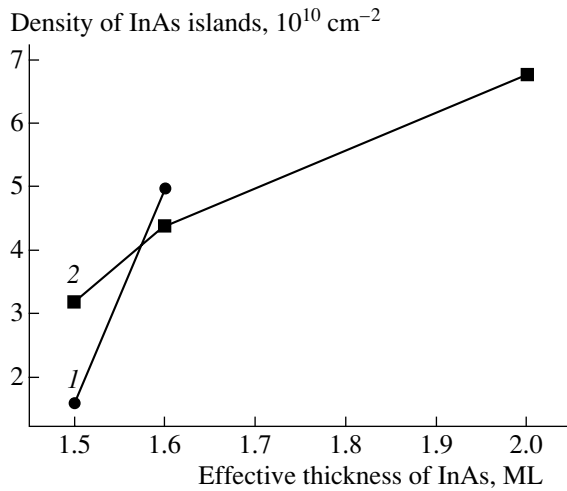Density of InAs islands, 10^{10} cm^{-2}

Fig. 3. Dependence of the surface density of quantum dots in the InAs/GaAs(100) system on the thickness of the deposited InAs layer at the surface temperatures (*1*) 420 and (*2*) 450°C.

dence of QD density is more complicated, since, after the deposition of 1.5 InAs MLs at a substrate temperature of 420°C, the density was lower than at 450°C, whereas for the effective thickness of 1.6 MLs, the opposite relation manifested itself (Fig. 3). Figure 3 shows QD surface density plots obtained by processing the TEM images for the samples with both 1.5 and 1.6 InAs MLs, and supplemented with data [12] on the dependence of the density of the structure with 2 InAs MLs on the thickness of InAs deposited at two different surface temperatures (420 and 450°C). As the surface temperature increases, we can see that, in the region of

InAs thickness above 1.6 MLs, the density of islands at a given InAs thickness decreases while, at 1.5 MLs, the density increases. Thus, near the critical thickness, there exists a "reversal" of the temperature dependence of the QD density, as illustrated in Fig. 3.

The behavior of the density of islands in relation to the thickness of the deposited material and surface temperature can be explained using the kinetic theory of QD formation [11–15]. It was shown in [16] that the formation of elastically strained QDs is possible only if the thickness H of the deposited layer exceeds the equilibrium thickness h_{eq} of the wetting layer (WL), $H > h_{eq}$. This equilibrium thickness corresponds to equality of the wetting and elastic energies in the WL [17]. For the parameters corresponding to the InAs/GaAs(100) system, estimations yield $h_{eq} \approx 1.0$–1.1 MLs [12]. In the case of deposition at a constant temperature T and a constant deposition rate V, the critical thickness H_c is a kinetic quantity equal to the maximum WL thickness at which the island nucleation rate attains a maximum [14]. In the case of a supercritical deposition thickness, the thickness of the WL h increases until the critical thickness H_c is attained; during this process, the volume of the islands is small and $H \approx h$. After attaining the critical thickness, the thickness of the WL decreases, the volume of the islands increases, and the amount of deposited material H grows until the growth is stopped at $H = H_0 = Vt_0$, where H_0 is the thickness of the deposited material at the instant when the source is switched off and t_0 is the switching-off time. In the absence of desorption, the equation for material balance at the surface is given by

$$H(t) = h(t) + G(t), \qquad (1)$$

where $H(t)$ is the amount of deposited material, $h(t)$ is the average WL thickness (generally, taking into account adatoms diffusing at the WL surface), $G(t)$ is the total volume of islands (expressed in MLs) per unit area of the surface, and t is the deposition time. According to the theory of nucleation [14–16], the function $G(t)$ is determined by the islands' nucleation rate $I(t)$ and growth rate $v(t)$:

$$G(t) = \mathrm{const} \int_0^t dt' I(t') \rho^{3/2}(t', t), \qquad (2)$$

$$\rho(t', t) = \int_{t'}^t d\tau v(\tau). \qquad (3)$$

Here, $\rho(t, t')$ is the "size" of an island, measured in the units of the lattice constant, when nucleated at instant t'. The nucleation rate I is normalized so that its dimension is 1/s. In expression (2) and in what follows, we disregard all constants on the order of unity. To apply formula (2), it is necessary to choose an island size at which the growth rate $v(t)$ does not depend on ρ. It is reasonable to assume [12–16] that, in the case of small

surface coverage, the islands absorb atoms from the surface at a rate proportional to the their perimeters. Thus, for the growth of three-dimensional islands of linear size L, we have

$$\frac{d(L^3)}{dt} \propto L \Rightarrow \rho \propto L^2. \qquad (4)$$

Hence, up to a constant, the size ρ is the area of the base of an island and the island volume is $L^3 \propto \rho^{3/2}$, thus giving the power of 3/2 in formula (2). Furthermore, it is known from the theory of nucleation that the islands are nucleated in a rather narrow time interval near the metastability maximum of the system [18]. In our case, the metastability maximum corresponds to the maximum of elastic stress at the point of the maximum WL thickness; therefore, the nucleation rate $I(t)$ can be written as

$$I(t) = I(H_c) f\left(\frac{t - t_c}{\Delta t}\right) \propto v \exp(-F(H_c)) f\left(\frac{t - t_c}{\Delta t}\right). \ (5)$$

Here, $I(H_c)$ is the nucleation rate at $h = H_c$, $F(H_c)$ is the activated nucleation barrier at $h = H_c$, and the nucleation rate must be proportional to the island growth rate v. The function f in (5) is a rapidly decreasing function of its argument and has a sharp maximum at $t = t_c = H_c/V$ (t_c is the growth time of the WL of critical thickness) [14]. The quantity Δt is the duration of the stage of island nucleation. It is clear from general considerations that the higher the deposition rate, the faster the island nucleation, since, in the case of supercritical thickness, the time scale of change in the surface state is set by the quantity $1/V$. Therefore,

$$\Delta t \propto \frac{1}{V}. \qquad (6)$$

By differentiating (1) with respect to time and then setting $t = t_c$ and taking into account that, by definition, $dh/dt = 0$ at $t = t_c$, $dH/dt = V$, and $\rho(t', t) \approx v(t - t')$ at t_c (for brevity, we write v instead of $v(t_c)$), we obtain, from (2)–(5),

$$V \approx v^{5/2} (\Delta t)^{3/2} \exp(-F(H_c)). \qquad (7)$$

With allowance for (6), it follows from (7) that

$$F(H_c) = \frac{5}{2} \ln(v/V). \qquad (8)$$

The quantity on the right-hand side of (8) is much greater than unity, since it contains the logarithm of a very large quantity, namely, the ratio v/V of the island growth rate (microprocess) and the deposition rate (macroprocess) [14]. In [12–15], this ratio was called the kinetic control parameter $Q \equiv v/V$; in the case of MBE, its typical values are $\sim 10^2$–10^4. If we assume that the island growth rate (due to diffusion from the surface) has an Arrhenius temperature dependence, $v \propto \exp(-E_D/k_BT)$, then

$$Q \equiv v/V \propto (1/V) \exp(-E_D/k_BT). \qquad (9)$$

Here, E_D is the activation barrier for diffusion from the surface into an island stimulated by elastic stresses [16]. Taking into account (5), (6), (8), and (9), we obtain the following expression for the island density in the supercritical region:

$$N \approx \int_0^\infty dt I(t) \approx Q^{-3/2} \approx V^{3/2} \exp\left(\frac{3E_D}{2k_BT}\right). \qquad (10)$$

Hence, in the region of supercritical thickness, the island density increases in response to an increase in the deposition rate, decreases as the surface temperature increases, and weakly depends on the thickness of the deposited layer (in the absence of secondary nucleation [19]). Dependence (10) has a purely kinetic nature and is almost unaffected by the thermodynamic characteristics of the system.

Expression (8) relates the thermodynamics of a heteroepitaxial system (the activation barrier for the islands) to the kinetics of MBE growth (the growth rate and characteristics of the diffusive flow from the surface into the islands). If the free energy of island formation is chosen as in [12–15], the activated nucleation barrier is $F(H) \cong T_e[T(H/h_{eq} - 1)^2]$. Then, we use (8) to obtain the formula for critical thickness:

$$H_c = h_{eq}\left[1 + \left(\frac{2}{5}\frac{T_e}{T \ln Q}\right)^{1/2}\right]. \qquad (11)$$

Here, T_e is a quasi-equilibrium parameter of the dimension of temperature containing the energy characteristics of the heteroepitaxial system (surface energy and elastic modulus) and the lattice mismatch ε_0 [12]. In particular, it follows from (11) that, for the materials under consideration, the critical thickness decreases as the surface temperature increases and weakly depends on the deposition rate.

In the case of a subcritical deposition thickness $H_0 < H_c$, the maximum metastability of the WL corresponds to $H = H_0$ (the maximum WL thickness under these circumstances). Thus, the nucleation rate $I(H_0)$ is much less than $I(H_c)$, and observation of subcritical InAs QDs requires exposure to the As$_4$ flow. The second important difference is that the structure of the subcritical QDs must be independent of the deposition rate V, since, for a long exposure, the deposition rate is not important. In the subcritical region, the stage of nucleation is a much longer process than for the supercritical deposition thickness. Therefore, the time scale of the nucleation stage is no longer controlled by the deposition rate; i.e., it is not possible to use relation (6). In the subcritical region, the duration of the nucleation stage can be estimated from (2): the nucleation is stopped when the volume of the islands $G(t)$ reaches unity,

$$G(t) \approx v^{5/2} (\Delta t)^{5/2} \exp(-F(H_0)) \approx 1. \qquad (12)$$

Table 2. Qualitative behavior of the quantum dot morphology in an InAs/GaAs(100) system at different effective InAs thicknesses

InAs deposition thickness	Behavior of the density and size of the quantum dots as temperature increases	Behavior of the density and size of the quantum dots as the deposition rate increases	Regime
Less than 1.6 MLs	Density increases Size decreases	Do not change	Thermodynamic
1.6–1.8 MLs	–	–	Transition
1.8–2.5 MLs	Density decreases Size increases	Density increases Size decreases	Kinetic

Hence, the duration of the nucleation stage is

$$\Delta t \propto \frac{1}{v} \exp\left[\frac{2F(H_0)}{5}\right]. \tag{13}$$

The surface density of subcritical QDs is given by

$$N \approx \int_0^\infty dt\, I(t) \approx v \exp(-F(H_0))\Delta t$$
$$\approx \exp\left[-\frac{3}{5}\frac{T_e}{(H_0/h_{eq}-1)^2}\right]. \tag{14}$$

Expression (14) contains only the thermodynamic characteristics of the system (T_e, T, H_0, and h_{eq}) and does not depend on the kinetics of MBE growth. The density of subcritical islands increases as the surface temperature and amount of deposited material increases.

However, the two limiting cases considered above cannot be applied to a description of the transition regime of island formation close to H_c, where both kinetic and thermodynamic factors are important. Estimation of the thickness range corresponding to the transition region [12] shows that the transition regime for the InAs/GaAs(100) system corresponds to $H_0 = H_c \pm 0.1$ MLs, i.e., to the approximate InAs thickness range 1.6–1.8 MLs. Thus, this theoretical analysis makes it possible to explain the observed effect of the "reversion" of the temperature dependence of the island density near the critical thickness.

On the basis of the obtained experimental data and their theoretical analysis, we can make some general conclusions about the character of the dependence of the morphology of InAs QDs observed on the GaAs (100) surface on the parameters controlling the MBE growth (the surface temperature T, deposition rate V, and effective deposition thickness H_0). These conclusions are listed in Table 2. The quasi-stationary lateral island size L_R is defined as the average size attained by QDs after absorbing all the $H_0 - h_{eq}$ MLs of the material from the surface. From the equation of material balance, we obtain

$$L_R \approx (H_0 - h_{eq})^{1/3} N^{-1/3}; \tag{15}$$

i.e., the QDs' size decreases as their density increases and vice versa. We note that the behavior of the size in

the subcritical region of the deposition thickness, as indicated in Table 2, was predicted theoretically, whereas the behavior of the density in both the subcritical and supercritical regions and of the size in the supercritical region is confirmed by the experimental results of this study and [11, 12].

In conclusion, we carried out experimental and theoretical investigations into the formation of InAs QDs on a GaAs (100) surface at a subcritical InAs deposition thickness (1.5–1.6 MLs). We discovered, using experimental methods, and theoretically justified the formation of QDs in the subcritical region. We showed that, in the subcritical and supercritical regions, the dependences of the morphology of QDs on the surface temperature are different. As the temperature increases, in the region of subcritical thickness values, the QD density increases and, in the region of supercritical thickness, it decreases. The reversion of the temperature dependence of the QD density near the critical thickness is related to the fact that, in the subcritical region, the QD morphology is thermodynamically controlled and, in the supercritical region, it is kinetically controlled.

REFERENCES

1. Zh. I. Alferov, Fiz. Tekh. Poluprovodn. (St. Petersburg) **32**, 3 (1998) [Semiconductors **32**, 1 (1998)].
2. D. Bimberg, M. Grundmann, and N. N. Ledentsov, *Quantum Dot Heterostructures* (Wiley, Chichester, 1999).
3. V. M. Ustinov, A. E. Zhukov, A. Y. Egorov, and N. A. Maleev, *Quantum Dot Lasers* (Oxford Univ. Press, Oxford, 2003).
4. G. E. Tsyrlin, N. P. Korneeva, V. N. Demidov, *et al.*, Fiz. Tekh. Poluprovodn. (St. Petersburg) **31**, 1230 (1997) [Semiconductors **31**, 1057 (1997)].
5. J. M. Moison, F. Houzay, F. Batthe, *et al.*, Appl. Phys. Lett. **64**, 196 (1994).

6. I. Mukhametzhanov, Z. Wei, R. Heitz, and A. Madhukar, Appl. Phys. Lett. **75**, 85 (1999).

7. Ch. Heyn, Phys. Rev. B **64**, 165306 (2001).

8. A. Polimeni, A. Patane, M. Cappizi, *et al.*, Phys. Rev. B **53**, R4213 (1996).

9. I. Daruka and A.-L. Barabasi, Phys. Rev. Lett. **79**, 3708 (1997).

10. M. Meixner, E. Schöll, V. A. Shchukin, and D. Bimberg, Phys. Rev. Lett. **87**, 236101 (2001).

11. A. A. Tonkikh, G. E. Cirlin, V. G. Dubrovskiǐ, *et al.*, Pis'ma Zh. Tekh. Fiz. **29** (16), 72 (2003) [Tech. Phys. Lett. **29**, 691 (2003)].

12. V. G. Dubrovskii, G. E. Cirlin, Yu. G. Musikhin, *et al.*, J. Cryst. Growth **267**, 47 (2004).

13. V. G. Dubrovskiǐ, A. A. Tonkikh, G. E. Cirlin, *et al.*, Pis'ma Zh. Tekh. Fiz. **30** (21), 72 (2004) [Tech. Phys. Lett. **30**, 920 (2004)].

14. V. G. Dubrovskii, G. E. Cirlin, and V. M. Ustinov, Phys. Rev. B **68**, 075409 (2003).

15. V. G. Dubrovskii, G. E. Cirlin, and V. M. Ustinov, Phys. Status Solidi B **241**, R42 (2004).

16. A. V. Osipov, F. Schmitt, S. A. Kukushkin, and P. Hess, Appl. Surf. Sci. **188**, 156 (2002).

17. P. Müller and R. Kern, Appl. Surf. Sci. **102**, 6 (1996).

18. F. M. Kuni and A. P. Grinin, Kolloidn. Zh. **46**, 23 (1984).

19. A. V. Osipov, S. A. Kukushkin, F. Schmitt, and P. Hess, Phys. Rev. B **64**, 205421 (2001).

20. V. G. Dubrovskii, J. Phys.: Condens. Matter **16**, 6929 (2004).

Translated by I. Zvyagin

Resonance Modulation of Electron–Electron Relaxation by a Quantizing Magnetic Field

V. I. Kadushkin

Esenin State Pedagogical University, Ryazan, 390000 Russia
e-mail: kadush@rspu.ryazan.ru
Submitted November 17, 2004; accepted for publication December 16, 2004

Abstract—It is found that a magnetic field turns on intersubband electron relaxation as the Landau levels of the spatial quantization subbands of a single heterojunction scan the Fermi level. The observed steady decrease in intersubband relaxation time as the magnetic field increases is attributed to the addition of electron–phonon interaction to electron–electron interaction. © 2005 Pleiades Publishing, Inc.

1. INTRODUCTION

It is known [1–3] that Shubnikov–de Haas magnetoresistance oscillations experience amplitude–frequency modulation in heavily doped nanostructures under conditions in which electrons fill not only the ground spatial-quantization subband (with energy corresponding to the conduction-band bottom E_m) but also the excited (E_p) subband. The observed features were attributed to intersubband electron–electron (e–e) interaction. Kinks in the magnetic-field dependence of the oscillation amplitude $\delta(1/B)$ directly indicate that there is competition between the intrasubband and intersubband relaxation processes [4–6]. In this study, the physical conditions for modulation (induced by a magnetic field) of the oscillation amplitudes for two-dimensional (2D) and quasi-2D electrons in the E_m and E_p spatial-quantization subbands are analyzed. It is shown that the characteristic kinks in the $\delta(1/B)$ curve correspond to resonance crossing of the borderline Fermi level E_F by N_m and N_p Landau levels, which turns on the intersubband e–e interaction. If a level with the number N_m is found in the gap between the Landau levels N_p and N_{p+1}, the intersubband e–e interaction is suppressed. Experiments involving $Al_xGa_{1-x}As(Si)/GaAs$ samples ($x = 0.28$) are analyzed in detail; in addition, the experimental data presented in [1, 3] are processed.

2. EXPERIMENTAL

Oscillations of the magnetoresistance in heterostructures with a 2D electron concentration of $(8.2–12.2) \times 10^{11}$ cm^{-2} in a magnetic field as high as 7.4 T and in the temperature range 1.69 K $\leq T \leq$ 20.2 K are analyzed. The filling of two spatial-quantization subbands with energies corresponding to the conduction-band bottom (E_m and E_p) is characteristic of the above range of electron concentrations.

Figure 1 shows the magnetic-field dependences of amplitudes of the Shubnikov–de Haas oscillations $\delta(1/B)$ for 2D electrons in the E_m subband and for quasi-2D electrons in the E_p subband of spatial quantization for one of the samples; the dependences are normalized by taking into account the finite temperature of the sample.

Approximations a, c, and e of portions of the $\delta(1/B)$ dependence were obtained using a modified method [7]; as a result, a single pole (focus) $\Phi_m^{a,c,e}$ was revealed. This circumstance indicates that there is a common (for portions a, c, and e) mechanism of nonthermal broadening that depends parametrically on the magnetic field. The variation in the slope of the dependences $\delta^{a,c,e}(1/B)$ for portions a, c, and e indicates that the Dingle temperature increases according to $T_D^a < T_D^c < T_D^e$. A poorly pronounced tendency towards variation in the slope $\delta^{b,d}(1/B)$ is observed for portions b and d ($T_D^b < T_D^d$).

3. DISCUSSION

Figure 2 shows a diagram representing scanning of the Fermi level by Landau levels with the numbers N_m and N_p. The Fermi level is taken as the energy origin; i.e., $E_F = 0$. The regions of the kinks a–b, b–c, and c–d in the dependence $\delta(1/B)$ are also indicated in Fig. 2. Qualitative representation of the scanning of the Fermi level by the Landau energy subbands $E(k_z)$ and the density-of-states functions $D(E)$ and $g(E)$ for 2D electrons in the E_m subband and quasi-2D electrons in the E_p subband of spatial quantization is also given. According to estimations of the characteristic scales, the electrons in the E_p subband are quasi-two-dimensional and the function $g_p(E)$ is close to the bulk function for the Landau levels $N_p = 0, 1, 2$.

Transitional regions a–b and c–d in the dependences $\delta(1/B)$ correspond to resonance magnetic fields at which the Fermi level is crossed by the Landau levels $N_m = 13$ (8) and $N_p = 2$ (1) of the E_m and E_p subbands.
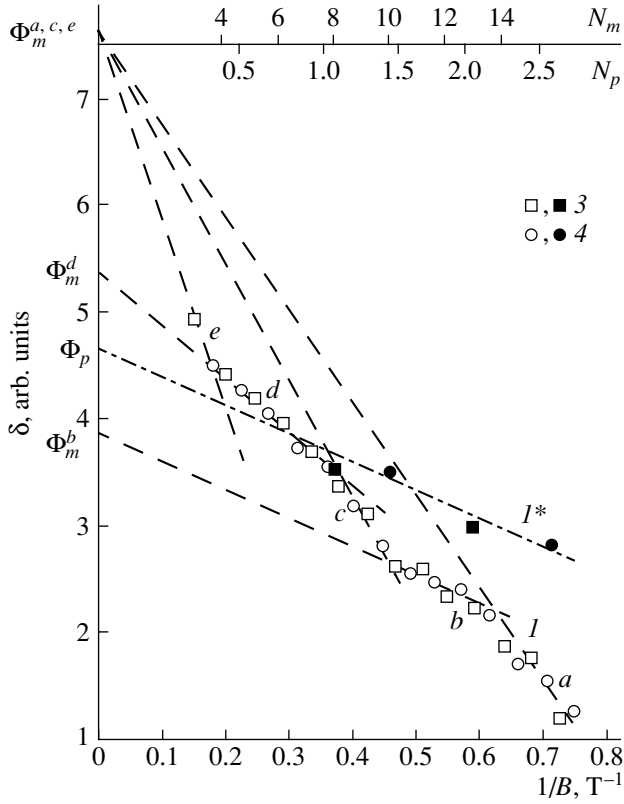
Fig. 1. Magnetic-field dependences of the normalized amplitude of magnetoresistance oscillations for the (*1*) ground E_m and (*1**) excited E_p subbands in sample 39A-III of $Al_xGa_{1-x}As(Si)/GaAs$ ($x = 0.28$). The concentration of 2D electrons $n_m = 10.6 \times 10^{11}$ cm^{-2} and the concentration of quasi-2D electrons $n_p = 0.88 \times 10^{11}$ cm^{-2}. $T = 4.2$ K. The squares (*3*) and circles (*4*) respectively indicate the positions of maxima and minima in the oscillations.

Fig. 2. Diagram illustrating the scanning of the Fermi level ($E_F = 0$) by the Landau quantum levels N_m and N_p; by the Landau subbands $E(k_z)$; and by the density-of-states functions $D(E)$ (for 2D electrons) and $g(E)$ (for quasi-2D electrons) in the subbands E_m and E_p, respectively. The regions corresponding to resonances *a–b* and *c–d* and also the region (*b–c*) corresponding to the position of the level N_m in the gap between the levels N_p and $N_p + 1$ are shown. Sample 39A-III, $T = 4.2$ K.

The *a–b* kink is almost of the resonance type; in contrast, there is a certain mismatch in the *c–d* transition: the Landau level with the number $N_m = 8$ intersects the Fermi level earlier (with respect to the magnetic field) than the Landau level $N_p = 1$.

As can be seen from the energy diagram, regions *a–b* and *c–d* correspond to physical conditions that are conducive to manifestation of intersubband interaction. Under these conditions, the maxima of the density-of-states function $D(E)$ for 2D electrons and $g(E)$ for quasi-2D electrons coincide with the Fermi level in relation to their energy to within $k(T + T_D)$. The magnetic field in the *b–c* region of the $\delta(1/B)$ dependence corresponds to an intermediate situation where the Landau level $N_m = 10$, which intersects the Fermi level, is found in the energy gap between the levels $N_p = 2$ and 1. The maximum of $D(E)$ is found in the region of the tail of the density of states $g(E)$ at $N_p = 2$ and in the region of the upper energy tail of $g(E)$ at $N_p = 1$. It is 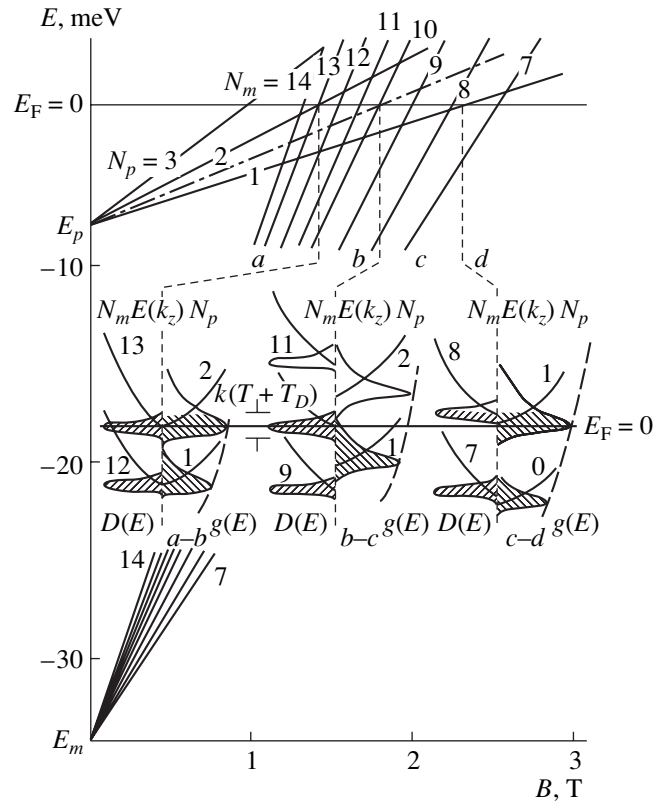this circumstance that causes the reduction (sometimes a complete suppression) of intersubband interaction between 2D and quasi-2D electrons in the E_m and E_p subbands.

In order to illustrate the correspondence between the situation under discussion and the transitional regions in the dependence $\delta(1/B)$, the scales of the Landau level numbers are shown in Fig. 1. It can be seen that the transition from portions *b* and *d* to steps *c* and *e* corresponds to half-integer values of N_p whereas the transition from steps *a* and *c* to regions *b* and *d* corresponds to integer values of N_p.

It follows from the expression for the Fermi energy

$$E_{F_{m,p}} = \frac{e\hbar B_{m,p}}{m^*}\left(N_{m,p} + \frac{1}{2}\right),$$

that the field $B_{mp} = B_m = B_p$ corresponds to a simultaneous (with respect to the magnetic field) intersection of the Fermi level by the Landau levels N_m and N_p. The field $B_{mp} = B_m = B_p$ is given by

$$B_{mp} = (\pi\hbar/e)\Delta n_{m,p}/\Delta N_{m,p}, \qquad (1)$$

Table 1. The time of collisional broadening $\tau_q = \tau_q^a,\ \tau_q^b,\ \ldots$ corresponding to portions $a, b, \ldots$ in the dependence $\delta(1/B)$

τ_q^i, 10^{-13} s	a	b	c	d	e	f	T, K
Our data	1.37	4.79	1.12	4.60	0.67	–	4.2
[1]	9.8	28.0	8.6	24.7	7.9	20.9	3.9
[3]	7.7	10.2	6.25	10.2	4.59	–	1.2

where $\Delta n_{m,p} = n_m - n_p$ and $\Delta N_{m,p} = N_m - N_p$. Only a technology-related spread in the value of $\Delta n_{m,p}$ can account for the fact that a broad spectrum is observed for amplitude–frequency modulation of the shape of the magnetoresistance oscillation. The modulation factor can vary from 100% to almost zero.

It was found that the observed special features of the dependences $\delta(1/B)$ could be reasonably and systematically explained by taking into account the notion [5, 6] that intrasubband and intersubband e–e interactions play a role in origination of the collisional broadening of the Landau levels.

The time $\tau_q = \hbar/2\pi k T_D$ is a combination of the contributions made by the independent intrasubband ($\tau_{ee}^{intra} = \tau_{ee}^{m,p}$) and intersubband ($\tau_{ee}^{inter} = \tau_{ee}^{mp}$) channels: $\tau_q^{-1} = \sum_i (\tau_{ee}^i)^{-1}$, where $i = m, p, mp$. In the situation corresponding to segments b and d in the dependence $\delta(1/B)$, the intersubband interaction is suppressed as a result of the energy gap between $D(E)$ and $g(E)$. The maxima of $D(E)$ for $N_m = 11$–9 are found in the $g(E)$ gap between $N_p = 2$ and 1. The time of nonthermal broadening depends on the time of intrasubband relaxation for the 2D and quasi-2D electrons as follows:

$$\frac{1}{\tau_q^{b,d}} = \frac{1}{\tau_{ee}^m} + \frac{1}{\tau_{ee}^p}. \qquad (2)$$

As the magnetic field increases, with the result that the maximum of $g(E)$ with $N_p = 2$ (1) approaches the maximum of $D(E)$ with $N_m = 12$ (8) and there is an almost resonance-type situation, intersubband e–e interaction

of the 2D and quasi-2D electrons in the E_m and E_p subbands comes into effect. In this case,

$$\frac{1}{\tau_q^{a,c,e}} = \frac{1}{\tau_{ee}^m} + \frac{1}{\tau_{ee}^p} + \frac{1}{\tau_q^{mp}}. \qquad (3)$$

The values of the parameter τ_q^{mp} that appears in (3) are different in regions a, c, and e. The existence of a single pole (focus) $\Phi_m^{a,c,e}$ testifies to the fact that the mechanism limiting the oscillations in regions a, c, and e is invariable. However, the variation in the slope of the corresponding segments indicates that one of the components in formula (3) has a parametric magnetic-field dependence. Therefore, the times of intersubband e–e interaction and the time of electron–phonon interaction τ_{e-ph} should be included (in addition to τ_{ee}^{mp}) in τ_q^{mp} [2, 8]. It is the dependence of τ_{e-ph} on the magnetic-field strength that is the cause of the variation in the slope of the curve $\delta(1/B)$ in portions a, c, and e.

According to (2) and (3), we should expect that

$$\tau_q^a > \tau_q^c > \tau_q^e, \quad \tau_q^b > \tau_q^d, \text{ and } \tau_q^d > \tau_q^c. \qquad (4)$$

The slopes of the dependence $\delta(1/B)$ in regions a–e (Fig. 1) and the slope in region f [1] were used to estimate the values of τ_q^a, τ_q^b, and so on, and the results are listed in Table 1. The estimates of τ_q obtained by processing the experimental data reported in [1, 3] are also listed. It can be seen that the times obtained experimentally are in good agreement with those expected according to relations (4).

The data listed in Table 1 and formulas (2) and (3) were used to estimate the values of τ_q^{mp}. The results of the calculations are listed in Table 2. It can clearly be seen that the estimates for τ_q^{mp} are almost the same for transitions from region a irrespective of the components (a–b, a–d, or a–f) used to construct expressions (2) and (3). A similar conclusion is valid concerning the values of τ_q^{mp} for regions c and e. Attention should be drawn to the decrease in the value of τ_q^{mp} occurring as the magnetic-field intervals for the corresponding regions increase; i.e.,

$$\tau_q^{mp}(a) > \tau_q^{mp}(c) > \tau_q^{mp}(e).$$

Table 2. The intersubband-relaxation time τ_q^{mp} for portions a, c, and e in the dependence $\delta(1/B)$ with respect to portions b, d, and f

τ_q^{mp}, 10^{-13} s	$a -$			$c -$			$e -$		
	$a-b$	$a-d$	$a-f$	$c-b$	$c-d$	$c-f$	$e-b$	$e-d$	$e-f$
Our data	1.97	2.0	–	1.4	1.45	–	0.82	0.82	–
[1]	14.4	16.5	18.5	12.4	13.0	14.5	11.0	11.6	12.8
[3]	31	31	–	16.5	16.5	–	8.2	8.2	–

It was assumed in the calculations that the quantities τ_{ee}^{m} and τ_{ee}^{p} are independent of the magnetic field, since they are related only to e–e interaction. The fact that segments b and d in the dependence $\delta(1/B)$ are almost parallel to each other (see Fig. 1), as well as the results of processing the experimental data reported in [1, 3], can serve as indirect verification of the above assumption.

An analysis of the times of the intersubband e–e relaxation τ_q^{mp} (Table 2) shows that these values are slightly larger than those of the intrasubband e–e relaxation τ_q^{i} (Table 1). This inference is in agreement with the results of a comparison of corresponding parameters performed using other independent methods [3, 9].

4. CONCLUSION

Thus, modulation of the time taken for nonthermal collisional broadening of the Landau levels by a quantizing magnetic field is ascertained. The mechanism of this modulation is related to a periodic initiation and suppression of intersubband e–e interaction. A variation in the magnetic field brings about scanning of the Fermi level by a system of N_m and N_p Landau levels of the ground E_m and excited E_p subbands of spatial quantization. If resonance crossing of the Fermi levels by the maxima of the density of states $D(E)$ and $g(E)$ for 2D and quasi-2D electrons occurs, intersubband e–e interaction (with an admixed electron–phonon relaxation) comes into effect. Away from the resonance, in a situation where the Landau level N_m is found in the gap between the levels N_p and $N_p + 1$, intersubband interaction is suppressed and the nonthermal broadening of the Landau levels is controlled by intrasubband e–e interaction. In addition to the modulation of the collisional-broadening time for the Landau levels, it is found that this time decreases nonmonotonically with an increase in the magnetic field. The cause of this decrease is related to the magnetic-field dependence of the time of electron–phonon relaxation.

Nonmonotonic dependences $\delta(1/B)$, similar to those shown in Fig. 1, were observed by Coleridge [1]. However, the discussion was restricted to comparison of an averaged approximation of $\delta^m(1/B)$ in the E_m subband with that of $\delta^p(1/B)$ in the E_p subband.

The observed modulation of electron–electron interactions by a magnetic field is accompanied by initiation or suppression of the intersubband component and is similar to stimulation of the intervalley transitions known as 2.5-order phase transitions [10].

REFERENCES

1. P. T. Coleridge, Phys. Rev. B **44**, 3793 (1991).
2. D. R. Leadley, R. Fletcher, R. J. Nicolas, *et al.*, Phys. Rev. B **46**, 12439 (1992).
3. R. M. Kusters, F. A. Wittenkamp, J. Singleton, *et al.*, Phys. Rev. B **46**, 10 207 (1992).
4. V. I. Kadushkin and F. M. Tsahhaev, Phys. Low-Dimens. Semicond. Struct., No. 1/2, 93 (2000).
5. V. I. Kadushkin and A. B. Dubois, Phys. Low-Dimens. Semicond. Struct., No. 7/8, 1 (2003).
6. V. I. Kadushkin, Fiz. Tekh. Poluprovodn. (St. Petersburg) **39**, 242 (2005) [Semiconductors **39**, 226 (2005)].
7. D. Shoenberg, *Magnetic Oscillations in Metals* (Cambridge Univ. Press, Cambridge, 1984; Mir, Moscow, 1986).
8. V. I. Kadushkin, Fiz. Tekh. Poluprovodn. (St. Petersburg) **38**, 412 (2004) [Semiconductors **38**, 397 (2004)].
9. D. R. Leadley, R. J. Nicholas, J. J. Harris, and C. T. Foxon, Semicond. Sci. Technol. **5**, 1061 (1990).
10. V. A. Kozlov, E. E. Narimanov, and K. A. Sakharov, Fiz. Tverd. Tela (St. Petersburg) **36**, 309 (1994) [Phys. Solid State **36**, 168 (1994)].

Translated by A. Spitsyn

AMORPHOUS, VITREOUS,
AND POROUS SEMICONDUCTORS

A Study of the Local Electronic and Atomic Structure in a-Si$_x$C$_{1-x}$ Amorphous Alloys Using Ultrasoft X-ray Emission Spectroscopy

V. A. Terekhov*^, E. I. Terukov**, I. N. Trapeznikova**, V. M. Kashkarov*, O. V. Kurilo*, S. Yu. Turishchev*, A. B. Golodenko*, and É. P. Domashevskaya*

*Voronezh State University, Voronezh, 394006 Russia
^e-mail: root@ftt.vsu.ru
**Ioffe Physicotechnical Institute, Russian Academy of Sciences, St. Petersburg, 194021 Russia
Submitted September 24, 2004; accepted for publication October 12, 2004

Abstract—X-ray spectroscopy has been used to obtain data on the local electronic and atomic structure of a-Si$_x$C$_{1-x}$:H(Er) alloys produced by plasma-enhanced chemical vapor deposition (PECVD) with various relative amounts of silane and methane in the gas mixture ($x = 0.3$–0.9). It is shown that the alloys contain silicon and carbon atoms in different coordination environments. Silicon is observed as elementary amorphous silicon and silicon carbide, and the relative amounts of these phases in the films depend on the composition of the gas mixture. Carbon atoms can form bonds with silicon in a coordination close to that found in crystalline silicon carbide, with a noticeable amount of C–H bonds also appearing. In addition, carbon can form an elementary carbon phase with various coordination numbers characteristic of graphite and diamond in the film. © 2005 Pleiades Publishing, Inc.

Amorphous a-SiC:H alloys are of particular interest in their role as wide-bandgap materials for electronics and solar power engineering and as materials for wear-resistant coatings. In addition, they deserve special attention from the standpoint of the physics of disordered systems, as various types of compositional disorder can be created in them.

The aim of this study was to obtain, using X-ray spectroscopy methods, data on the local electronic and atomic structure of a-Si$_x$C$_{1-x}$:H(Er) alloys prepared by plasma-enhanced chemical vapor deposition (PECVD) with various relative amounts of silane and methane in the gas mixture ($x = 0.3$–0.9).

Information about the energy distribution of silicon valence electrons in the films under study was obtained from Si $L_{2,3}$ emission spectra (soft X-ray emission spectroscopy (SXES)), which reflect the distribution of the density of $3s$ states of Si, recorded with an RSM-500 spectrometer-monochromator. Data on the type of density-of-states distribution for silicon and carbon near the bottom of the conduction band were obtained from spectra of the quantum yield of X-ray photoemission near the Si $L_{2,3}$ and C K edges (provided by X-ray absorption near-edge structure (XANES) spectroscopy). These spectra yield information about the near-edge fine structure of X-ray absorption by a-Si$_x$C$_{1-x}$:H(Er) and reflect the distribution of Si $3s$ states and C $2p$ states in the conduction band. The XANES spectra were recorded on the Russo-German channel of the BESSY-II synchrotron.

The energy distribution of the emission intensity $I(E)$ depends on the number of electrons that have passed from a certain region of the valence band to a core level vacancy and is described by the expression

$$I(E) \propto \sum_f \delta(E - E_f)|M_{0f}|^2, \qquad (1)$$

where $M_{0f} = \int \psi_0^* H' \psi_f dr$ is the matrix element for the transition from an f state in the valence band, characterized by the wave function ψ_f and energy E_f, to a core level with the wave function ψ_0, and H' is the electromagnetic field perturbation operator. The total density of electronic states $g(E)$ is given by the expression

$$g(E) = \frac{1}{V}\sum_f \delta(E - E_f), \qquad (2)$$

where V is volume.

Comparison of expressions (1) and (2) suggests that, because of the strong localization of the core function ψ_0 of an emitting atom, the intensity $I(E)$ reflects the density of electronic states whose wave functions make a noticeable contribution in the vicinity of this atom, i.e., the energy distribution of the local density of electronic states [1, 2].

Data on the distribution of states in the conduction band were obtained from the spectral dependence of the quantum yield of photoemission in the X-ray range,
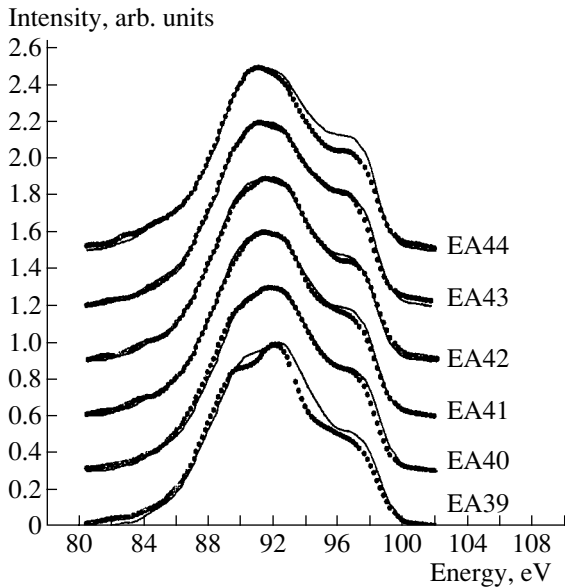
Fig. 1. Si $L_{2,3}$ X-ray emission spectra of the samples under study: (points) experimental data and (solid lines) the result of modeling.
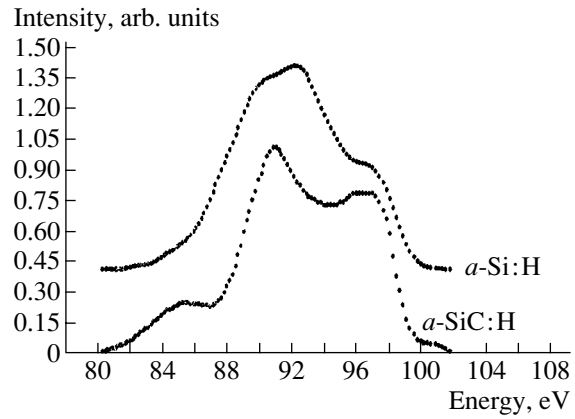

Fig. 2. Si $L_{2,3}$ emission spectra of the references used in modeling the spectra of the films.

which is proportional to the absorption coefficient μ near the absorption edges:

$$\mu(E) \propto \sum_{k} \delta(E - E_k)|M_{k0}|^2. \qquad (3)$$

Emission spectra of various samples of a-Si$_x$C$_{1-x}$:H(Er) alloys are shown in Fig. 1. The compositions of the initial gas mixture, normalized to unity, are listed in the table. It can be seen that the shape of the spectra varies in response to the composition of the gas mixture. In order to analyze this variation, which reflects the variation of the phase composition of the films, these spectra were compared with typical spectra of a-Si:H and a-SiC:H, which were used as reference spectra (Fig. 2).

The spectrum of amorphous hydrogenated silicon a-Si:H has the following characteristic shape: a broad main peak at 89–92 eV, which corresponds to Si 3s states, and a rather strong shoulder in the a-Si:H spec-

trum to the right of the main peak, which is due to hybridization of the Si 2s state and Si 3p states constituting the top of the valence band.

The spectrum of amorphous silicon carbide has three characteristic peaks. The main peak, with the highest intensity, is associated with Si 3s states and lies at ~91 eV. A broader and less intense peak corresponding to the 2p states of carbon, hybridized with Si 3s states, lies at 96 eV. The third feature, a weakly pronounced peak at 85 eV, corresponds to C 2s states with an admixture of Si 3s states.

Visual analysis of the spectra in Figs. 1 and 2 shows that, as we would expect, the spectrum of sample EA39, which had the lowest content of carbon, is close to the reference spectrum of a-Si:H. As the concentration of carbon in the gas mixture increases, the shape and position of the peaks in the spectra of the samples under study gradually change, acquiring a number of features characteristic of the spectra of a-SiC:H. In order to quantitatively account for the data thus observed, a phase analysis of the samples was performed using the procedure described in [3], which consists in mathematical modeling of the spectra of the samples under study on the basis of the spectra of the reference samples of a-Si:H and a-SiC:H (Fig. 2).

Phase composition of a-Si$_x$C$_{1-x}$: H⟨Er⟩ films in relation to the composition of the gas mixture

Sample no.	Composition of the gas mixture		Amount of a reference phase, %		Error, %	Type of coordination of C atoms	Phase composition of samples	C–H
	SiH$_4$	CH$_4$	a-Si:H	a-SiC:H				
EA39	0.9	0.1	100	–	5	SiC	a-Si:H, SiC, C–H	+
EA40	0.8	0.2	87	13	2	$sp^2 + sp^3$	a-Si:H, a-SiC:H, C($sp^2 + sp^3$)	–
EA41	0.7	0.3	79	21	3	SiC	a-Si:H, a-SiC:H, SiC, C–H	+
EA42	0.6	0.4	83	17	3	$sp^2 + sp^3$	a-Si:H, a-SiC:H, C($sp^2 + sp^3$)	–
EA43	0.4	0.6	74	26	4	$sp^2 + sp^3$	a-Si:H, a-SiC:H, C($sp^2 + sp^3$)	–
EA44	0.3	0.7	66	34	6	SiC	a-Si:H, a-SiC:H, SiC, C–H	+
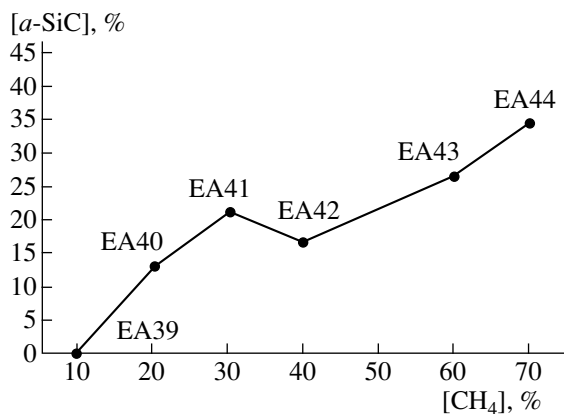
Fig. 3. Content of *a*-SiC vs. the amount of CH$_4$ in the gas mixture for samples EA39–EA44.

Fig. 4. Si $L_{2,3}$ XANES spectra: (a) *a*-Si$_x$C$_{1-x}$:H samples produced from gas mixtures with various relative amounts of the components and (b) a typical sample (EA42) and reference samples of *c*-Si, *a*-Si:H, and SiO$_2$.

The results of this modeling are shown in Fig. 1 (solid line) in comparison with the experimental spectra (points). It can be seen that the model spectra are in good agreement with the experimental data. Therefore, it can be stated that the relative amounts of *a*-Si:H and *a*-SiC:H phases, listed in the table, are close to the true values. The variation of the phase composition, shown in Fig. 3, reflects the tendency toward formation of *a*-SiC:H in the samples in response to a change in the composition of the gas mixture.

Thus, the mathematical analysis confirms that, for all the samples prepared from gas mixtures containing 10 to 70% CH$_4$, the composition of the films is at least two-phase and the silicon atoms have two different local environments: one close to that in elementary amorphous silicon and the other similar to that in stoichiometric silicon carbide. As the content of carbon in the alloy increases (from sample EA39 to EA44), the fraction of the carbide phase rises to 35% at a 70% CH$_4$ concentration in the gas phase.

The absorption spectra silicon $L_{2,3}$ (XANES) confirm that *a*-Si:H and carbide phases are present in the samples. Figure 4a shows Si $L_{2,3}$ XANES spectra of the films under study and Fig. 4b shows spectra of the reference samples of crystalline Si (*c*-Si), *a*-Si:H, and SiO$_2$. The spectra of the X-ray photoemission from SiC (α and β modifications), used here as reference spectra, were reported in [4, 5].

A comparative analysis demonstrated the presence of two types of spectra:

(1) For some of the samples (EA39 and EA44), the main peak lies at around 107–107.5 eV and weak shoulders are present at 104.5 and 105.5 eV. These features become more pronounced as the concentration of carbon in the gas mixture is raised. One more shoulder at 108.5 eV (position of the main peak in SiO$_2$ and common for surface states of Si) is smoothed out if we consider sample EA44 instead of sample EA39. This means that the type of local environment of the Si atoms is close to that characteristic of SiC.
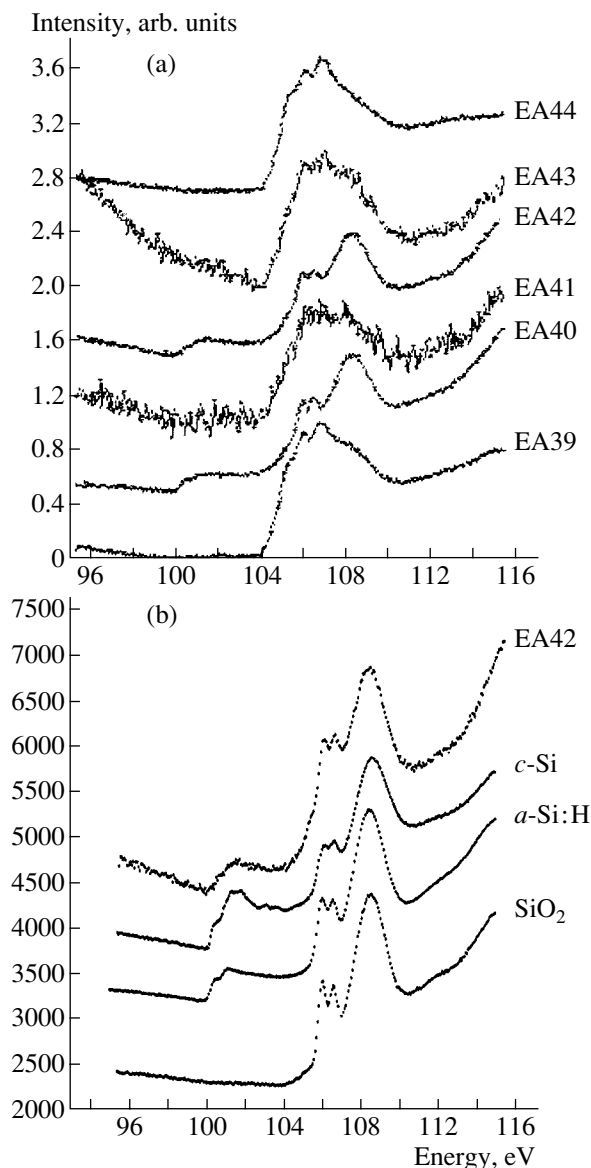
(2) For other samples (EA40 and EA42), the shape of the spectrum and the energy position of the spectral features, as well as that of the absorption edge (~100 eV), are similar to those observed for the *a*-Si:H reference, which confirms that an amorphous silicon phase predominates in these films. A weak shoulder at 104.4–105.5 eV reveals the presence of a minor amount of carbon in the Si environment.

(3) The spectra of samples EA41 and EA43 show features of both types, which may indicate that a carbon layer (up to 5 nm thick) is possibly present on the surface of the two-phase films.
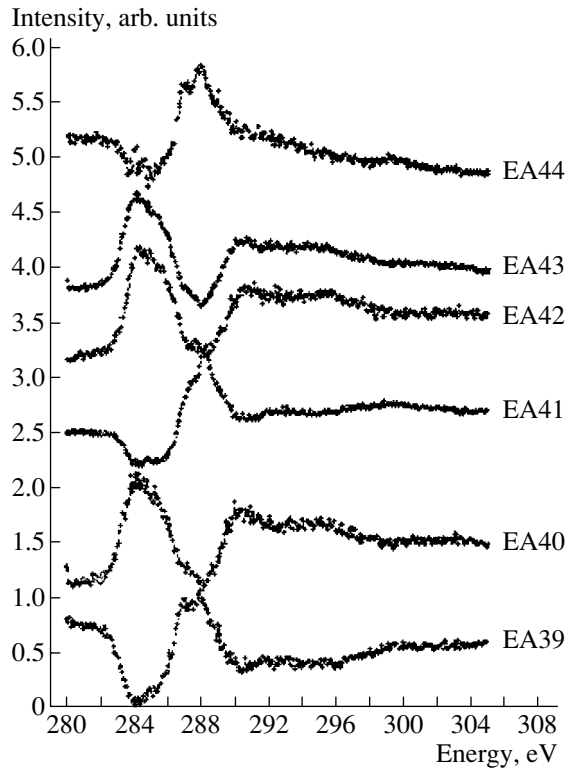
Fig. 5. C K XANES spectra of the a-Si$_x$C$_{1-x}$:H samples under study.

Fig. 6. C K XANES spectra of typical samples and reference samples: a-Si$_{0.4}$C$_{0.6}$:H(Er) (EA43 film), a-Si$_{0.7}$C$_{0.3}$:H(Er) (EA41 film, diamond, SiC, and graphite) [6]; and two-phase CVD diamond film [8].

Analysis of the C K absorption spectra (XANES) shown in Fig. 5 demonstrates the existence of two types of spectra, which do not show any gradual variation in their shape in response to the composition of the gas phase (nor do the Si $L_{2,3}$ XANES spectra of these films). Comparison of the spectra with the published data [6–8] suggests the following:

(i) In some of the samples (EA39, EA41, and EA44), the main absorption edge lies at ~287 eV, which is close to the position of the main absorption edge of crystalline SiC (~286 eV), but the spectrum contains an additional peak at 288 eV, which is associated with C–H bonds [7]. Therefore, the local environment of carbon is close to that characteristic of silicon carbide.

(ii) Other samples (EA40, EA42, and EA43) show two types of carbon coordination: diamond-like sp^3 (a broadened absorption edge at about 290 eV) and graphite-like sp^2 (a broad peak at 284–286 eV, characteristic of graphite). The spectra obtained are close to those of the two-phase films studied in [8].

Thus, the results obtained indicate that carbon may have different coordination numbers in the films studied.

The data obtained are summarized in the table, which lists the following: the phase composition of the films (relative amounts of a-Si:H and a-SiC:H), found by means of a modeling analysis of the emission spectra of the films in comparison with reference spectra,

and the accuracy of these determinations (Figs. 1–3); coordination of carbon atoms, found by analysis of C K XANES spectra in Figs. 5 and 6; data on the existence of C–H bonds, indicated by the characteristic peak at 288 eV in the C K XANES spectra (Fig. 5); and phase composition of the a-Si$_x$C$_{1-x}$:H(Er) films under study (in the summarizing eighth column).

Thus, the results obtained in our study of a-Si$_x$C$_{1-x}$:H(Er) films PECVD-grown from gas mixtures with various relative amounts of the components SiH$_4$ and CH$_4$ demonstrated that the films incorporate silicon and carbon atoms with different coordination numbers. Silicon is observed as elementary amorphous silicon and silicon carbide, and the relative amounts of these phases in the films depend on the composition of the gas mixture. Carbon atoms can form bonds with silicon in a coordination close to that found in crystalline silicon carbide, with a noticeable amount of C–H bonds also being formed. In addition, carbon can form a phase of elementary carbon with different coordinations of atoms, characteristic of both graphite and diamond, in the films.

REFERENCES

1. *The Physics of Hydrogenated Amorphous Silicon*, Ed. by J. D. Joannopoulos and G. Lucovsky (Springer, New York, 1984; Mir, Moscow, 1988), Part 2.

2. V. A. Nemoshkalenko, *Theoretical Fundamentals of X-ray Emission Spectroscopy* (Naukova Dumka, Kiev, 1974) [in Russian].

3. É. Yu. Manukovskiĭ, Candidate's Dissertation (Voronezh, 2000).

4. V. A. Fomichev, I. I. Zhukova, and I. K. Polushina, J. Phys. Chem. Solids **29**, 1025 (1968).

5. V. A. Fomichev, Fiz. Tverd. Tela (Leningrad) **9**, 3034 (1967) [Sov. Phys. Solid State **9**, 2398 (1967)].

6. M. M. Garcia, I. Jimenez, L. Vazquez, *et al.*, Appl. Phys. Lett. **72**, 2105 (1998).

7. M. Lubbe, P. R. Bressler, W. Braun, *et al.*, J. Anal. Chem. **361**, 602 (1998).

8. Y. Muramatsu, H. Takenaka, Y. Ueno, *et al.*, als.lbl.gov/als/compendium/AbstractManager/frontend/pagAuthors2.php?PersonID=10.

Translated by M. Tagirdzhanov

Optical and Electrical Properties of Thin Wafers Fabricated from Nanocrystalline Silicon Powder

N. N. Kononov*^, G. P. Kuz'min*, A. N. Orlov**, A. A. Surkov*, and O. V. Tikhonevich*

*Prokhorov General Physics Institute, Russian Academy of Sciences, ul. Vavilova 38, Moscow, 119991 Russia
^e-mail: nnk@kapella.gpi.ru
***Natural Sciences Center at the Prokhorov General Physics Institute, Russian Academy of Sciences,
ul. Vavilova 38, Moscow, 119991 Russia*
Submitted October 25, 2004; accepted for publication November 29, 2004

Abstract—The infrared transmittance spectra and dark conductivity of wafers fabricated from nanocrystalline silicon powder (nc-Si) have been studied. The initial nc-Si powder is first synthesized by laser-induced silane dissociation, with the temperature of the surrounding buffer gas varied from 20 to 250°C, and then compacted at pressures from 10^8 to 10^9 Pa. It is found that compaction of the nc-Si powder results in formation of Si–H, Si–CH$_x$, and O$_y$–Si–H$_x$ structures ($x, y = 1$–3). The formed structures break down under annealing, with the Si–H and Si–CH$_x$ complexes disintegrating at the lowest annealing temperature ($t = 160$°C). The dark conductivity of the nc-Si wafers is shown to increase along with the buffer gas temperature at which the starting powder was prepared. Two temperature regions are found in which the dark conductivity behaves in radically different ways. At wafer temperatures $T \geq 270$ K, conductivity is mediated by free carriers, whereas, at lower temperatures, electron transport is governed by hopping conduction over localized states in the band gap. © 2005 Pleiades Publishing, Inc.

1. INTRODUCTION

Nanocrystalline silicon (nc-Si) is a promising material in relation to the production of optoelectronic devices (such as solar cells and thin-film transistors [1], gas sensors [2, 3], and nanostructured ceramic material [4]).

The structural element most frequently employed in studies of the properties of nanocrystalline silicon is thin (10–100 nm) films deposited on various substrates. The technology used to fabricate such films is based on deposition of Si clusters onto a substrate. The clusters are formed in an RF discharge plasma as a result of the dissociation of silane molecules (plasma-enhanced chemical vapor deposition (PECVD)).

Silane molecules (SiH$_4$) can also be dissociated by heating a silane jet with radiation from a CW CO$_2$ laser (laser-induced chemical vapor deposition (LICVD)). This heating is made possible by the fact that the most intense CO$_2$ laser emission lines, for instance, $P(18)$ and $P(20)$ (which have wave numbers $\nu_{18} = 945.98$ cm^{-1} and $\nu_{20} = 944.19$ cm^{-1}), are found in the absorption band of SiH$_4$ molecules. This band is related to bending vibrations and is centered near the wave number $\nu_{SiH_4} = 970$ cm^{-1} [5]. However, since the center of this band and the intense laser emission lines are widely spaced, the absorption in silane is not sufficiently strong, which reduces the laser-induced heating efficiency. This difficulty can be surmounted by obtaining lasing at other rotational levels of the 00^01–10^00 vibrational transition in CO$_2$ molecules with the use of a diffraction grating

installed in the CO$_2$ laser cavity; however, this procedure would involve unavoidable laser power losses and a corresponding increase in technological costs.

In order to attain noticeable absorption of CO$_2$ laser radiation, it is necessary to maintain a sufficiently high pressure in the silane jet. Since the transverse expansion of the jet characteristic of LICVD is restricted by the coaxial flow of a buffer gas (argon or helium) that propagates parallel to the jet and is involved in the formation of silicon particles, it is also necessary to maintain a fairly high pressure of the buffer gas in the reactor chamber. For this reason, the technology involved in the preparation of nanosized Si particles associated with CO$_2$-laser-induced decomposition of silane can be realized only at reactor buffer gas pressures of $\gtrsim 100$ Torr. At the same time, as has been shown by numerous studies (see, e.g., [6]), the average particle size, when all the other conditions are equal, increases with the buffer gas pressure in the reactor chamber. Therefore, this technology permits preparation of Si powder with a maximum in the particle-size distribution in the region of $\gtrsim 10$ nm.

In order to reduce the buffer gas pressure but maintain the level of laser radiation absorption in the silane jet, we heated the buffer gas in the area of nanoparticle formation to a temperature of 200–300°C. This heating gave rise to an increase in the original silane jet temperature and a substantial rise in the absorption of the CO$_2$ laser radiation in the jet. As a result, we succeeded in initiating an optical discharge at buffer gas pressures
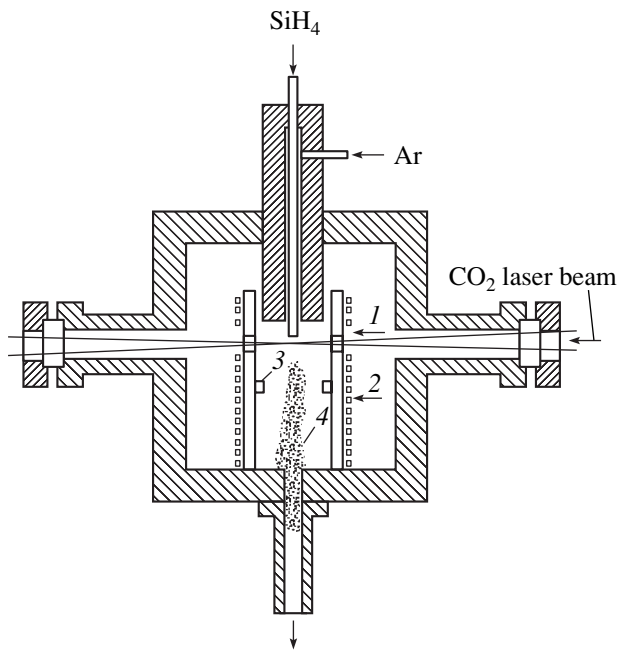
Fig. 1. Schematic representation of the chamber used in the synthesis of the nanocrystalline silicon powder. (*1*) A quartz cylinder, (*2*) a heater for the buffer gas flow, (*3*) a thermocouple, and (*4*) the synthesized *nc*-Si powder.

≥ 50 Torr at a focused laser radiation intensity of $\sim 10^3$ W/cm^2.

By increasing the buffer gas temperature in the synthesis zone, we can also control the structure of the forming Si particles. This effect is primarily due to the enhanced diffusive mobility of the Si atoms, which accounts for the formation of nanocrystals with a lower defect concentration [7]. In addition, at higher buffer gas temperatures, hydrogen atoms present in the products of the silane dissociation penetrate more intensively into the Si nanoparticle network, as they passivate lattice defects, such as monovacancies and divacancies, that are formed in the course of particle synthesis.

2. EXPERIMENTAL

The initial powdered samples of nanosized silicon were obtained in a gas dynamic reactor at SiH$_4$ and Ar (used as the buffer gas) flow rates of 100 and 1000 cm^3/min, respectively. The average particle size in *nc*-Si powder samples prepared at a buffer gas temperature $t_{Ar} = 20°C$ was ~ 20 nm [8].

Near the zone where the nanoparticles were produced, the buffer gas was heated to 300°C by a Nichrome spiral, which was contained in a high-temperature ceramic material mounted on a vertical cylindrical quartz cup. The gas temperature was measured using a thermocouple fixed on the inner cup wall (see Fig. 1). The opposite sides of the cup were pierced by

holes to let the focused CO$_2$ laser beam heating the silane jet pass through.

Powder samples contained in a special hardened-steel die were compacted at pressures ranging from 10^8 to 10^9 Pa, which produced disc-shaped wafers that were 50- to 100-μm thick and 1 cm in diameter.

The *nc*-Si wafers and initial powder samples were annealed in an argon atmosphere at temperatures of up to 400°C and in vacuum at up to 800°C.

The transmittance spectra of the initial *nc*-Si powder and of the wafers fabricated from it were measured with a Specord-800 double-beam spectrophotometer with a resolution of 4 cm^{-1}.

In order to measure the dark conductivity, the nanocrystalline silicon wafers were clamped between two titanium discs with a diameter of 1 cm, which served as electrodes. The titanium electrodes were chosen, after a series of measurements with electrodes compossed of different metals, because they exhibited the lowest contact resistance (0.8 Ω) when brought in contact with reference wafers of doped crystalline *n*-Si with a resistivity of 10 Ω cm.

The dark conductivity measurements were performed during the first three hours after the preparation of the powder and fabrication of the wafers when the surface oxide layer was still sufficiently thin. The ohmic character of the titanium/*nc*-Si contacts was confirmed by the linear run of the *I–V* curve for each sample. In order measure the current passing through an *nc*-Si wafer, it was connected in series to a precision resistor and the voltage drop across this resistor was then measured using a Shch-68003 high-resistance voltmeter. The sign of the thermopower, when determined in the same geometry, showed that all the wafers had *n*-type conductivity.

3. INFRARED ABSORPTION SPECTRA

The transmittance spectra of the initial *nc*-Si samples prepared at different buffer gas temperatures differ very little from each other and contain very poorly pronounced vibrational bands (Fig. 2, curve *1*). Compaction of the powder, however, initiates formation of intense absorption bands centered at 2070, 2170, 2210, 2850, 2930, 2990, and 3420 cm^{-1} (identified with arrows).

A characteristic feature of the absorption peak near 2070 cm^{-1} is the dependence of its height on the buffer gas temperature t_{Ar} in the nanoparticle formation zone. Figure 2 shows the transmittance spectra of wafers fabricated from *nc*-Si powders synthesized at different buffer argon flow temperatures (curves *2*, *3*). A comparison of these spectra shows that the intensity of the peak at 2070 cm^{-1} is noticeably higher than the intensities of the peaks located near 2170 and 2210 cm^{-1} if the initial powder was formed at a higher temperature. Since the band at 2070 cm^{-1} is related to vibrational absorption by Si–H bonds [9], the increase in the peak height sug-

gests that the hydrogen concentration in the *nc*-Si powder samples synthesized at higher temperatures is higher.

Annealing the wafers in an argon atmosphere for 30 min results in the disappearance of the peaks centered at 2070, 2170, 2850, 2930, and 2990 cm^{-1}, with the annealing temperature needed for the 2070, 2850, 2930, and 2990 cm^{-1} peaks to vanish being low ($t = 160°C$) whereas the 2170 cm^{-1} peak disappears only at temperatures above 300°C.

At the same time, the absorption intensity in the peak at 2210 cm^{-1} hardly changes if the wafer is annealed in argon up to $t = 300°C$. Noticeable changes in the shape of this peak are observed to occur after the annealing temperature reaches 400°C. Annealing in vacuum for 30 min at 700°C results in complete disappearance of this peak. At argon annealing temperatures above 400°C, the broad absorption band centered at 3420 cm^{-1} noticeably decreases in height; interestingly, the disappearance of this band is accompanied by formation of a fairly narrow peak at a wave number of 3750 cm^{-1}.

The peak at 2210 cm^{-1} is related to vibrational absorption in the O_3–Si–H structures [10, 11], and the absorption band at 2170 cm^{-1} may be associated with the existence of both SiH_2–SiH_3 chain structures [12] and O_2–Si–H_2 groups [13]. In order to identify which of these structural groups accounts for the band, we performed a comparative analysis of the transmittance spectra of a wafer annealed in argon and of another wafer fabricated from *nc*-Si powder that was preannealed in the same conditions (see Fig. 2, curves *5* and *4*). It was found that preannealing the powder barely affects the intensity of the absorption bands centered at 2210 and 3420 cm^{-1}, whereas the other bands can be eliminated by this procedure. Hence, the 2210 and 3420 cm^{-1} bands are thought to originate from the presence of structural oxygen-containing bonds in the nanosized-silicon wafers. The change observed in the intensity of the absorbance peak centered at 2170 cm^{-1} and associated with the wafer made of preannealed powder occupies an intermediate place in the dynamics between the bands at 2210 and 3420 cm^{-1} and the other absorption bands. More specifically, the height of the 2170 cm^{-1} peak associated with the preannealed starting powder decreases relative to that of the 2210 cm^{-1} peak, but the decrease in the absorption is substantially smaller than that of the other peaks. We may therefore safely maintain that the peak at 2170 cm^{-1} is also accounted for by the presence of oxygen-containing bonds, i.e., of O_2–Si–H_2 groups, in the structural network of nanoparticles in the wafer under study. If the band centered at 3420 cm^{-1} is assigned to vibrational absorption by water molecules [5], the most probable cause of the appearance of the above peaks is exposure of the initial powder to a moisture-containing atmosphere.

Water adsorption on the surface of the nanoparticles may also be responsible for the absorbance peak near 3750 cm^{-1}, which, as has already been mentioned,
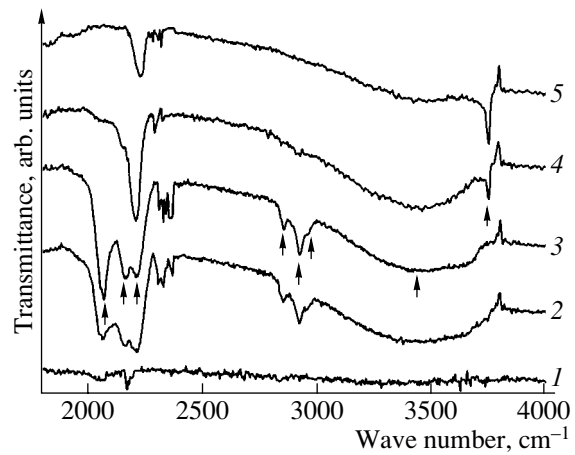

Fig. 2. Infrared transmittance spectra of (*1*) the initial powder and (*2–5*) *nc*-Si wafers prepared at a pressure of 5×10^8 Pa. The argon temperature at which the initial *nc*-Si powder samples were prepared $t_{Ar} = (1, 2)$ 20 and (*3–5*) 200°C. Spectrum *4* corresponds to the case where the initial powder was annealed at 400°C for 30 min, and spectrum *5* was obtained after the wafer was annealed at 400°C for 30 min.

appears in the spectra of the wafers annealed at temperatures $t > 400°C$. According to [14, 15], this peak can be assigned to vibrational absorption by O–H groups in ≡Si–OH bonds. Such bonds form, in this case, in the reaction $H_2O + ≡Si–O–Si≡ \longrightarrow ≡Si–OH + HO–Si≡$.

We attribute the peaks at the wave numbers 2850, 2930, and 2990 cm^{-1} to vibrational absorption by the CH_x groups ($x = 1$–3) in the Si–CH_x structures [16]. Remarkably, the Si–CH_x absorbance peaks in the wafers increase in intensity as the exposure time of the initial powder to air increases. This behavior implies that *nc*-Si powder intensively adsorbs the carbon present in air. A similar property has been found in nanosized particles obtained by ultrasonic comminution of samples of porous silicon [16].

Thus, strong compaction of the nanocrystalline powder gives rise to efficient formation of bonds between silicon, hydrogen, oxygen, and carbon atoms. We attribute this process primarily to rupture of the Si–Si structural bonds in the compacted powder. This rupture brings about the creation of a noticeable concentration of unsaturated silicon atom valence bonds that subsequently become saturated and form Si–H, O_y–Si–H_x, and Si–CH_x structures.

4. DARK CONDUCTIVITY

Figure 3 shows the dependences of dark conductivity σ on reciprocal temperature $1/T$ for two wafers formed from *nc*-Si powders that were synthesized at different temperatures in the buffer argon flow. For brevity, we henceforth refer to *nc*-Si powder samples prepared at temperatures $t_{Ar} = 20$ and 200°C as low- and high-temperature powders, respectively.
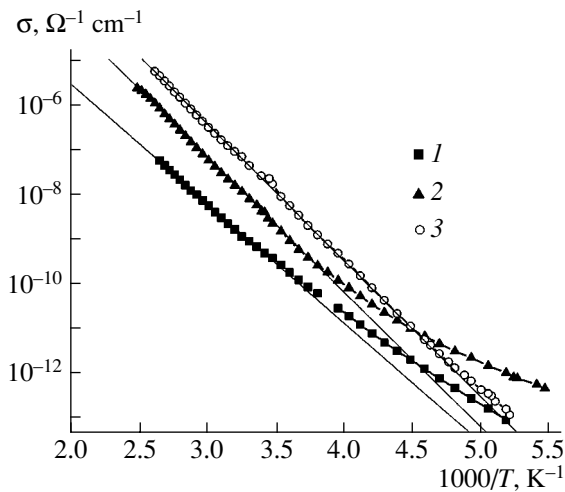
Fig. 3. Dark conductivity of the wafers vs. the reciprocal temperature $1/T$. The argon temperature at which the starting powder was prepared t_{Ar} = (*1*) 20 and (*2*, *3*) 200°C. Curve *3* corresponds to a wafer annealed in argon at 350°C for 1 h.
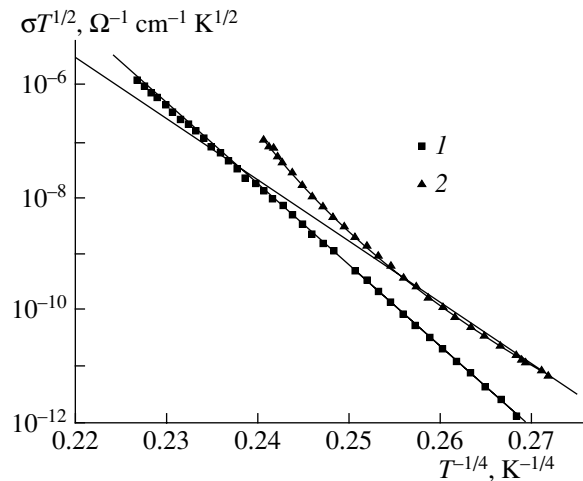

Fig. 4. Temperature dependences of wafers' conductivity plotted on the $\log(\sigma T^{1/2})$ –$T^{-1/4}$ scale. The argon temperature at which the starting powder was prepared t_{Ar} = (*1*) 20 and (*2*) 200°C (see Fig. 3, curves *1* and *2*).

The dependences show that the conductivity of the wafer formed from high-temperature powder exceeds that of the wafer made of low-temperature powder by nearly an order of magnitude. Curves *1* and *2* also show that, for both wafers, there exist two temperature domains in which the behavior of the dark conductivity obeys two different laws. In the temperature region $T >$ 270 K, the conductivity can be satisfactorily approximated by the relation $\sigma = \sigma_0\exp(-\Delta E/kT)$ (ΔE is the activation energy and k is the Boltzmann constant), whereas, at lower temperatures, deviation from this law is observed. Annealing the wafers in argon at temperatures $t > 300$°C results, however, in the exponential relation becoming a good approximation for the wafer dark conductivity practically throughout the entire temperature range under consideration, i.e., within the range 180 K $\leq T \leq$ 400 K (Fig. 3, curve *3*).

The values of dark conductivity at room temperature ($T = 290$ K), the constant σ_0, and the activation energy ΔE for the wafers fabricated from low- and high-temperature *nc*-Si powder, as well as for a wafer fabricated from high-temperature powder and subjected for 1 h to annealing in an argon environment at $t = 350$°C, are listed in the table. The conductivity of these wafers is described by curves *1*, *2*, and *3* in Fig. 3.

Conductivity of the wafers

Sample	t_{Ar}, °C	t, °C	σ, Ω^{-1} cm^{-1}	σ_0, Ω^{-1} cm^{-1}	ΔE, eV
1	20	–	4×10^{-10}	5.5×10^{-1}	0.53
2	200	–	2×10^{-9}	6.5×10^{1}	0.6
3	200	350	2×10^{-8}	4×10^{2}	0.6

As can be seen from the table, room-temperature dark conductivity increases by an order of magnitude if the wafer was formed from high-temperature *nc*-Si powder and increases by another order of magnitude if the wafer was annealed in argon for an hour at $t =$ 350°C. At this point, it attains $\sigma = 2 \times 10^{-8}$ Ω^{-1} cm^{-1}, which is comparable to the characteristic conductivities of thin films of undoped amorphous silicon [17, 18].

The exponential temperature dependence of the conductivity suggests that electron transport at temperatures $T \gtrsim 270$ K in the samples under study involves free carriers. The corresponding activation energies ΔE are close to half of the band gap in crystalline silicon. The band gap for the low-temperature powder, which we derived from absorbance spectra in the visible region [8], is 1.1 eV. Since, for the wafer made of this powder, $\Delta E = 0.53$ eV, it can be maintained that the Fermi level in this wafer lies near the midgap.

At temperatures $T < 270$ K, we observe considerable deviations from the exponential law in the behavior of the dark conductivity. At the same time, on constructing the temperature dependences in the form $\log(\sigma T^{1/2})$ vs. $T^{-1/4}$ (see Fig. 4), we found that $\sigma = AT^{-1/2}\exp(-BT^{-1/4})$ is a good approximation. This relation gives grounds to assume that, for temperatures $T < 270$ K, carrier transport in the wafers is dominated by hopping conduction over localized states in the band gap near the Fermi level [17]. The origin of these states can be related, first, to unsaturated silicon valence bonds at the nanoparticle surfaces and, second, to lattice defects in the amorphous silicon component that is present in the initial powder [8].

The electronic density of states in the band gap near the Fermi level $N(E_F)$ was estimated from a numerical

analysis of the constants (*A* and *B*) that appear in the approximation relation for hopping conductivity. It was found that $N(E_F)$ for the wafer made of low-temperature powder is substantially larger than 10^{18} eV^{-1} cm^{-3}, which is characteristic of thin amorphous silicon films [17]. However, for the wafer fabricated from high-temperature powder, $N(E_F) \approx 4 \times 10^{15}$ eV^{-1} cm^{-3}, which is considerably less than the above value and is comparable to the density of states in almost defect-free polymorphic silicon [19, 20].

As was mentioned above, as a result of the wafer fabricated from high-temperature *nc*-Si powder being annealed in argon, its low-temperature conductivity acquires a band pattern (curve *3*, Fig. 3). This means that 1-hr annealing at a temperature $\gtrsim 350°C$ makes it possible to efficiently reduce the density of defect states by at least two orders of magnitude.

5. CONCLUSION

We studied the effects produced by compaction of nanocrystalline silicon powder under pressures of up to 10^9 Pa. The compacted wafers were up to 100 μm thick, consisted of *nc*-Si, and were found to be fairly strong. The *nc*-Si powder used in the preparation of these wafers could be produced at argon flow temperatures ranging from 20 to 250°C in the zone of synthesis.

The properties of the wafers were determined from a study of IR transmittance spectra and dark conductivity. It was found that compaction initiates the formation of bonds between silicon atoms, which are the basic constituents of the powder, and the atoms of hydrogen, oxygen, and carbon present on the surface of the silicon nanoparticles in these wafers. Wafers prepared from *nc*-Si powder synthesized at higher buffer argon temperatures reveal a more clearly pronounced hydrogen microstructure compared to those fabricated from low-temperature powder. Annealing a wafer in an argon environment brings about rupture of most of the bonds thus formed, with a low annealing temperature being required for rupture of the Si–H and Si–CH$_x$ ($x = 1$–3) bonds. Water molecules adsorbed on the surface of nanoparticles act as a source for the formation of Si–OH structural groups during the annealing process.

Investigation of the temperature dependence of the dark conductivity showed that, at temperatures $T \geq 270$ K, charge transport in the *nc*-Si wafers is effected by free carriers. For temperatures below 270 K, the carrier transport is effected by hopping conduction over localized states in the band gap near the Fermi level. A numerical analysis of the approximation relation characteristic of this type of conduction revealed that *nc*-Si powder prepared at higher buffer argon temperatures can be used to produce a material with a lower density of states in the band gap than that synthesized at lower temperatures. It is shown that the density of states in the band gap decreases substantially when the wafers are annealed at temperatures above 350°C.

We believe that optimization of the parameters at which the initial nanosized silicon powder is prepared and development of a sequence of technological processes for its doping will permit fabrication of wafers with properties meeting the requirements set for the structural components employed in photovoltaic devices and thin-film transistors.

REFERENCES

1. J. Meier, R. Fluckiger, H. Keppner, and A. Shar, Appl. Phys. Lett. **65**, 860 (1994).
2. O. I. Bomk, L. G. Ilchenko, V. V. Ilchenko, *et al.*, Sens. Actuators B **62**, 131 (2000).
3. V. Strikha, V. Skryshevsky, V. Polishuk, *et al.*, J. Porous Mater. **7**, 111 (2000).
4. J. Costa, P. Poura, J. K. Morante, and E. Bertran, J. Appl. Phys. **83**, 7879 (1998).
5. K. Nakamoto, *Infrared Spectra of Inorganic and Coordination Compounds* (Wiley, New York, 1963; Mir, Moscow, 1966).
6. P. Roca i Cabarrocas, S. Hammea, S. N. Sharma, *et al.*, J. Non-Cryst. Solids **227–230**, 871 (1998).
7. H. Shirai, T. Arai, and T. Nakamura, Appl. Surf. Sci. **113–114**, 111 (1997).
8. G. P. Kuz'min, M. E. Karasev, E. M. Khokhlov, *et al.*, Laser Phys. **10**, 934 (2000).
9. S. Shuppler, S. L. Friedman, M. A. Marcus, *et al.*, Phys. Rev. B **52**, 4910 (1995).
10. H. Richter and L. Ley, J. Appl. Phys. **52**, 7281 (1981).
11. Xi-Mao Bao, Xiang He, Ting Gao, *et al.*, Solid State Commun. **109**, 169 (1999).
12. M. H. Brodsky, M. Cardona, and J. J. Cuomo, Phys. Rev. B **16**, 3556 (1977).
13. H. Fujiwara, Y. Toyoshima, M. Kondo, and A. Matsuda, Phys. Rev. B **60**, 13598 (1999).
14. V. G. Plotnichenko, V. O. Sokolov, and E. M. Dianov, J. Non-Cryst. Solids **261**, 186 (2000).
15. T. D. Shen, I. Shmagin, C. C. Koch, *et al.*, Phys. Rev. B **55**, 7615 (1997).
16. R. A. Bley, S. M. Kanzlarich, J. E. Davis, and H. W. H. Lee, Chem. Mater. **8**, 1881 (1996).
17. N. F. Mott and E. A. Davis, *Electronic Processes in Non-Crystalline Materials*, 2nd ed. (Clarendon, Oxford, 1979; Mir, Moscow, 1982).
18. *Amorphous Semiconductors*, Ed. by M. H. Brodsky (Springer, New York, 1979; Mir, Moscow, 1982).
19. J. P. Kleider, C. Longeaud, M. Gautier, *et al.*, Appl. Phys. Lett. **75**, 3351 (1999).
20. O. Saadan, S. Lebib, A. V. Kharchenko, *et al.*, J. Appl. Phys. **93**, 9371 (2003).

Translated by G. Skrebtsov

<div align="center">

**AMORPHOUS, VITREOUS,
AND POROUS SEMICONDUCTORS**

</div>

Magnetic Properties of Iron-Modified Amorphous Carbon

S. G. Yastrebov*^, V. I. Ivanov-Omskiĭ*, V. Pop,
C. Morosanu***, A. Slav***, and J. Voiron******

*Ioffe Physicotechnical Institute, Russian Academy of Sciences, Politekhnicheskaya ul. 26, St. Petersburg, 194021 Russia
^e-mail: yastrebov@mail.ioffe.ru
**Babes-Bolyai University, 400084 Cluj-Napoca, Romania
***National Institute for Material Physics, P.O. Box MG-7, R-76900 Magurele, Bucharest, Romania
****Laboratoire L. Néel, 25 Avenue des Martyrs, BP166, 38042 Grenoble, France
Submitted December 8, 2004; accepted for publication December 22, 2004

Abstract—The structure and magnetic properties of films of iron-modified amorphous carbon (*a*-C:Fe) prepared by magnetron cosputtering of iron and graphite targets are studied. X-ray diffraction measurements show that iron enters the samples in the form of Fe nanocrystals that are typically about 20 nm in size and also forms nanocrystals of hexagonal iron carbide. The temperature dependences of the magnetization, measured under cooling in zero and nonzero magnetic fields, are studied. At temperatures $T \lesssim 8$ K, a magnetic transition, which provides evidence for the onset of magnetic ordering in the material, is observed to occur. The magnetization isotherms obtained in the 8- to 20-K temperature range are in agreement with this observation. It is shown that a modified version of Langevin's formalism adequately describes the observed features of *a*-C:Fe film magnetization. © 2005 Pleiades Publishing, Inc.

1. INTRODUCTION

Introduction of a magnetic metal into carbon in the form of nanosized clusters, a process frequently called encapsulation, favors their stabilization and protects them against corrosive attack from an ambient medium. Materials containing such embedded clusters have good prospects for application in systems for ultrahigh-density magnetic recording [1–5].

In this paper, we report the results of studying the structure and magnetic properties of films containing more than 60 at % of iron, which is far above the percolation threshold of exchange interaction between atoms and their clusters.

2. FILM COMPOSITION AND STRUCTURE

Iron clusters were encapsulated into films of amorphous carbon (*a*-C:Fe) by RF magnetron cosputtering of graphite and iron targets. The techniques used for sample preparation and iron concentration determination are described in detail in [6].

The elemental composition, thickness, and density of the films were determined by methods customarily employed in nuclear physics for elemental analysis, more specifically, by Rutherford backscattering spectrometry and nuclear reactions using a beam of deuterons with the energy $E_d = 1$ MeV [6]. The analysis showed that the samples have the concentration ratio [Fe]/[C] = 0.62 when there is a small amount of oxygen present ([O]/[C] = 0.05), a film thickness of 0.95 μm, and an average material density ρ = 3.9 g/cm³.

The structure of the *a*-C:Fe films was studied by X-ray diffraction with Cu–*K*α radiation using a Philips PW1050/2 diffractometer. The characteristic dimensions of coherent scattering regions for X-ray radiation were derived using the well-known Scherrer relation [7, 8]

$$D = \frac{K\lambda}{\Delta(2\theta)_i \cos\theta_{0i}}, \qquad (1)$$

where $K = 0.94$ is Scherrer's constant, D is the lateral dimension of the coherent scattering region, λ is the radiation wavelength (in our case, of Cu–*K*α radiation), 2θ is the scattering angle, θ_{0i} is the angle of the *i*th maximum in the diffraction pattern, and $\Delta(2\theta)_i$ is the half-width of the *i*th diffraction line.

Figure 1 shows the diffraction pattern of an *a*-C:Fe sample. An analysis of the lines in the diffraction pattern indicates that, in addition to the amorphous carbon matrix, elemental iron and iron carbide nanoclusters are present in the sample. Note the large number of α-Fe reflections in comparison with only two reflections due to hexagonal Fe_2C. This observation attests to the high structural quality of α-Fe nanoclusters and to the presence of a [100]-oriented texture. The fact that there are only two iron carbide reflections may indicate the low concentration, defect-rich state, or low structural dimensionality of this component. It is also conceivable that the carbide forms low-dimensional shells around the metal nanoclusters, similarly to the case of nickel nanoparticles described in [9].

The size of the clusters can be inferred from estimates of the sizes of the coherent scattering regions,

which were obtained using expression (1) and are listed in Table 1 for the main diffraction peaks. As follows from Table 1, the size of the nanoclusters ranges from a few nanometers to tens of nanometers.

Following [10], we succeeded in determining the size distribution functions for the nanoclusters. This procedure involves an algorithm used widely in analysis of small-angle X-ray scattering. We use the following relation for the wave vector s_i of radiation scattered within an angle 2θ:

$$s_i = \frac{4\pi \sin(\theta - \theta_{0i})}{\lambda}.$$

For an ensemble of clusters differing in shape, we can employ an approximate expression for the size distribution function:

$$D\left(s_i \approx \frac{2}{R_{gi}}\right) \approx \frac{s_i^4 I(s_i)}{\int_0^\infty t^3 i_0(t)dt}. \qquad (2)$$

Here, R_{gi} is the gyration radius of the ith ensemble of clusters (for instance, for a sphere, $R_g^2 = (3/5)R^2$, where R is the geometric radius of the cluster [10]), and $i_0(t)$ is the form factor. Since the particle shape is a priori not known, the expression relating the gyration radius to the geometric cluster radius is also unknown; therefore, the maximum cluster size obtained by applying expression (2) to the experimental data displayed in Fig. 1 was reduced to the value given in Table 1. The size distribution function of coherent X-ray scattering regions reconstructed in this way for the amorphous carbon matrix is shown in Fig. 2. We can clearly see that this function has a maximum at $D \approx 2$ nm and that the peak shape deviates markedly from a Gaussian curve, which implies manifestation of correlation effects during the formation of the amorphous matrix. The distribution functions for the iron and iron carbide nanoclusters are shown in Fig. 3. The size distribution of the iron nanoclusters attains a maximum at $D \approx 24$ nm, with the peak shape approaching that of a Gaussian curve. This observation suggests that the iron nanoclusters were formed under nearly equilibrium conditions. The latter statement correlates with the above observation on the high structural quality of the iron clusters and the small relative deviation of iron cluster size from its average value, as is indicated by the small width of the distribution function in Fig. 3. As can be seen from Fig. 3, the distribution for the iron carbide clusters is substantially wider and peaks at $D \approx 77$ nm. The latter estimate appears to be too large, possibly because of contributions from X-ray scattering mechanisms other than those associated with the size. In any case, this esimate is certainly inconsistent with the observation of a small
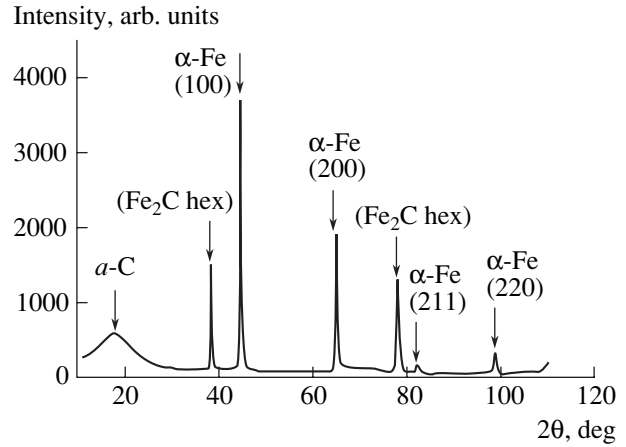
Fig. 1. Typical X-ray diffraction pattern of a sample of iron-modified amorphous carbon. The peak at 17.98° is related to the contribution from regions with coherent X-ray scattering in the amorphous carbon matrix to the total X-ray scattering; the peaks at 38.15° and 77.74° are contributions from iron carbide. The peaks at 44.40°, 64.85°, 82.20°, and 98.47° are due to scattering from the (110), (200), (211), and (220) α-Fe planes, respectively.
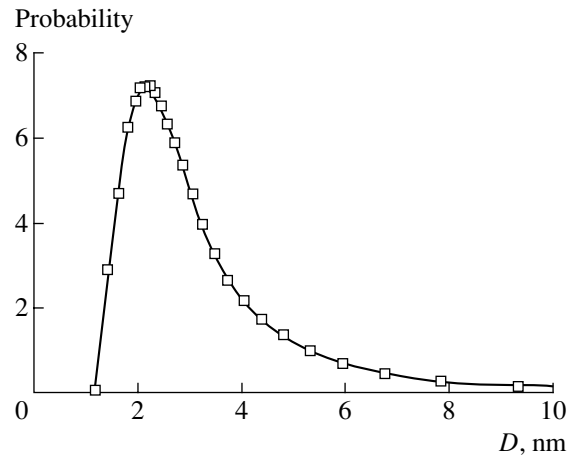

Fig. 2. Size distribution function for coherent scattering regions in the amorphous carbon matrix.

number of X-ray reflections from the iron carbide. With regard to the dimensions of the iron nanoclusters, the above estimate of 24 nm is close to the value reported in [11] (20 nm) for the diameter of a single-domain iron cluster.

Table 1

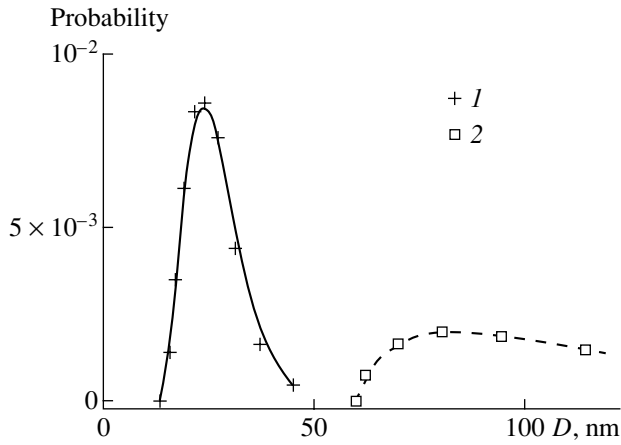| Peak in Fig. 1	Peak 2θ position (deg)	Peak half-width $\Delta(2\theta)_i$ (deg)	Lateral cluster size D, Å
a-C	17.98	3.97	20
(Fe$_2$C hex)	38.15	0.12	800
α-Fe	44.10	0.41	240

Probability

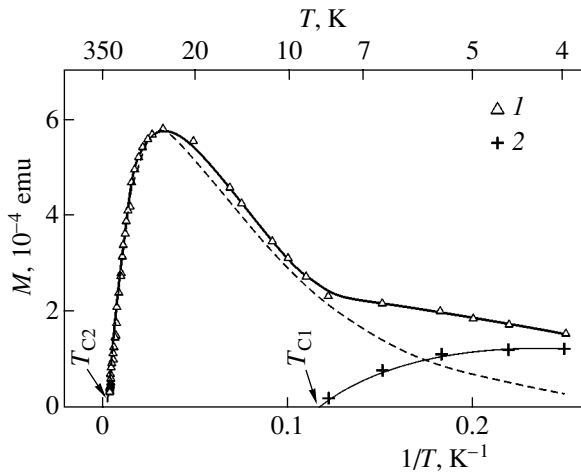**Fig. 3.** Size distribution function for the (*1*) α-Fe and (*2*) Fe$_2$C nanocrystals.

Fig. 4. Temperature dependences of the magnetic moment *M* measured in the ZFC mode. The open triangles represent experimental points; the dashed curve represents the contribution made to the magnetic moment by a magnetic cluster subsystem with a Curie temperature $T_{C2} \approx 330$ K calculated from Eq. (4); the crosses (*2*) show differences between the experimental points and calculated (dashed) curve; the thin solid line represents the fitting of the difference with Eq. (4); the bold solid line is sum of the dashed and thin solid lines; and the arrows identify the Curie temperatures of the two magnetic subsystems.

3. MAGNETIC PROPERTIES

The magnetization of the films under study was measured in a 10- to 300-K temperature range. The measurements were performed using a Quantum Design MPMS SQUID magnetometer in two operating modes. In the first mode (ZFC), the sample was cooled to 10 K in a zero magnetic field and was then heated to 300 K in a magnetic field $B = 0.01$ T. In the second mode (FC), the sample was both cooled and heated in a magnetic field $B = 0.01$ T. Magnetization isotherms were obtained using an Oxford Vibrating Sample Magnetometer.

The temperature dependence of magnetization *M* for the ZFC mode is shown in Fig. 4. An increase in temperature from 4 to 8 K brings about a slight increase in magnetization, which is then replaced by a faster rise at the inflection point ($T_{C1} \approx 8$ K). This point can be identified with the temperature of a phase transition or, in other words, the blocking temperature for the moment of interaction. In the temperature region 8 K < T < 30 K, the magnetization rises faster and attains a maximum at ≈30 K. As the temperature is increased still further to T > 30 K, the magnetization falls off linearly with reciprocal temperature. By extrapolating the experimental data to a zero magnetization on the reciprocal temperature axis, we can determine the temperature of yet another magnetic phase transition at $T_{C2} = 330$ K, which corresponds to complete magnetic disorder and is usually called the Curie temperature. The proportionality of magnetization to reciprocal temperature observed in this region suggests that a modified version of Langevin's formalism is most suitable for interpretation of the experimental data. The modification consists in taking into account the activation-type dependence of the concentration of free magnetic moments on temperature. We write the temperature dependence of this concentration as

$$n_j = n_{0j} \exp\left(-\frac{\Delta E_j}{kT}\right). \quad (3)$$

Here, ΔE_j is the activation energy that characterizes interaction among the magnetic moments; *k* is the Boltzmann constant; and n_{0j} is the concentration of free magnetic moments at the limit of $T \longrightarrow \infty$, with index *j* labeling the given magnetic moment subsystem.

In order to discriminate between the two contributions to the experimental temperature dependence of the magnetization corresponding to the two cluster subsystems ($j = 1, 2$) with characteristic average sizes of 20 and 70 nm, which were revealed in X-ray diffraction measurements, we use Langevin's formalism for the magnetization of a unit volume:

$$M_j = m_{0j} n_{0j} L(A_j) \exp\left(-\frac{\Delta E_j}{kT}\right). \quad (4)$$

Here, $L(A_j)$ is the Langevin function

$$L(A_j) = \frac{\exp A_j + \exp(-A_j)}{\exp A_j - \exp(-A_j)} - \frac{1}{A_j},$$

$$A_j = \frac{\varepsilon_j}{k}\left(\frac{1}{T} - \frac{1}{T_{Cj}}\right);$$

ε_j is the magnetization energy in a given magnetic field; m_{0j} is the component of spontaneous magnetic moments along the field direction; and T_{Cj} is the temperature of the *j*th magnetic phase transition.

Figure 4 presents, in addition to the experimental data, their fitting with Eqs. (3) and (4) (dashed line) using a previously determined Curie temperature $T_{C2} \approx$

330 K. We can clearly see that, at high temperatures, the experimental data are described adequately by the classical theory of paramagnetism. A noticeable difference appears below the temperature of the magnetization maximum. The deviation of the experimental magnetization from the calculations performed in terms of Langevin's formalism for the temperature T_{C2} is shown in Fig. 4 with crosses (*2*). This discrepancy indicates that spontaneous magnetization appears at temperatures below $T_{C1} \approx 8$ K, which can be identified with a second Curie point. By substituting this temperature into Eq. (4), we can adequately describe the low-temperature behavior of this contribution to the spontaneous magnetization, as is seen from the thin solid line in Fig. 4. Finally, inclusion of the contributions to the magnetization corresponding to the two magnetic moment subsystems (with the characteristic temperatures T_{C1} and T_{C2}) in Langevin's formalism completes the description of the temperature dependence of magnetization in the ZFC mode (the bold solid line in Fig. 4). The parameters obtained by least-squares fitting are listed in Table 2.

Let us now analyze the results of magnetization measurements performed in the FC mode (cooling in a magnetic field $B = 0.01$ T) and presented graphically in Fig. 5. As can be seen, when heated in a magnetic field $B = 0.01$ T, the FC magnetization of a sample is independent of temperature up to ≈ 27 K. As the temperature is further increased, the magnetization falls off (after a slight bend) in inverse proportion to the temperature and vanishes, as in the ZFC case, at $T_{C2} = 330$ K. The fitting of the experimental data to Eq. (4), with the parameters listed in Table 2 ($j = 3$), is shown in Fig. 5 by a solid line. This case corresponds to the paramagnetic state of a system of magnetic moments. The crosses in Fig. 5 represent deviation of the approximation from the experimental data. Note the similarity of this difference to the temperature behavior of the ZFC magnetization in Fig. 4, which can be attributed to a manifestation of spontaneous magnetization that cannot be suppressed by the magnetic field $B = 0.01$ T. The approximation of the difference values using Eq. (4), performed with the parameters from Table 2 for $j = 2$, is represented by the dashed line. The closeness of the parameters obtained in the two cooling modes for $j = 2$ indicates that the same subsystem of magnetic moments manifests itself in both experiments; moreover, interaction between these moments accounts for the spontaneous magnetization of the samples under study at low temperatures.

Thus, the experimental temperature dependence of the magnetization can be adequately fitted using Langevin's formalism for three magnetic-moment subsystems with different types of exchange coupling, which brings about the formation of two subsystems with spontaneous magnetization at the Curie temperatures $T_{C1} \approx 8$ K and $T_{C2} \approx 330$ K.

Figure 6 shows magnetization isotherms for one of the samples under study. At temperatures $T \approx T_{C1}$, we

Table 2

Cooling mode	Sub-system index	$m_{0j}n_{0j}$, emu	ε_j, eV	ΔE_j, eV	T_{Cj}, K
ZFC	1	3.9×10^{-4}	1.9×10^{-3}	2.4×10^{-4}	8
	2	1.4×10^{-3}	9×10^{-3}	1.3×10^{-3}	330
FC	2	2.3×10^{-4}	9×10^{-3}	1.3×10^{-3}	330
	3	5.8×10^{-4}	2.1×10^{-2}	0	330

Note: The ZFC mode corresponds to cooling under at $B = 0$ regime; the FC mode corresponds to cooling at $B = 0.01$ T

observe a clearly pronounced hysteresis with a feature near a zero magnetic field. This feature reflects the contribution to the magnetization at $T \approx T_{C1}$ due to two subsystems with spontaneous magnetization, which differ in a coercive field. At temperatures above T_{C1}, it is a subsystem that exhibits a weak coercive force and most probably consists of single-domain α-Fe clusters that contributes to the magnetization. The small size of these clusters does not provide magnetic-moment pinning strong enough to produce a measurable coercive force. At temperatures $T \approx T_{C1}$, exchange coupling among the clusters becomes strong enough for a hysteresis loop to be formed. Now, the coercive force corresponding to the low-temperature phase of spontaneous magnetization is ~125 Oe, whereas the remanent magnetization is the sum of the magnetizations of single-domain clusters, which are magnetically coupled to different extents depending on their separation. Only some of the clusters, located at distances close enough for exchange coupling to manifest itself, contribute to
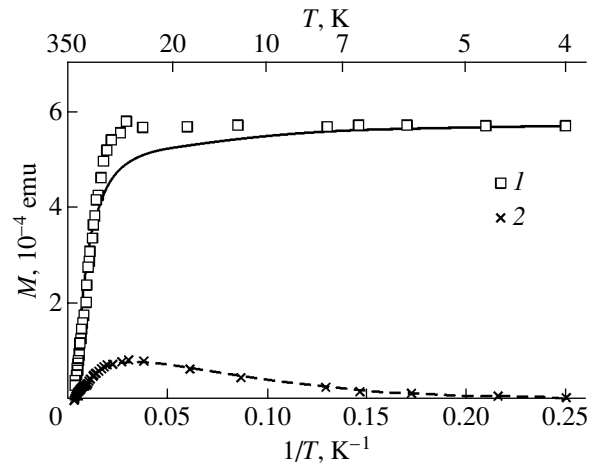

Fig. 5. Temperature dependences of the magnetic moment M measured in the FC mode. Squares *1* represent the experimental data, and the solid line represents the results of the calculation using Eq. (4) with the parameters from Table 2. The crosses (*2*) indicate differences between the experimental points and the calculated curve. The dashed line is an approximation of the differences using expression (4) and the parameters from Table 2.
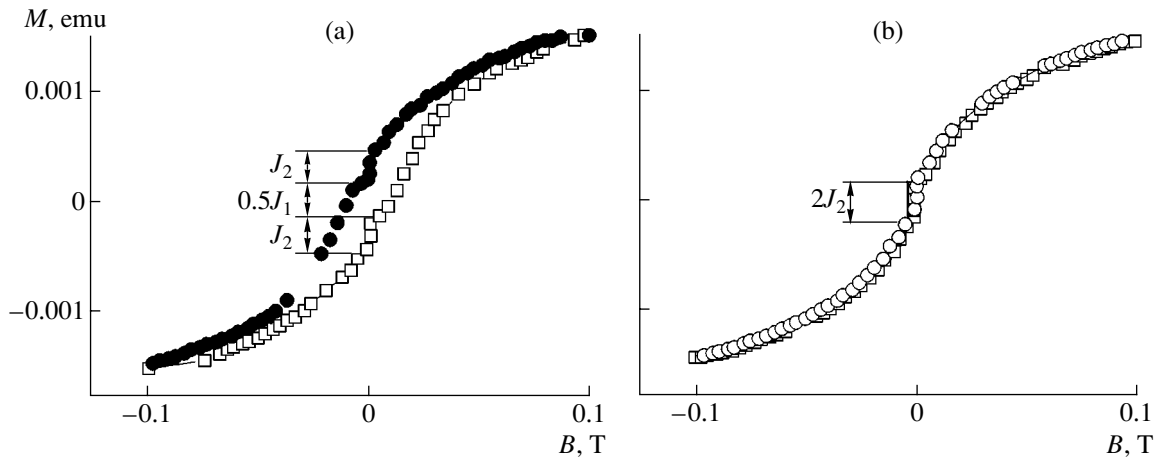
Fig. 6. Magnetization isotherms measured at two temperatures: T = (a) 10 and (b) 20 K.

the coercive force; the other clusters form a magnetic phase with a weak, almost zero, coercive force. As can be seen from Fig. 6a, remanent magnetization $J_1 \approx 6.54 \times 10^{-4}$ emu corresponds to a phase with a higher coercive force, whereas remanence $J_2 \approx 3.1 \times 10^{-4}$ emu corresponds to a phase with suppressed exchange interaction among the clusters. The ratio of these values is the ratio of the iron atom concentrations in these two phases, which is found to be on the order of unity. A comparison of the remanent magnetization J_2 at a temperature of 10 K (Fig. 6a) with that at 20 K (Fig. 6b) reveals a slight increase in the magnetization from 1.8×10^{-4} to 3×10^{-4} emu. This increase may, however, be caused by inaccuracy in separation of the contributions from the two magnetic subsystems. Nevertheless, the magnetization isotherms confirm the existence of two magnetic subsystems in the samples under study, which correlates with measurements of the temperature dependences of the magnetization.

4. CONCLUSIONS

In summary, magnetron cosputtering of graphite and iron brings about formation of encapsulated iron nanocrystals (~20 nm in size) in the amorphous carbon matrix and, also, nanocrystals of hexagonal iron carbide.

The temperature dependences of magnetization and its isotherms indicate that magnetic subsystems differing in their coercive force and magnetic ordering temperature are formed in the films immediately after their preparation.

Transition between the subsystems is observed to occur at a temperature of about 8 K and can be attributed to the onset of exchange coupling among the clusters at low temperatures. It is shown that a modified version Langevin's formalism adequately describes the features observed in the magnetization of the *a*-C:Fe films under study.

REFERENCES

1. T. Hayashi, S. Hirono, M. Tomita, *et al.*, Nature **381**, 772 (1996).

2. J. Jiao and S. Seraphin, J. Appl. Phys. **83**, 2442 (1998).

3. T. Cabioch, A. Naudon, M. Jaouen, *et al.*, Philos. Mag. B **79**, 501 (1999).

4. J.-J. Delaunay, T. Hayashi, M. Tomita, *et al.*, J. Appl. Phys. **82**, 2200 (1997).

5. T. K. Zvonareva, E. I. Ivanova, G. S. Frolova, *et al.*, Fiz. Tekh. Poluprovodn. (St. Petersburg) **36**, 734 (2002) [Semiconductors **36**, 695 (2002)].

6. S. G. Yastrebov, V. I. Ivanov-Omskiĭ, F. Dumitrache, and C. Morosanu, Fiz. Tekh. Poluprovodn. (St. Petersburg) **37**, 490 (2003) [Semiconductors **37**, 473 (2003)].

7. A. A. Rusakov, *X-ray Diffraction Study of Metals* (Atomizdat, Moscow, 1977) [in Russian].

8. B. E. Warren, *X-ray Diffraction* (Dover, New York, 1990).

9. J. Gavillet, A. Loiseau, C. Journet, *et al.*, Phys. Rev. Lett. **87**, 275504 (2001).

10. G. M. Plavnik, Crystallography **24**, 737 (1979).

11. S. Gangopadhyay, G. C. Hadjipanayis, B. Dale, *et al.*, Phys. Rev. B **45**, 9778 (1992).

Translated by G. Skrebtsov

Photosensitive Properties and a Mechanism for Photogeneration of Charge Carriers in Polymeric Layers Containing Organometallic Complexes

E. L. Aleksandrova*, M. Ya. Goĭkhman**, I. V. Podeshvo**, and V. V. Kudryavtsev**

*Ioffe Physicotechnical Institute, Russian Academy of Sciences, Politekhnicheskaya ul. 26, St. Petersburg, 194021 Russia
**Institute of Macromolecular Compounds, Russian Academy of Sciences, Bol'shoĭ proezd 31, St. Petersburg, 199004 Russia
Submitted December 14, 2004; accepted for publication December 28, 2004

Abstract—New polyamide acids (prepolymers of polybenzoxazinimides) containing 2,2-biquinolyl units in their main chain are synthesized. It is shown that these polymers form stable complexes with acids derived from the transition and rare-earth metals. The results of photophysical studies support the assumption that the process of generation of free charge carriers via a state of a pair bound by a Coulomb interaction includes two stages and that metal–polymer complexes are involved in this process. The quantum yield of photogeneration amounts to 0.007–0.05. © 2005 Pleiades Publishing, Inc.

1. INTRODUCTION

Polymeric organometallic complexes [1] belong to one of the most promising classes of materials in relation to the formation of media for optoelectronics. These materials exhibit pronounced semiconducting properties. Since it is possible to obtain thin transparent layers of optical quality, the materials under consideration apparently have the potential to form detecting media. Organic complexes of a number of transition metals with various ligands are of most interest among this class of polymeric media [2–5]. These complexes have already been used with good results in luminescent sensors of oxygen concentration [5, 6], electroluminescent devices [7, 8], and photovoltaic cells [9, 10]. The presence of efficient charge transfer between the metal atoms and organic aromatic ligands in these complexes makes it possible to hope that they can be used for the formation of not only light-sensitive detecting media but also photorefractive media for holography [11]. At the same time, the efficient luminescence of these complexes, whose spectral region can be varied according to the choice of metal atom [2–4, 7, 8], means that polymeric organometallic complexes undoubtedly show potential with respect to optoelectronic applications.

In this paper, we report the results of studying the photosensitive properties of polymeric films that contain organometallic complexes and the mechanism of charge-carrier generation in these complexes; in addition, we intend to clarify the role of a metal atom in the primary photophysical processes.

2. EXPERIMENTAL

We studied polyamide acids (PAAs) that contained *bis*-trimethyllithiomidodiphenyloxide and biquinolyl (co-PAA) or only biquinolyl (homo-PAA) units. In Fig. 1, we illustrate PAA synthesis by low-temperature polycondensation. The ratio between m and n is $m : n = 80 : 20\%$ for co-PAA, with $n = 100\%$ for homo-PAA.

We poured 0.002 mol of methylene-*bis*-anthranylic acid and 6.5 ml of *N*-methylpyrrolidine into a two-neck circular-bottom flask equipped with a stirrer; the solution was then stirred until the acid was completely dissolved; and, finally, the solution was cooled to –15°C. We then added 0.0004 mol of dichloranhydryde of 2,2'-biquinolyl–4,4'-dicarboxylic acid and 0.0016 mol of dichloranhydryde of *N*,*N*'-diphenyloxide-*bis*-(trimellithimido) acid. The suspension was stirred for 50 min at –15°C, 0.05 ml of propylene oxide was then added to the suspension outside the cooling bath, and the suspension was again stirred for 4–5 h at room temperature. The obtained polymeric solution was used to mould films on a glass substrate. These films were then dried at a temperature of 100°C until a constant mass was attained. The film thickness was 1–3 μm.

Synthesis of metal–polymer complexes of the biquinolyl-containing (BQ) co-PAA with copper (PAA–Cu$^+$), terbium (PAA–Tb^{3+}), and lanthanum (PAA–La^{3+}) was carried out at the prepolymer stage. Figure 2 illustrates the structure of the complex of this polymer with a chloride of monovalent copper.

The obtained complexes are easily dissolved in *N*-methylpyrrolidine (up to 15%), whereas the products

formed during their cyclization are insoluble in organic solvents. As was mentioned above, the complexes are formed at room temperature as a result of mixing solutions of co-PAA and CuCl (or TbCl$_3$ and LaCl$_3$) in *N*-methylpyrrolidine (N-MP).

In order to form complexes of homo-PAA and ruthenium (PAA–Ru^{2+}), we applied the method of so-called molecular assembly. Using this method, we first synthesized a low-molecular [Ru(bPy)$_2$]Cl$_2$ complex with the following structure:
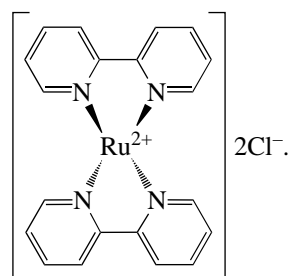
We then synthesized the PAA–Ru^{2+} complex using the interaction of the above low-molecular complex with a homo-PAA
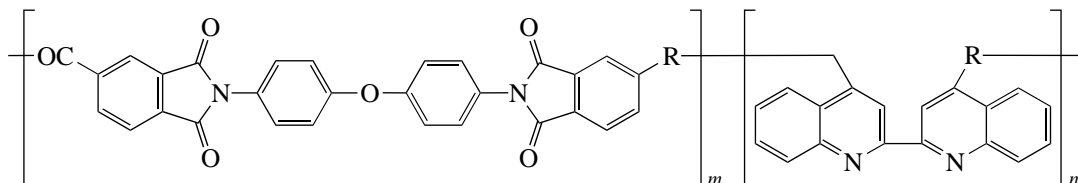
at 190°C in an *N*-MP. The obtained metal–polymer complex had the following structure:
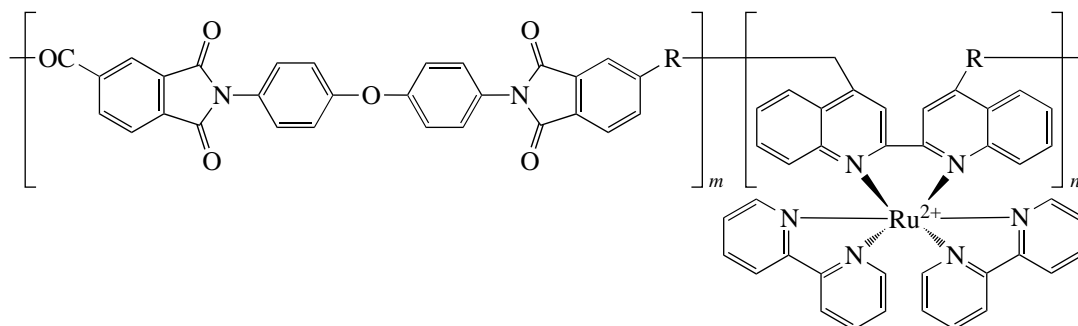
Films containing fullerene were prepared by mixing solutions of a corresponding polymer with fullerene (C$_{60}$: C$_{70}$ = 87 : 13) in *N*-MP. The content of fullerene in the polymer amounted to 1 mol %.

The photosensitive characteristics and quantum yield of charge-carrier photogeneration η were measured in a photographic mode (see [12]) in the spectral range 400–800 nm and at the electric-field strength $E = (0.1–1.0)E_0$, where E_0 is the limiting electric-field strength for a specific material. We used the Onsager model and the field dependences η(E) to determine the quantum yield of coupled pairs η$_0$ and the thermalization radius r_T. The absorption coefficient α was measured using a Perkin-Elmer spectrophotometer. The photosensitivity $S_{0.1}$ was determined from the falloff of a layer's surface potential V to 10% of its initial value ($\Delta V/V = 0.1$) when the layer was exposed to either monochromatic light or light from a KGM-300 halogen lamp (integrated $S_{0.1}$).

3. RESULTS AND DISCUSSION

The absorption α(λ) and photosensitivity $S_{0.1}$(λ) spectra of the films containing polymeric complexes of

various metals and of the initial polymers are shown in Figs. 3a and 3b.

It can be seen that the formation of a complex with a metal (Me) is accompanied by the appearance of a new absorption band (curves *1–4* in Fig. 3a) that is not present in the spectra of the initial polymers (curves *5, 6* in Fig. 3a). The position of the peak of the absorption band related to the complexes (Fig. 3a) depends on the valence of the metal. The energy corresponding to this peak decreases as the metal's valence decreases, which correlates with the previously observed effect [13] of a shift in the absorption-band peak to longer wavelengths as Me$^+$ is replaced by Me^{2+} and also as the ionization potential for the metal atom decreases. This behavior indicates that an electron is transferred from the metal atom to the ligand.

It can be seen from the spectra of photosensitivity (Fig. 3b) and the quantum yield of photogeneration (Fig. 3c) that the complexes of monovalent copper (curve *1*) exhibit the highest sensitivity to light. Examination of the quantum-yield spectra for the complexes under consideration shows that this yield first decreases in the spectral region of 400–500 nm, which corresponds to the copolymer's intrinsic photosensitivity,
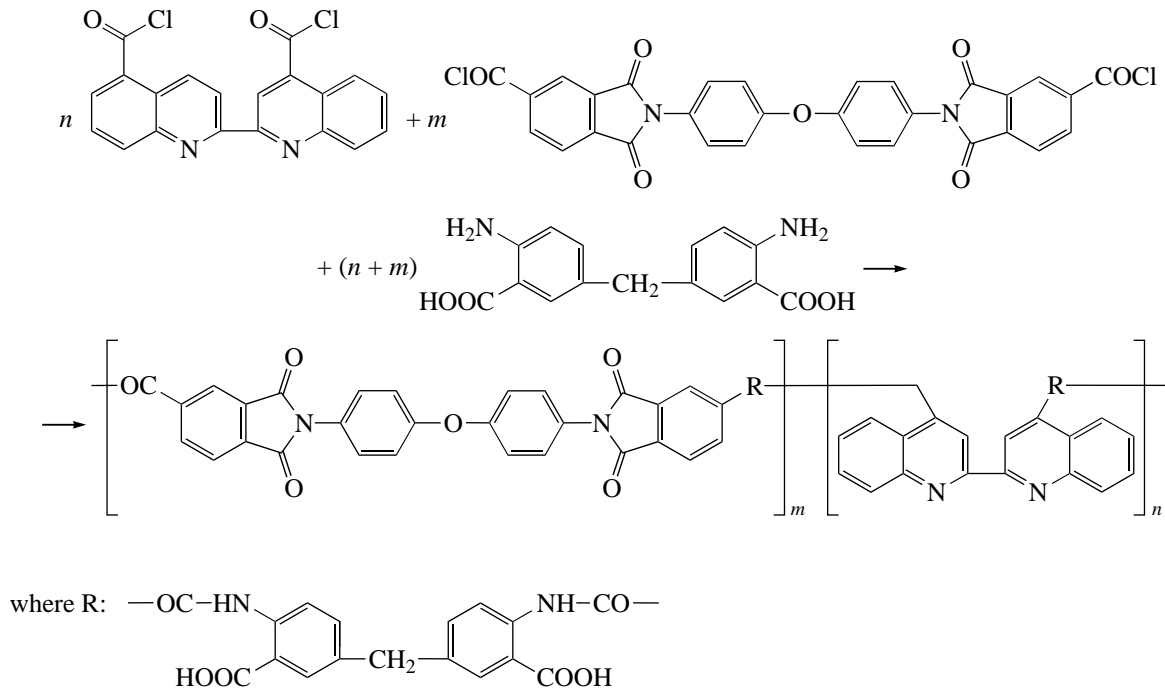
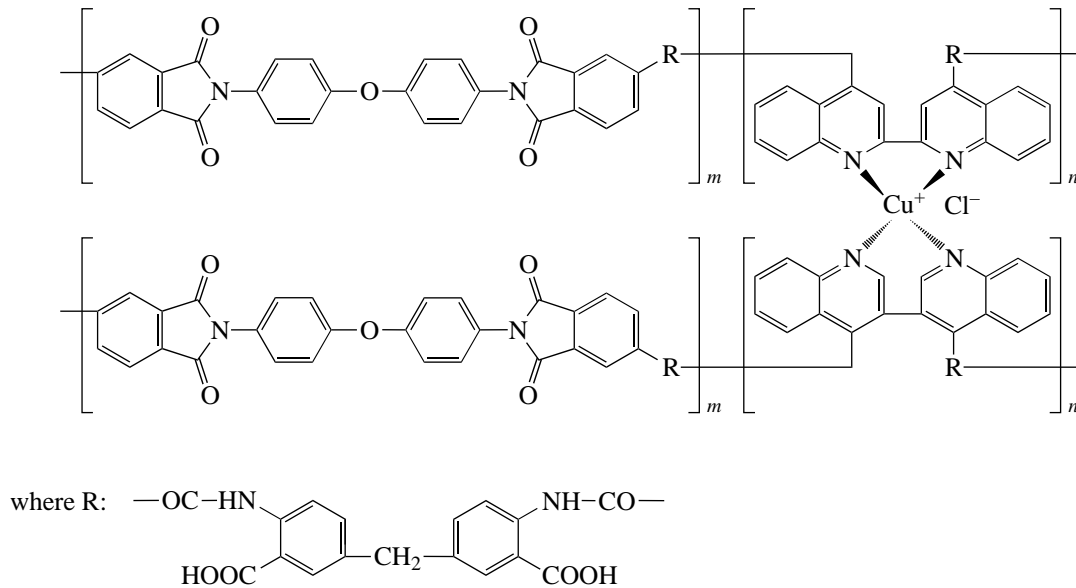**Fig. 1.** Synthesis of polyamide acids (PAAs).

Fig. 2. The structure of the complex consisting of a co-PAA polymer and a chloride of monovalent copper.

and then increases again by a factor of 1.5–2 in the absorption band of the complex (550–700 nm) (Fig. 3c, curve *1*).

The charge-carrier quantum yield for the PAA–Cu^+ complex is constant in the absorption band and amounts to 0.03 for the metal–polymer complex and to 0.045 for the samples with the added sensitizer (fullerene). The thermalization radius r_T determined from the field dependences of the quantum yield $\eta(E)$ is equal to 2.2–2.5 nm for the complexes studied, while the quantum yield for the formation of coupled pairs $\eta_0 = 0.08$ for the complexes with copper, which are most sensitive to light, and $\eta_0 = 0.005$ for the complexes with lanthanum, which are least sensitive to

Absorption, %

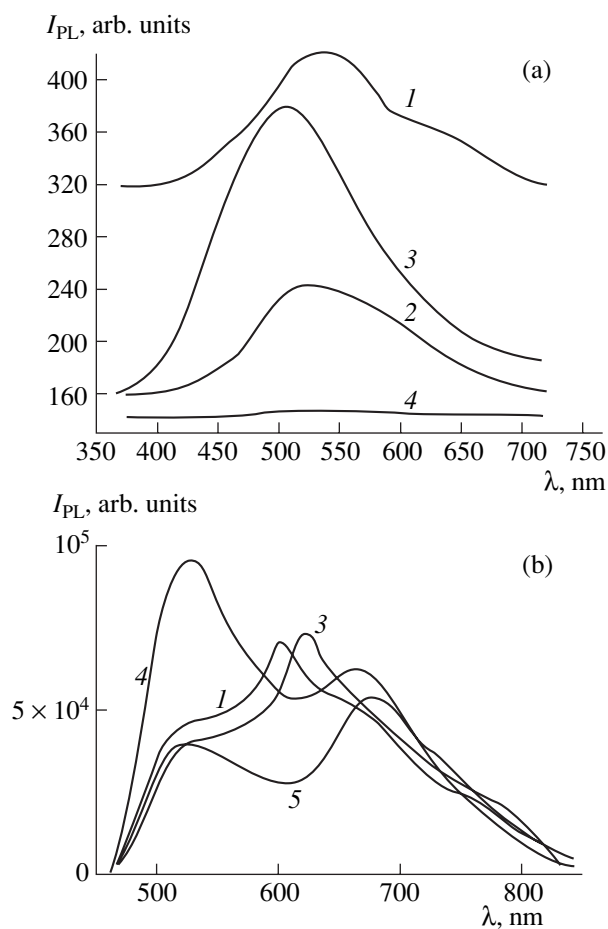I_{PL}, arb. units

$S_{0.1}$, cm^2/J

I_{PL}, arb. units

Fig. 4. Luminescence spectra obtained using excitation with light at a wavelength in the vicinity of (a) 337 and (b) 585 nm: (*1*) PAA–Cu$^+$, (*2*) PAA–Tb^{3+}, (*3*) PAA–Ru^{2+}, (*4*) PAA, and (*5*) PAA–Cu$^+$ + fullerene.

η

Fig. 3. Spectra of (a) absorption, (b) photosensitivity, and (c) quantum yield of photogeneration: (*1*) PAA–Cu$^+$, (*2*) PAA–Ru^{2+}, (*3*) PAA–Tb^{3+}, (*4*) PAA-La^{3+}, (*5*) PAA, and (*6*) homo-PAA.

light. The quantum yield η for charge-carrier photogeneration is 0.025 for the complexes based on ruthenium. The value of η is a factor of 1.5 larger for the complexes with fullerene than for the complexes without fullerene.

A comparison of the luminescence spectra of the complexes studied in [14, 15], which were excited with nitrogen laser radiation at a wavelength of 337 nm and pulse duration of 6–8 ns (the spectra were measured during the 1-μs period of persistent luminescence after the excitation pulse at a temperature $T = 300$ K) (Fig. 4a, curves *1–3*), with the spectra of the initial co-PAA (Fig. 4a, curve *4*) shows that the peaks of the corresponding bands coincide. This circumstance indicates that photoexcitation energy is not transferred from a polymer molecule after absorbing a photon to the organometallic complex. If excitation with radiation possessing a longer wavelength is used, bands peaked at 605 and 615 nm appear in the luminescence spectra of the complexes that involve copper and ruthenium, respectively (Fig. 4b, curves *1, 3*). The introduc-

tion of an efficient acceptor (fullerene) into a film containing an organometallic complex brings about a quenching of the absorption band related to the metal complex (Fig. 4b, curve *5*).

The photosensitivity spectra (Fig. 3b) correlate with the absorption spectra (Fig. 3a). The photosensitivity of the films including the Cu^+ complex is 3×10^4 cm^2/J and the quantum yield $\eta \approx 0.03$–0.05. For the Ru^{2+} complex, the photosensitivity $S_{0.1}$ is 8×10^3 cm^2/J in the spectral range 400–550 nm and the quantum yield $\eta \approx 0.02 \pm 0.01$; $\eta \approx 0.004$–0.007 for the terbium and lanthanum complexes. The photosensitivity of the metal–polymer complexes based on terbium and lanthanum is nearly equal to that of PAA ($S_{0.1} \lesssim 2 \times 10^3$ cm^2/J), which is lower by almost an order of magnitude than the photosensitivity for the Cu^+ complex. The quantum yield for the terbium- and lanthanum-based complexes is comparable to the value of η for PAA (0.01 ± 0.003).

The quantum yield for the formation of coupled pairs is also at its highest for the copper-based complex. This yield equals $\eta_0 = 0.08 \pm 0.03$ and is constant within the absorption band. Taking into account the concentration C_C of the metal complex formed by the BQ units of neighboring chains in the case where, as can be seen from Fig. 2, there are approximately ten elementary copolymer units to each complex molecule (i.e., $C_C = 0.1$), we find that the quantum yield of photogeneration in the PAA–Me complex (the probability of generation of free charge carriers by a single molecule of the complex) is equal to 0.3 for the copper-based complex. The thermalization radius, determined from the field dependences of the quantum yield $\eta(E)$, is equal to 2.5 ± 0.3 nm.

The observed variation in the absorption spectra and drastic decrease in the photosensitivity of a polymer as a result of its cylclization show that the polymeric chains themselves, which contain photoactive nitrogen-containing biquinolyl and bipyridyl groups and also carboxyl groups, play a dominant role in the primary photophysical processes. In contrast, the effect of a metal is observed only in the absorption region of the organometallic complex.

Apparently, the photogeneration mechanism is in accordance with the Onsager mechanism (as is typical of organic semiconductors, including polyimides [16–19]) both in the absorption region of nitrogen-containing photoactive groups (this region corresponds to a long-wavelength luminescence band that is located at 510–530 nm and shifts somewhat depending on the metal type; see Fig. 4a, curves *1–3*) and in the absorption region of the complex in which charge transfer brings about the formation of a coupled pair. The thermalization radius is equal to ~2 nm (which is typical of polyimides [16–19]) in the region of absorption in a PAA (400–500 nm) and equals 3.0–3.5 nm in the region of absorption in the copper-containing complex. A com-

parison of the thermalization radii shows that they increase. This increase is evidently caused by an increase in the size of the absorbing center, which verifies our assumption that complex formation has a pronounced effect on charge-carrier generation.

Excess photon energy is lost (thermalization of a charge carrier bound by the Coulomb interaction occurs) in the same unit of the polymeric chain that contains an organometallic complex. A further separation of charges is accomplished as a result of thermal–field dissociation in an external electric field. The charge carriers become free at distances of about 15 nm.

4. CONCLUSION

Thus, the results obtained in this study show that polymer layers containing organometallic complexes may have the potential to be important components in the fabrication of photosensitive materials and electroluminescent devices.

REFERENCES

1. M. I. Bessonov, M. M. Koton, V. V. Kudryavtsev, and L. A. Laĭus, in *Polyimides: A Class of Heat-Resistant Polymers*, Ed. by M. I. Bessonov (Nauka, Leningrad, 1983) [in Russian].

2. F. N. Castellano, T. A. Heimer, and G. J. Meyer, Chem. Mater. **6**, 1041 (1994).

3. K. Matsui and F. Momose, Chem. Mater. **9**, 2588 (1997).

4. F. Momose, K. Maedo, and K. Matsui, J. Non-Cryst. Solids **244**, 74 (1999).

5. V. I. Zemskiĭ, A. V. Veresov, and L. Yu. Kolesnikov, Pis'ma Zh. Tekh. Fiz. **20** (9), 74 (1994) [Tech. Phys. Lett. **20**, 374 (1994)].

6. M. Ahmat, N. Mohammad, and J. Abdullah, J. Non-Cryst. Solids **290**, 86 (2001).

7. B. Wang and M. R. Vasilevski, J. Am. Chem. Soc. **119**, 12 (1996).

8. J. K. Mwaura, M. K. Mathai, C. Chen, *et al.*, J. Macromol. Sci. A **40**, 1253 (2003).

9. S. C. Yu, X. Gong, and W. K. Chan, Macromolecules **31**, 5639 (1998).

10. R. Mozarkal, Y. G. Kim, and J. Kumar, J. Macromol. Sci. A **40**, 1317 (2003).

11. Z. Peng, A. R. Charavi, and L. Yu, Appl. Phys. Lett. **69**, 4002 (1996).

12. E. L. Aleksandrova and Yu. A. Cherkasov, Opt. Spektrosk. **64**, 1047 (1988) [Opt. Spectrosc. **64**, 624 (1988)].

13. Y. Mori and K. Maeda, J. Chem. Soc., Perkin Trans. 2, 1969 (1997).

14. E. L. Aleksandrova, M. Ya. Goĭkhman, V. V. Kudryavtsev, *et al.*, Opt. Zh. **68** (11), 67 (2001) [J. Opt. Technol. **68**, 849 (2001)]; Fiz. Tekh. Poluprovodn. (St. Petersburg) **37**, 846 (2003) [Semiconductors **37**, 818 (2003)].

15. É. A. Lebedev, M. Ya. Goĭkhman, M. E. Kompan, *et al.*, Fiz. Tekh. Poluprovodn. (St. Petersburg) **37**, 844 (2003) [Semiconductors **37**, 816 (2003)].

16. R. D. Gillard and R. E. Hill, J. Chem. Soc. **11**, 1217 (1974).

17. B. V. Kotov, V. I. Berendyaev, B. M. Rumyantsev, *et al.*, Vysokomol. Soedin., Ser. A **39**, 720 (1997).

18. E. L. Aleksandrova and Yu. A. Cherkasov, Opt. Zh. **67** (3), 43 (2000) [J. Opt. Technol. **67**, 241 (2000)].

19. E. L. Aleksandrova, G. E. Nosova, E. A. Solovskaya, *et al.*, Fiz. Tekh. Poluprovodn. (St. Petersburg) **38**, 678 (2004) [Semiconductors **38**, 652 (2004)].

Translated by A. Spitsyn

High-Power Flip–Chip Blue Light-Emitting Diodes Based on AlGaInN

**D. A. Zakheĭm*^, I. P. Smirnova*, I. V. Roznanskiĭ*, S. A. Gurevich*, M. M. Kulagina*,
E. M. Arakcheeva*, G. A. Onushkin**, A. L. Zakheĭm**, E. D. Vasil'eva***, and G. V. Itkinson*****

*Ioffe Physicotechnical Institute, Russian Academy of Sciences, Politekhnicheskaya ul. 26, St. Petersburg, 194021 Russia
^e-mail: mitya@quantum.ioffe.ru
***Science-and-Technology Center for Microelectronics and Submicrometer Heterostructures at the Ioffe Physicotechnical
Institute (Russian Academy of Sciences), St. Petersburg, 194021 Russia*
***ZAO Svetlana–Optoelektronika, St. Petersburg, 194156 Russia
Submitted October 5, 2004; accepted for publication November 28, 2004

Abstract—The design and fabrication of a high-power light-emitting diode chip that has an active-region area of 1 mm^2 and emits at a wavelength of 460 nm are described. The chip structure is developed on the basis of numerical simulation and is intended for flip–chip assembly. The use of two-level interconnections for an *n*-type contact made it possible to obtain an unprecedentedly low series resistance (0.65 Ω) and a high uniformity of pump-current distribution. Light-emitting diodes based on the developed design operate in the continuous-wave mode in a current range of 0–2 A, and their highest emission power is 430 mW. © *2005 Pleiades Publishing, Inc.*

1. INTRODUCTION

The recent significant progress achieved in the field of epitaxial growth of high-quality heterostructures based on AlGaInN has made it possible to obtain large values of external quantum efficiency for light-emitting diodes that emit in the visible and near-ultraviolet regions of the spectrum. For example, a quantum efficiency in excess of 50% (in excess of 35%) was obtained at low pump-current densities for light-emitting diodes (LEDs) that emit at a wavelength of 460 nm (400 nm) [1]. Such high efficiencies make it possible to use these LEDs in white-light sources, with the result that they can compete with traditional incandescent, fluorescent, and even halogen lamps.

However, in addition to high quantum efficiency, LEDs should also exhibit a high emission power if they are to be used as light sources. At the same time, a rather rapid decrease in efficiency as the pump-current density increases is characteristic of all the currently available heterostructures that are based on nitrides belonging to the Group III elements. This decrease necessitates the use of LED crystals with a large active region. In this situation, the problem of maintaining an acceptable level of uniformity of the pump-current density over the area of an emitting *p–n* junction becomes of primary importance. The reason is that LED heterostructures are grown, as a rule, on an insulating sapphire substrate, and the conductance of a thin (4–5 μm) *n*-GaN layer is not high enough to ensure uniform distribution of the pump current over the active region if the linear dimensions of a crystal exceed 300–400 μm. The efforts of numerous research teams are now being directed towards finding a solution to this problem. For

example, the Lumileds Co. developed the so-called interdigital structure for their high-power LED chips [2], while the OSRAM Co. employs laser-induced separation of an insulating substrate [3], which makes it possible to use the vertical structure of the chip.

In addition to ensuring uniform distribution of the pump current in high-power LEDs, there are also a number of other important problems to be solved. For example, the internal reflection of generated optical radiation at the interfaces of a semiconductor with air and/or the sapphire substrate is a serious obstacle to a further increasing the external quantum efficiency of LEDs. Numerous studies have attempted to find a way to increase the efficiency of extraction of radiation from a LED chip. The most effective solutions appear to be the formation of light-scattering surfaces [4], formation of a microcavity within the active region [5], and the use of a photonic crystal [6]. A further important challenge is to minimize the series resistance of a LED and satisfy the conditions for efficient heat removal from the active region, since the operating currents can be as high as several amperes.

The so-called flip–chip structure of an emitting crystal [2, 7] appears to show the most promise in relation to finding solutions to the above problems and to the fabrication of high-power LEDs. In this design, both areas making contact with *n*- and *p*-type materials are located at the same (front) surface and the crystal is mounted on a heat sink on its front surface. In addition, a combination of metals with high reflectivity (typically based on Ag) is used as the contact for *p*-GaN, while light is extracted through the transparent sapphire substrate. This design makes it possible to increase the effi-

ciency of emission extraction from the crystal by a factor of 1.6–2 compared with the conventional variant, in which a thin transparent *p*-type contact is used [8]. In addition, thermal resistance between the LED's active region and the heat sink is minimized in the flip–chip design since the heat from the *p–n* junction is removed through a thin (0.1–0.3 μm) GaN layer rather than through the sapphire substrate, which has a low thermal conductivity.

2. NUMERICAL SIMULATION
OF THE CURRENT FLOW

Thus, the objective of this study was to design and fabricate a LED crystal that has an active-region area of ~1 mm^2 and can be used in flip–chip assembly. We also aimed to solve the above-mentioned problems of minimizing the series resistance and attuning a high uniformity in the distribution of the pump-current density. Furthermore, we intended to minimize the portion of the crystal's passive region occupied by *n*-type contact areas and to increase the efficiency of light extraction. When designing the structure, we used a numerical simulation of the three-dimensional (3D) pattern of the current distribution in the crystal.

The numerical model used in the computations is based on calculation of the potentials and currents in a 3D linear grid of resistances by solving a system of Kirchhoff linear equations. The grid included three types of resistances that corresponded to the volume resistivity of the *n*-GaN material used and to the specific contact resistances of the *n*- and *p*-type contacts. The volume resistivity of *p*-GaN was not considered separately (this resistivity was included in the contact resistance of the *p*-type contact), since the thickness of the *p*-type layer in LED heterostructures based on AlGaInN is very small and the lateral spread of the current over this layer can be disregarded. In addition, the current–voltage characteristic of the *p–n* junction itself was not introduced into the model, since the junction does not make a noticeable contribution to the total LED differential resistance under the conditions of high current densities (in which case, the *p–n* junction is completely on).

The use of special algorithms for the numerical solution of a system of linear equations (the multifrontal method of LU factorization for sparse matrices [9]) made it possible to perform calculations for grids that contained as many as 10^5 nodes. In turn, this circumstance allowed us to correctly describe the 3D distribution of the pump-current density in LED chips with a complex configuration of contact areas. The calculated distributions of the current density over the active-region area of the chip were compared with the experimental data obtained by scanning the near-field emission of the LED chip [10].

3. FABRICATION OF THE SAMPLES

In order to determine the parameters of the LED heterostructure, we fabricated medium-power LED chips that had a simple rectangular *p*-type contact with an area of 350 × 450 μm^2. The chips also had a fork-shaped *n*-type contact that enclosed the *p*-type contact on three sides. When fabricating these LEDs, we used a commercial structure that was based on AlGaInN and emitted at a wavelength of 460 nm. The fabrication process included the etching-assisted formation of a two-level mesa structure using reactive ion etching in an atmosphere of Cl$_2$: BCl$_3$: Ar. The first etching (to a depth of 0.5 μm) was carried out so as to expose areas for deposition of the *n*-type contact. The second etching, to a depth of 5–6 μm (i.e., to the sapphire substrate), was performed over the entire perimeter of a LED chip and was intended to increase the efficiency of light extraction from the chip by introducing additional light reflection from the side walls of the mesa structure; these walls had an inclination of 45° with respect to the vertical plane [8].

In order to form the patterns of all the contact areas, we used explosive photolithography. When forming the contacts, we thoroughly treated the gallium nitride surface in order to remove the surface oxide before depositing the metals. The chemical treatment of the GaN surface before depositing the *p*-type contact included two stages. The samples were first boiled in an HCl : HNO$_3$ (3 : 1) solution for 10 min prior to formation of a photolithographic mask and were then treated in a solution of buffer etchant for 5 min. The reflecting *p*-type contact consisted of a thin (4 nm) Ni layer and a thick (200 nm) Ag layer, both of which were formed using the thermal-evaporation method. The reflectivity of this contact amounted to ~85% at a normal incidence of light and a wavelength of 460 nm. A conventional Ti/Al metal combination, deposited using magnetron sputtering in an Ar atmosphere, was employed for the *n*-type contact. In order to obtain a low-resistivity ohmic contact, we etched the *n*-type GaN surface using argon ions immediately prior to the deposition of the metals. After being annealed in a nitrogen atmosphere, both contact areas were reinforced with a Au layer.

Then, the *n*- and *p*-type contact areas intended for flip–chip assembly were reinforced with a galvanic 3-μm-thick Au layer, and the sapphire substrate was first thinned to a thickness of 150–200 μm and then cut into separate chips using laser cutting. The chips were mounted on subchip plates that consisted of chips of oxidized silicon with a deposited corresponding interconnection of the contact areas. Finally, the obtained chips were soldered to a copper heat sink and covered with a lens made of epoxy resin [11].

In Fig. 1, we show the dependences of the emission power and external quantum efficiency of emission for the LEDs on the pump current (these dependences were measured in a continuous-wave mode). As can be seen from Fig. 1, the highest optical-emission power exceeds

150 mW at a pump current of 800 mA, while the highest external quantum efficiency is ~21% at a pump current of 10 mA. The differential series resistance of the LEDs is 1.8 Ω in a pump-current range from 400 to 800 mA. We also studied the distribution of the optical-emission power over the chip area at various pump currents. Experimental data indicate that the emission power is fairly uniform at pump currents as high as 800 mA: deviation of the emission power from the mean value does not exceed 20%, which is in good agreement with the results of calculations. However, the calculations show that the uniformity of distribution of the pump-current density over the active region of the chips is appreciably impaired as the linear dimensions of the active region are increased. Consequently, a more complex topology of the contact areas is required for LED chips with a large area.

The chip we designed on the basis of a numerical simulation, with an active-region area of ~1 mm², is shown in Fig. 2. In this chip, the *n*-type contact (*1*) consists of a "fork" that envelops the *p*-type contact (*2*) and has four fragments incorporated into the region of the *p*-type contact. These fragments have an angular shape and are connected electrically using special bridges (*3*) that are formed above the *p*-type contact and are insulated from the contact with an insulating layer (*4*). This structure makes it possible to attain very high uniformity in the distribution of the pump-current density in the active region and also minimize the passive-region area occupied by the *n*-type contact, since the conductors that deliver the current to the middle of a chip are located at the second level of the metallic coating. The main technological difficulty in implementing the suggested structure is related to ensuring reliable electrical isolation of the metal layers. In this study, we chose SiO₂, deposited onto a rotating substrate using a magnetron-sputtering method in an H₂ : Ar atmosphere, as the isolating insulator. It is well known that an insulator deposited using this method exhibits a higher density and that the probability of its electrical breakdown is much lower than for SiO₂ deposited in an atmosphere of pure Ar [12]. The thickness of the insulating layer was 0.25 μm. With respect to electrical breakdown, the most critical spot is where the insulating layer overlaps the edge of the *p*-type contact area. Since the thickness of the metal layer for the *p*-type contact is comparable with that of the insulator, the metal edge formed using explosive photolithography should have a gentle slope. This requirement is satisfied by using a reverse photolithographic mask, i.e., a mask whose wall has a negative inclination with respect to the surface. Apart from deposition of the intermediate insulator, all the other technological operations involved in fabricating the LED chips (including the etching of the mesa structure) were identical to those used for a medium-area chip. As before, the chips were mounted on a chip holder and were then encapsulated.
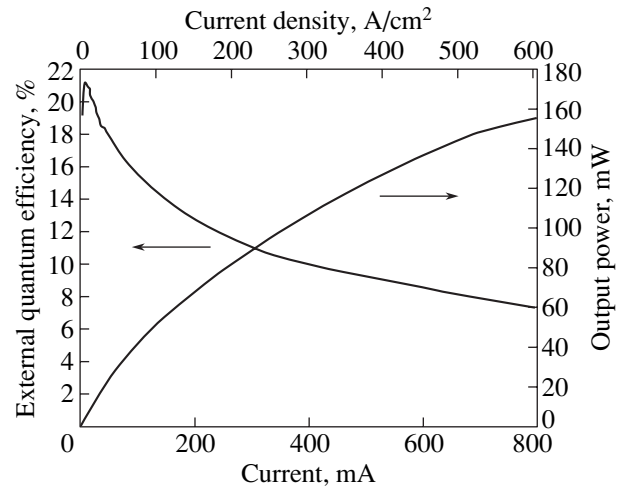
Fig. 1. Dependences of the emission power and external quantum efficiency on the pump current for the medium-power light-emitting diodes.
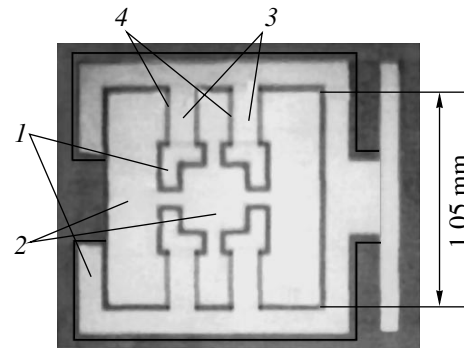

Fig. 2. Exterior view of a chip from a high-power light-emitting diode.

4. DISCUSSION

Figure 3 (on the left) illustrates the calculated distribution of the pump-current density over the active region of a chip. The darker regions correspond to a higher current density. The experimental distribution of the optical-emission power at a pump current of 1 A is also shown In Fig. 3 (on the right). Both the results of the calculations and the experimental data are indicative of very high uniformity of the pump-current distribution. Regions where the current density (and, correspondingly, the emission power) is somewhat higher than the average value are observed only in the immediate vicinity of the *n*-type contact. The calculated root-mean-square deviation of the pump-current density from the average value is no larger than 20%. It is worth noting that this deviation is larger for the interdigital structure used by Lumileds because this structure includes regions where the current density noticeably exceeds its average value. Such regions are inevitably formed close to the bases of the pins and are surrounded on three sides by the *n*-type contact. In addition, in this
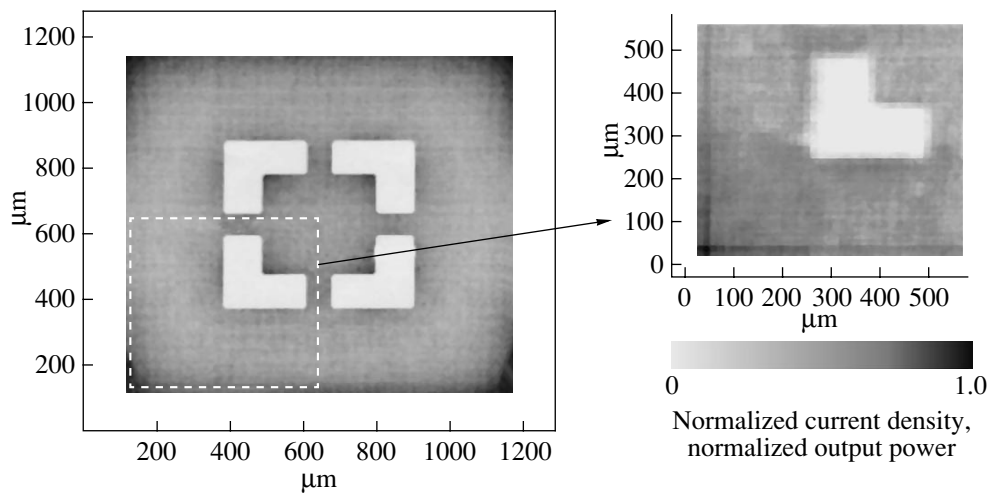
Fig. 3. The calculated (on the left) distribution of the pump-current density over the active-region area of a light-emitting-diode chip and the experimental distribution (on the right) of optical power at a pump current of 1 A.

structure, the ratio between the areas of the passive and active regions of the chips is appreciably larger than in the variant with two-level connections to the *n*-type contact that we suggested.
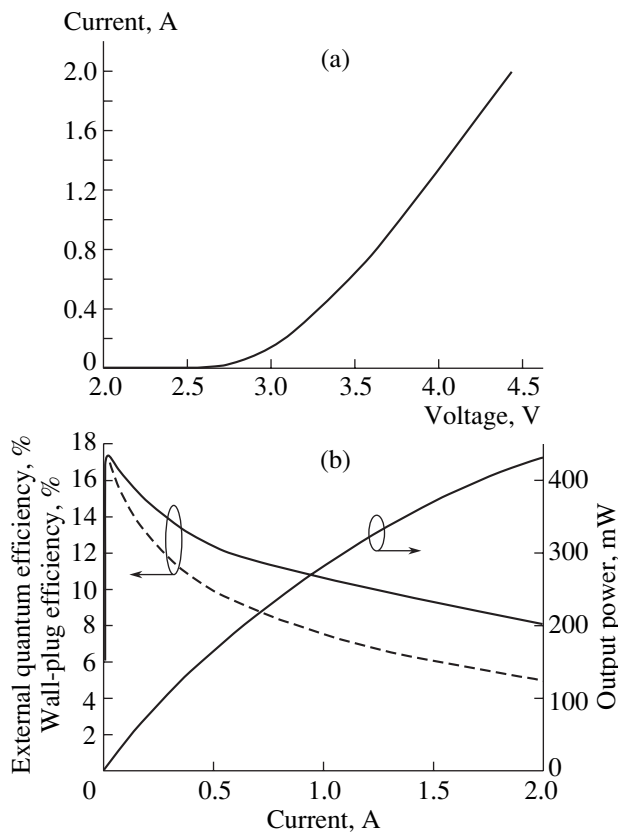

Fig. 4. (a) The current–voltage characteristic and (b) the dependences of the emission power, external quantum efficiency (the solid curve), and wall-plug efficiency (dashed curve) on the pump current for a high-power light-emitting diode.

The main characteristics of the fabricated high-power LEDs are shown in Fig. 4. In Fig. 4a, we show the current–voltage LED characteristic measured in the continuous mode. The dynamic series resistance is equal to 0.65 Ω in the current range 0.5 to 2 A. It is noteworthy that the above value of the series resistance is smaller than that claimed by Lumiled for their Luxeon LEDs (0.8 Ω) [13]. In Fig. 4b, we show the luminance–current characteristics of the LEDs and, also, the dependences of the external quantum and wall-plug efficiencies of the LEDs on the pump current. The obtained external quantum and wall-plug efficiencies of the LEDs are equal to 17.5% and are attained at a pump current of ~50 mA. The highest optical-emission power of the LEDs in the continuous-wave mode of operation is equal to 430 mW at a pump current of 2 A. It is worth noting that the commercial AlGaInN-based heterostructure used in this study does not feature unprecedentedly high internal quantum efficiency; as a result, the obtained LEDs do not exhibit an unprecedentedly high efficiency either. However, our chip and heat sink structure allows the LEDs to operate in the current range 0–2 A and yields unprecedentedly small values for the series electrical resistance.

It is noteworthy that the largest values of the external quantum efficiency for the chips with high-power LEDs (17.5%) are somewhat smaller than those for the chips with medium-power LEDs (21%), in spite of the fact that these LEDs were fabricated on the basis of the same epitaxial heterostructure. This difference between quantum efficiencies indicates that the efficiency of light extraction decreases as the chip size increases, since the specific contribution of the light reflected from the inclined side walls of the mesa structure to the total optical flux is smaller for the larger chips [8]. This means that, for chips with a large area, the problem of increasing the efficiency of emission extraction by forming scattering surfaces at the interfaces between

the semiconductor and the substrate and/or between the semiconductor and the metal is of primary importance, since optimization of the inclination of the mesa-structure side walls does not yield an appreciable effect in this case.

5. CONCLUSION

Thus, in this paper, we reported the results of studying a new light-emitting diode (LED) based on an AlGaInN heterostructure formed on a sapphire substrate. This LED features an unprecedentedly low series resistance and a high uniformity of distribution of the pump-current density over its active-region area. The active-region area of the chip is 1 mm^2. Two-level connections to the n-type contacts are used, with intermediate electrical isolation supplied by an insulating layer. The fabricated LEDs emit at a wavelength of 460 nm and operate in the pump-current range 0–2 A (in the continuous-wave mode). In this case, the highest emission power equals 430 mW and the highest external quantum and wall-plug efficiencies are equal to 17.5%.

REFERENCES

1. M. Yamada, T. Mitani, Y. Narukawa, *et al.*, Jpn. J. Appl. Phys., Part 2 **41**, L1431 (2002).

2. J. J. Wierer, D. A. Steigerwald, M. R. Krames, *et al.*, Appl. Phys. Lett. **78**, 3379 (2001).

3. V. Harle, B. Hahn, J. Baur, *et al.*, Proc. SPIE **5187**, 34 (2004); http://compoundsemiconductor.net/articles/news/7/9/4/1.

4. T. Fujii, Y. Gao, R. Sharma, *et al.*, Appl. Phys. Lett. **84**, 855 (2004).

5. Y. C. Shen, J. J. Wierer, M. R. Krames, *et al.*, Appl. Phys. Lett. **82**, 2221 (2003).

6. J. J. Wierer, M. R. Krames, J. E. Epler, *et al.*, Appl. Phys. Lett. **84**, 3885 (2004).

7. I. P. Smirnova, D. A. Zakheim, I. V. Rozhanskiĭ, *et al.*, in *Proceedings of International Symposium on Nanostructures: Physics and Technology* (St. Petersburg, 2004), p. 99.

8. V. A. Zabelin, D. A. Zakheim, and S. A. Gurevich, IEEE J. Quantum Electron. **40**, 1675 (2004).

9. T. A. Davis, *UMFPACK Version 4.1 User Guide*; http://www.cise.ufl.edu/research/sparse/umfpack/(2003).

10. G. A. Onushkin, D. A. Zakgeĭm, I. P. Smirnova, *et al.*, in *Abstracts of 3rd All-Russian Conference on Gallium, Indium, and Aluminum Nitrides: Structures and Devices* (Moscow, 2004), p. 96.

11. D. A. Zakgeĭm, I. P. Smirnova, E. M. Arakcheeva, *et al.*, in *Abstracts of 3rd All-Russian Conference on Gallium, Indium, and Aluminum Nitrides: Structures and Devices* (Moscow, 2004), p. 138.

12. T. Serikawa and T. Yachi, J. Electrochem. Soc. **131**, 2105 (1984).

13. Luxeon® III Emitter, *Technical Datasheet DS45*, http://www.lumileds.com/pdfs/DS45.PDF.

Translated by A. Spitsyn

A Ferroelectric Field Effect Transistor Based on a Pb(Zr$_x$Ti$_{1-x}$)O$_3$/SnO$_2$ Heterostructure

I. E. Titkov^, I. P. Pronin, D. V. Mashovets, L. A. Delimova, I. A. Liniĭchuk, and I. V. Grekhov

Ioffe Physicotechnical Institute, Russian Academy of Sciences, St. Petersburg, 194021 Russia
^e-mail: ITitkov@mail.ioffe.ru
Submitted December 15, 2004; accepted for publication December 29, 2004

Abstract—The possibility of fabricating a ferroelectric FET based on a Pb(Zr$_x$Ti$_{1-x}$)O$_3$/SnO$_2$ (PZT/SnO$_2$) heterostructure is investigated. Sb-doped epitaxial SnO$_2$/Al$_2$O$_3$ thin film deposited by YAG laser ablation from a metal target is used as the FET channel. The highest obtained electron mobility in the channel is 25 cm^2/(V s) at an electron density of 8×10^{19} cm^{-3}. The possibility of growing PZT film directly on SnO$_2$ film using two different techniques, laser ablation and magnetron sputtering, is demonstrated. Both methods have been used in the fabrication of Au/PZT/SnO$_2$ capacitor heterostructures, whose top Au electrode is 250×250 μm^2 in size. These cells demonstrate a capacitance of 1000 pF at a 10-V bias and remnant polarization up to 16 μC/cm^2. A Au/PZT/SnO$_2$/Al$_2$O$_3$ transistor structure with 94% modulation of the channel current is fabricated. The difference in the channel current under the effect of positive and negative remnant polarization of the undergate ferroelectric is 37%. © 2005 Pleiades Publishing, Inc.

1. INTRODUCTION

In principle, ferroelectric (FE) random access memory based on an FE field-effect transistor (FFET) has a number of advantages over other types of memories: it is nonvolatile, nondestructively readable, demonstrates low power consumption, and has a fast access time [1–4]. A variety of circuit designs for FFET-based memory systems have been proposed [5].

As early as 1995, Nakamura *et al.* [2] proposed producing FFETs by simple replacement of the subgate insulator in a Si MOSFET. However, no reliable device corresponding to modern requirements yet exists due to problems with the direct growing of FE films on an Si substrate [2, 3]. The insertion of a buffer layer between Si and the FE leads to a significant degradation of the device parameters and complicates the technology.

Another approach to solving this problem is the formation of FFETs based on materials with a perovskite structure, which was proposed in 1995 by Watanabe [6]. We also showed that it is possible to produce such a device based on a perovskite PZT/La$_x$Sr$_{1-x}$CuO$_4$/NdGaO$_3$ heterostructure [7, 8] (PZT is Pb(Zr$_x$Ti$_{1-x}$)O$_3$). A significant drawback of this structure is the low mobility of carriers in the La$_x$Sr$_{1-x}$CuO$_4$ channel, which is below 1 cm^2/(V s) at room temperature. This property imposes fundamental restrictions on transistor operation speed.

In this study, we investigate the possibility of producing an FFET based on a PZT/SnO$_2$/Al$_2$O$_3$ heterostructure. This structure seems promising because the electron mobility in laser-deposited SnO$_2$/Al$_2$O$_3$ epitaxial films is high [9, 10] and the FE PZT layer can be grown directly on SnO$_2$ [11]. An additional important advantage of the PZT/SnO$_2$/Al$_2$O$_3$ heterostructure is its high (about 96%) transparency in the visual spectral range [11], which opens up the prospect of its application in logic and memory units in liquid-crystal displays and transistors.

Similar FFET structures were studied in [12, 13], but the maximum electron mobility reached in an SnO$_2$ channel grown on the PZT film did not exceed 8 cm^2/(V s).

As was shown in [10, 14, 15], the mobility in laser-deposited single-crystal SnO$_2$ films can reach 37–40 cm^2/(V s) at doping above 10^{19} cm^{-3}. In polycrystalline films, this value is obtained only when the chemical potential level lies below that at the charged faces of the crystallites. For SnO$_2$:Sb, this condition is reached at a Sb concentration below 10^{18} cm^{-3}, but, in this case, the FET channel resistance becomes too high. Moreover, the conductivity of such films is highly temperature- and gas-sensitive [14]. Prins *et al.* [12] calculated the optimal range of channel parameters providing the best transistor operation. The thickness (20 nm) and doping level (10^{19} cm^{-3}) of our structures fall within this range.

2. FABRICATION OF SnO$_2$:Sb EPITAXIAL FILMS

In order to obtain high electron mobility, the SnO$_2$:Sb films were deposited onto an optically polished surface of a single-crystal α-Al$_2$O$_3$ substrate at a temperature of 670°C in an oxygen atmosphere at
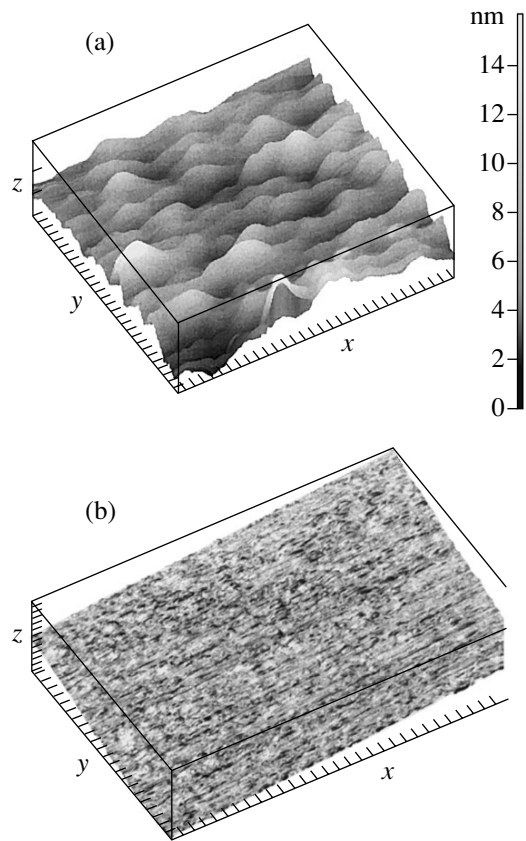
Fig. 1. AFM images (semicontact scanning mode) of the surface profile of SnO$_2$ films deposited by laser ablation of (a) a ceramic target (for a film thickness of 40 nm and scale factors of 100 nm for x, y and 5 nm for z) and (b) a metal target (for a film thickness of 30 nm and scale factors of 100 nm for x, y and 10 nm for z).

Fig. 2. XRD (CuK_α) spectra of the PZT/SnO$_2$/Al$_2$O$_3$ structures: (a) a 40-nm-thick SnO$_2$ film deposited by laser ablation of a ceramic target onto a ($10\bar{1}2$) Al$_2$O$_3$ substrate, and a 210-nm-thick PbZr$_{0.52}$Ti$_{0.48}$O$_3$ film deposited at $T =$ 375°C; (b) a 30-nm SnO$_2$ film deposited by laser ablation of a metallic target onto a (0001) Al$_2$O$_3$ substrate, and 250-nm-thick PZT film deposited by laser ablation from a Pb$_{0.95}$La$_{0.05}$Zr$_{0.2}$Ti$_{0.8}$O$_3$ target at $T =$ 670°C. Inset: X-ray rocking curve measured for the SnO$_2$ film near the (002) Bragg reflection.

0.15 Torr. Two types of sapphire substrates were used: (0001) c-cut and ($10\bar{1}2$) r-cut. Two rotating ceramic (SnO$_2$ + Sb$_2$O$_3$) or metallic (Sn:Sb) targets were synchronously ablated by two Q-switched YAG lasers ($\lambda =$ 1064 nm).[1] The pulse energy of these lasers was 200 mJ, and they had a width of 15 ns and a repetition rate of 25 Hz. The distance between the target and the substrate 35 mm. For the ceramic targets, it was necessary to install an additional screen to protect the substrate from direct hits by solid fragments of the target, which were several micrometers in size. However, this screen nearly halved the growth rate. Without a screen, the growth rate of an SnO$_2$ film was 70 Å/min.

Films deposited by laser ablation of a ceramic target onto an r-cut surface demonstrated a clearly pronounced (101) texture, but, in contrast to the films obtained in [10], they were polycrystalline (Figs. 1a, 2a). The average size of the SnO$_2$ crystallites can be esti-

mated as 400 nm (Fig. 1a). The Hall mobility of electrons in the SnO$_2$ films did not exceed 5 cm^2/(V s) at room temperature. Au/PZT/SnO$_2$ capacitors based on these structures had a low (<1 V) breakdown voltage or were short-circuited. We attribute these properties to the high density of through defects in an FE film. Since the thermal expansion coefficient of the used PZT composition nearly coincides with that of SnO$_2$, the high number of defects in the PZT films can be attributed to the coarse-grain structure of the SnO$_2$ surface.

Most of the films deposited by laser ablation of a metal Sn:Sb target onto a c-cut surface were single-crystal in form and had a finer surface profile than the films obtained from ceramic targets (Figs. 1b, 2b). The rocking curves (see the inset in Fig. 2b) indicate the

---

[1] Synchronous ablation of targets by two crossed beams gives rise to a vertical plasma torch with a reduced concentration of coarse fragments. This method significantly improves the surface morphology of a deposited film.
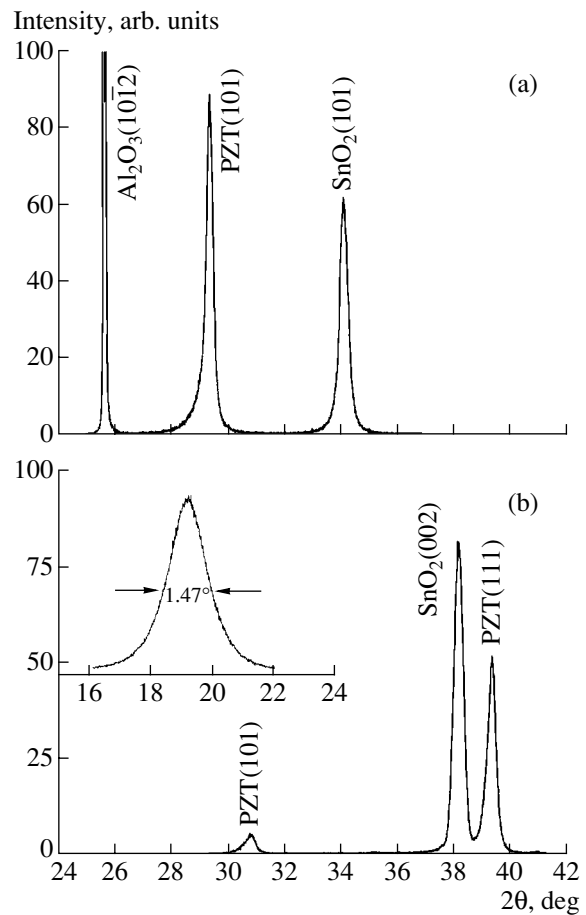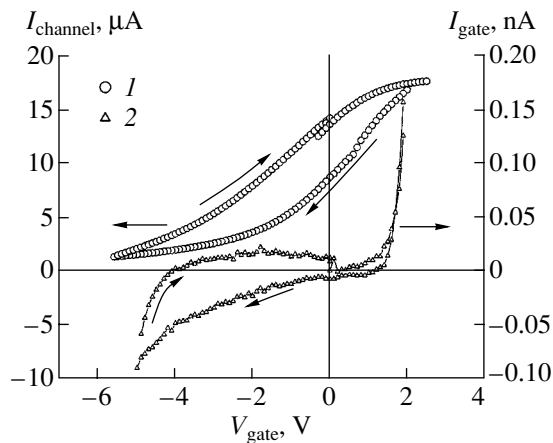
Fig. 3. (*1*) Channel current in a FFET vs. the gate voltage. (*2*) I–V characteristic of the gate. Channel resistance was 440 kΩ.

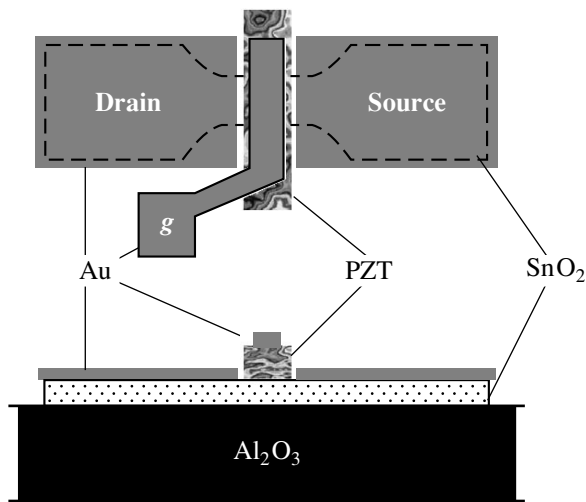**Fig. 4.** Structure of a model FFET. The channel thickness is 20 nm, the FE thickness is 300 nm, and the subgate region is $230 \times 320\ \mu m^2$. *g* Stands for gate.

domination of the single-crystal phase along with a (001) texture. At thicknesses above 60 nm, a polycrystalline phase and a diffraction peak from the (101) plane appears, which confirms the experimental data of [9], where a physical substantiation of the effect was also presented.

The deposition conditions, such as the oxygen pressure in the chamber and the distance between the target and the substrate, were optimized under experimental conditions so as to exclude the presence of unoxidized tin metal in the films.

The Hall mobility reached 25 $cm^2/(V\ s)$ at room temperature. The $Au/PZT/SnO_2$ capacitor cells based on these films, which had a top contact of $250 \times 250\ \mu m^2$ in area, demonstrated reproducible diode-type current–voltage (I–V) characteristics, with forward and

reverse breakdown voltages of no lower than 2 V. Figure 3 shows an *I–V* characteristic typical of thick (250–300 nm) PZT films.

3. FABRICATION OF PZT FILMS

3.1. Laser Ablation

$PbZr_xTi_{1-x}O_3$ films were deposited from ceramic targets possessing two different compositions, Zr/Ti = 20/80 and 52/48, with excess Pb. The lasers were operated in the same mode as for the SnO_2 films. The films were deposited in an oxygen atmosphere at a pressure of 0.15 Torr. The substrate temperature was varied between 375 and 670°C. The samples were cooled in a furnace in oxygen at atmospheric pressure.

As can be seen from the X-ray diffraction (XRD) spectra shown in Figs. 2a and 2b, PZT predominantly grows with a [111] texture on (001) SnO_2, and [101] texture on (101) the SnO_2 films.

X-ray fluorescence microanalysis using a Cameca machine showed that the composition of the films is fairly homogeneous over the film area, but it does not always correspond to stoichiometry. If targets without an excess of Pb are used, a Pb deficiency is observed in the grown films, which usually hinders the formation of the perovskite phase.

3.2. Magnetron Sputtering

$PbZr_{0.54}Ti_{0.46}O_3$ films doped with 3% Nb were deposited at a substrate temperature of 130°C. Annealing was performed at 570°C for 3 h (the samples were heated at the rate of 300 K/h and cooled over the course of 12 h with a furnace).

XRD spectra revealed that the PZT films had a polycrystalline structure, as reflections from all the crystal planes were present. A weak (111) texture was observed.

4. $Au/PZT/SnO_2/Al_2O_3$ HETEROSTRUCTURES

In the search for optimal deposition technology and to perform quick testing of electrical properties, we fabricated $Au/PZT/SnO_2/Al_2O_3$ capacitor structures. The contacts were deposited by thermal sputtering of Au onto a cold substrate through Si masks. The area of the top electrode was $250 \times 250\ \mu m^2$. As a result of the sufficiently high doping level for this type of film, the bottom common contact to the SnO_2:Sb film was ohmic.

A model transistor structure was also fabricated (Fig. 4). It differed from the structures studied in [12, 13] in that its SnO_2:Sb channel was grown on a single-crystal α-Al_2O_3 substrate. Under these circumstances, the electron mobility in the channel can reach ~40 $cm^2/(V\ s)$ [9–15], which is a high value for this material, even at a high doping level ~$10^{19}\ cm^{-3}$.
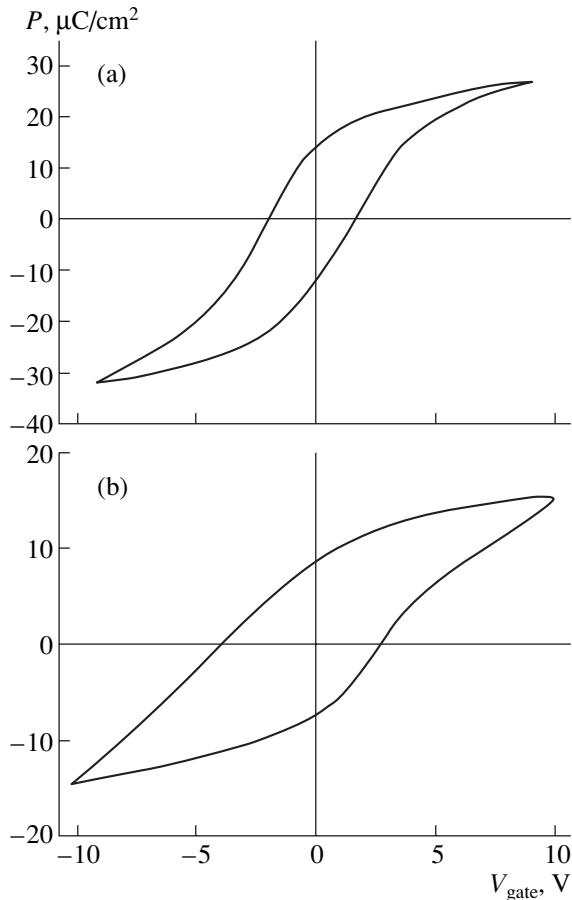
Fig. 5. FE hysteresis loops of Au/PZT/SnO$_2$/Al$_2$O$_3$ capacitor structures measured by the Sawyer–Tower method. (a) A PbZr$_{0.54}$Ti$_{0.46}$O$_3$:Nb film with a of thickness 300 nm, which was deposited by magnetron sputtering and annealed at T = 570°C. (b) A Pb$_{0.95}$La$_{0.05}$Zr$_{0.2}$Ti$_{0.8}$O$_3$ film with a thickness of 250 nm, with was deposited by a laser at T = 670°C.

5. EXPERIMENTAL RESULTS AND DISCUSSION

The highest measured capacitance of the laser-deposited Au/PZT/SnO$_2$/Al$_2$O$_3$ structures, where PZT represents Pb$_{0.95}$La$_{0.05}$Zr$_{0.2}$Ti$_{0.8}$O$_3$, was 1000 pF at a limiting voltage of ±10 V, the remnant polarization was 10 μC/cm^2, and the dielectric constant of PZT ε = 450.

In the transistor structure, the modulation of channel current, I–V characteristics, and hysteresis gate loops $P(V_{gate})$, were measured; here P is the FE polarization. FE hysteresis loops (Fig. 5) were measured using the Sawyer–Tower method at a frequency of 100 Hz.

At a donor concentration of 4×10^{19} cm^{-3}, the modulation of the channel conduction reached 94% (Fig. 3). The difference between the channel current at negative and positive remnant polarizations of the subgate FE was ~37%. The hysteresis loops of the gate $P(V_{gate})$ were similar to those for the capacitor structures (Fig. 5b).

It is noteworthy that, as can be ascertained from the "diode-type" shape of the I–V characteristic, PZT film behaves like a p-type semiconductor, which is usually related to the presence of Pb vacancies.

6. CONCLUSION

The possibility of fabricating FFETs based on a PZT/SnO$_2$ heterostructure has been demonstrated.

The highest quality SnO$_2$ films were obtained from laser ablation of a metallic target onto a c-cut sapphire at a substrate temperature of 670°C. The mobility in these films reached 25 cm^2/(V s) at the electron density 8×10^{19} cm^{-3}, and the Au/PZT/SnO$_2$ heterostructures demonstrated reproducible I–V characteristics that had a breakdown voltage of no less than 2 V.

The possibility of directly growing PZT/SnO$_2$ perovskite structures using magnetron and laser deposition was also studied. Under laser deposition onto a (001) SnO$_2$ film, PZT film predominantly grows in the [111] orientation, while, for deposition onto a (101) SnO$_2$ film, the PZT orientation is [101].

A model Au/PZT/SnO$_2$/Al$_2$O$_3$ FFET with 94% modulation of the channel conduction has been fabricated. The difference between the channel currents at positive and negative remnant polarizations of the subgate FE was 37%.

It is worth noting that, in contrast to [13], the obtained modulation of the channel current exhibits the so-called anomalous hysteresis loop: at the ascending branch of the gate bias V_{gate}, the current is higher than at the descending branch (Fig. 3, curve 1). This behavior of the modulation curve can be related to the electric field of charges that migrate in the ferroelectric, which induces a slow (in the range from several seconds to tens of minutes) charge variation at the SnO$_2$/PZT interface in an external electric field. The inversion of C–V characteristics from the normal to anomalous hysteresis at different rates of the bias application was observed in [16]; this behavior was attributed to a slow relaxation of charged states at the semiconductor–ferroelectric interface. A high concentration of migrating charges related to a deviation of the PZT composition from stoichiometry impairs the information storage when the transistor is used as a memory element. Nevertheless, we believe that this is not a fundamental problem and it can be resolved by improving the technology of the PZT film deposition.

REFERENCES

1. Shu-Yau Wu, IEEE Trans. Electron Devices **21**, 499 (1974).

2. T. Nakamura, Y. Nakao, A. Kamisawa, and H. Takasu, in *Proceedings of IEEE ISSCC* (San Francisco, 1955), p. 68.

3. H. Ishiwara, T. Shimamura, and E. Tokumitsu, Jpn. J. Appl. Phys. **36** (3B), 1655 (1997).

4. Yil Suk Yang, In-kyu You, Won Jae Lee, *et al.*, J. Korean Phys. Soc. **40**, 701 (2002).

5. Ali Sheikholeslami and P. Glenn Gulak, Proc. IEEE **88**, 667 (2000).

6. Y. Watanabe, Appl. Phys. Lett. **66**, 1770 (1995).

7. I. A. Veselovskiĭ, I. V. Grekhov, L. A. Delimova, and I. A. Liniĭchuk, Pis'ma Zh. Tekh. Fiz. **27** (1), 39 (2001) [Tech. Phys. Lett. **27**, 17 (2001)].

8. I. Grekhov, L. Delimova, I. Liniichuk, *et al.*, Integr. Ferroelectr. **43**, 175 (2002).

9. J. E. Dominguez, L. Fu, and X. Q. Pan, Appl. Phys. Lett. **79**, 614 (2001).

10. J. E. Dominguez, L. Fu, and X. Q. Pan, J. Appl. Phys. **89**, 6056 (2001); http://www.mse.engin.umich.edu/research/ centers/caem/mrsec/publications/SnO2 fPLD JAP0 1/SnO2 Epitaxy JAP01.pdf.

11. H. L. M. Chang, H. Zhang, Z. Shen, and Q. Wang, J. Mater. Res. **9**, 3108 (1994).

12. M. W. J. Prins, S. E. Zinnemers, J. F. M. Cillessen, and J. B. Giesbers, Appl. Phys. Lett. **70**, 458 (1997).

13. M. W. J. Prins, K.-O. Grosse-Holz, G. Muller, *et al.*, Appl. Phys. Lett. **68**, 3650 (1996).

14. M. W. J. Prins, K.-O. Grosse-Holz, J. F. M. Cillessen, and L. F. Feiner, J. Appl. Phys. **83**, 888 (1998).

15. J. E. Dominguez, L. Fu, and X. Q. Pan, Appl. Phys. Lett. **81**, 5168 (2002).

16. W. P. Li, R. Zhang, J. Shen, *et al.*, Appl. Phys. Lett. **77**, 24 (2000).

Translated by D. Mashovets